TECHNICAL UNIVERSITY OF MOLDOVA

JOURNAL OF ENGINEERING SCIENCE

Technical and applied scientific publication founded on 9 February 1995
Alternative title: Meridian ingineresc

2026
Vol. XXXIII (1)

ISSN 2587-3474
eISSN 2587-3482

TECHNICAL UNIVERSITY OF MOLDOVA (PUBLISHING HOUSE)
„TEHNICA UTM" (PRINTING HOUSE)

According to the Decision of the NAQAER No. 12 from 23.02.2024, JES is classified as B+ journal

Main subjects areas of the Journal of Engineering Science:

A. Industrial Engineering

- Mechanical Engineering and Technologies
- Applied Engineering Sciences and Management
- Materials Science and New Technologies
- Electrical Engineering and Power Electronics
- Light Industry, New Technologies and Design

B. Electronics and Computer Science

- Electronics and Communication
- Microelectronics and Nanotechnologies
- Biomedical Engineering
- Computers and Information Technology

C. Architecture, Civil and Environmental Engineering

- Architecture, Urbanism and Cadaster
- Civil Engineering and Management
- Energy Efficiency and New Building Materials
- Environmental Engineering

D. Food Engineering

- Food Technologies and Food Processes
- Food Industry and Management
- Biotechnologies, Food Chemistry and Food Safety

The structure of the journal corresponds to the classification of scientific publications: ***Engineering, Multidisciplinary.***

How to publish a paper:

1. Send the manuscript and information about the author to the **Editorial Board address:** jes@meridian.utm.md
2. Manuscripts are accepted only in English, by e-mail, in template file (www.jes.utm.md)
3. After a review, you will be notified of the editorial board's decision.
4. After the Journal has been published, we will send it to you immediately by mail.

Editor-in-Chief
Dr. hab. prof. univ. Viorel BOSTAN
Technical University of Moldova
viorel.bostan@adm.utm.md

Editorial Board

Responsible Editor
Dr. hab. Rodica STURZA
Editorial Board address: jes@meridian.utm.md

Editorial Production:
Dr. hab. Aliona Ghendov-Moșanu
Dr. Nicolae Trifan
Dr. Svetlana Caterinciuc
Dr. Rodica Cujba

CONTENT

CUPRINS

D. Food Engineering

Journal of Engineering Science *Vol. XXXIII, no. 1 (2026), pp. 8 - 20*
Fascicle *Industrial Engineering* *ISSN 2587-3474*
Topic *Mechanical Engineering and Technologies* *eISSN 2587-3482*

https://doi.org/10.52326/jes.utm.2026.33(1).01
UDC 621.67:532.5:004.94

APPLICATION OF FLUID-STRUCTURE INTERACTION SIMULATIONS IN THE OPTIMISATION CYCLE OF CENTRIFUGAL PUMP IMPELLERS

Viorel Bostan[1], ORCID: 0000-0002-2422-3538,
Andrei Petco[1,2*], ORCID: 0009-0004-0577-3296,
Dumitru Odainîi[1], ORCID: 0000-0001-6587-6247,
Dmitrii Croitor[1], ORCID: 0009-0005-9033-8543,
Vadim Zubac[1], ORCID: 0009-0002-5003-0729,
Nadejda Proca[1,2], ORCID: 0009-0004-7854-7599

[1] *Technical University of Moldova, 168 Stefan cel Mare Blvd., Chisinau, MD-2004, Republic of Moldova*
[2] *S.R.L. "CRIS" 68/2-69 Albisoara str., Chisinau, MD-2005, Republic of Moldova,*
* Corresponding author: Andrei Petco, *andrei.petco@if.utm.md*

Received: 12. 18. 2025
Accepted: 22. 01. 2026

Abstract. The integration of fluid-structure interaction (FSI) simulations into the design cycle of centrifugal pump impellers is an important part of this methodology, ensuring the safe conduct of bench tests. This study evaluates the behaviour of the CH 100/32-11-1 pump impeller using a combined numerical workflow involving ANSYS CFX and Mechanical. After a thorough analysis of mesh convergence, the hydraulic loads obtained from Computational Fluid Dynamics (CFD) data were transferred to the structural domain for quantitative assessment of equivalent stresses and strains. The analysis shows that the maximum equivalent stress for the optimised geometry is 24.45 MPa, which is within the tensile strength limit of PA12, confirming the feasibility of manufacturing a functional prototype using a Selective Laser Sintering (SLS). A comparative assessment with respect to the CH 6.3/20-1.1-2 and CH 100/125-75-5 models shows a non-linear scaling of structural loads, with the latter demonstrating critical failure stresses (51.7 MPa) exceeding the material's strength limits. The results confirm that the Fluid-Structure Interaction (FSI) numerical model is an important filter in the preparation stage for prototyping turbomachinery components using additive technologies.

Keywords: *Additive Manufacturing, Centrifugal pump, impeller, Computational Fluid Dynamics, Fluid-Structure Interaction.*

Rezumat. Integrarea simulărilor de interacțiune fluid-structură (FSI) în ciclul de proiectare al rotoarelor pompelor centrifuge este o parte importantă a acestei metodologii, asigurând efectuarea în siguranță a testelor pe banc de încercare. Acest studiu evaluează comportamentul rotorului pompei CH 100/32-11-1 utilizând un flux de lucru numeric combinat care implică ANSYS CFX și Mechanical. După o analiză amănunțită a convergenței plasei, încărcările hidraulice obținute din datele de Dinamică Computațională a Fluidelor (CFD) au fost transferate în domeniul structural pentru evaluarea cantitativă a tensiunilor și deformărilor echivalente. Analiza arată că tensiunea echivalentă maximă pentru geometria

optimizată este de 24,45 MPa, ceea ce se încadrează în limita de rezistență la tracțiune a PA12, confirmând fezabilitatea fabricării unui prototip funcțional utilizând sinterizarea selectivă cu laser (SLS). O evaluare comparativă în raport cu modelele CH 6.3/20-1.1-2 și CH 100/125-75-5 arată o scalare neliniară a încărcărilor structurale, acesta din urmă demonstrând tensiuni critice de rupere (51,7 MPa) care depășesc limitele de rezistență ale materialului. Rezultatele confirmă faptul că modelul numeric de interacțiune fluid-structură (FSI) este un filtru important în etapa de pregătire pentru prototiparea componentelor turbomașinilor folosind tehnologii aditive.

Cuvinte cheie: *fabricație aditivă, pompă centrifugă, rotor, dinamică computațională a fluidelor, interacțiune fluid-structură.*

1. Introduction

Centrifugal pumps are one of the most widely used types of pumps, serving as the primary means of transporting a wide range of liquids in various operating and outdoor conditions in industries such as chemical and petrochemical, food, pharmaceutical industry, food industry, mining [1] , energy sector [2,3] , as well as in areas such as water supply [4,5], wastewater treatment and agricultural irrigation. This type of pump is also quite common in the transport sector, from automotive and rail transport [6] to the aerospace industry [7].

It should also be noted that, in the context of the global drive for energy efficiency and carbon footprint reduction, many countries are setting targets for improving energy efficiency. The current global drive for economic efficiency and environmental sustainability is clearly reflected in the 2015 Paris Agreement on climate change. In order to fulfil the commitments made by the EU under this agreement, a number of measures have been taken, including a commitment by EU governments to pay particular attention to energy efficiency and to set a target of increasing energy efficiency by at least 32.5% by 2030 (compared to 2020) [8,9].

These commitments are forcing manufacturers [10,11], including centrifugal pump manufacturers, to optimise the design of their equipment [12,13]. Thus, the optimisation of centrifugal pump flow parts has evolved from a purely engineering task into an economic and environmental requirement. According to the American Hydraulic Institute, pumps account for up to 20% of energy consumption in developed countries [14,15] . At the same time, a life cycle cost (LCC) analysis of pump units shows that the initial capital costs of purchasing equipment account for only about 10-15% of total costs, with the rest being energy and maintenance costs [15]. The problem of optimising the flow parts of pumps, primarily the impellers, is a pressing one, and even a slight increase in hydraulic efficiency at the design and optimisation stage of the impeller design can lead to significant long-term resource savings, offsetting the operating costs associated with energy consumption.

However, the problem of optimisation is not limited to energy performance. Modern operating conditions often force pump units to operate in modes that are far from the Best Efficiency Point (BEP), which leads to the occurrence of unsteady hydraulic phenomena such as reverse currents, vortex formation in inter-blade channels and cavitation [16–18]. These processes not only reduce the energy efficiency, but also generate intense pressure pulsations, causing increased vibration and fatigue wear of structures.

Traditional design methodologies based on empirical data [19,20], combined with iterative testing of physical prototypes, are inefficient due to their labour intensity and long development times. The geometry of the impeller is characterised by a number of interrelated

variables, including blade angles β, meridional section shape, etc., which in turn means that changing any of these factors leads to a non-linear response of the system, making impeller modelling in modern conditions extremely difficult without the use of CFD simulations.

Since the application of direct optimisation methods in conjunction with CFD calculations requires significant computing power and cannot be performed with a large number of geometric parameters, surrogate modelling methods such as the Kriging method [21], artificial neural networks (ANN) [22] and methods based on the Response Surface Methodology (RSM) [23–25] have become widely used. The construction of a response surface allows the dependence of target functions on geometric parameters to be approximated, after which a global search for the optimum is carried out using stochastic optimisation algorithms, such as genetic (evolutionary) algorithms, for example NSGA-II [5,26,27].

Despite the widespread use of this class of pumps [19], conditions at customer facilities and in the systems that serve them dictate operating requirements that often cannot be predicted by classical models [19,28] of materials science and hydrodynamics, which often leads to significant deviations from the parameters in BEP. Under extreme conditions, the assumption of steady-state operation loses its relevance, and dynamic factors such as rotor-stator interaction (RSI), pulsation, inlet recirculation and cavitation have an increasing influence [18,29]. The complexity of the fluid flow structure in the flow path of centrifugal pumps, coupled with their importance for various industrial sectors, makes the simulation of the dynamic interaction between hydraulic forces and rotor design one of the central areas of the research in the field of pump reliability.

When using surrogate modelling methods for pump impellers, the resulting geometric models require experimental validation, especially when it comes to optimised shapes with complex geometry. It is extremely important to study the interaction between the fluid and the structure (FSI) during the operation of a centrifugal pump, especially for impellers without a shroud as well as prototypes of impellers created using additive technologies. An impeller optimised exclusively on the basis of hydrodynamic efficiency may have insufficient rigidity or natural frequencies that coincide with the blade pitch frequency, which will lead to resonance. Ignoring blade deformations under the action of hydrodynamic loads and centrifugal forces can distort the calculated geometry of the flow path, negating the results of optimisation. To verify the obtained geometry, an FSI analysis is performed, implemented directly into the optimisation cycle, considering vibrations [30] and stresses [16,31] as limiting factors or additional objective functions. This approach allows the creation of a pump design that not only has good energy characteristics but also structural reliability, enabling it to withstand intense dynamic loads.

Figure 1. Optimisation pipeline.

Mathematical modelling of FSI in turbomachinery is a complex multiphysics simulation task that requires simultaneous solution of equations describing fluid motion and structural deformation.

The flow is modelled using Navier-Stokes equations, specifically their Reynolds-averaged variant (Reynolds Navier-Stokes averaging, RANS), to account for the moving boundaries of the deforming impeller.

The RANS turbulence model is a statistical turbulence model due to the use of the corresponding averaging method used to formulate the equations. The application of averaging processes requires the introduction of additional unknown terms consisting of products of variable quantities that serve as additional stress factors in the fluid.

Given that the study was conducted under steady-state conditions, a turbulence model based on the Reynolds-Averaged Navier-Stokes (RANS) (Eq.1 and 2) equations was selected. This approach employs statistical averaging to derive the governing equations, which significantly reduces the computational resources needed [32–34].

$$\frac{\partial \overline{u_i}}{\partial x_j} = 0 \tag{1}$$

$$\overline{u_j}\frac{\partial \overline{u_i}}{\partial x_j} - \frac{\partial}{\partial x_j}\left[(\nu - \nu_T)\left(\frac{\partial \overline{u_i}}{\partial x_j} - \frac{\partial \overline{u_j}}{\partial x_i}\right)\right] + \frac{1}{\rho}\frac{\partial \overline{\tilde{p}}}{\partial x_j} = 0 \tag{2}$$

The monolithic approach solves the equations of fluid motion and structural deformation within a single mathematical model, ensuring strict conservation of energy at the interface and reliability for problems with a strong added mass effect, but due to its high computational cost, it is used less frequently. It should also be noted that the mechanical characteristics of materials used in additive manufacturing are characterised by small deformations, so in the case of this study, preference was given to a split approach, in which the fluid motion and structural deformation domains are solved separately and linked via boundary conditions at the interface.

Within the framework of the split approach, a one-way connection is used, which ignores the feedback of structural deformation with the flow field, which is sufficient for static stress analysis.

When using this method, the iterative feedback loop of the two-way connection is not taken into account, which significantly speeds up the process.

The choice of structural material for additive manufacturing of centrifugal pump impeller prototypes is dictated by the need to ensure sufficient specific strength and rigidity. As part of the digital research, a comparative analysis of the properties of three common thermoplastics was also carried out: polyamide-12 (PA-12 Industrial), acrylonitrile butadiene styrene (ABS) and polyethylene terephthalate glycol (PETG).

Most of the calculations presented were performed on PA-12 simulating the use of the selective laser sintering (SLS) method.

This material demonstrates a high degree of isotropy of mechanical properties and structural integrity. According to a study [35], sintered PA-12 samples are characterised by a tensile strength in the range of 45–50 MPa, which correlates with the manufacturer's declared value for the PA-12 Industrial material used (48.7 MPa) [36]. A key advantage of PA-12 is its ability to undergo plastic deformation before failure and its high impact strength, which is critical for preventing failure under pulsation loads resulting from rotor-stator interaction [37]. Unlike polyamides, materials used in extrusion technologies, such as ABS and PETG, exhibit pronounced anisotropy of properties depending on the orientation of the print layers [38].

2. Materials and Methods

A CH 100/32-11-1 centrifugal canned monoblock pump was selected as the base object for numerical modelling and verification. This unit belongs to the class of single-stage centrifugal pumps and is characterised by the following design parameters (Table 1).

Table 1

CH 100/32-11-1 (4) Pump parameters

Parameter	Designation	Value	Units
Nominal flow rate	Q_{nom}	100	m^3/h
Nominal head	H_{nom}	32	m
Working feed interval	Q_{op}	65...140	m^3/h
Permissible cavitation margin	$NPSH_r$	3.5	m
Nominal motor power	P_n	11.0	kW
Temperature of pumped liquid	T	-40...+40	°C
Cooling type	-	W/L (Air)	-

The CFD part of the study was performed in ANSYS CFX. A detailed full-scale hydraulic model was used for the CFD simulation, including the suction pipe, rotating impeller, and casing volute discharge. The stationary and rotating domains were connected via a common Frozen rotor interface to maintain mass and momentum conservation during the transition between frames. The exact implementation of the boundary conditions is schematically shown in Fig. 2.

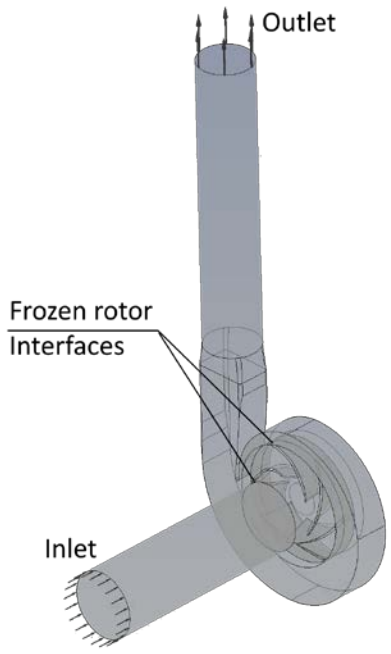

Figure 2. Geometric model with initial and boundary conditions specified.

The boundary condition at the Inlet was characterised by a total pressure condition P_{inlet} = 10 m. The inlet flow assumes a single-phase liquid water medium with a turbulence intensity of 1%, in accordance with recommendations for real pumping systems to obtain a stable upstream flow.

A mass flow boundary condition Q_{outlet} = 31 kg/s was set at the Outlet of the domain. For transport variables related to turbulence at the outlet, a zero gradient condition was implemented at the outlet of the calculation domain. The simulation was performed under isothermal conditions at a liquid temperature of 25 °C, with a reference pressure set at P_{ref}= 0 atm. A rotation speed of n = 2950 min^{-1} was specified for the impeller domain.

Due to significant computational costs and the formulation of the problem using the FSI one-way coupling model, the Reynolds-Navier-Stokes (RANS) equations were solved using a steady-state formulation. In this research, the SST (Menter's Shear Stress Transport) turbulence model, eq. (3) and (4), is used [39]:

$$\frac{\partial(\rho k)}{\partial t}+\frac{\partial\left(\rho u_j k\right)}{\partial x_j}=P-\beta^*\rho\omega k+\frac{\partial(\rho k)}{\partial x_j}\left[(\mu+\sigma_k\mu_t)\frac{\partial k}{\partial x_j}\right] \tag{3}$$

$$\frac{\partial(\rho\omega)}{\partial t}+\frac{\partial\left(\rho u_j\omega\right)}{\partial x_j}=\frac{\gamma}{v_t}P-\beta\rho\omega^2+\frac{\partial}{\partial x_j}\left[(\mu+\sigma_\omega\mu_t)\frac{\partial\omega}{\partial x_j}\right]+2(1-F_1)\frac{\rho\sigma_{\omega2}}{\omega}\frac{\partial k}{\partial x_j}\frac{\partial\omega}{\partial x_j} \tag{4}$$

where: xj represents the partial spatial coordinates, with the subscript j indicating the spatial directions (x, y, z), uj denotes the mean flow velocity components in the j- direction, k is the turbulent kinetic energy, ω represents the specific dissipation rate, μ is the dynamic viscosity, νt is the turbulent kinematic viscosity, μt is the turbulent (eddy) viscosity, ρ is the fluid density and P is the turbulence production term.

Convergence conditions were chosen to attain convergence while optimising computational resources. A finite total of 1000 iterations for calculations were designated, and the computations also conclude when a tolerance level for the root mean square residual error of 10^{-6} is attained. This method guarantees numerical convergence with reduced execution time. CFD calculation results are presented in Fig. 3.

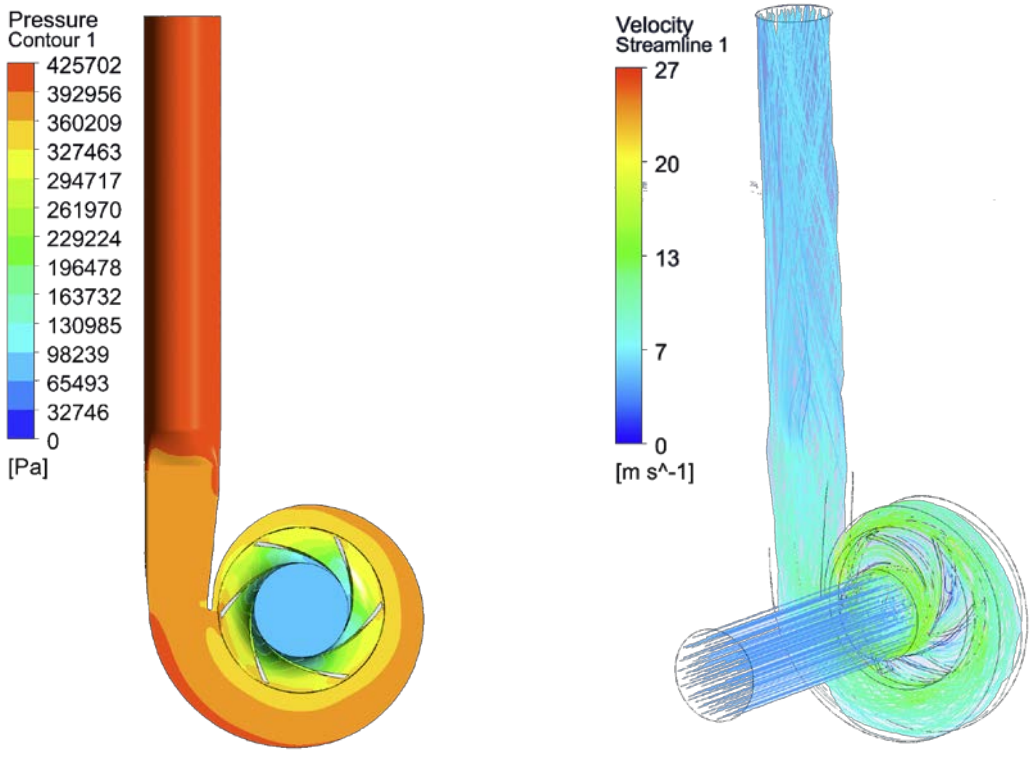

(a) (b)

Figure 3. Pressure field distribution and streamlines indicating flow velocity.

In the next stage of the study, the data obtained in the CFD simulation using the ANSYS Workbench platform was transferred to ANSYS Mechanical. The simulation area was limited to the impeller itself and its associated components, namely the shaft and bearings (Fig. 4). Simplifying the shaft and bearings is a common approach in such tasks, where the main focus is on the impeller design [30].

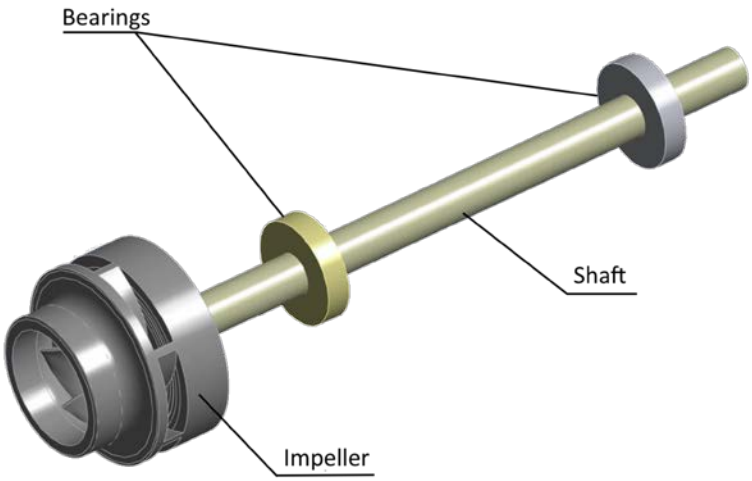

Figure 4. Geometric model used in FSI simulation.

A fragment of the discretised geometric model used in this calculation is shown in Fig. 5. To achieve an optimal compromise between computational efficiency and numerical accuracy, the shaft and bearing components were discretised using a maximum element size of ΔS = 2.5 mm. In contrast, the impeller, being a critical component with complex geometry, required a finer discretisation; a maximum element size of ΔS = 0.9 mm was applied to accurately solve the problem. In the final calculation, a grid with $9.037 \cdot 10^6$ elements was used.

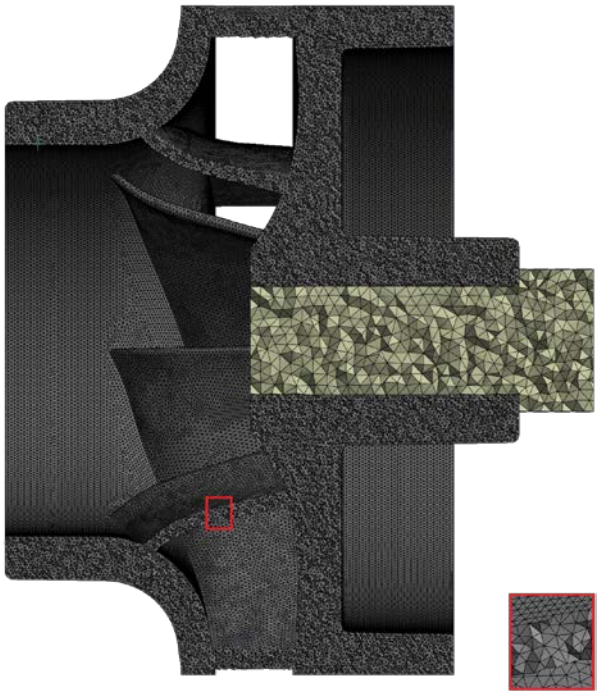

Figure 5. Discretisation model.

In order to verify the accuracy of the results obtained, a convergence analysis was performed. Its results are presented in Fig. 6. It can be noted that convergence was achieved for all parameters: deformation, displacement, and stress.

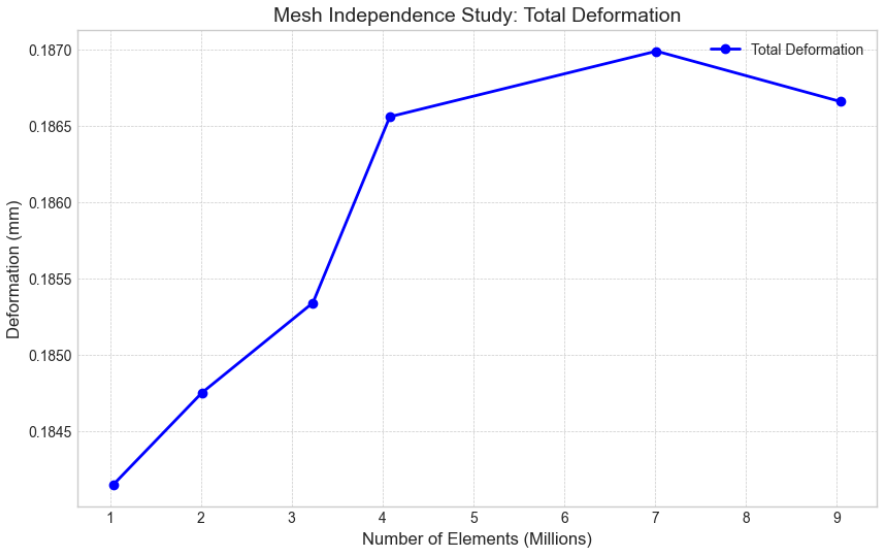

(a)

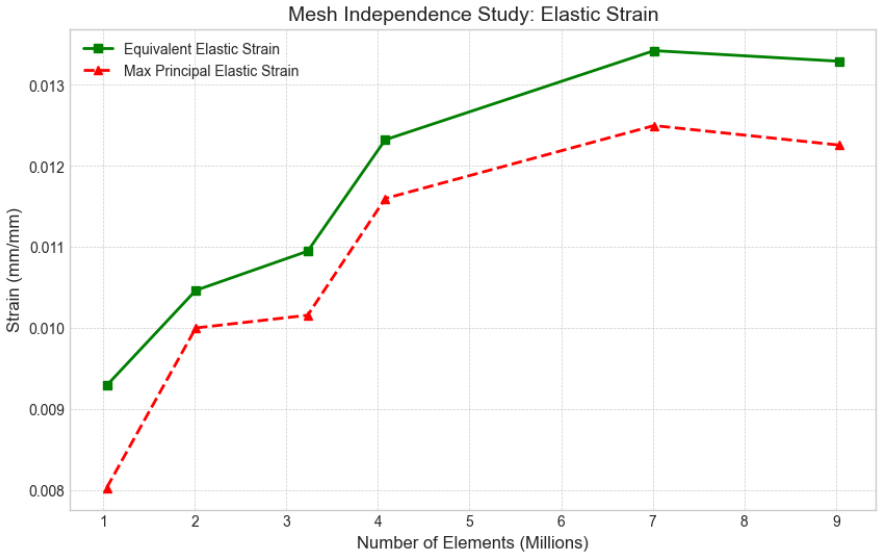

(b)

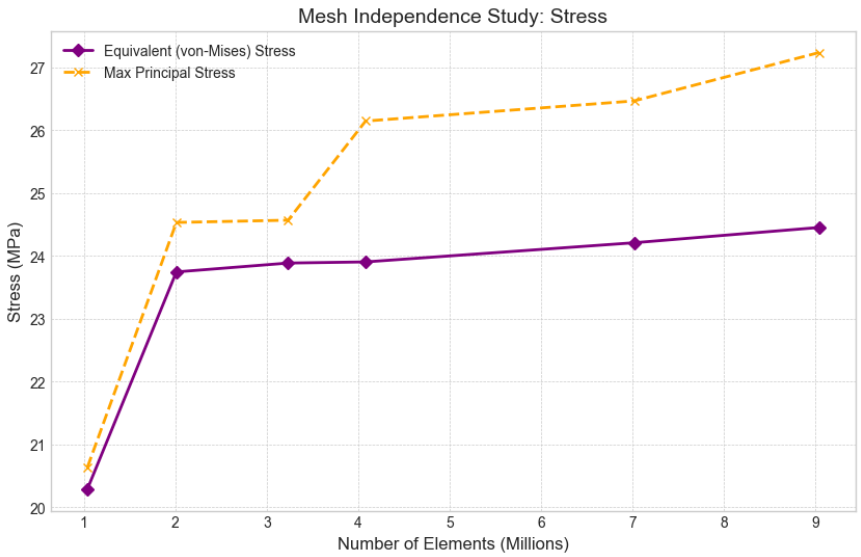

(c)

Figure 6. Convergence plots for: a) Deformation vs. Number of elements in mesh, b) Strain vs. Number of elements in mesh, c) Stress vs. Number of elements in mesh.

The study of stresses and deformations was carried out using the Transient-Structural module from ANSYS Mechanical. The calculation is based on the equation of motion of a linearly elastic body, which in matrix form (Eq. 5) is represented by the following mathematical model [40]:

$$M_s\ddot{u} + C_s\dot{u} + K_s u = F_s\,, \tag{5}$$

where: u denotes the displacement vector, $\dot{u}$ - velocity vector, $\ddot{u}$ - acceleration vector, M_s - the mass matrix, C_s - damping matrix, K_s - stiffness matrix and F_s represents the applied vector.

Considering the equivalent stiffness of the link, we derived the Eq.6 [31]:

$$M_s\ddot{u} + C_s\dot{u} + K_s u + K_{fs}p = F_s\,, \tag{6}$$

where:$K_{fs} = -R$ represents the equivalent stiffness and p denotes the fluid pressure.

3. Results

The calculation results show that the equivalent stress reaches 24.45 MPa, which is still less than the tensile strength of the PA-12 Industrial material (48.7 MPa). It should also be noted that the deformations are within the normal range. This means that this impeller prototype can be produced using the SLS method and tested for hydraulic characteristics (Fig. 7).

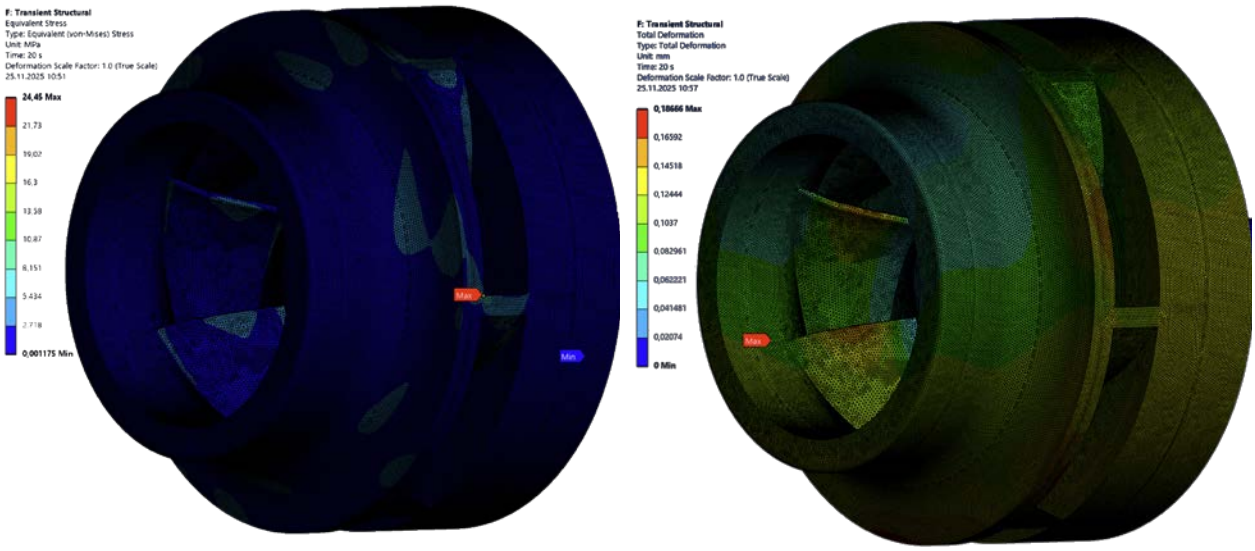

Figure 7. Simulation results for pump CH 100/32-11-1.

Using a similar pipeline, the results for two more pumps, CH 6.3/20-1.1-2 and CH 100/125-75-5, were analysed. The parameters of these two pumps are presented in Table 2.

Table 1

Pump characteristics

Model	CH 6.3/20-1.1-2	CH 100/32-11-1	CH 100/125-75-5
Nominal flow rate Q_{nom} , m^3/h	6.3	100	100
Nominal head H_{nom}, m	20	32	125
Motor power N, kW	1.1	11	75
Specific speed, n_q	13	36.5	13.2

In the case of the CH 6.3/20-1.1-2 pump, the equivalent stress was 11.809 MPa, which allows the prototype of this impeller made of PA-12 to be used in bench tests, but for the CH 100/125-75-5 pump, the equivalent stress was already 51.7 MPa, a value that exceeds the strength limit of this material (Fig. 8).

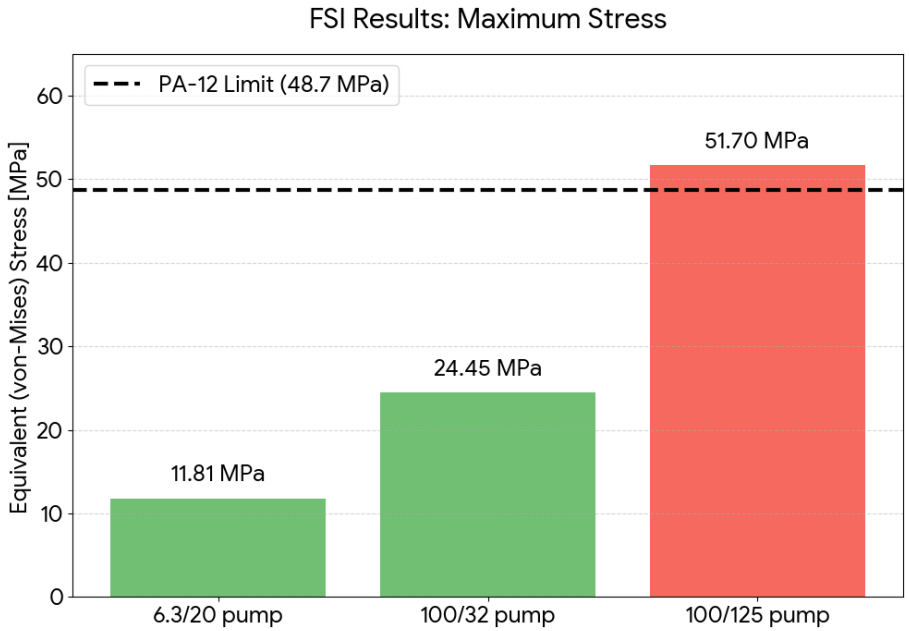

Figure 8. Equivalent stress values obtained during FSI simulation.

If we analyse and compare the stress distribution in the CH 100/32-11-1 pump impeller with the distribution obtained for the CH 100/125-75-5 pump (Fig. 9), we can see that the stress pattern is similar. The area with the highest stress is the outer part of the impeller. It should also be noted that the main stress concentrator is located at the blade outlet in the area of the junction with the hub and shroud surfaces.

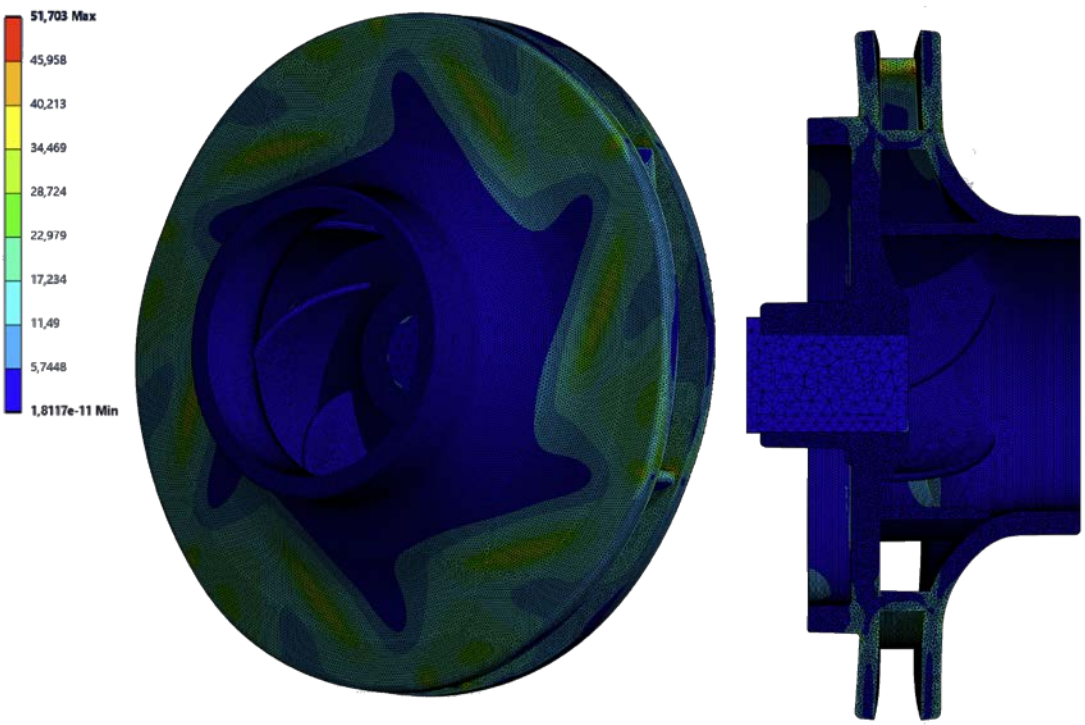

Figure 9. Stress distributions obtained in simulations for pump CH 100/125-75-5.

4. Discussion

The data obtained in the study are important for developers of this type of pump in the Republic of Moldova and can be used in optimisation cycles to obtain new pump components, with the aim of expanding the range of centrifugal pumps and thus increasing the competitiveness of enterprises producing centrifugal pumps in Moldova. As a direction for further research, the authors plan to continue developing a line of centrifugal pumps with different parameters, incorporating FSI simulation into the optimisation cycle.

5. Conclusions

This study successfully demonstrates the application of a joint CFD/FEA workflow to verify the structural integrity of impeller prototypes intended for additive manufacturing using PA12 Industrial.

The results obtained for the CH 100/32-11-1 pump confirm the suitability of PA12 material for this specific hydraulic specification. Numerical results indicate a maximum equivalent stress of 24.45 MPa under nominal operating conditions. When compared to the material's tensile strength limit of 48.7 MPa, this gives a safety factor of approximately 2.0. The CH 100/32-11-1 prototype has been tested for structural reliability for production using SLS technologies and subsequent experimental verification of its hydraulic characteristics.

A comparative analysis was performed for pumps of different sizes, which highlights the limitations of the application of this material. While the CH 6.3/20-1.1-2 model demonstrated a maximum equivalent stress value of 11.8 MPa, which is significantly below the critical threshold, the larger CH 100/125-75-5 model demonstrated the limits of the polymer's application. In the latter case, the equivalent stress reached 51.7 MPa, exceeding the structural capacity of the industrial material PA12. This fact represents a non-linear relationship between pump size, hydraulic power and structural load and serves as evidence of the need to use FSI simulation in the optimisation cycle.

The resulting stress distribution is uneven, but similar in shape for all three pumps. Critical stress concentration zones are invariably located at the rear edge of the blade, in particular at the joints with the surfaces of the impeller's hub and shroud. This localization is explained by the superposition of the centrifugal forces of the body and the maximum pressure difference occurring at the outlet of the impeller. Thus, the presented numerical model confirms the possibility of using PA12 Industrial for prototyping impellers using CFD/FSI simulation to evaluate mechanical properties.

Acknowledgments: This research is financially supported by the National Agency for Research and Development, research programme: "Young researchers", Financing agreement no. 159TC. "Optimising the energy efficiency of centrifugal pumps using CFD methods and algorithms based on Artificial Intelligence." Period: 2025-2026

Conflicts of Interest: The authors declare no conflict of interest.

References

1. Yuan, J., Shi, J., Fu, Y., Chen, H., Lu, R. & Hou, X. (2022) Analysis of fluid-structure coupling dynamic characteristics of centrifugal pump rotor system. *Energies,* 15, 2133.
2. Bogdanovic-Jovanovic, J., Stamenkovic, Z., Kocić, M. & Petrović, J. (2024) Performance prediction of centrifugal norm pumps operating as turbines. *Fluids,* 9, 190.
3. Renzi, M. & Rossi, M. (2019) A generalized theoretical methodology to forecast flow coefficient, head coefficient and efficiency of pumps-as-turbines (PaTs). Vol. 158, p. 134.

4. Bostan, V. & Petco, A. (2023) Study of the empirical models' applicability for calculating the centrifugal pump's impellers geometric parameters. *Journal of Engineering* Science, pp. 8–22.
5. Bostan, V. & Petco, A. (2024) Design and optimization of the centrifugal pump impeller for wastewater. Vol. 46, pp. 362–369.
6. Liu, H., Jiang, L., Wang, Y., Hočevar, M., Yan, J. & Chen, J. (2022) Optimization and CFD performance analysis of an automotive coolant pump. *Advances in Mechanical Engineering*, 14, 168781322210816.
7. Malael, I. & Gherman, G.B. (2018) Numerical investigation of a new LH2 centrifugal pump concept used in space propulsion. *INCAS Bulletin*, 10, 65–74.
8. Ciucci, M. (2023) Politica energetică: principii generale. Available online: https://eur-lex.europa.eu/legal-content/RO/TXT/PDF/?uri=CELEX:32023L1791 (Accessed: 15.11.2025).
9. Document de reflecție (2019) Către o Europă durabilă până în 2030. Available online: https://eur-lex.europa.eu/legal-content/RO/TXT/PDF/?uri=CELEX:32023L1791 (Accessed: 15.11.2025).
10. Stroncea, A., Toca, A. & Nițulenco, T. (2023) Considerations regarding the optimal dimensional design of machining technologies. *ACTA TECHNICA NAPOCENSIS - Series: Applied Mathematics, Mechanics, and Engineering*, 66.
11. Mazuru, S. & Scaticailov, S. (2023) New technological solution for manufacturing precessional gears with non-standard profile. *ACTA TECHNICA NAPOCENSIS - Series: Applied Mathematics, Mechanics, and Engineering*, 66.
12. Kim, B., Siddique, M.H., Samad, A. & Lee, D.-E. (2022) Optimization of centrifugal pump impeller for pumping viscous fluids using direct design optimization technique. *Machines,* 10, 774.
13. Górecki, J., Klimentov, K., Popov, G., Kostov, B. & Ibrahim, S. (2024) Studying the impact of diffuser return guide vanes on the energy performance of a multistage centrifugal pump. *Applied Sciences,* 14, 10991.
14. Kaya, D., Yagmur, E.A., Yigit, K.S., Kilic, F.C., Eren, A.S. & Celik, C. (2008) Energy efficiency in pumps. *Energy Conversion and Management*, 49, 1662–1673.
15. National Renewable Energy Laboratory (NREL) (n.d.) Pump life cycle costs: A guide to LCC analysis for pumping systems: Executive summary. Available online: https://docs.nrel.gov/docs/fy01osti/29084.pdf (Accessed: 15.11.2025).
16. Arocena, V.M. & Danao, L.A.M. (2023) Improving the modeling of pressure pulsation and cavitation prediction in a double-volute double-suction pump using mosaic meshing technology. *Processes,* 11, 660.
17. Li, Y., Feng, G., Li, X., Si, Q. & Zhu, Z. (2018) An experimental study on the cavitation vibration characteristics of a centrifugal pump at normal flow rate. *Journal of Mechanical Science and Technology*, 32, 4711–4720.
18. Bostan, V. & Petco, A. (2025) Analysis of cavitation phenomenon as a criterion for optimization of centrifugal pump design. *ACTA TECHNICA NAPOCENSIS - Series: Applied Mathematics, Mechanics, and Engineering*, 68.
19. Gülich, J.F. (2020) Centrifugal Pumps. Cham: *Springer International Publishing*.
20. Lobanoff, V.S. & Ross, R.R. Centrifugal Pumps: Design and Application. Available online: https://www.abebooks.com/9780872012004/Centrifugal-Pumps-Design-Application-Lobanoff-087201200X/plp (Accessed: 15.11.2025).
21. Xu, K., Wang, G., Wang, L., Yun, F., Sun, W., Wang, X. & Chen, X. (2020) Parameter analysis and optimization of annular jet pump based on Kriging model. *Applied Sciences*, 10, 7860.
22. Drăgan, V., Dumitrescu, O., Dobromirescu, C. & Popa, I.F. (2024) Satellite thermal management pump impeller design and optimization. *Inventions,* 9, 54.
23. Bostan, V. & Petco, A. (2024) Minimizing blade-fluid energy losses in centrifugal hydraulic pump impellers. *ACTA TECHNICA NAPOCENSIS - Series: Applied Mathematics, Mechanics, and Engineering*, 67.
24. Cao, W., Wang, H., Yang, X. & Leng, X. (2023) Optimization of guide vane centrifugal pumps based on response surface methodology and study of internal flow characteristics. *Journal of Marine Science and Engineering*, 11, 1917.
25. Pagayona, E. & Honra, J. (2024) Multi-criteria response surface optimization of centrifugal pump performance using CFD for wastewater application. *Modelling,* 5, 673–693.
26. Shojaeefard, M.H., Hosseini, S.E. & Zare, J. (2019) CFD simulation and Pareto-based multi-objective shape optimization of the centrifugal pump inducer applying GMDH neural network, modified NSGA-II, and TOPSIS. *Structural and Multidisciplinary Optimization*, 60, 1509–1525.
27. Zhang, J., Zhu, H., Yang, C., Li, Y. & Wei, H. (2011) Multi-objective shape optimization of helico-axial multiphase pump impeller based on NSGA-II and ANN. *Energy Conversion and Management*, 52, 538–546.
28. Bostan, V., Petco, A. & Șaragov, I. (2023) Empirical models' applicability for calculating the centrifugal pump's impellers geometric parameters. *Journal of Engineering Science*, 30, 8–19.

29. Shen, Z., Wang, C., Zhang, J., Qiu, S. & Lin, R. (2024) Study on part-load cavitation in high-specific-speed centrifugal pump. *Water,* 16, 2180. doi:10.3390/w16152180.
30. Yuan, J., Shi, J., Fu, Y., Chen, H., Lu, R. & Hou, X. (2022) Analysis of fluid-structure coupling dynamic characteristics of centrifugal pump rotor system. *Energies,* 15, 2133.
31. Yin, T., Pei, J., Yuan, S., Osman, M., Wang, J. & Wang, W. (2017) Fluid-structure interaction analysis of an impeller for a high-pressure booster pump for seawater desalination. *Journal of Mechanical Science and Technology*, 31, 5319–5328.
32. Nonino, M., Ballarin, F. & Rozza, G. (2021) A monolithic and a partitioned, reduced basis method for fluid–structure interaction problems. *Fluids,* 6, 229.
33. Benra, F.-K., Dohmen, H., Pei, J. & Schuster, S. (2011) A comparison of one-way and two-way coupling methods for numerical analysis of fluid-structure interactions. *Journal of Applied Mathematics*.
34. Li, W., Ji, L., Shi, W., Zhou, L., Jiang, X. & Zhang, Y. (2016) Vibration characteristics of the impeller at multi-conditions in mixed-flow pump under the action of fluid-structure interaction. *Journal of Vibroengineering*, 18, 3213–3224.
35. Goodridge, R.D., Tuck, C.J. & Hague, R.J.M. (2012) Laser sintering of polyamides and other polymers. *Progress in Materials Science,* 57, 229–267.
36. Sinterit (n.d.) PA12 Industrial Powder | Polyamide 12 for 3D Printing | Sinterit. Available online: https://sinterit.com (Accessed: 15.11.2025).
37. Greiner, S., Wudy, K., Lanzl, L. & Drummer, D. (2017) Selective laser sintering of polymer blends: Bulk properties and process behavior. *Polymer Testing*, 64, 136–144.
38. Tymrak, B.M., Kreiger, M. & Pearce, J. (2014) Mechanical properties of components fabricated with open-source 3-D printers under realistic environmental conditions. *Materials & Design,* 58, 242–246.
39. Menter, F.R. (1994) Two-equation eddy-viscosity turbulence models for engineering applications. *AIAA Journal*, 32, 1598–1605.
40. Fu, Y., Yuan, J., Yuan, S., Pace, G., d'Agostino, L., Huang, P. & Li, X. (2015) Numerical and experimental analysis of flow phenomena in a centrifugal pump operating under low flow rates. *Journal of Fluids Engineering*, 137, 011102.

Citation: Bostan, V., Petco, A., Odainii, D., Croitor, D., Zubac, V., Proca, N. (2026). Application of fluid-structure interaction simulations in the optimisation cycle of centrifugal pump impellers. *Journal of Engineering Science*. 2026, 33 (1), pp. 8-20. https://doi.org/10.52326/jes.utm.2026.33(1).01.

Submission of manuscripts: jes@meridian.utm.md

Journal of Engineering Science *Vol. XXXIII, no. 1 (2026), pp. 21 - 36*
Fascicle *Industrial Engineering* *ISSN 2587-3474*
Topic *Materials Science and New Technologies* *eISSN 2587-3482*

https://doi.org/10.52326/jes.utm.2026.33(1).02
UDC 544.6:621.382: 539.2

THEORETICAL PRINCIPLES GOVERNING ELECTROCHEMICAL IMPEDANCE SPECTROSCOPY IN NANOSTRUCTURED SEMICONDUCTOR ELECTRODES

Simon Busuioc*, ORCID: 0009-0006-2601-4015

National Center for Materials Study and Testing, Technical University of Moldova, Stefan cel Mare Blvd. 168, Chisinau, MD-2004, Republic of Moldova
* Corresponding author: Simon Busuioc, *simon.busuioc@cnstm.utm.md*

Received: 12. 18. 2025
Accepted: 25. 01. 2026

Abstract. Electrochemical impedance spectroscopy (EIS) provides a powerful means of probing interfacial and charge-transport phenomena in semiconductor electrodes, yet interpretation becomes increasingly difficult when applied to nanostructured materials. Semiconductor nanowires, nanotubes, and porous films exhibit high surface areas, heterogeneous morphologies, and defect-rich interfaces, all of which modify their impedance response. Theoretical principles regarding EIS behavior in such systems are presented, beginning with semiconductor–electrolyte junction formation, space-charge layer development, band bending and the influence of surface states. Key elements of equivalent-circuit descriptions are examined, including double-layer capacitance, charge-transfer resistance and diffusion-related impedance contributions. Special emphasis is placed on constant-phase elements and distributed models required to capture non-ideal capacitive behavior characteristic of nanoscale electrodes. Common challenges in spectral interpretation, such as overlapping time constants, non-uniform current distribution and deviations from classical Randles-type responses, are summarized within a unified theoretical framework to support reliable modelling and analysis.

Keywords: *Electrochemical response, nanostructured semiconductors, space-charge layer, charge-transfer resistance, equivalent circuit.*

Rezumat. Spectroscopia de impedanță electrochimică (EIS) reprezintă un instrument puternic pentru investigarea fenomenelor interfaciale și a transportului de sarcină în electrozii semiconductori, însă interpretarea devine semnificativ de complexă în cazul materialelor nanostructurate. Nanofirele, nanotuburile și peliculele poroase pe bază de semiconductori se caracterizează prin suprafețe mari, morfologii heterogene și interfețe bogate în defecte, factori care influențează profund răspunsul în impedanță. În această lucrare sunt expuse principiile teoretice esențiale ale comportamentului EIS în astfel de sisteme, începând cu formarea joncțiunii semiconductor–electrolit, dezvoltarea stratului de sarcină spațială, îndoirea benzilor de energie și influența stărilor de suprafață. Sunt analizate elementele cheie ale circuitelor echivalente — inclusiv capacitatea dublu strat, rezistența la transfer de sarcină și contribuțiile impedanței asociate cu difuziunea. Se acordă o atenție specială elementelor cu fază constantă (CPE) și modelelor de circuit care descriu diferențele spațiale ale

proprietăților electrochimice pe diferite regiuni ale structurii electrodului, necesare pentru a surprinde comportamentul capacitiv neideal caracteristic electrozilor la scala nanometrică. Provocările comune în interpretarea spectrelor, precum constantele de timp suprapuse, distribuția neuniformă a curentului și abaterile față de răspunsurile clasice de tip Randles, sunt integrate într-un cadru teoretic unitar pentru a susține o modelare și analiză fiabilă.

Cuvinte-cheie: *răspuns electrochimic, semiconductori nanostructurați, strat de sarcină spațială, rezistență la transferul de sarcină, circuit echivalent.*

1. Introduction

Electrochemical impedance spectroscopy (EIS) is widely used to investigate interfacial charge-transfer processes, mass transport, and adsorption phenomena in electrochemical systems [1]. The technique allows separation of these processes according to their characteristic time constants, thereby yielding quantitative parameters such as charge-transfer resistance, double-layer capacitance, and diffusion coefficients. Historically, EIS models and equivalent-circuit interpretations have been developed primarily for metallic or macroscopically homogeneous electrodes, where relatively simple charge-transfer and transport mechanisms dominate the interfacial response [2].

Electrochemical methods offer a broad range of applications in the processing and modification of semiconductor materials. Electrochemical etching is commonly used for the controlled formation of porous semiconductors, resulting in porous layers with tunable morphology and porosity [3–9], or, in more advanced cases, nanowire and nanochannel networks that can exhibit partial or preferential alignment relative to the substrate [3], [10] Such structures are particularly attractive due to their high surface area and the possibility of controlling charge transport pathways through geometrical design. In addition, electrochemical deposition represents a versatile and cost-effective approach for the fabrication of hybrid structures based on semiconductor materials, enabling the localized deposition of metallic nanodots or thin metallic phases onto semiconductor surfaces [11], [12]. This approach allows control over particle size, distribution, and surface coverage, which is essential for tuning interfacial properties and functional performance in applications such as sensing, catalysis, and energy-related devices.

Nanostructured semiconductor electrodes—such as metal-oxide nanowires, nanotubes, and porous films—introduce considerably greater complexity owing to their high surface-to-volume ratios, morphological heterogeneity, and intrinsic semiconductor electronic properties.

Phenomena including space-charge regions, surface defect states, and band bending strongly affect the impedance response and frequently cause deviations from ideal capacitive or diffusive behavior [13–15]. Nanoscale transport pathways distributed active sites, and geometric non-uniformity commonly give rise to depressed semicircles, non-integer phase angles, and overlapping relaxation-time distributions in the recorded spectra [16].

Reliable interpretation of such spectra requires theoretical frameworks that combine semiconductor physics with established impedance-modelling tools, incorporating elements such as space-charge capacitance, surface-state contributions, diffusion/reaction elements, and distributed or transmission-line representations.

This review study provides a structured overview of these theoretical principles, with emphasis on their application to the accurate analysis and modelling of impedance data obtained from nanostructured semiconductor electrodes.

2. Semiconductor–Electrolyte Interface Theory

The interface between a semiconductor electrode and an electrolyte plays a primary role in determining the electrochemical impedance response. At the interface, the semiconductor's energy levels adjust to match the electrochemical potential of the electrolyte, leading to the formation of a space-charge region within the semiconductor [17]. The width and properties of this region depend on the doping type, doping concentration, applied potential, and surface states present on the electrode. A simple scheme is represented in Figure 1.

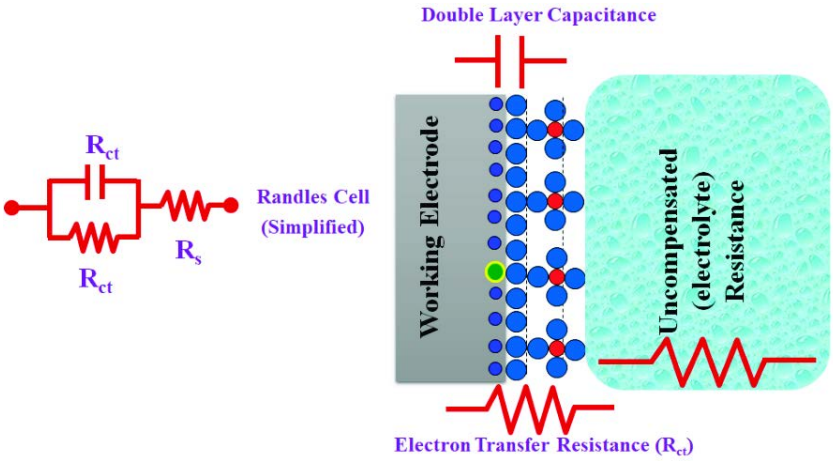

Figure 1. Illustration of the Randles circuit and double-layer structure.
Reproduced from [2] *Electrochemical Impedance Spectroscopy (EIS): Principles, Construction, and Biosensing Applications. Sensors*, 2021, 21, 6578, under **CC BY 4.0**.
https://doi.org/10.3390/s21196578

2.1 Space-Charge Layer Formation

For an n-type semiconductor in contact with an electrolyte, the Fermi level of the semiconductor adjusts to achieve equilibrium with the redox potential of the solution. This equilibration results in band bending near the surface, creating a depletion or accumulation layer depending on the relative energy levels [18]. The space-charge capacitance, C_{sc}, associated with this layer can be expressed using the Mott–Schottky relation:

$$\frac{1}{C_{sc}^2} = \frac{2}{\varepsilon\varepsilon_0 e N_D}\left(V - V_{fb} - \frac{k_B T}{e}\right) \quad (1)$$

where:

- C_{sc} is the space-charge capacitance (F·m^{-2}),
- ε is the semiconductor dielectric constant,
- ε_0 is the vacuum permittivity,
- e is the elementary charge,
- N_D is the donor density for n-type semiconductors,
- V is the applied potential,
- V_{fb} is the flat-band potential,
- k_B is the Boltzmann constant,
- T is the absolute temperature.

This equation establishes a direct relationship between the measured capacitance and the semiconductor doping density, enabling analysis of electronic properties from EIS measurements as seen in Figure 2 [19].

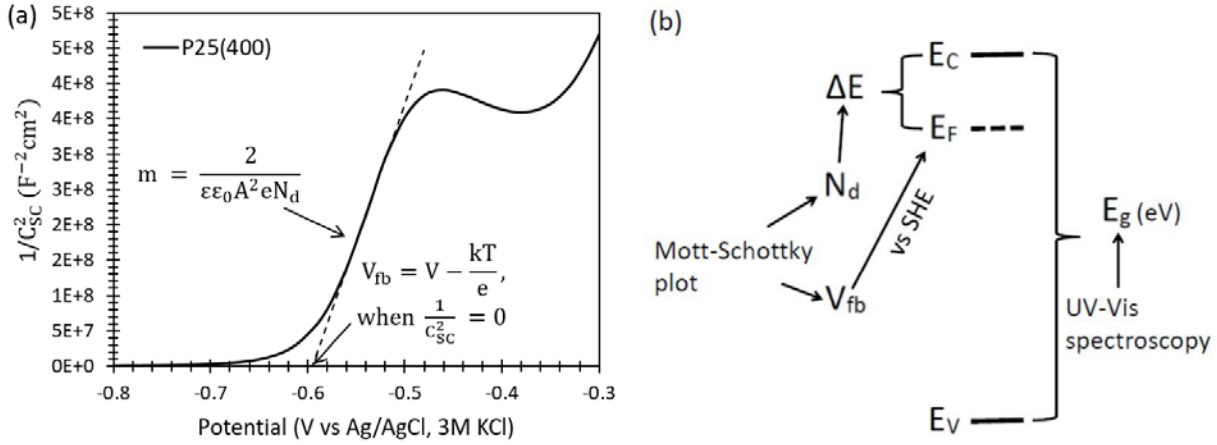

Figure 2. Mott–Schottky analysis and band edge diagram for TiO_2.
Reproduced from [20] *Effects of Mott–Schottky Frequency Selection and Other Controlling Factors on Flat-Band Potential and Band-Edge Position Determination of TiO_2. Catalysts*, 2023, 13, 1000, under **CC BY 4.0**.
https://doi.org/10.3390/catal13061000.

2.2 Influence of Surface States

Surface states, arising from defects, dangling bonds, or adsorbed species, introduce additional energy levels within the bandgap of the semiconductor. These states can trap charge carriers, leading to non-ideal capacitance behavior and frequency-dependent responses in impedance spectra [21]. The contribution of surface states, C_{ss}, can be incorporated into the total interfacial capacitance, C_{int}, as [22]:

$$\frac{1}{C_{int}} = \frac{1}{C_{sc}} + \frac{1}{C_{ss}} + \frac{1}{C_{dl}} \quad (2)$$

where C_{dl} is the double-layer capacitance formed at the semiconductor–electrolyte interface.

2.3 Bending and Charge-Transfer Kinetics

Band bending at the semiconductor surface directly influences the rate of electron transfer across the interface. A higher degree of band bending can increase the effective barrier for charge transfer, thereby increasing the observed charge-transfer resistance, R_{ct}, in EIS spectra [23]. For a simple redox reaction at the interface, the charge-transfer resistance can be related to the exchange current density, i_0, via [22]:

$$R_{ct} = \frac{RT}{nFi_0} \quad (3)$$

where:

- R is the universal gas constant,
- T is the temperature,
- n is the number of electrons involved,
- F is the Faraday constant,
- i_0 is the exchange current density.

Surface states and nano structuring can modify i_0 and introduce distributed kinetics, which are often represented in EIS by constant-phase elements (CPE) instead of ideal capacitors [23].

3. Double-Layer Capacitance and Charge Transfer Resistance

The electrochemical response of nanostructured semiconductor electrodes is largely determined by interfacial capacitance and charge-transfer kinetics. At the electrode–

electrolyte interface, ions in the electrolyte form an electrical double layer (EDL) adjacent to the semiconductor surface. This layer acts as a capacitance, commonly denoted as the double-layer capacitance, C_{dl}, and contributes directly to the impedance spectrum [24].

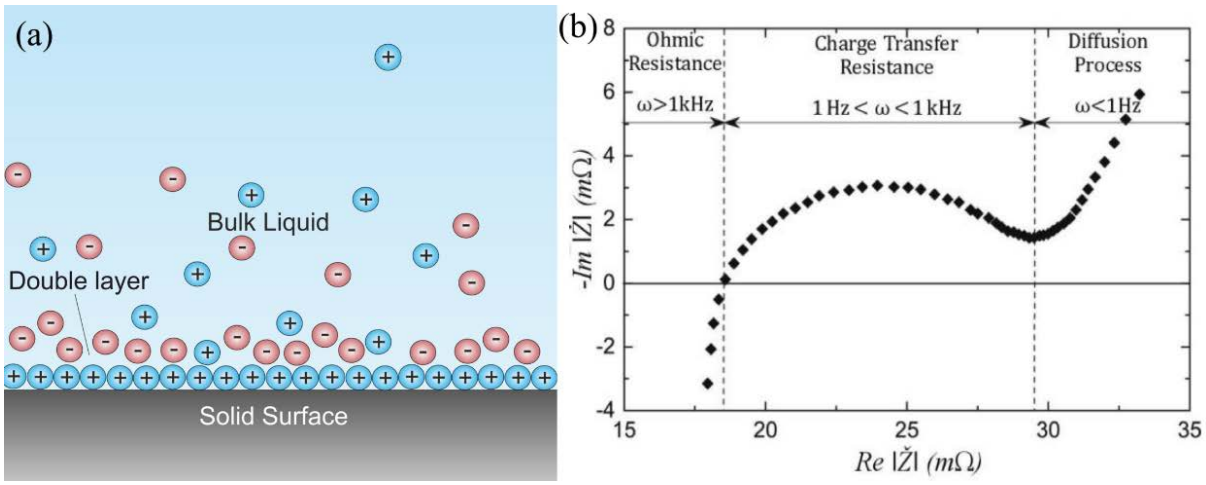

Figure 3. a) Schematic representation of the electrical double layer at a solid–liquid interface.

Source: *Double Layer* by *Gringer*, licensed under **CC BY-SA 3.0**. https://commons.wikimedia.org/wiki/File:Double_Layer.png. b) Nyquist plot indicating ohmic resistance, charge-transfer resistance, and diffusion processes.

Reproduced from [25] *Impact of Relaxation Time on Electrochemical Impedance Spectroscopy Characterization of the Most Common Lithium Battery Technologies—Experimental Study and Chemistry-Neutral Modeling. Smart Cities*, 2023, 12, 77, under **CC BY 4.0**. https://doi.org/10.3390/wevj12020077

3.1 Double-Layer Capacitance

The double-layer capacitance (Figure 3a) arises due to separation of charges at the interface and is classically modeled by the Helmholtz or Gouy–Chapman theories [26, 27]. The Helmholtz model describes a compact layer of ions of thickness $d$at the electrode surface:

$$C_{dl} = \frac{\varepsilon\varepsilon_0}{d} \tag{4}$$

where:

- $C_{dl}$is the double-layer capacitance (F·m^{-2}),
- $\varepsilon$is the dielectric constant of the electrolyte,
- $\varepsilon_0$is the vacuum permittivity,
- $d$is the effective thickness of the Helmholtz layer.

For nanostructured electrodes, deviations from ideal capacitive behavior often occur due to surface roughness, heterogeneous morphology, and porous architectures [28]. These deviations are frequently represented in EIS spectra using constant-phase elements (CPE), which account for non-ideal frequency-dependent behavior:

$$Z_{CPE} = \frac{1}{Q(j\omega)^n} \tag{5}$$

where:

- $Z_{CPE}$is the impedance of the CPE,
- $Q$is the CPE parameter related to capacitance,
- $j$is the imaginary unit,

- $\omega$is the angular frequency,
- $n$is an exponent (0 < n≤ 1), representing deviation from ideal capacitive behaviour.

3.2 Charge-Transfer Resistance

Charge-transfer resistance, R_{ct}, (Figure 3b) quantifies the resistance to electron transfer across the electrode–electrolyte interface. It is inversely proportional to the exchange current density, i_0, of the redox reaction occurring at the interface [29]:

$$R_{ct} = \frac{RT}{nFi_0} \tag{6}$$

where:

- $R$is the universal gas constant (J·mol^{-1}·K^{-1}),
- $T$is the absolute temperature (K),
- $n$is the number of electrons transferred,
- $F$is the Faraday constant (C·mol^{-1}),
- $i_0$is the exchange current density (A·m^{-2}).

In nanostructured electrodes, the effective R_{ct}may vary across the surface due to differences in local conductivity, surface states, and electronic defects, which can introduce distributed kinetics. In EIS spectra, charge-transfer resistance typically manifests as the diameter of the semicircular region in the Nyquist plot. Non-uniform electrode surfaces often produce depressed semicircles, which are effectively modeled using CPEs in parallel with R_{ct} [30].

3.3 Interplay Between Double-Layer Capacitance and Charge-Transfer Resistance

The overall impedance of the electrode–electrolyte interface is determined by the combined effects of double-layer capacitance and charge-transfer resistance. In the simplest form, this combination is represented by the parallel configuration of $C_{dl}$and R_{ct}, often included in the classical Randles equivalent circuit:

$$Z_{interface} = R_s + \frac{1}{\frac{1}{R_{ct}} + j\omega C_{dl}} \tag{7}$$

where R_s is the series resistance of the electrolyte and contacts. For nanostructured electrodes, distributed capacitances, surface heterogeneity, and deviations from ideal behaviour necessitate the use of CPEs or extended transmission-line models for accurate representation [23].

4. Equivalent Circuit Models

The interpretation of electrochemical impedance spectroscopy (EIS) (Figure 4a) data relies heavily on the use of equivalent circuit models that translate frequency-domain measurements into physically meaningful parameters. For semiconductor electrodes, equivalent circuits must incorporate contributions from double-layer capacitance, charge-transfer resistance, space-charge capacitance, surface states, and diffusion processes. The choice of circuit depends on electrode morphology, surface heterogeneity, and the degree of non-ideal behavior observed in impedance spectra [23].

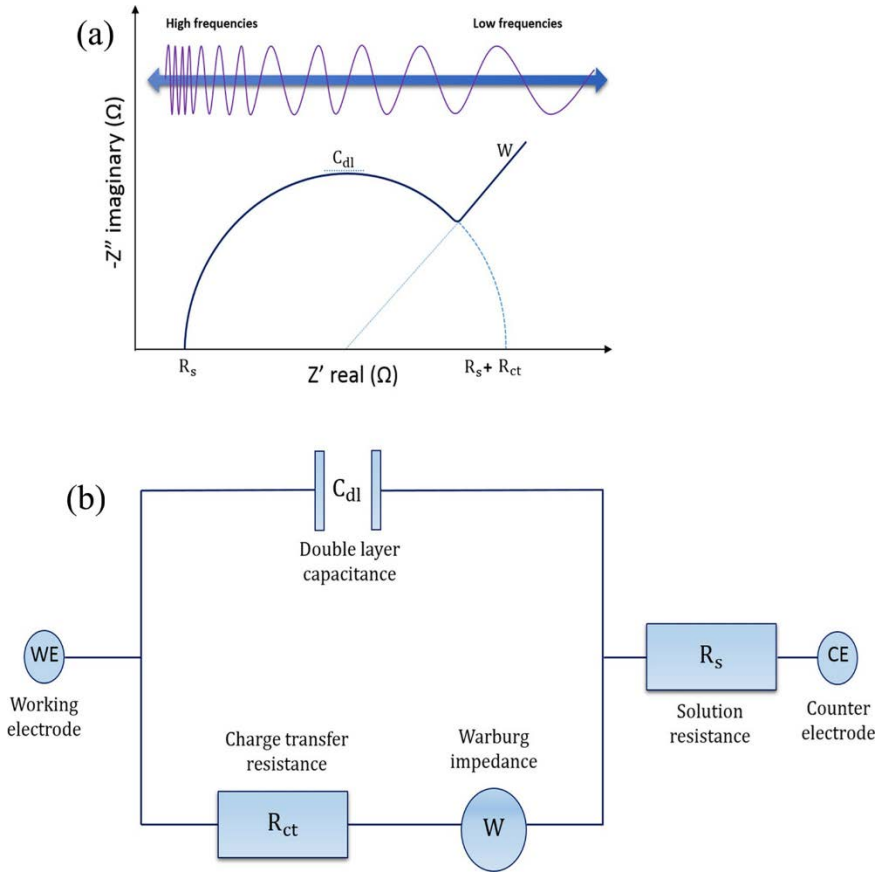

Figure 4. General scheme of a Nyquist plot and Randles' equivalent circuit (showing R_s, R_{ct}, $C_{dl}$and Warburg W).

Adapted from [31] *A review on impedimetric immunosensors for pathogen and biomarker detection. Medical Microbiology and Immunology* 209:343–362 (2020), under **CC BY 4.0**.
https://doi.org/10.1007/s00430-020-00668-0

4.1 Classical Randles Circuit

The Randles circuit (Figure 4b) represents the simplest model for an electrochemical interface, consisting of the series resistance of the electrolyte (R_s) in series with a parallel combination of the charge-transfer resistance (R_{ct}) and the double-layer capacitance (C_{dl}):

$$Z(\omega) = R_s + \frac{1}{\frac{1}{R_{ct}} + j\omega C_{dl}} \tag{8}$$

where $\omega$is the angular frequency. In EIS spectra, the diameter of the semicircle in the Nyquist plot corresponds to R_{ct}, while C_{dl} determines the curvature of the semicircle. For ideal electrodes, the Randles model accurately describes the high- and mid-frequency response, but deviations appear for nanostructured systems due to surface heterogeneity [9, 16].

4.2 Constant-Phase Element (CPE)

Nanostructured semiconductor electrodes often exhibit non-ideal capacitive behavior due to surface roughness, distributed reaction sites, or inhomogeneous conductivity. These effects are represented in equivalent circuits by a constant-phase element (CPE), whose impedance is given by [32]:

$$Z_{CPE} = \frac{1}{Q(j\omega)^n} \tag{9}$$

where:

- $Q$is a CPE constant related to capacitance,
- n($0 < n \leqslant 1$) quantifies the deviation from ideal behaviour.

When $n = 1$, the CPE reduces to an ideal capacitor; when $n < 1$, it models a distributed or non-uniform capacitance commonly observed in nanostructured electrodes [2].

4.3 Warburg Impedance

Diffusion-controlled processes in electrochemical systems contribute a frequency-dependent impedance, known as Warburg impedance (Z_W). For semi-infinite linear diffusion, $Z_W$is expressed as:

$$Z_W = \sigma \frac{1-j}{\sqrt{\omega}} \tag{10}$$

where $\sigma$is the Warburg coefficient, dependent on the diffusion coefficient and concentration of electroactive species.

For finite-length diffusion (e.g., in nanowire arrays), the Warburg element is modified to account for boundary conditions:

$$Z_W = R_W \frac{\tanh(j\omega\tau_D)^{1/2}}{(j\omega\tau_D)^{1/2}} \tag{11}$$

where $\tau_D$is the diffusion time constant.

Warburg elements typically appear in the low-frequency region of EIS spectra, manifesting as linear tails in Nyquist plots [2].

4.4 Distributed Transmission-Line Models

For high-aspect-ratio nanostructures such as nanowires, nanotubes, and porous films, interfacial and bulk resistances and capacitances are distributed along the electrode structure. Transmission-line models represent the electrode as a series of infinitesimal resistive and capacitive elements, capturing the spatial distribution of impedance contributions:

$$Z_{TL} = \sqrt{\frac{R_b+R_{ct}}{j\omega C_{dl}}} \coth[\sqrt{(R_b + R_{ct})j\omega C_{dl}}] \tag{12}$$

where $R_b$is the bulk resistance of the electrode.

Transmission-line circuits provide a more realistic representation of the frequency response for nanostructured electrodes than lumped-element models, particularly when multiple processes overlap [33].

5. Frequency-Dependent Behavior of Nanostructured Electrodes

Electrochemical impedance spectroscopy (EIS) characterizes electrochemical systems by measuring their response over a range of frequencies. In nanostructured semiconductor electrodes, the impedance response is governed by a combination of double-layer capacitance, charge-transfer resistance, space-charge capacitance, surface states, and diffusion processes, each dominating specific frequency regions [34].

5.1 High-Frequency Region

At high frequencies (typically >10 kHz), the impedance response is dominated by the series resistance (R_s) of the electrolyte and contacts, as well as the interfacial capacitances. In nanostructured electrodes, this region is particularly sensitive to the distributed double-

layer capacitance (C_{dl}) and space-charge capacitance (C_{sc}). Non-uniform surfaces or high surface-area architectures can produce depressed semicircles in Nyquist plots, reflecting non-ideal capacitive behavior represented by constant-phase elements (CPEs) [2].

5.2 Mid-Frequency Region

The mid-frequency range (typically 10 Hz–10 kHz) is predominantly influenced by charge-transfer resistance (R_{ct}) at the semiconductor–electrolyte interface. The parallel combination of R_{ct} and interfacial capacitances produces semicircular features in Nyquist plots, whose diameter corresponds to the magnitude of R_{ct}. In nanostructured electrodes, distributed reaction sites and surface states can broaden or depress the semicircle, requiring CPEs in parallel with R_{ct} for accurate modelling [35].

5.3 Low-Frequency Region

At low frequencies (<10 Hz), mass transport and diffusion processes dominate. The Warburg impedance (Z_W) represents semi-infinite linear diffusion, producing a 45° linear segment in the Nyquist plot. For nanostructured electrodes with finite-length diffusion paths, the Warburg element exhibits frequency-dependent saturation, and the linear region bends toward a vertical line at very low frequencies, indicating diffusion limitations [36]. Transmission-line models effectively capture these spatially distributed diffusion effects, particularly in high-aspect-ratio nanostructures such as nanowire arrays.

5.4 Bode Plot Interpretation

Bode plots provide additional insight by representing the magnitude and phase of impedance as functions of frequency. High-frequency peaks in phase plots correspond to capacitive behavior of the double-layer and space-charge regions, while mid-frequency peaks indicate the presence of charge-transfer processes. Low-frequency tails reflect diffusion-controlled kinetics. Nanostructured electrodes often exhibit multiple overlapping peaks due to distributed capacitances and inhomogeneous reaction rates, which can complicate simple Randles-type interpretations [35].

5.5 Distributed Effects and Non-Ideal Behavior

Nano structuring introduces heterogeneity, resulting in non-ideal, frequency-dependent behavior that cannot be accurately captured by simple lumped-element circuits. Constant-phase elements, transmission-line models, and distributed Warburg elements are required to account for these effects. Proper analysis of frequency-dependent responses allows for separation of capacitive, resistive, and diffusive contributions, facilitating a mechanistic understanding of electrochemical processes in nanostructured semiconductor electrodes [37].

6. Diffusion and Warburg Impedance

Diffusion processes play a crucial role in the low-frequency behavior of electrochemical systems, particularly in nanostructured semiconductor electrodes where transport pathways are often spatially constrained. The Warburg impedance (Z_W) is commonly employed to describe frequency-dependent diffusion phenomena in electrochemical impedance spectroscopy (EIS) [37].

6.1 Semi-Infinite Linear Diffusion

For semi-infinite diffusion, where the diffusion layer is effectively unlimited compared to the electrode dimensions, the Warburg impedance is defined as [38]:

$$Z_W = \sigma \frac{1-j}{\sqrt{\omega}} \quad (13)$$

where:

- $Z_W$is the Warburg impedance (Ω),
- $\sigma$is the Warburg coefficient, dependent on the diffusion coefficient $D$and concentration of electroactive species C^*,
- $j$is the imaginary unit,
- $\omega$is the angular frequency (rad·s^{-1}).

The Warburg coefficient σcan be expressed as [38]:

$$\sigma = \frac{RT}{n^2F^2A\sqrt{2DC^*}} \quad (14)$$

where:

- $R$is the universal gas constant (J·mol^{-1}·K^{-1}),
- $T$is the absolute temperature (K),
- $n$is the number of electrons transferred,
- $F$is the Faraday constant (C·mol^{-1}),
- $A$is the electrode surface area (m^2),
- $D$is the diffusion coefficient (m^2·s^{-1}),
- $C^*$is the bulk concentration of the redox species (mol·m^{-3}).

In Nyquist plots, semi-infinite diffusion manifests as a 45° linear segment at low frequencies, indicating a balance between resistive and capacitive contributions from ion transport.

6.2 Finite-Length Diffusion

In nanostructured electrodes, diffusion paths are often limited by nanoscale geometry, electrode thickness, or porous architecture. Finite-length diffusion modifies the Warburg impedance according to the following expression [39]:

$$Z_W = R_W \frac{\tanh((j\omega\tau_D)^{1/2})}{(j\omega\tau_D)^{1/2}} \quad (15)$$

where:

- $R_W$is the Warburg resistance,
- $\tau_D = \frac{L^2}{D}$is the diffusion time constant,
- $L$is the effective diffusion length.

This formulation accounts for saturation of the Warburg impedance at very low frequencies, which appears as a bending of the 45° line toward the vertical axis in Nyquist plots. Such behavior is particularly relevant for arrays of nanowires, nanotubes, and porous films, where diffusion limitations can dominate low-frequency impedance [40].

6.3 Integration with Equivalent Circuits

Warburg elements are commonly incorporated into equivalent circuits to model diffusion-limited processes. In the classical Randles circuit, a semi-infinite Warburg element (Z_W) is connected in series with $R_{ct}$and parallel to C_{dl}:

$$Z_{total} = R_s + \frac{1}{\frac{1}{R_{ct}+Z_W} + j\omega C_{dl}} \quad (16)$$

For nanostructured electrodes, transmission-line models or distributed Warburg elements are preferred to account for spatial heterogeneity and overlapping time constants [38].

6.4 Implications for Nanostructured Electrodes

Diffusion processes in nanostructured electrodes are strongly affected by geometry, pore size, and electrode thickness. The Warburg impedance provides a quantitative tool to evaluate diffusion coefficients, effective path lengths, and limitations in ion transportation. Correct modeling of Warburg contributions is essential for separating resistive, capacitive, and diffusion-controlled components of impedance spectra, enabling accurate interpretation of electrochemical kinetics at the nanoscale.

7. Modeling Impedance of Semiconductor Nanostructures

The accurate modeling of electrochemical impedance spectra in semiconductor nanostructures requires integration of interfacial capacitances, charge-transfer resistance, and diffusion contributions, while accounting for the spatial heterogeneity and nanoscale morphology of the electrode [37]. Nanostructured electrodes, including metal-oxide nanowires, nanotubes, and porous films, exhibit distributed electrical properties that cannot be fully represented by classical lumped-element circuits [41].

7.1 Distributed Equivalent-Circuit Models

For nanostructured electrodes, distributed equivalent-circuit models are employed to represent spatially varying resistive and capacitive elements. Transmission-line models, often composed of repeated series combinations of resistance (R_b), charge-transfer resistance (R_{ct}), and double-layer or space-charge capacitance (C_{dl} or C_{sc}), provide a more realistic description:

$$Z_{TL} = \sqrt{\frac{R_b+R_{ct}}{j\omega C_{dl}}}\coth[\sqrt{(R_b+R_{ct})j\omega C_{dl}}] \quad (17)$$

where $R_b$is the bulk resistance of the electrode and cothdenotes the hyperbolic cotangent function. These models capture frequency-dependent behavior resulting from the extended geometry and heterogeneity of nanoscale electrodes [42].

7.2 Integration of Space-Charge and Surface-State Effects

Space-charge regions and surface states significantly influence the interfacial impedance of semiconductor electrodes. The total interfacial capacitance, C_{int}, is expressed as a series combination of space-charge capacitance (C_{sc}), surface-state capacitance (C_{ss}), and double-layer capacitance (C_{dl}) as mentioned in Equation (2). The incorporation of C_{ss} is particularly important for nanostructured electrodes where surface defects and adsorbed species are abundant. Non-ideal behavior introduced by surface-state distribution can be represented using constant-phase elements (CPE) to accurately model the frequency-dependent response [43].

7.3 Modeling Charge-Transfer and Diffusion Processes

Charge-transfer resistance (R_{ct}) and diffusion-controlled impedance (Warburg element, Z_W) are combined in equivalent circuits to capture mid- and low-frequency spectral features. For nanostructured electrodes, overlapping time constants from distributed $R_{ct}$and finite-length diffusion paths necessitate modified Warburg elements or transmission-line approaches:

$$Z_{total} = R_s + \frac{1}{\frac{1}{R_{ct}+Z_W}+(j\omega C_{dl})^n} \quad (18)$$

where n represents the exponent of the CPE, reflecting non-ideal capacitive behavior.
This formulation enables deconvolution of contributions from charge-transfer kinetics, interfacial capacitances, and diffusion phenomena [35].

7.4 Challenges in Modeling Nanostructured Impedance

Accurate modeling of nanostructured semiconductor electrodes is complicated by several factors [44]:

1. Surface heterogeneity: Nanostructured electrodes contain distributed active sites, which produce non-uniform charge-transfer kinetics.
2. Overlapping time constants: Multiple processes may occur over similar frequency ranges, complicating spectral interpretation.
3. Non-ideal capacitive behavior: High surface area and roughness result in frequency-dependent capacitance, requiring CPE modeling.
4. Finite diffusion paths: Diffusion limitations in nanowires, nanotubes, and porous electrodes produce deviations from classical Warburg behavior.

Addressing these challenges requires careful selection of equivalent-circuit elements and fitting strategies, combined with theoretical understanding of semiconductor electrochemistry at the nanoscale.

8. Limitations of EIS Interpretation in Nanomaterials

Electrochemical impedance spectroscopy (EIS) is useful tool for probing interfacial processes and charge transport in semiconductor electrodes. However, its interpretation in nanostructured materials is subject to several inherent limitations due to the complexity of nanoscale morphologies, distributed kinetics, and non-ideal capacitive behavior [45].

Nanostructured electrodes often display non-ideal capacitive responses arising from surface roughness, porosity, and heterogeneous distributions of surface states. Constant-phase elements (CPEs) are commonly used to model these deviations; however, the physical interpretation of CPE parameters is not straightforward. The exponent $n$in a CPE reflects the degree of deviation from ideal capacitance, but it does not directly quantify specific physical features such as pore size, surface roughness, or defect density. Consequently, extrapolating mechanistic insights solely from CPE parameters may be ambiguous [46].

Multiple electrochemical processes, including double-layer charging, charge transfer, and diffusion, may occur over similar frequency ranges in nanostructured electrodes. Overlapping time constants complicate the separation of individual contributions and can lead to misinterpretation of impedance spectra. In particular, mid-frequency semicircles may contain contributions from both $R_{ct}$and space-charge effects, while low-frequency tails may simultaneously reflect diffusion and adsorption processes [35].

Finite diffusion lengths in nanowire arrays, nanotubes, and porous films introduce deviations from classical semi-infinite Warburg behavior. Standard Warburg models may underestimate the impact of restricted diffusion or misrepresent the low-frequency impedance, leading to inaccurate extraction of diffusion coefficients. Transmission-line models offer improvements but still require assumptions regarding uniformity of nanostructure dimensions and porosity [35].

Nanostructured electrodes exhibit spatial variations in doping, morphology, and electronic properties. These inhomogeneities create distributed resistive and capacitive

behavior that cannot be fully captured by simple equivalent circuits. Fitting EIS data to classical models without accounting for heterogeneity may produce parameters that lack direct physical meaning or predictive power [47].

Accurate EIS interpretation also depends on experimental factors such as temperature stability, electrode preparation, electrolyte composition, and instrumentation limitations. Noise, parasitic inductance, and limited frequency range can obscure or distort impedance features, further complicating analysis in nanoscale systems [2].

Conclusions

Electrochemical impedance spectroscopy is a powerful way to study what happens at the interface of nanostructured semiconductor electrodes. The overall impedance comes from several factors working together: the double-layer capacitance, charge-transfer resistance, space-charge capacitance, surface states, and different types of diffusion. Because nano structuring creates complexity and non-ideal behavior, researchers often rely on constant-phase elements (CPEs), Warburg elements, and distributed or transmission-line equivalent circuits to describe the system accurately.

At high frequencies, the response is mainly shaped by interfacial and space-charge capacitances. In the mid-frequency range, charge-transfer reactions dominate. At low frequencies, diffusion processes take over—and in nanostructured materials, the limited diffusion length means that classic Warburg models often need to be adjusted. Transmission-line models are especially helpful here because they can represent spatial variations and the overlapping time constants that commonly appear in nanowires, nanotubes, and porous electrodes.

Still, interpreting EIS data for nanostructured electrodes isn't always straightforward. Non-ideal capacitive behavior, overlapping timescales, restricted diffusion, and surface irregularities can make analysis tricky. Getting reliable electrochemical parameters requires thoughtful experimental design, choosing the right equivalent-circuit model, and taking into account the nanoscale structure of the electrode.

Building a solid theoretical understanding of impedance in these systems makes it possible to evaluate interfacial reactions, diffusion limits, and charge-transfer processes with confidence. These insights are valuable for designing advanced electrodes with optimized performance for applications such as energy conversion, catalysis, and sensing.

Funding

This work was funded by Ministry of Education and Research from the Republic of Moldova, institutional subprogram #02.04.02 "Development of technologies and investigation of the properties of layered semiconductor compounds, hybrid nanostructures and laser sources".

Conflicts of Interest

The author declares no conflicts of interest. The funders had no role in the design of the study; in the collection, analyses, or interpretation of data; in the writing of the manuscript; or in the decision to publish the results.

References

1. Zhang H, Sun Z, Sun K, et al (2025) Electrochemical Impedance Spectroscopy-Based Biosensors for Label-Free Detection of Pathogens. Biosensors 15:443. https://doi.org/10.3390/bios15070443

2. Magar HS, Hassan RYA, Mulchandani A (2021) Electrochemical Impedance Spectroscopy (EIS): Principles, Construction, and Biosensing Applications. Sensors 21:6578. https://doi.org/10.3390/s21196578
3. Monaico, E. (2022). Micro- and nano-engineering of III-V and II-VI semiconductor compounds and metal nanostructures based on electrochemical technologies for multifunctional applications. Chișinău: Technical University of Moldova. Available at: http://repository.utm.md/handle/5014/21913
4. Tiginyanu IM, Monaico EV (2024) Self-organized porous semiconductor compounds. In: Encyclopedia of Condensed Matter Physics. Elsevier, pp 350–374. doi: 10.1016/B978-0-323-90800-9.00105-0.
5. Monaico EV, Monaico EI, Ursaki VV, Tiginyanu IM (2023) Porous Semiconductor Compounds with Engineered Morphology as a Platform for Various Applications. Phys Status Solidi RRL – Rapid Res Lett 17:2300039. https://doi.org/10.1002/pssr.202300039
6. Monaico EI, Monaico EV, Ursaki VV, Tiginyanu IM (2021) Evolution of Pore Growth in GaAs in Transitory Anodization Regime from One Applied Voltage to Another. Surf Eng Appl Electrochem 57:165–172. https://doi.org/10.3103/S106837552102006X
7. Monaico E, Tiginyanu I, Ursaki V (2020) Porous semiconductor compounds. Semicond Sci Technol 35:103001. https://doi.org/10.1088/1361-6641/ab9477
8. Monaico EI, Monaico EV, Ursaki VV, Tiginyanu IM (2025) Micro- and Nano-Integration in the Production of GaAs and Ga2O3 Nanowire Arrays by Top-Down Design. J Manuf Mater Process 9:376. https://doi.org/10.3390/jmmp9110376
9. Monaico EV, Tiginyanu IM (2025) How Semiconductor Terminology has Been Enriched by Research of Electrochemical Pore Etching and Electrodeposition. In: Sontea V, Tiginyanu I, Railean S (eds) 7th International Conference on Nanotechnologies and Biomedical Engineering. Springer Nature Switzerland, Cham, pp 311–321. doi: 10.1007/978-3-032-06494-3_31.
10. Monaico EI, Monaico EV, Ursaki VV, Tiginyanu IM (2025) Micro- and Nano-Integration in the Production of GaAs and Ga2O3 Nanowire Arrays by Top-Down Design. J Manuf Mater Process 9:376. https://doi.org/10.3390/jmmp9110376
11. Monaico EV (2024) Micro- and nano-engineering of semiconductor compounds and metal structures based on electrochemical technologies. Ann Acad Romanian Sci Ser Phys Chem 9:85–107. https://doi.org/10.56082/annalsarsciphyschem.2024.1.85
12. Monaico EI, Monaico EV, Ursaki VV, Tiginyanu IM (2022) Controlled Electroplating of Noble Metals on III-V Semiconductor Nanotemplates Fabricated by Anodic Etching of Bulk Substrates. Coatings 12:1521. https://doi.org/10.3390/coatings12101521
13. Krawczyk M, Korbutowicz R, Suchorska-Woźniak P (2024) Impedance Spectroscopy Study of Charge Transfer in the Bulk and Across the Interface in Networked SnO2/Ga2O3 Core–Shell Nanobelts in Ambient Air. Sensors 24:6173. https://doi.org/10.3390/s24196173
14. Busuioc S, Monaico EV (2024) Electrochemical Impedance Spectroscopy for NonEnzymatic Glucose Detection Using ZnO Nanowire Arrays: Substrate Impact Analysis. University Politehnica of Bucharest, Bucharest, Romania, p 30. [Online]. Available: http://www.physics.pub.ro/Site_Conferinta_PM-8/Abstracts_Book.pdf
15. Busuioc S, Monaico EV (2025) Influence of Surface Pre-treatment and Thermal Annealing on the Electrochemical and Wettability Behavior of Copper. In: Sontea V, Tiginyanu I, Railean S (eds) 7th International Conference on Nanotechnologies and Biomedical Engineering. Springer Nature Switzerland, Cham, pp 215–226. doi: 10.1007/978-3-032-06494-3_23.
16. Iram S, Mahmood A, Ehsan MF, et al (2021) Impedance Spectroscopic Study of Nickel Sulfide Nanostructures Deposited by Aerosol Assisted Chemical Vapor Deposition Technique. Nanomaterials 11:1105. https://doi.org/10.3390/nano11051105
17. Leks B, Parzuch A, Nawaz N, et al (2025) Influence of Electrolyte Composition on the Semiconductor–Electrolyte Interface (SEI) Built-In for Enhanced Photoelectrochemical (PEC) Processes. Molecules 30:885. https://doi.org/10.3390/molecules30040885
18. Al-Hilli S, Willander M (2009) The pH Response and Sensing Mechanism of n-Type ZnO/Electrolyte Interfaces. Sensors 9:7445–7480. https://doi.org/10.3390/s90907445
19. Lee SF, Jimenez-Relinque E, Martinez I, Castellote M (2023) Effects of Mott–Schottky Frequency Selection and Other Controlling Factors on Flat-Band Potential and Band-Edge Position Determination of TiO2. Catalysts 13:1000. https://doi.org/10.3390/catal13061000
20. Lee SF, Jimenez-Relinque E, Martinez I, Castellote M (2023) Effects of Mott–Schottky Frequency Selection and Other Controlling Factors on Flat-Band Potential and Band-Edge Position Determination of TiO2. Catalysts 13:1000. https://doi.org/10.3390/catal13061000

21. Brett CMA (2022) Electrochemical Impedance Spectroscopy in the Characterisation and Application of Modified Electrodes for Electrochemical Sensors and Biosensors. Molecules 27:1497. https://doi.org/10.3390/molecules27051497
22. Bard AJ, Faulkner LR (2001) Electrochemical methods: fundamentals and applications, 2. edition. Wiley, New York Weinheim
23. Lazanas A, Prieto Simón B (2025) A Guide to Recognizing Your Electrochemical Impedance Spectra: Revisions of the Randles Circuit in (Bio)sensing. Sensors 25:6260. https://doi.org/10.3390/s25196260
24. Ferre F, Breuiller M, Cedard L (1975) Human placental delta5-3beta hydroxysteroid dehydrogenase activity (delta5-3beta HSDH): intracellular distribution, kinetic properties, retroinhibition and influence of membrane delipidation. Steroids 26:551–570. https://doi.org/10.1016/0039-128x(75)90050-1
25. Hosen MS, Gopalakrishnan R, Kalogiannis T, et al (2021) Impact of Relaxation Time on Electrochemical Impedance Spectroscopy Characterization of the Most Common Lithium Battery Technologies—Experimental Study and Chemistry-Neutral Modeling. World Electr Veh J 12:77. https://doi.org/10.3390/wevj12020077
26. Helmholtz H von (1879) Studien über elektrische Grenzschichten. Ann Phys 243:337–382. https://doi.org/10.1002/andp.18792430702
27. Bolt GH (1955) Analysis of the validity of the Gouy-Chapman theory of the electric double layer. J Colloid Sci 10:206–218. https://doi.org/10.1016/0095-8522(55)90027-1
28. Miszczyk A (2025) Direct Measurement of Effective Electrical Capacitance in Systems with a Constant-Phase Element Behavior Using the Example of Barrier Coatings. Coatings 15:1429. https://doi.org/10.3390/coatings15121429
29. (1924) On the determination of molecular fields. —II. From the equation of state of a gas. Proc R Soc Lond Ser Contain Pap Math Phys Character 106:463–477. https://doi.org/10.1098/rspa.1924.0082
30. Cuevas AL, Dominguez A, Zamudio-García J, et al (2024) Optical and Electrochemical Properties of a Nanostructured ZnO Thin Layer Deposited on a Nanoporous Alumina Structure via Atomic Layer Deposition. Materials 17:1412. https://doi.org/10.3390/ma17061412
31. Leva-Bueno J, Peyman SA, Millner PA (2020) A review on impedimetric immunosensors for pathogen and biomarker detection. Med Microbiol Immunol (Berl) 209:343–362. https://doi.org/10.1007/s00430-020-00668-0
32. Brug GJ, Van Den Eeden ALG, Sluyters-Rehbach M, Sluyters JH (1984) The analysis of electrode impedances complicated by the presence of a constant phase element. J Electroanal Chem Interfacial Electrochem 176:275–295. https://doi.org/10.1016/S0022-0728(84)80324-1
33. De Levie R (1963) On porous electrodes in electrolyte solutions. Electrochimica Acta 8:751–780. https://doi.org/10.1016/0013-4686(63)80042-0
34. Barsoukov E, Macdonald JR (2005) Impedance Spectroscopy: Theory, Experiment, and Applications, 1st ed. Wiley. doi: 10.1002/0471716243.
35. Lazanas ACh, Prodromidis MI (2023) Electrochemical Impedance Spectroscopy—A Tutorial. ACS Meas Sci Au 3:162–193. https://doi.org/10.1021/acsmeasuresciau.2c00070
36. Bumberger AE, Nenning A, Fleig J (2024) Transmission line revisited – the impedance of mixed ionic and electronic conductors. Phys Chem Chem Phys 26:15068–15089. https://doi.org/10.1039/d4cp00975d
37. Da Silva GMG, Faia PM, Mendes SR, Araújo ES (2024) A Review of Impedance Spectroscopy Technique: Applications, Modelling, and Case Study of Relative Humidity Sensors Development. Appl Sci 14:5754. https://doi.org/10.3390/app14135754
38. Nuñez Perez FA (2025) Analytical–Computational Integration of Equivalent Circuit Modeling, Hybrid Optimization, and Statistical Validation for Electrochemical Impedance Spectroscopy. Electrochem 6:35. https://doi.org/10.3390/electrochem6040035
39. Fortuna L, Garraffa G (2025) Characteristic Value Techniques to Approximate Warburg Diffusion Devices. Energies 18:3408. https://doi.org/10.3390/en18133408
40. Lasia A (2014) Electrochemical Impedance Spectroscopy and its Applications. Springer New York, New York, NY Springer New York, 2014. doi: 10.1007/978-1-4614-8933-7.
41. Song J, Bazant MZ (2018) Electrochemical Impedance Imaging via the Distribution of Diffusion Times. Phys Rev Lett 120:. https://doi.org/10.1103/physrevlett.120.116001
42. Costa R, Voroshylova IV, Cordeiro MNDS, et al (2018) Enhancement of differential double layer capacitance and charge accumulation by tuning the composition of ionic liquids mixtures. Electrochimica Acta 261:214–220. https://doi.org/10.1016/j.electacta.2017.12.134

43. Gelderman K, Lee L, Donne SW (2007) Flat-Band Potential of a Semiconductor: Using the Mott–Schottky Equation. J Chem Educ 84:685. https://doi.org/10.1021/ed084p685
44. Fabregat-Santiago F, Bisquert J, Garcia-Belmonte G, et al (2005) Influence of electrolyte in transport and recombination in dye-sensitized solar cells studied by impedance spectroscopy. Sol Energy Mater Sol Cells 87:117–131. https://doi.org/10.1016/j.solmat.2004.07.017
45. Bredar ARC, Chown AL, Burton AR, Farnum BH (2020) Electrochemical Impedance Spectroscopy of Metal Oxide Electrodes for Energy Applications. ACS Appl Energy Mater 3:66–98. https://doi.org/10.1021/acsaem.9b01965
46. Córdoba-Torres P, Mesquita TJ, Nogueira RP (2015) Relationship between the Origin of Constant-Phase Element Behavior in Electrochemical Impedance Spectroscopy and Electrode Surface Structure. J Phys Chem C 119:4136–4147. https://doi.org/10.1021/jp512063f
47. Das S, Banerjee A, Nandi U, Ghosh A (2025) Critical review on the analysis of electrochemical impedance spectroscopy data. J Appl Phys 138:. https://doi.org/10.1063/5.0275205

Citation: Busuioc, S. (2026). Theoretical principles governing electrochemical impedance spectroscopy in nanostructured semiconductor electrodes. *Journal of Engineering Science*. 2026, 33 (1), pp. 21-36. https://doi.org/10.52326/jes.utm.2026.33(1).02.

Submission of manuscripts: jes@meridian.utm.md

Journal of Engineering Science *Vol. XXXIII, no. 1 (2026), pp. 37 - 52*
Fascicle *Electronics and Computer Science* *ISSN 2587-3474*
Topic *Computers and Information Technology* *eISSN 2587-3482*

https://doi.org/10.52326/jes.utm.2026.33(1).03
UDC 004.8:004.94:004.31:57.087

ADAPTIVE COMPUTING STRUCTURES FOR SERVICE-ORIENTED MULTI-AGENT SYSTEMS BASED ON KNOWLEDGE MODELS

Vadim Struna[1*], ORCID: 0000-0001-6579-3054,
Victor Ababii[1], ORCID: 0000-0002-0769-8144,
Viorica Sudacevschi[1], ORCID: 0000-0003-0125-3491,
Silvia Munteanu[1], ORCID: 0000-0003-0749-8457,
Olesea Borozan[1], ORCID: 0000-0003-1091-5506,
Victoria Alexei[1], ORCID: 0000-0003-4560-3131

[1]*Technical University of Moldova, Ștefan cel Mare, 168, Chișinău, MD-2004, Republic of Moldova*
* Corresponding author: Vadim Struna, *vadim.struna@iis.utm.md*

Received: 01. 24. 2026
Accepted: 02. 27. 2026

Abstract. This paper proposes an adaptive computing framework for service-oriented multi-agent systems, based on knowledge models inspired by the hierarchical organization of the human brain. The approach integrates neurophysiological principles of conscious and subconscious processing with rigorous mathematical formalization and hardware-oriented architectural design. The conscious–subconscious interaction is modeled as a two-level computational hierarchy, in which subconscious processing is fast, parallel, adaptive, and high-dimensional, and conscious processing is deliberative, symbolic, and low-dimensional, being responsible for control, planning, and decision-making. An attention-based coupling mechanism controls the flow of information between the two levels, allowing for dynamic adaptation and efficient use of resources. Based on this model, a heterogeneous hardware architecture is proposed that maps subconscious processing to NPU/GPU accelerators, and conscious processing to CPU units. The framework is extended to multi-agent systems, in which each agent implements a conscious–subconscious hierarchy, and the emergent coordination is achieved through a collective conscious level. The approach supports distributed intelligence, scalability, and adaptive service composition.

Keywords: *conscious–subconscious processing, cognitive architectures, distributed intelligence, heterogeneous hardware, hierarchical computing, knowledge models, mathematical modeling, physiology of the human brain.*

1. Introduction

The accelerated evolution of distributed computing systems, driven by the growing complexity of digital environments and rising demands for flexibility, scalability and autonomy, has led to the emergence of new design paradigms based on adaptivity and distributed intelligence. In this context, service-oriented multi-agent systems represent a promising solution for modeling and managing complex, dynamic and heterogeneous processes, characteristic of modern applications in areas such as intelligent infrastructures, cyber-physical systems, the Internet of Things (IoT) and critical situation management [1].

A major challenge in the development of service-oriented multi-agent systems lies in their ability to adapt in real time to rapid and unpredictable changes in the environment, the continuous evolution of functional requirements and the dynamic integration of new resources and services, including AI- and machine-learning-based services. Traditional computational structures, rigid and predefined, can no longer sustain the complexity and dynamism necessary for the emergence of self-organizing intelligent behaviors at the system level. In this context, adaptive computing structures and architectures based on continuous learning become essential, facilitating the dynamic reorganization of components, optimal redistribution of tasks, autonomous adjustment of agent behavior and efficient integration of emerging technologies, depending on context, objectives and performance criteria [2, 8, 9].

A central role in achieving adaptivity is played by knowledge models, which provide formal mechanisms for representing, acquiring, inferring and updating knowledge, both at the agent level and as well at the system level. The integration of knowledge models into service-oriented multi-agent system architectures enables agents to make informed decisions, anticipate environmental developments, and effectively to coordinate the services offered. Thus, knowledge becomes not only an information resource, but also an active factor of control, structural adaptation and continuous learning within intelligent systems [3–7, 10–12].

The present paper aims to develop service-oriented adaptive multi-agent systems, based on hierarchical knowledge models inspired by the conscious–subconscious interaction. It is proposed to develop mathematical models for formalizing the functioning mechanisms inspired by the human brain and for describing the behavior of multi-agent systems, as well as the development of heterogeneous hardware architectures, which combine neural accelerators (NPU/GPU) for subconscious processing with CPU units for deliberative control, supporting adaptive learning and decision-making algorithms. The expansion to multi-agent systems will integrate collective coordination mechanisms and emerging behavior, ensuring scalability, fault tolerance and interoperability in dynamic environments. This approach will enable the development of autonomous cognitive platforms capable of managing complex services and supporting applications in areas such as digital twins, autonomous robotics and smart environments.

2. Physiology of the human brain. The conscious and subconscious

The study of consciousness and subconscious processes is one of the most complex and challenging directions of modern neuroscience. Consciousness is investigated both as a subjective phenomenon and as a result of the coordinated activity of neural networks, while the subconscious is analyzed as a fundamental mechanism of rapid and efficient adaptation to the environment. Modern perspectives in cognitive neuroscience emphasize the interdisciplinary nature of this issue, integrating data from neurophysiology, cognitive psychology and computational modeling. Seth and Bayne [22] provide a synthesis of the theories of consciousness and justify the relevance of the research topic. Additionally, Gazzaniga et al. [18] highlight the perspective of cognitive neuroscience on consciousness and the integration of neuroanatomical structure with cognitive functions.

The human brain is a highly complex biological system, made up of about 86 billion neurons interconnected by dynamic synaptic networks. Its functioning is based on the propagation of action potentials, on chemical and electrical synaptic transmission, as well as on synaptic plasticity mechanisms, considered essential for learning and memory processes [19]. From a functional perspective, cortical structures are involved in higher cognitive processes,

while subcortical structures and the brainstem support automatic and vital processes. This organization allows the simultaneous emergence of conscious and subconscious processes in a unitary system [18].

Consciousness (≈10% of human brain activity) represents the upper level of the rational decision-making center, being relatively slow and operating based on predefined patterns. It is responsible for analytical thinking, intentional planning, and processing information that we are immediately aware of. The conscious is associated with mental states accessible to subjective reporting, such as perception, attention and deliberative reasoning. Neuroimaging studies indicate that these processes are correlated with the activation of fronto-parietal networks and with the mechanisms of global information integration. The Global Neuronal Workspace theory holds that information becomes conscious when it is amplified and widely distributed in the cortex [16, 20]. The dynamics of neuronal synchronization and cortical "binding" processes, researched by Baars in [1, 13], are essential for maintaining conscious content.

The subconscious (≈90% of the human brain's activity) represents a vast array of automated, autonomous processes based on long-term experience, habits, and memories. These processes are extremely fast, capable of processing up to 20 million bits of information per second. The subconscious comprises cognitive processes that take place without direct access to consciousness, but that significantly influence behavior and decision-making. These processes are fast, parallel, and energy-efficient, being associated with structures such as the amygdala, hippocampus, and basal ganglia. The role of subconscious emotions in regulating behavior and in decision-making is evidenced by Damasio's studies [15]. Network models of the emotional brain, researched by Pessoa in [21], show that affective and cognitive processes are deeply interconnected, even in the absence of explicit awareness. Also, social and adaptive behaviors are often mediated by subconscious mechanisms demonstrated by Stanley and Adolphs in [23].

The relationship between the conscious and the subconscious is a two-way and dynamic one. Predictive coding models describe the brain as an inference system that generates subconscious predictions and uses conscious processes to correct significant prediction errors [14]. The principle of free energy, researched by Friston in [17], provides a unifying mathematical framework, according to which both conscious and subconscious processes aim to minimize uncertainty and internal errors. Emotions and subconscious somatic markers decisively influence conscious rational processes, confirming the interdependence of the two levels [15]. The conscious monitors and interprets cognitive activity, and delegates routine tasks to the subconscious level, while the subconscious provides decisions based on experience (intuition) and automatically manages processes, freeing up conscious resources.

Modern approaches treat consciousness as an emergent property of information integration into complex neural networks. Integrated Information Theory (IIT), researched by Tononi et al. in [24], proposes a formal measure of the level of consciousness, based on the degree of informational integration. Recent comparative analyses [22], highlight the complementarity between IIT, *the Global Neuronal Workspace* and predictive models. Also, mathematical formulations inspired by Bayesian inference provide a rigorous framework for describing the conscious–subconscious interaction [17].

Understanding the relationship between the conscious and subconscious has major implications in areas such as clinical neuropsychology, cognitive artificial intelligence, and

adaptive systems. Models inspired by *Global Workspace* and *predictive coding* have influenced the development of hybrid cognitive architectures in artificial intelligence [13, 14]. Also, the concepts of information integration are theoretically explored in the context of complex artificial systems [24].

Therefore, the conscious and the subconscious are not separate entities, but complementary functional levels of brain activity. The subconscious provides efficiency and quick adaptation, while the conscious provides deliberative control and cognitive flexibility. Neurophysiological data and modern theoretical models support the idea that the interaction between these levels is essential for the coherent functioning of the human brain [19, 22].

3. Mathematical Modeling of Conscious–Subconscious Interaction

The functioning of the human brain is based on a clear functional separation between subconscious, fast, automatic and distributed processes and conscious processes, characterized by global integration, deliberation and decision-making control. This duality constitutes a relevant biological model for the design of adaptive computational structures and service-oriented multi-agent systems.

From a mathematical perspective, the conscious–subconscious interaction can be described by a nonlinear dynamical system, in which the global state is decomposable into two functional subspaces: one associated with local and implicit processing (subconscious), and one associated with global and explicit processing (conscious). Subconscious processes operate on the basis of dynamic attractors and implicit knowledge, ensuring rapid and robust reactions, while conscious processes achieve informational integration, contextual evaluation and decision selection [25].

Consciousness emerges when the level of information integration and synchronization exceeds a critical threshold, allowing global access to relevant representations. The subconscious continuously provides content and preliminary assessments, which are amplified, filtered and stabilized at the conscious level. This bidirectional interaction enables adaptive optimization of system behavior in dynamic environments.

The conscious–subconscious model thus provides a formal framework for defining the mechanisms of hierarchical control and decision-making emergence in adaptive systems, constituting a conceptual bridge between cognitive physiology and advanced computational architectures based on knowledge models.

The neurophysiological state space represents a multidimensional space of neuronal and physiological variables, in which each point corresponds to a distinct functional state of the brain. We will consider the human brain as a complex, distributed and nonlinear dynamic system, described by a state space (1):

$$B = \langle \mathrm{N}, S, D, F \rangle, \tag{1}$$

where:

$\mathrm{N} = \left\{ n_i, i = \overline{1,N} \right\}$ - is the total number of neurons;

$S \subset \mathbb{R}^N$ - it is the space of neural states;

D - represents the temporal dynamics of neurons;

F - are the functions of information processing.

The overall state of the brain at time t is defined as (2):

$$\mathrm{X}(t)=\left[x_1(t),x_2(t),...,x_N(t)\right]\subset S, \tag{2}$$

where $x_i(t)$ represents the activation potential of the neuron i.

Fundamental neuronal dynamics represent the totality of biophysical and mathematical mechanisms that determine the temporal evolution of neuronal activity, constituting the basis of all cognitive and behavioral processes. Therefore, the general dynamics of the neural system can be expressed by a system of nonlinear differential equations (3):

$$\frac{d\mathrm{X}(t)}{dt}=F\left(\mathrm{X}(t),u(t),\eta(t)\right), \tag{3}$$

where:

$u(t)$ - are the set of external stimuli (sensory inputs for perceiving the environment);

$\eta(t)$ - is neurophysiological noise;

F - is the nonlinear operator of synaptic interaction.

Conscious–subconscious functional decomposition represents the conceptual separation of cognitive processes into explicit and implicit components, used for the analysis and modeling of cognitive and neurophysiological dynamics. The state space is decomposed into two functional subspaces (4):

$$S=S_C\oplus S_{SC}, \tag{4}$$

where:

S_C - is the subspace of the conscious;

S_{SC} - is the subspace of the subconscious.

The global condition is expressed as (5):

$$\mathrm{X}(t)=\mathrm{X}_C(t)+\mathrm{X}_{SC}(t). \tag{5}$$

Conscious modeling is the process of formalizing explicit cognitive mechanisms and their dynamics, in order to analyze, simulate and implement them in natural or artificial cognitive systems. The conscious is associated with integrative, global processes that are accessible to cognitive reporting. From a mathematical point of view, it can be expressed by the expression (6):

$$\mathrm{X}_C(t)=\mathrm{P}_C\left(\mathrm{X}(t)\right), \tag{6}$$

where P_C is a space projection operator $\mathrm{X}(t)$ on the conscious subspace $\mathrm{X}_C(t)$.

The dynamics of conscious processes are defined by the system of differential equations (7):

$$\frac{d\mathrm{X}_C(t)}{dt}=F_C\left(\mathrm{X}_C(t),\mathrm{X}_{SC}(t)\right). \tag{7}$$

The conscious manifests itself as a cognitive regime in which information is integrated at a global level, allowing the coherent coordination of perceptual, memory and decision-making processes.

Subconscious modeling is the formalization of implicit cognitive processes and their dynamics, in order to analyze their interaction with the conscious level and their role in

adaptive behavior. The subconscious, associated with automated, fast, local processes that are poorly accessible to introspection, is defined by the expression (8):

$$\mathrm{X}_{SC}(t)=\mathrm{P}_{SC}\left(\mathrm{X}(t)\right), \tag{8}$$

where P_{SC} is a space projection operator $\mathrm{X}(t)$ on the subconscious subspace $\mathrm{X}_{SC}(t)$

The dynamics of subconscious processes are defined by the system of differential equations (9):

$$\frac{d\mathrm{X}_{SC}(t)}{dt}=F_{SC}\left(\mathrm{X}_{SC}(t),u(t)\right). \tag{9}$$

Subconscious processes are governed by attractor-type dynamics, corresponding to neuronal and behavioral patterns stabilized by learning, which determine automatic and adaptive responses.

The mechanism of emergence of consciousness is the process by which the dynamic interactions of neural networks lead to the emergence of a global cognitive regime, characterized by informational integration and access to the conscious level. Consciousness appears as an emergent phenomenon when the degree of synchronization and integration exceeds a critical threshold defined by the expression (10):

$$C(t)=\begin{cases}1, & if\ \Phi(t)\geq\Phi_{crit},\\ 0, & after.\end{cases} \tag{10}$$

where:

$\Phi(t)$ - is the measure of informational integration;

Φ_{crit} - is the threshold of awareness.

The conscious–subconscious interaction is a two-way process through which the conscious and subconscious levels cooperate and influence each other in the functioning of the cognitive system. This interaction constitutes the functional coupling between explicit and implicit cognitive processes, through which information is generated, selected and used in adaptive behavior. The bidirectional coupling is modeled and formalized by the system of differential equations (11):

$$\begin{cases}\dfrac{d\mathrm{X}_{C}}{dt}=F_{C}\left(\mathrm{X}_{C},\mathrm{X}_{SC}\right),\\ \dfrac{d\mathrm{X}_{SC}}{dt}=F_{SC}\left(\mathrm{X}_{SC},\mathrm{X}_{C}\right).\end{cases} \tag{11}$$

The contribution of the subconscious to the conscious decision is calculated on the basis of the expression (12):

$$D(t)=\alpha\mathrm{X}_{C}(t)+(1-\alpha)\mathrm{X}_{SC}(t),\quad \forall\alpha\in[0,1]. \tag{12}$$

Physiological and cognitive interpretation highlights the fact that the functioning of the brain is based on a hierarchical and complementary architecture between the subconscious and the conscious. The subconscious provides parallel, fast and metabolically efficient processing, automatically managing most sensory and behavioral information, while the conscious achieves the global, slow and energy-intensive integration necessary for voluntary control, decision-making and flexible adaptation. The interaction between these

two levels allows the brain to function as a self-organizing adaptive system, capable of continuously optimizing the relationship between energy efficiency and cognitive complexity in relation to the environment.

4. Hardware Architecture of the Computing System Based on Hierarchical Conscious–Subconscious processing

The synthesis of the hardware architecture for artificial intelligence systems with hierarchical processing is based on the mathematical formalization of the conscious–subconscious interaction. The architecture is designed as a heterogeneous system, in which the subconscious level performs local, parallel and fast processing, using neuromorphic processing units, TPU/NPU accelerators and associative memory for distributed inference and reactive control. The conscious layer operates on CPUs and many-core, integrating global data, knowledge bases, and planning and decision-making mechanisms. The interaction between levels is governed by an informational threshold module, which evaluates the integration measure Φ and enables global processing, according to the expression (10) $\Phi \geq \Phi_{crit}$. This structure allows the emergence of global decision-making, the maintenance of information coherence and the adaptive optimization of behavior in service-oriented multi-agent systems. Hardware synthesis thus integrates the principles of cognitive hierarchy and parallel processing with the requirements of performance, scalability and energy efficiency, providing an implementable framework for cognitive and autonomous AI systems. The hardware architecture of the computing system based on conscious–subconscious hierarchical processing is shown in Figure 1 (*generated with the support of AI ChatGPT-5.2*).

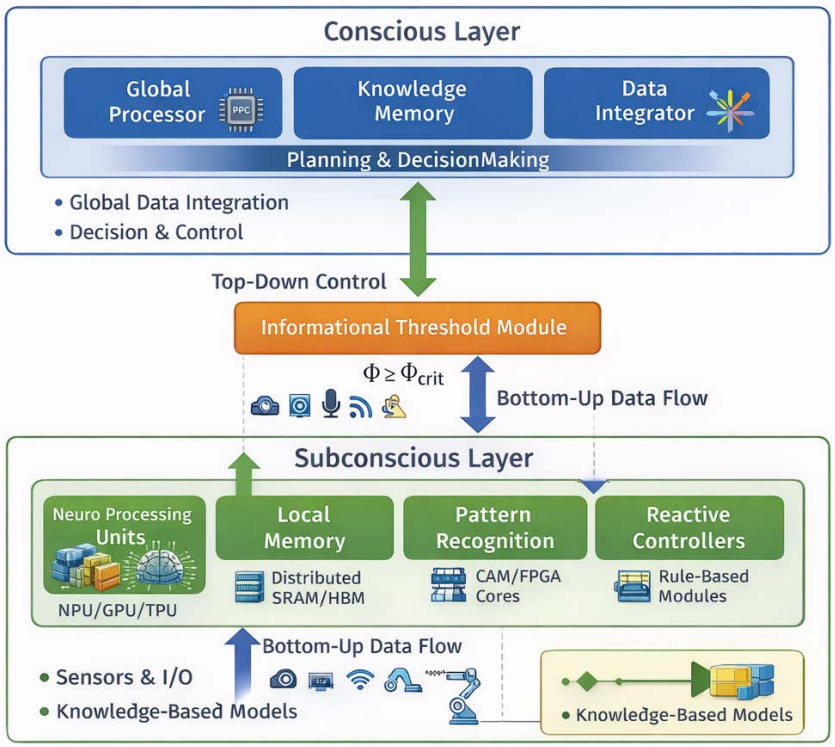

Figure 1. Hardware architecture of the computing system.

Functional specification of hardware architecture:

Conscious Layer – the upper level of architecture; responsible for the global integration of information, planning, decision-making and top-down control over the subconscious level;

Global Processor (CPU / Many-Core / PPC architectures) – responsible for global decision processing and data integration; executes symbolic reasoning and strategic planning algorithms, receives bottom-up input from the subconscious module and generates top-down commands to the subconscious module;

Knowledge Memory – responsible for storing explicit information, rules, behavior patterns, and historical data; provides quick access to data for contextual assessments and integrated inferences, and serves as a reference for top-down control and consolidation of emerging decisions;

Data Integrator – ensures the aggregation of multiple data streams from the subconscious level and from external sensors; achieves the reconciliation and correlation of information, reduces redundancy and inconsistencies and prepares the input for decision-making at the conscious level;

Top-Down Control – flow of commands and constraints transmitted to the subconscious level; activates the conscious for global decision and planning and receives parameters and objectives from the conscious layer, adjusting local processing and task prioritization;

Bottom-Up Data Flow – flow of information preliminarily processed in the subconscious and sent for integration and global evaluation at the conscious level; collects data and patterns from the Subconscious Layer and transmits them to the threshold and conscious module for global decision;

Informational Threshold Module – applies the computational model in expression (10) to assess entropy and correlation between data streams; filters and aggregates inputs from the subconscious level and determines when information is propagated to the conscious level;

Subconscious Layer – the lower level of the architecture, responsible for fast processing, local inference, pattern recognition and reactive control; works as a parallel and distributed system with very low latency;

Neuro Processing Units (NPU/GPU/TPU architectures) – process data in parallel for pattern recognition and automatic inference, handle continuous inputs from sensors and I/O, and execute fast prediction and associative inference algorithms;

Local Memory – includes distributed SRAM/HBM and content-addressable memories (CAM) for quick access to information; stores default knowledge and recurring patterns and enables local reactions without immediately involving the conscious level;

Pattern Recognition – detects patterns, anomalies and complex relationships in input data; uses dedicated FPGAs and accelerators for parallel inference and prepares data for bottom-up propagation to the informational threshold module;

Reactive Controllers – include rule-based modules and predefined logic for immediate response to stimuli and ensure stability and rapid reaction in distributed systems;

Sensors & I/O (External Interface) – functions for collecting data from the physical environment or other systems; provide bottom-up input to the Subconscious Layer and collect feedback for adaptation, ensuring connectivity with external systems;

Knowledge-Based Models – include modules integrated at both the subconscious and conscious levels; they represent explicit (conscious) and implicit (subconscious) knowledge, and serve for inference, planning, and adaptive control.

The proposed hardware architecture implements a hierarchical conscious–subconscious processing, combining a fast and parallel subconscious level with an integrative

and deliberative conscious level. The informational threshold module coordinates the two-way interaction, allowing global decisions to emerge only when informational integration exceeds a critical threshold $\Phi \geq \Phi_{crit}$. This structure ensures adaptability, information coherence, and energy efficiency, providing a scalable framework for service-oriented cognitive and multi-agent AI systems.

5. A Mathematical Model for Multi-Agent Systems Based on Conscious–Subconscious Hierarchical Computation

Multi-Agent Systems (MAS) are an essential framework for modeling and implementing complex distributed systems, characterized by autonomy, interaction and emergent behavior. As modern applications become increasingly dynamic and unpredictable, classical approaches, based exclusively on local rules or global optimization, prove insufficient to explain the adaptability and efficiency of natural systems.

In this context, a mathematical model of a Multi-Agent System based on a conscious–subconscious hierarchical calculation is proposed, inspired by the cognitive architecture of the human brain. The model distinguishes between a subconscious level, responsible for fast, parallel, and reactive processing, and a conscious level, dedicated to global integration, coordination, and deliberative decision-making.

By formally defining agents, internal states, and mechanisms of interaction, this framework provides a rigorous basis for the analysis of emerging behavior. It also allows the evaluation of the adaptability and efficiency of complex multi-agent systems.

We will consider a Multi-Agent system represented by the expression (13):

$$MAS = \langle A, E, I, T \rangle, \tag{13}$$

where:

$A = \{A_1, A_2, ..., A_M\}$ - is the set of agents;

$E \subset \mathbb{R}^M$ - represents the environment of the Multi-Agent system;

I - represents the interactions between agents;

T - is the temporal dynamics.

Each agent $A_j, \forall j = \overline{1,M}$ is defined as a hierarchical cognitive agent defined by the expression (14):

$$A_j = \langle S_j, C_j, U_j, \Pi_j \rangle, \tag{14}$$

where:

S_j - is the subconscious subsystem;

C_j - is the conscious subsystem;

U_j - is the learning mechanism;

Π_j - is the decision policy.

The hierarchical state space represents the organization of the set of states of a system on interdependent functional levels, allowing the description of multi-scalar dynamics and control and emergence mechanisms. The agent state $A_j, \forall j = \overline{1,M}$ is composed of two subspaces defined by the expression (15):

$$x_j(t)=\left(x_j^{sub}(t),x_j^{con}(t)\right), \tag{15}$$

where:

$x_j^{sub}(t)\in\mathbb{R}^m$ - is the subconscious state (implicit, continuous);

$x_j^{con}(t)\in\mathbb{R}^\kappa$ - is the conscious state (explicit, discrete);

provided that $m\gg\kappa$.

The dynamics of the subconscious correspond to a level of fast and parallel processing. These ensure short response time, prediction and pattern recognition, being characterized by stable local developments and automatic reactions that provide informational support for conscious processes. The dynamics of the subconscious are modeled as a continuous nonlinear dynamic system defined by the expression (16):

$$\dot{x}_j^{sub}=f_{sub}\left(x_j^{sub}(t),u_j(t),e_j(t)\right), \tag{16}$$

where:

$u_j(t)$ - the set of local stimuli;

$e_j(t)\in E$ - is the activity environment for the agent $A_j,\forall j=\overline{1,M}$.

The dynamics of consciousness correspond to a slow and deliberative level of processing, characterized by global integration of information, executive control and intentional decision-making. The conscious is modeled as a discrete system with a reduced state, based on the expression (17):

$$x_j^{con}(k+1)=f_{con}\left(x_j^{con}(k),y_j^{sub}(k)\right), \tag{17}$$

where:

$$y_j^{sub}(k)=P\left(x_j^{sub}(t_k)\right), \tag{18}$$

is the informational projection of the subconscious to the conscious (attention / selection).

The attention mechanism and cognitive threshold describe the processes by which information is selected and amplified, and only representations that exceed a certain level of activation or relevance become accessible to conscious processing. Subconscious–conscious transfer occurs only if condition (19) is met:

$$\left\|y_j^{sub}(k)\right\|>\theta_j, \tag{19}$$

where θ_j is the cognitive threshold of the agent, which formalizes the appearance of intuition, alerts or cognitive conflicts.

The hierarchical decision-making policy is a mechanism for selecting actions, structured on functional levels, which allows the coordination of quick local decisions with global deliberative decisions. The agent's decision is the result of a hierarchical merger, defined by the expression (20):

$$a_j(k)=\Pi_j\left(x_j^{con}(k),x_j^{sub}(t)\right), \tag{20}$$

where the subconscious $x_j^{sub}(t)$ provides quick suggestions and the conscious $x_j^{con}(k)$ strategically validates decisions.

Formally, the hierarchical decision-making policy can be calculated based on the expression (21):

$$\Pi_j = \alpha\Pi_{sub} + (1-\alpha)\Pi_{con}, \tag{21}$$

where $\alpha \in [0.7,...,0.95]$.

Conscious–subconscious learning and transfer is the process by which explicit cognitive strategies are internalized as implicit mechanisms, leading to behavior automation and increased adaptive efficiency. The learning process is modelled as a gradual consolidation and takes place according to the expression (22):

$$U_j:\ x_j^{sub}(t+1) = x_j^{sub}(t) = \eta\nabla J_j, \tag{22}$$

where:

J_j - is the performance function;

η - is the learning rate.

It has been shown that repeated conscious rules are internalized at the subconscious level and can be expressed by the expression (23):

$$x_j^{sub} \leftarrow \lim_{k\to\infty}\left(x_j^{con}(k)\right). \tag{23}$$

The interaction between agents represents the set of mechanisms through which autonomous agents exchange information and coordinate their actions, leading to the emergence of collective behavior. The interaction between agents takes place predominantly at the subconscious level and is shaped by the expression (24):

$$x_j^{sub}(t+1) = f_{sub}\left(x_j^{sub}(t), x_i^{sub}(t)\right). \tag{24}$$

At the same time, the coordination of interaction between agents at a global level is managed at a conscious level, based on the model in the expression (25):

$$x_j^{con}(k+1) = g\left(x_j^{con}(k), M_{ij}(k)\right), \tag{25}$$

where M_{ij} are the symbolic messages sent between agents.

The emergence of collective behavior is the process by which local interactions between autonomous agents lead to the emergence of coherent global patterns, without being explicitly imposed by centralized control. The emerging behavior of the Multi-Agent system is evaluated based on the expression (26):

$$B_{global} = \lim_{K\to\infty}\sum_{i=1}^{K}\Pi_i. \tag{26}$$

The emerging behavior of the Multi-Agent System results from local subconscious interactions and global strategic conscious interactions.

6. Hardware Architecture of the Multi-Agent Computing System

A complete hardware architecture is proposed for a service-oriented Multi-Agent Computing System, designed directly on the basis of the conscious–subconscious hierarchical mathematical model. This architecture explicitly translates the functional structure of agents

and their interactions into hardware and software components, providing a robust framework for implementing distributed cognitive services.

Each agent integrates two levels of processing:

Subconscious level – dedicated to fast, parallel and energy-efficient processing. This layer is responsible for executing automatic reactions, learned patterns, and local inference, being implemented through massive parallel computing units such as GPUs, NPUs, or dedicated AI accelerators;

Conscious level – responsible for the global integration of information, deliberative decision-making and coordination of services at the system level. It is achieved through CPU/TPU control cores or specialized processors, which manage attention, cognitive thresholds, and hierarchical decision policies.

Communication between levels and agents is achieved through data buses, shared memory and asynchronous messaging, allowing dynamic coupling and the emergence of collective behavior without the need for rigid centralized control. Each agent is capable of acting autonomously, but integrated into an ecosystem of distributed services, favoring the scalability, adaptability and robustness of the system.

This approach allows the direct mapping of the conscious–subconscious mathematical model on heterogeneous infrastructures, facilitating the development of service-oriented, adaptive, scalable and energy-efficient multi-agent systems, capable of supporting complex cognitive services in distributed environments.

The hardware architecture of the service-oriented Multi-Agent Computing System is shown in Figure 2 (*generated with the support of AI ChatGPT-5.2*), where the following are mentioned:

Intelligent agent – is the basic unit of the multi-agent system. Each agent is autonomous, capable of perceiving the environment, making decisions and acting, integrating two distinct cognitive levels: conscious and subconscious. The Agents interact with each other to support distributed services and emerging behaviors at the system level;

Conscious level – intended for slow, sequential and energy-intensive processing. It functions as a central system, solving planning and deliberative adjustment tasks;

Deliberative decision – evaluates complex options, analyzes risks and plans strategic actions;

Planning and control – coordinates the agent's behavior in the medium and long term, integrating local and global objectives;

Global integration – synchronizes information from the subconscious level and from other agents, allowing coherent and adaptive decision-making;

Subconscious level – intended for massive, parallel, low-latency processing. It supports the automation of behaviors and the transfer of knowledge from the conscious level;

Fast processing – executes calculations and automatic reactions for immediate responses to stimuli;

GPU/NPU/AI accelerators – the subconscious level uses specialized computing units for parallel, energy-efficient processing;

Local inference/automatic reactions – implementation of learned behavioral patterns and reactive decisions, without deliberative involvement of the conscious level;

Communication and interaction – carries out the exchange of information between agents and between the conscious and subconscious levels, ensuring the emergence of collective behavior for local control and global coordination of services;

Distributed messaging – asynchronous communication between agents and distributed services;

Data bus – fast and structured transfer of data between hardware and software components;

Shared memory – allows shared access to information and synchronization of statuses between agents;

Hardware and platforms – allow the flexible implementation of the multi-agent architecture, adapted to the requirements of performance, latency and energy consumption;

Integrated SoC systems – compact, integrated systems for edge and intelligent IoT applications;

Edge Cluster – a group of distributed, fast-processing, and scalable servers located close to the data source;

HPC / TPC systems – high-performance computing infrastructure for large-scale intensive simulations and processing.

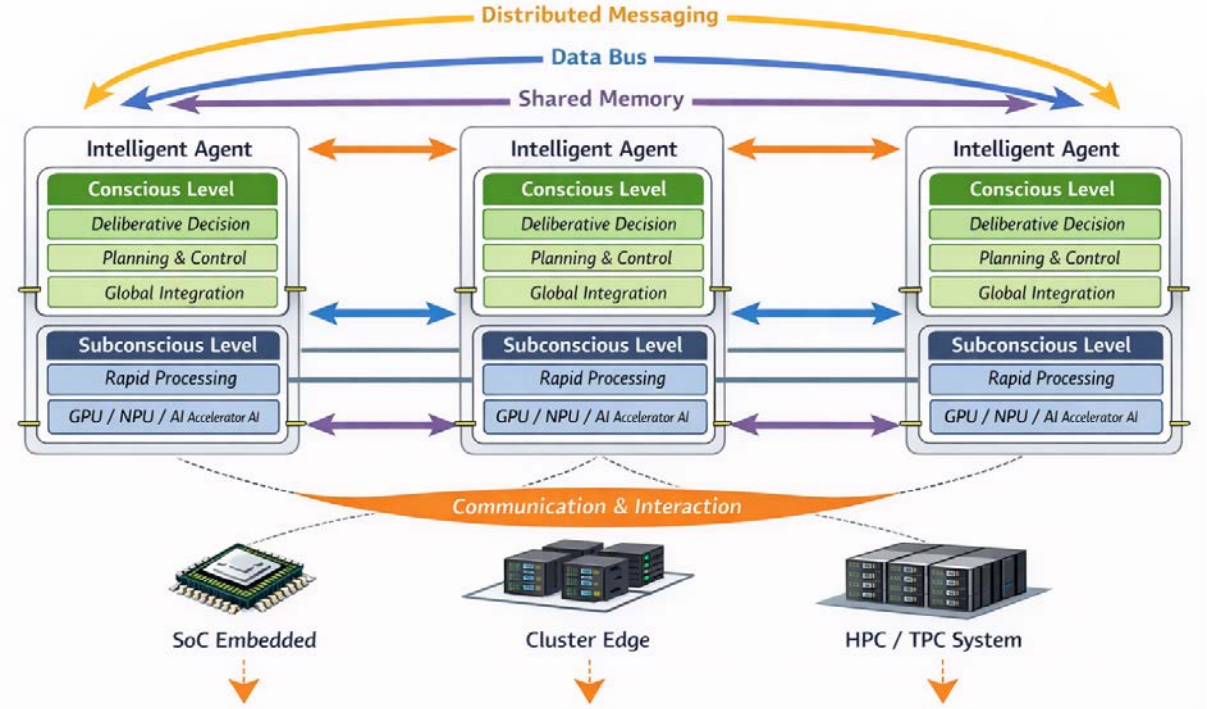

Figure 2. Hardware architecture of the Multi-Agent Computing System.

The proposed hardware architecture implements a Multi-Agent Computing System based on conscious–subconscious hierarchical processing, in which each agent is realized as a cognitive SoC, and global coordination is ensured by a collective conscious level.

7. Conclusions

This paper presented a comprehensive interdisciplinary framework for adaptive computational structures in service-oriented multi-agent systems, grounded in knowledge models inspired by the hierarchical organization of the human brain. By systematically integrating neurophysiological principles, mathematical formalization, and hardware-oriented architectural design, the proposed approach lays a unified foundation for next-generation intelligent systems.

Starting from the physiology of the human brain, the study highlights the functional asymmetry between conscious and subconscious processes, emphasizing the rapid, parallel and implicit processing at the subconscious level, in parallel with the strategic, deliberative and symbolic role of conscious processing. This biological perspective provides a scientifically justified paradigm for hierarchical information processing in artificial systems.

The mathematical modeling of conscious–subconscious interaction formalizes this paradigm through a two-level computational framework, in which subconscious dynamics are represented by continuous, adaptive and high-dimensional processes, while conscious processing functions as a discrete, low-dimensional level dedicated to control and decision-making. The introduction of attention and coupling operators allows for a dynamic information flow and adaptive tuning between these levels, ensuring both computational efficiency and interpretability.

Based on this formalization, a hardware architecture for hierarchical conscious–subconscious processing is proposed, demonstrating how heterogeneous computational elements—such as NPUs, GPUs, and CPUs—can be structurally and functionally aligned with distinct cognitive roles. This architecture supports real-time adaptive behaviors, scalability, and energy efficiency, reflecting essential properties of biological cognitive systems.

Extending the model from the individual level, a mathematical framework for multi-agent systems is developed, in which each agent incorporates a local conscious–subconscious hierarchy, and coordination at the higher level emerges through collective conscious mechanisms. This formulation allows for distributed decision-making, cooperative adaptation and knowledge sharing in service-oriented environments, without introducing centralized control blockages.

Finally, the hardware architecture of the Multi-Agent Computing System demonstrates the feasibility of practical implementation of the proposed model in real computational infrastructures. By combining autonomous cognitive agents with a level of collective coordination, the architecture supports modularity, fault tolerance and dynamic service composition, essential properties for modern distributed and intelligent systems.

In conclusion, the proposed adaptive computing structures represent a significant step towards cognitive, knowledge-oriented multi-agent systems, in which neurobiological inspired hierarchy, rigorous mathematical modeling and conscious hardware architecture design converge in a coherent framework. Future research directions are aimed at experimental validation, analysis of the dynamics of learning processes at the multi-agent level, as well as the integration of ethical and explainability constraints in the conscious decision layer.

Acknowledgments: This research was carried out within the 020404 Institutional Project, with the technical and technological support provided by the "Artificial Intelligence and Multi-Agent Systems" Laboratory, within the Department of Informatics and Systems Engineering, Technical University of Moldova.

During the preparation of this study, the authors used ChatGPT-5.2 for grammar checking, correct wording of text, and evaluation of the correctness of scientific results. The authors have reviewed the result and take full responsibility for the content of this publication.

Contribution of authors:

Vadim Struna: Conceptualization, Methodology, Resources, Writing – original draft.

Victor Ababii: Conceptualization, Formal analysis, Methodology, Resources, Writing – original draft.
Viorica Sudacevschi: Methodology, Project administration, Writing – review & editing.
Silvia Munteanu: Formal analysis, Resources.
Olesea Borozan: Formal analysis, Resources, Writing – review & editing.
Victoria Alexei: Validation, Investigation, Writing – review & editing.

Conflicts of Interest: The authors declare no conflict of interest.

References

1. Borangiu, T.; Trentesaux, D.; Leitão, P.; Cardin, O.; & Lamouri, S. (Eds.). (2021). *Service Oriented, Holonic and Multi-Agent Manufacturing Systems for Industry of the Future: Proceedings of SOHOMA 2020* (Vol. 952). Springer Nature, 544 p., https://doi.org/10.1007/978-3-030-69373-2.
2. Li, A.; Xie, Y.; Li, S.; Tsung, F.; Ding, B.; & Li, Y. (2024). Agent-oriented planning in multi-agent systems. *arXiv preprint arXiv:2410.02189*, https://doi.org/10.48550/arXiv.2410.02189.
3. Wold, H. (1982). Models for knowledge. *The making of statisticians*, pp. 189-212, Springer, New York, NY. https://doi.org/10.1007/978-1-4613-8171-6_14.
4. Antonelli, C. (2005). Models of knowledge and systems of governance. *Journal of institutional economics*, *1(1)*, pp. 51-73, https://doi.org/10.1017/S1744137405000044.
5. Munir, K.; & Anjum, M. S. (2018). The use of ontologies for effective knowledge modelling and information retrieval. *Applied computing and informatics, 14(2)*, pp. 116-126, https://doi.org/10.1016/j.aci.2017.07.003.
6. Haslinda, A.; Sarinah, A. (2009). A review of knowledge management models. *Journal of international social research, 2(9)*, pp. 187, ISSN 1307-9581.
7. Noy, N.F.; Fergerson, R.W.; Musen, M.A. (2000). The knowledge model of Protégé-2000: Combining interoperability and flexibility. *In International conference on knowledge engineering and knowledge management*, pp. 17-32, Berlin, Heidelberg: Springer Berlin Heidelberg, https://doi.org/10.1007/3-540-39967-4_2.
8. Ababii, V.; Sudacevschi, V.; Munteanu, S.; Carbune, V.; Borozan, O. (2025) Multi-Coalition Multi-Agent decision making system synthesis. *In International Journal of Computing, 24(3)*, pp. 513-519, ISSN 1727-6209, https://doi.org/10.47839/ijc.24.3.4188.
9. Ababii, V.; Cărbune, V.; Sudacevschi, V.; Marusic, G.; Braniște, R.; Drumea, N. (2025) Sistem Multi-Agent pentru monitorizarea și predicția proceselor de mediu. *Akademos, 1(76)*, pp. 22-30, https://doi.org/10.52673/18570461.25.1-76.01.
10. Struna, V.; Borozan, O.; Carauș, A. (2023) Knowledge models for evolutionary systems with artificial intelligence. *In Proceedings of the Twelfth Conference "Informatics and Computer Technologies Problems" (ICTP – 2023)*, pp. 38-41, Chernivtsi, Ukraine, 10–12 November, 2023.
11. Ababii, V.; Strună, V.; Sudacevschi, V.; Borozan, O.; Munteanu, S. (2024) Method for knowledge acquisition based on image processing for decision-making systems. *In Electronics, Communications and Computing (IC ECCO-2024): The conference program and abstract book: 13th intern. conf.,* pp. 165-166, Chișinău: Tehnica-UTM, 17-18 Oct. 2024. Technical University of Moldova, ISBN: 978-9975-64-480-8 (PDF).
12. Struna, V.; Ursu A.; Kapusteanski, M. (2024) Analiza modelelor de cunoștințe pentru sisteme cu inteligență artificială. *In Technical Scientific Conference of Undergraduate, Master and PhD Students*, Universitatea Tehnică a Moldovei, 27-29 Martie 2024. Chișinău, 2024, vol. 1, pp. 392-394. ISBN 978-9975-64-458-7, ISBN 978-9975-64-459-4.
13. Baars, B. J.; Franklin, S.; Ramsoy, T. Z. (2013) Global workspace dynamics: Cortical "binding and propagation" enables conscious contents. *Frontiers in Psychology*, 4, 200. https://doi.org/10.3389/fpsyg.2013.00200.
14. Clark, A. (2016) *Surfing Uncertainty: Prediction, Action, and the Embodied Mind*. Oxford University Press. https://doi.org/10.1093/acprof:oso/9780190217013.001.0001.
15. Damasio, A. (2018) *The Strange Order of Things: Life, Feeling, and the Making of Cultures*. NY: Pantheon Books, 336p.
16. Dehaene, S. (2014) *Consciousness and the Brain: Deciphering How the Brain Codes Our Thoughts*. Viking Press, 363p., ISBN: 978-0-698-15140-6.

17. Friston, K. (2019) A free energy principle for a particular physics. *arXiv preprint*, arXiv:1906.10184. https://doi.org/10.48550/arXiv.1906.10184.
18. Gazzaniga, M. S.; Ivry, R. B.; Mangun, G. R. (2019) *Cognitive Neuroscience: The Biology of the Mind* (5th ed.). W. W. Norton & Company, ISBN: 978-0-393-60317-0.
19. Kandel, E. R.; Koester, J. D.; Mack, S. H.; Siegelbaum, S. A. (2021) *Principles of Neural Science* (6th ed.). McGraw-Hill Education, 108p., ISBN: 978-1-25-964224-1.
20. Mashour, G. A.; Roelfsema, P.; Changeux, J.-P.; Dehaene, S. (2020) Conscious processing and the global neuronal workspace hypothesis. *Neuron*, 105(5), pp. 776-798. https://doi.org/10.1016/j.neuron.2020.01.026.
21. Pessoa, L. (2017) A network model of the emotional brain. *Trends in Cognitive Sciences*, 21(5), pp. 357–371. https://doi.org/10.1016/j.tics.2017.03.002.
22. Seth, A. K.; Bayne, T. (2022) Theories of consciousness. *Nature Reviews Neuroscience*, 23, pp. 439–452. https://doi.org/10.1038/s41583-022-00587-4.
23. Stanley, D. A.; Adolphs, R. (2013) Toward a neural basis for social behavior. *Neuron*, 80(3), pp. 816–826. https://doi.org/10.1016/j.neuron.2013.10.038.
24. Tononi, G.; Boly, M.; Massimini, M.; Koch, C. (2016) Integrated information theory: From consciousness to its physical substrate. *Nature Reviews Neuroscience*, 17(7), pp. 450–461. https://doi.org/10.1038/nrn.2016.44.
25. Friston, K. (2010) The free-energy principle: A unified brain theory? *Nature Reviews Neuroscience*, 11(2), pp. 127–138. https://doi.org/10.1038/nrn2787.

Citation: Struna, V., Ababii, V., Sudacevschi, V., Munteanu, S., Borozan, O. and Alexei, V. (2026). Adaptive computing structures for service-oriented multi-agent systems based on knowledge models. *Journal of Engineering Science*. 2026, 33 (1), pp. 37-52. https://doi.org/10.52326/jes.utm.2026.33(1).03.

Submission of manuscripts: jes@meridian.utm.md

Journal of Engineering Science *Vol. XXXIII, no. 1 (2026), pp. 53 - 55*
Fascicle *Electronics and Computer Science* *ISSN 2587-3474*
Topic *Computers and Information Technology* *eISSN 2587-3482*

https://doi.org/10.52326/jes.utm.2026.33(1).04
UDC 004.8:004.032.26:37.018:005.3

MULTI-AGENT SYSTEM FOR PLANNING THE EDUCATIONAL CONTINGENT USING NEURAL NETWORKS

Radu Melnic[1*], ORCID: 0000-0002-3709-4739

[1]*Technical University of Moldova, Ștefan cel Mare, 168, Chișinău, MD-2024, Republic of Moldova*
* Corresponding author: Radu Melnic, *radu.melnic@adm.utm.md*

Received: 01. 14. 2026
Accepted: 02. 24. 2026

Abstract. This paper is dedicated to the development and validation of an intelligent architecture for educational cohort planning, based on the integration of multi-agent systems with artificial neural networks. The research is motivated by the need to efficiently manage educational data flows characterized by high volume, temporal dynamics, and uncertainty, in the context of demographic and socio-economic changes. To this end, a formal model is proposed that describes agents' decision-making dynamics, inter-agent coordination mechanisms, and the neural learning process used to predict key educational indicators. To validate the proposed solution, an experimental dataset covering the period 2020–2024 was used, reflecting the educational trajectory from high school graduation to the completion of undergraduate studies. The experimental results highlight stable convergence of the learning process, a reduction in prediction error, and the model's ability to approximate nonlinear relationships between demographic and socio-economic factors and educational indicators. The multi-agent architecture enables efficient distribution of computational tasks, scalability, and adaptability to changes in the educational environment. The proposed solution provides robust decision support for educational management and may serve as an essential formal basis for the development of advanced intelligent systems for institutional planning.

Keywords: *decision support, parallel processing, educational data streams, machine learning, online learning, educational forecasting, distributed architectures, optimization, educational management, temporal data, neural inference, adaptivity.*

1. Introduction

Educational cohort planning involves complex processes of prediction, optimization, and coordination, characterized by temporal dynamics, uncertainty, and interdependence among multiple decision-making entities. Classical centralized models [1], based on statistical analyses or rigid expert systems [2, 3], exhibit significant limitations in terms of scalability, adaptability, and the ability to integrate heterogeneous and distributed educational data.

In this context, Multi-Agent Systems (MAS) [4] provide an appropriate computational framework for the distributed modeling of the educational planning process, in which autonomous, reactive, and cognitive agents represent educational institutions, academic

programs, student cohorts, and decision-making factors. Each agent is endowed with local mechanisms for perception, reasoning, and action, while the global behavior of the system emerges from interactions such as cooperation, negotiation, and inter-agent coordination [5].

The integration of artificial neural networks [6, 7] into the MAS architecture [8] enables agents to be equipped with advanced machine learning and nonlinear prediction capabilities [9]. Neural models can be used to estimate enrollment dynamics, retention, and graduation flows, as well as to identify latent patterns in historical educational, demographic, and socio-economic data. In the proposed architecture, neural networks are implemented either at the agent level (agent-level learning) or at the level of global coordination, supporting the continuous adaptation of planning strategies [10–17].

The present research is oriented toward the development of an intelligent Multi-Agent System based on neural networks for educational cohort planning, in which learning, prediction, and decision-making mechanisms are integrated within a modular and scalable architecture. The proposed approach contributes to improving forecasting accuracy, optimizing the allocation of educational resources, and supporting strategic decision-making in a dynamic and uncertain educational environment.

2. Mathematical Model of the Proposed Multi-Agent System

Multi-Agent System (*MAS*) is defined as a tuple (1):

$$MAS = \langle A, E, O, I, P \rangle \tag{1}$$

where:

$A = \{a_1, a_2, ..., a_N\}$ is the set of agents involved in the monitoring and management of the educational process;

E is the dynamic educational environment, which represents a complex and adaptive learning system in which the interaction between actors, content, and technologies generates flexible, personalized, and evolving educational processes;

O represents the set of strategic objectives, achieved through an adaptive planning mechanism under variable environmental conditions (including educational cohort planning);

I represents the ensemble of communication and coordination relations among agents: communication (messages, signals, data), cooperation (coordinated work to achieve a common objective), negotiation and decision coordination, competition or conflict resolution, synchronization of actions in time and space, etc.;

P represents the agents' decision policies and models their decision-making behavior.

Each agent ... $a_i, \forall i = 1,...,N$ is characterized by the set (2):

$$a_i = \langle S_i, A_i, \pi_i, ANN_i \rangle \tag{2}$$

where:

$S_i, \forall i = 1,...,N$ is the domain of internal configurations that describe the agent's state space $S_i = \{s_{i1}, s_{i2}, ..., s_{im}\}$ (observable states, internal states, latent states, etc.)

$A_i, \forall i = 1,...,N$ is the domain of operational decisions available to the agent $A_i = \{a_{i1}, a_{i2}, ..., a_{im}\}$, where each a is an action with respect to: the degree of freedom, the capacity to influence the environment, and the right and level of modeling of the decision-making process;

$\pi_i : S_i \to A_i, \forall i = 1,...N$ is the decision policy expressed by a function that governs the agent's behavior by mapping states S_i into actions A, with the aim of optimizing an objective O;

$ANN_i, \forall i = 1,...,N$ is the adaptive component of the system, responsible for learning the relationships among data through a neural network.

The global state of the educational system at time *t* is defined by the expression (3):

$$S(t) = \bigcup_{i-1}^{N} \left(S_i(t) \right) \tag{3}$$

For an educational agent a_i the state is defined by the expression (4):

$$S_i(t) = \left[E_i(t), R_i(t), C_i(t), D_i(t) \right] \tag{4}$$

where:

$E_i(t)$ is the number of enrollments in the study programs;

$R_i(t)$ is the proportion of participants who continue their educational trajectory (promotion rate);

$C_i(t)$ is the functional potential of the institution to fulfill its educational mission;

$D_i(t)$ is the set of population and socio-economic variables that influence the evolution of the educational system, expressed through demographic factors (population size, age distribution, birth and death rates, migration, etc.) and socio-economic factors (income level, employment rate, education level, access to resources and services, social status, public policies, and economic context, etc.).

3. Agent Model for Prediction of Educational Processes Based on Neural Network

The neural inference mechanism is based on artificial neural networks capable of learning complex and nonlinear relationships from historical and current educational data. It processes indicators such as retention rates, institutional capacity, and demographic and socio-economic factors to construct relevant internal representations of the system. Based on these representations, the model generates estimates regarding the future evolution of the educational cohort and the demand for resources. The mechanism continuously adapts by updating its parameters according to new data, thereby increasing prediction accuracy. In this way, neural inference provides decision support for strategic planning and the optimization of educational processes.

Let $x_i(t) \in \mathbb{R}^n$ be the input vector of agent a_i, defined by expression (5):

$$x_i(t) = \left[E_i(t-1), R_i(t-1), C_i(t-1), D_i(t-1) \right] \tag{5}$$

The prediction of the educational cohort is performed by a neural network based on expression (6):

$$\widehat{E}_i(t+1) = f_{Q_i}\left(x_i(t) \right) \tag{6}$$

where:

f_{Q_i} is the neural approximation function that models the complex and nonlinear relationships between the system's input and output variables. By adjusting its internal weights, it enables precise estimation of the behavior and future evolution of the educational process;

Q_i represents the set of trainable weights that encode the knowledge learned from the available data $x_i(t)$. These weights are iteratively adjusted during the training process to minimize the prediction error. They determine the model's ability to generalize and produce accurate estimates for new situations.

The associated loss function is the mathematical criterion (7) used to evaluate the difference between the values predicted by the model and the actual observed values. It quantifies the prediction error and provides an optimization signal for the learning process. By minimizing the loss function, the model adjusts its trainable weights to improve estimation accuracy. The choice of loss function directly influences the stability, convergence, and overall performance of the neural model:

$$L_i\left(Q_i\right)=\frac{1}{T}\sum_{t=1}^{T}\left\|E_i(t+1)-\widehat{E}_i(t+1)\right\|^2 \tag{7}$$

The decision-making dynamics of agents, implemented based on the neural model, reflect how decisions are continuously adapted according to the predictions and inferences generated by the neural network. The neural model processes the current states of the environment $x_i(t)$ and provides estimates that guide the selection of agents' actions. As new data become available, the model parameters are updated, resulting in corresponding modifications to the decision policies. This interaction between learning and decision-making enables agents to respond effectively to changes and uncertainties. Consequently, the global behavior of the multi-agent system becomes adaptive and oriented toward optimizing the established objectives O.

Accordingly, an agent's policy is defined as the formal mechanism (8) that establishes the mapping between perceived environmental states and selected actions. It functions as a decision rule that transforms available information into concrete operational decisions. The policy integrates the predictions provided by the neural model with the agent's objectives and constraints. By continuously updating its parameters, the policy allows the agent's behavior to adapt to changes in the environment. In this way, the agent can act autonomously, rationally, and in a manner oriented toward optimizing system performance:

$$\pi_i(t)=\arg\max_{a\in A_i}\left(\mathrm{E}\left[U_i\left(S_i(t),a\right)\right]\right) \tag{8}$$

In model (8) the utility function U_i is the mathematical criterion that quantifies the degree to which an agent's objectives are satisfied following an action or decision. It allows the comparison of alternatives and guides the decision-making process toward maximizing the overall performance of the educational system, where:

$$U_i=\alpha_i+\beta_i+\gamma_i, \tag{9}$$

Expression (9) defines the utility function U_i of agent i as a weighted combination of multiple performance criteria. The term α_i reflects the importance of decision accuracy, β_i measures the efficiency of resource utilization, and γ_i penalizes violations of constraints. The coefficients α,β,γ control the trade-offs between quality, efficiency, and adherence to limitations in the agent's decision-making process, subject to the condition $\left(\alpha,\beta,\gamma\right)\in\mathbb{R}^+$.

4. Inter-Agent Interaction and Coordination

Inter-agent interaction and coordination represent the process through which agents in an educational system communicate and cooperate to achieve their individual and collective objectives. This includes the exchange of information, synchronization of actions, and adaptation of strategies based on the behaviors of other agents. Through coordination, agents can avoid conflicts, optimize resource utilization, and enhance the overall efficiency of the educational system. Continuous interaction generates emergent dynamics, in which collective behavior is not merely the sum of individual behaviors. Thus, inter-agent cooperation and communication are essential for the adaptive functioning and performance of a complex multi-agent educational system.

Interactions are modeled using a graph (10), where nodes represent agents and edges indicate the relationships or information exchanges between them. This representation allows visualization of the communication structure and coordination flows within the system. Furthermore, graphs facilitate the analysis of collective dynamics and the identification of critical points for optimizing cooperation among agents:

$$G = \left(A, I\right), \tag{10}$$

where edges represent information exchanges (11):

$$m_{ij}(t) = \phi\left(S_i(t), S_j(t)\right). \tag{11}$$

The state of an agent (12) is updated according to a mechanism that integrates information received from the external environment and the outcomes of previous actions. This includes modifying internal values, objectives, and the level of available resources. The updating process is based on mathematical functions or neural models that determine how new data influence future decisions. Through this update, the agent can respond adaptively to environmental changes and the behavior of other agents. Thus, the agent's state continuously reflects the current situation and conditions its decision-making policies:

$$S_i(t+1) = \varphi\left(S_i(t), A_i(t), \sum_{j \in N_i}\left(m_{ij}(t)\right)\right) \tag{12}$$

5. The Overall Optimization Goal

The global optimization objective represents the main goal pursued by the entire Multi-Agent System as a whole. It synthesizes collective performance by integrating the results and actions of individual agents. The objective may include criteria such as maximizing efficiency, reducing costs, improving service quality, or adhering to constraints. Within the decision-making process, each agent adjusts its behavior to contribute to the achievement of this common objective. Thus, global optimization ensures coherence, adaptability, and overall performance of the educational system.

Educational cohort planning is formulated as a distributed optimization problem, in which multiple agents make autonomous but interdependent decisions for efficient resource allocation and activity scheduling. Each agent optimizes a local sub-objective while simultaneously contributing to the achievement of the global objective of the educational system. This approach allows continuous adaptation to demographic and socio-economic changes as well as to institutional constraints:

$$\min_{\{\pi_i\}} \sum_{i=1}^{N} L_i\left(Q_i\right), \tag{13}$$

subject to:

$$\sum_{i=1}^{N} \widehat{E}_i(t) \le \sum_{i=1}^{N} C_i(t) \tag{14}$$

and $\widehat{E}_i(t) \ge 0, \ \forall i$.

Convergence and adaptivity are essential properties of intelligent and multi-agent systems. Convergence describes the system's ability to reach, over time, a stable state or an optimal solution through iterative learning and decision-making processes. Adaptivity reflects the agents' ability to modify their behavior in response to changes in the environment and new information. Together, these two characteristics ensure the stability of the system's operation under dynamic and uncertain conditions. Consequently, the system can maintain optimal performance even in the presence of disturbances or contextual variations.

The learning process is iterative, involving repeated updates of the model parameters based on prediction errors obtained at each step. At each iteration, the system evaluates current performance and adjusts its internal mechanisms to reduce deviations from the established objectives. This continuous process enables progressive improvement in accuracy and allows the model to adapt to new data and changing conditions:

$$Q_i^{(k+1)} = Q_i^{(k)} - \eta \nabla_{Q_i} ANN_i, \tag{15}$$

where η is the learning rate, a parameter that controls the magnitude of weight updates and influences the speed and stability of the model's convergence process.

The system converges to a distributed equilibrium as a result of repeated interactions among agents and local optimization processes. Each agent adjusts its decisions based on its own information and exchanges with other agents, without requiring centralized control. This equilibrium reflects a stable state in which local objectives are aligned with the system's global objective. Convergence is supported by learning mechanisms and inter-agent coordination. Thus, the system maintains stability and performance even in dynamic and uncertain environments:

$$\lim_{t \to \infty} \left\| S(t+1) - S(t) \right\| \to 0. \tag{16}$$

6. Synthesis of the Multi-Layer Architecture of the Multi-Agent System

The synthesis of the multi-layer architecture of the multi-agent system describes the hierarchical organization of the system's functional components across distinct levels. Each layer fulfills a specific role, ranging from data perception and collection to decision-making and global coordination. The proposed architecture (see Figure 1) is organized hierarchically into functional layers, enabling clear separation of responsibilities, modularity, reusability, and scalability. The system integrates a distributed multi-agent framework with neural learning mechanisms at both local and global levels.

Functional description of the multi-agent architecture:

Data & Environment Layer represents the external educational environment and provides the raw data necessary for the planning process, including historical educational information, demographic and socio-economic data, institutional capacities, and educational policy factors;

Perception & Preprocessing Layer handles data acquisition, filtering, and preprocessing from the educational environment, ensuring normalization, anomaly detection, and transformation into input vectors suitable for intelligent agents and neural models;

Multi-Agent Layer represents the set of specialized autonomous agents (institutional, program-level, cohort-level, and policy agents) that model the decision-making entities within the educational system and interact through mechanisms of cooperation, negotiation, and information exchange;

Decision & Planning Layer integrates the results of neural predictions into distributed decision-making policies, allowing agents to generate optimal plans for resource allocation and educational cohort sizing under institutional constraints;

Coordination & Communication ensures inter-agent synchronization and coordination through message exchanges, consensus mechanisms, and conflict resolution, contributing to the coherence of system-level decisions;

Execution & Feedback Layer implements the generated decisions, monitors the outcomes, and provides adaptive feedback to agents and neural models, supporting continuous learning and strategy adjustment.

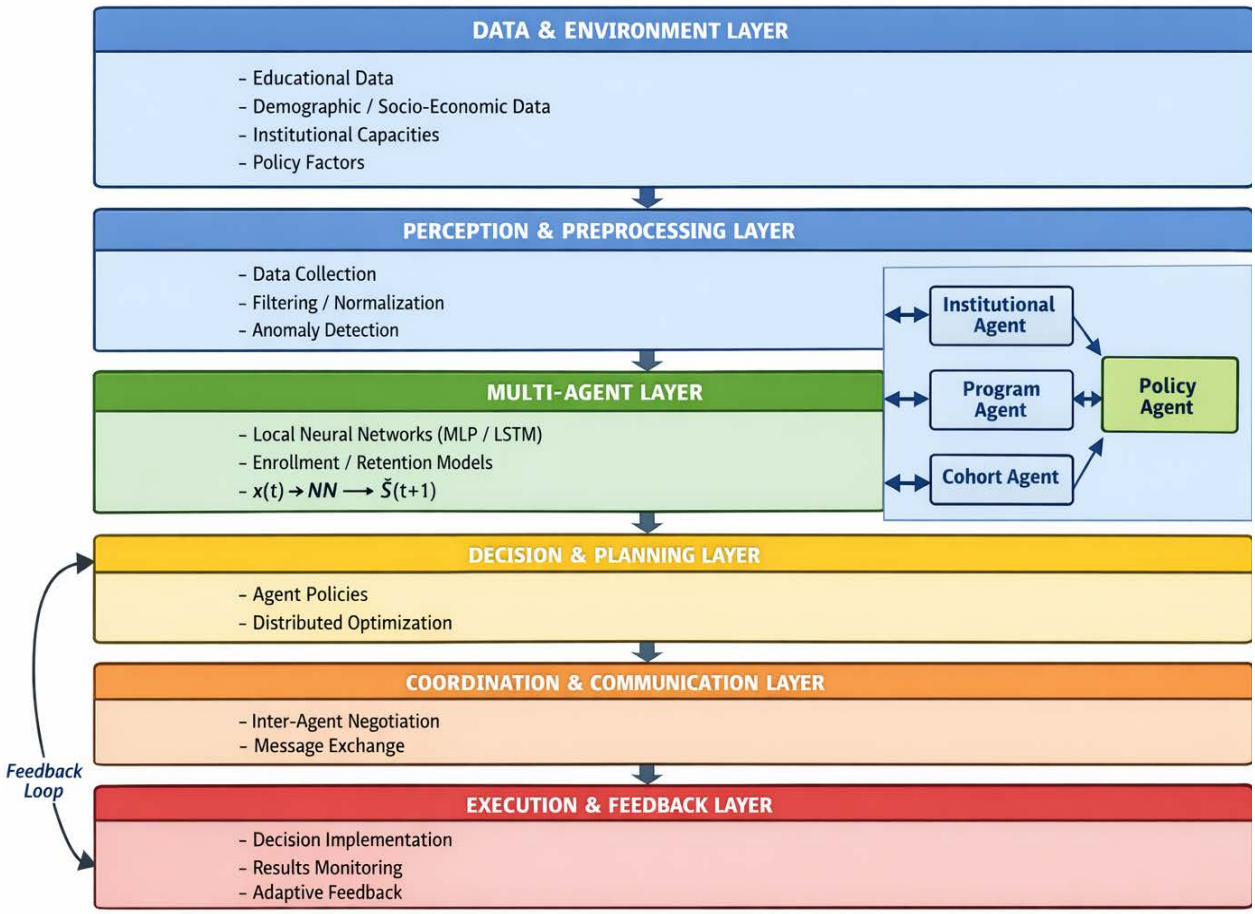

Figure 1. Layered architecture of the multi-agent system based on neural networks for educational contingent planning.

The multi-layer architecture is designed to apply the mathematical models defined earlier in this work, ensuring a direct correspondence between the theoretical formulation and practical implementation. Each layer incorporates components that reflect the variables, constraints, and optimization functions of the mathematical model. This alignment allows for experimental validation of theoretical hypotheses through simulations and controlled experiments. Consequently, the architecture facilitates the coherent integration of decision-making, learning, and coordination mechanisms within a unified formal framework.

7. Modeling the Dataset for ANN Training

Modeling the dataset for training the ANN represents the process of selecting, structuring, and preprocessing the data used to train the artificial neural network. This process includes preprocessing raw data to identify relevant variables (inputs and outputs), cleaning the data, handling missing values, and normalizing them to ensure stable learning. The dataset is organized as pairs of (input data, labels/target values) corresponding to the prediction objective. Additionally, the data are divided into training, validation, and test subsets to evaluate performance and prevent overfitting. Proper dataset modeling is essential for the accuracy, generalization, and efficient convergence of the neural network.

Thus, defining the educational dataset involves identifying and selecting relevant information for modeling and analyzing educational processes. This includes establishing input variables, performance indicators, and target values necessary for training intelligent models. The process requires structuring data from heterogeneous sources, such as academic records, demographic data, and institutional indicators. A rigorous dataset definition ensures the consistency, quality, and relevance of the results obtained.

Let the educational process be defined by the dataset (17):

$$D = \left\{ \left(\mathrm{x}^{(k)}, \mathrm{y}^{(k)} \right) \middle| k = 1,2,...,K \right\}, \tag{17}$$

where:

$\mathrm{x}^{(k)} \in \mathbb{R}^n$ represents the input vector of the model, encompassing educational characteristics relevant for analysis and prediction. This may include indicators such as academic performance, retention rates, institutional capacity, and demographic factors. The input vector supplies the information required for the model to learn the relationships between input data and the predicted outcomes;

$\mathrm{y}^{(k)} \in \mathbb{R}^m$ represents the desired output vector of the model, corresponding to the predicted outcomes of the educational process. This may include indicators such as the forecasted educational cohort, retention rates, and graduation rates. The output vector enables the assessment of model performance and provides a basis for informed educational planning decisions;

n and m respectively, represent the dimensions of the input and output vectors;

K represents the set of subsets used for the ANN training process.

Figure 2 shows the structure of the raw data for modeling an educational process with admission based on the Baccalaureate diploma, a 4-year study program, and 8 semesters, as applied at the Technical University of Moldova.

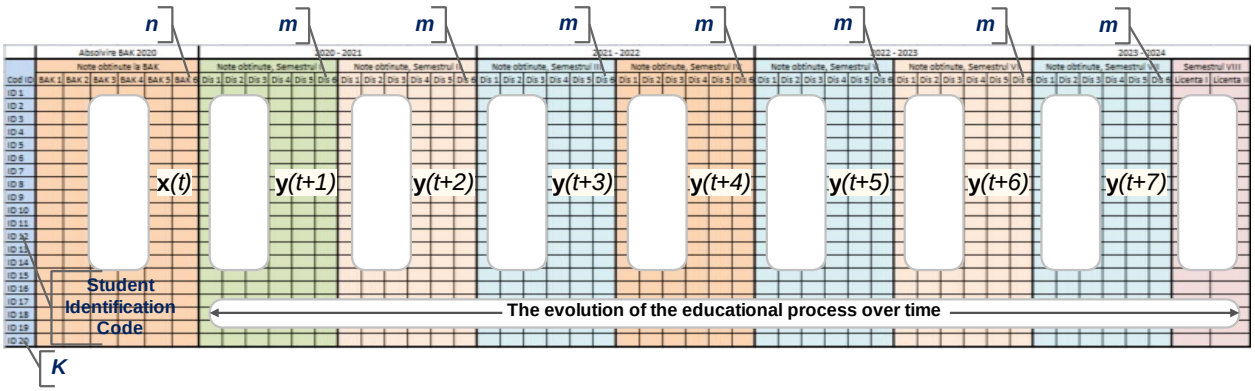

Figure 2. Raw data structure for modeling an educational process.

Specification of the raw data structure:

Student Identification Code - represents a unique identifier assigned to each student, used for academic records, management of educational data, and tracking the educational trajectory within the information system;

K - the number of data subsets, or the number of students involved in the modeling process;

n - the dimension of the input vector, or the number of grades obtained at BAK included in the modeling process;

m - the dimension of the output vector, or the number of grades (subjects) involved in the modeling process across the study semesters;

x*(t)* – the input vector of dimension *n*;

y*(t+1)*... **y***(t+8)* - the output vectors of dimension *m*.

For modeling the dataset used for ***ANN*** training, two variants of multi-agent computing architectures are analyzed:

a) ***Sequential***, as defined by the mathematical model (18):

$$\begin{aligned} &\mathrm{y}(t+1)=f_1\left(\mathrm{x}(t)\right);\\ &\mathrm{x}(t+1)=\mathrm{y}(t+1),\mathrm{y}(t+2)=f_2\left(\mathrm{x}(t+1)\right);\\ &\ldots\\ &\mathrm{x}(t+7)=\mathrm{y}(t+7),\mathrm{y}(t+8)=f_8\left(\mathrm{x}(t+7)\right). \end{aligned} \tag{18}$$

a) ***Complex***, as defined by the mathematical model (19):

$$\begin{aligned} &\mathrm{y}(t+1)=f_1\left(\mathrm{x}(t)\right);\\ &\mathrm{x}(t+1)=\cup\left(\mathrm{x}(t),\mathrm{y}(t+1)\right),\mathrm{y}(t+2)=f_2\left(\mathrm{x}(t+1)\right);\\ &\mathrm{x}(t+2)=\cup\left(\mathrm{x}(t+1),\mathrm{y}(t+2)\right),\mathrm{y}(t+3)=f_3\left(\mathrm{x}(t+2)\right);\\ &\ldots\\ &\mathrm{x}(t+7)=\cup\left(\mathrm{x}(t+6),\mathrm{y}(t+7)\right),\mathrm{y}(t+8)=f_8\left(\mathrm{x}(t+7)\right). \end{aligned} \tag{19}$$

8. Mathematical Model of Neural Network Learning Process

A multilayer neural network can be defined as a function composition that maps input data to output results through multiple hierarchical processing layers. Each layer performs a linear transformation followed by a nonlinear activation function. This structure allows the network to capture and represent complex, nonlinear relationships among the system's variables (20):

$$f_Q(\mathrm{x})=f^{(L)}\left(f^{(L-1)}\left(\ldots\left(f^{(1)}(\mathrm{x})\right)\right)\right), \tag{20}$$

where the index L denotes the layer number in the ANN topology, and for each layer $l\subset L$ the function is defined as (21):

$$\begin{aligned} &\mathrm{z}^{(l)}=\mathrm{W}^{(l)}\mathrm{a}^{(l-1)}+\mathrm{b}^{(l)},\\ &\mathrm{a}^{(l)}=\sigma^{(l)}\left(\mathrm{z}^{(l)}\right) \end{aligned}, \tag{21}$$

where:

$\mathrm{a}^{(0)}=\mathrm{x}$ the input vector containing the educational features;

$\mathrm{W}^{(l)}\in\mathbb{R}^{n_l\times m_l}$ the weight matrix, representing the numerical structure that defines the strength and influence of each connection between neurons. It is iteratively adjusted during

training to enable the neural network to learn the complex relationships between input data and desired outputs;

$\mathrm{b}^{(l)} \in \mathbb{R}^{n_l}$ the bias vector, which introduces a constant term to each neuron. It is adjusted during training to allow the network to modify the activation threshold and more accurately model the complex relationships between inputs and outputs;

$\sigma^{(l)}\left(z^{(l)}\right)$ the activation function, which applies a nonlinear transformation to the aggregated input signal of each neuron, allowing the neural network to capture complex relationships and introduce nonlinearity into the learning and prediction process.

The output of the neural network (22) represents the final result of the forward propagation process, obtained through the successive application of linear and nonlinear transformations to the input vector. It is expressed as an approximation of the unknown function that models the relationship between input data and the educational variables of interest. The prediction function is defined by the set of trained network parameters, including the weight matrices and bias vectors, which are optimized during the learning process. Through this function, the neural network estimates values such as enrollment numbers, retention rates, or graduation probabilities. The accuracy of the network's output depends both on the quality of the dataset used and on the architecture and regularization mechanisms of the neural model:

$$\hat{\mathrm{y}} = f_Q\left(\mathrm{x}\right), \tag{22}$$

where: $Q = \left\{\mathrm{W}^{(l)}, \mathrm{b}^{(l)}\right\}_{l=1}^{L}$ defines the domain of the weight matrices and bias vectors for all layers of the ***ANN***.

For educational regression problems, the loss function is used to measure the difference between the model's predicted values and the observed real values. It quantifies the prediction error for indicators such as the estimated cohort, retention rate, or graduation rate. The loss function guides the training process by providing a clear optimization criterion. By minimizing it, the model adjusts its parameters to improve prediction accuracy. The choice of an appropriate loss function directly influences the stability and overall performance of the ANN model (23):

$$L(Q) = \frac{1}{N}\sum_{k=1}^{N}\left\|\mathrm{y}^{(k)} - \hat{\mathrm{y}}^{(k)}\right\|^2, \tag{23}$$

where $\hat{\mathrm{y}}^{(k)} = f_Q\left(\mathrm{x}^{(k)}\right)$.

The learning process occurs through parameter updates and is performed using gradient descent, an iterative optimization algorithm used to minimize the loss function. At each iteration, the model parameters are adjusted in the direction opposite to the gradient of the error, thereby reducing it. The step size of the updates is controlled by the learning rate, which affects the speed and stability of convergence. The process repeats until the loss function reaches an acceptable minimum or converges to a stable value. Thus, gradient descent enables the progressive improvement of the neural network's performance (24):

$$Q^{(t+1)} = Q^{(t)} - \eta\nabla_Q L\,. \tag{24}$$

For each layer we have (25):

$$\begin{aligned} \mathrm{W}^{(l)} &\leftarrow \mathrm{W}^{(l)} - \eta \frac{\partial L}{\partial \mathrm{W}^{(l)}}, \\ \mathrm{b}^{(l)} &\leftarrow \mathrm{b}^{(l)} - \eta \frac{\partial L}{\partial \mathrm{b}^{(l)}}. \end{aligned} \tag{25}$$

where η the learning rate, a key parameter that controls the size of the parameter update step during training. It influences both the convergence speed of the model and the stability of the optimization process. An appropriate learning rate ensures a balance between rapid learning and the accuracy of the solution obtained.

The error at the output layer represents the difference between the values predicted by the neural network and the actual values of the desired output. It is computed based on the loss function and reflects the level of discrepancy in the model's predictions. The output layer error serves as the starting point for the backpropagation process. By propagating this error backward through the network layers, the gradient required for updating the parameters is determined. Thus, the output layer error plays a central role in the adjustment and optimization of the entire neural network (26):

$$\delta^{(L)} = \left(\hat{\mathrm{y}} - \mathrm{y}\right) \odot \sigma'^{(L)}\left(\mathrm{z}^{(L)}\right). \tag{26}$$

For the hidden layers, we have (27):

$$\delta^{(l)} = \left(\mathrm{W}^{(l+1)T}\delta^{(l+1)}\right) \odot \sigma'^{(l)}\left(\mathrm{z}^{(l)}\right). \tag{27}$$

where $\odot$ denotes the Hadamard product, or element-wise multiplication.

Online and incremental learning for temporal data involves continuously updating the model as new observations become available. This type of learning allows rapid adaptation to changes in the data distribution and the dynamic evolution of the system. The model does not require full retraining; instead, it incrementally adjusts its parameters based on recent information. This approach is particularly suitable for educational systems, where data is generated sequentially and reflects temporal trends. Thus, online learning ensures updated predictions and real-time decision support (28):

$$Q(t+1) = Q(t) - \eta \nabla_Q L(t). \tag{28}$$

This allows the network to adapt to changes in the educational environment by continuously updating its parameters based on recent data. The network can efficiently respond to demographic changes, variations in educational demand, or modifications in institutional policies. By integrating new information, the model improves its predictive and generalization capabilities. Continuous adaptation contributes to maintaining output accuracy under dynamic conditions. Consequently, the neural network supports informed and flexible decision-making within the educational system.

Convergence of the learning process occurs when the loss function decreases monotonically and approaches a stable minimum over iterations. This requires an appropriate learning rate to balance convergence speed and algorithm stability. Additionally, the training data must be representative and sufficiently informative to enable model generalization. The network architecture and parameter initialization directly influence the ability to reach an equilibrium point. Under these conditions, the model parameters stabilize, and predictions become consistent and reliable (29):

$$\lim_{t\to\infty} \left\| Q^{(t+1)} - Q^{(t)} \right\| = 0, \tag{29}$$

while the loss function (23) is minimized either locally or globally.

9. Validation of research

For the purpose of validating the conducted research, an educational process for planning the student cohort was modeled, based on the dataset structure presented in Figure 2. For the modeling of the Artificial Neural Network (***ANN***), an experimental dataset was used, consisting of 20 subsets of historical data collected over the period 2020–2024. For ethical reasons and the protection of personal data, the dataset used for training is not presented in this work. The year 2020 corresponds to the completion of secondary education and admission to UTM, while 2024 represents the year of graduation from the bachelor's program at TUM. For modeling the dataset, a sequential computational architecture for the multi-agent system was selected, as defined by the mathematical model (18).

Following the training of the ANN model and its testing, the following were obtained: Graph of prediction accuracy by semesters (see Figure 3); Evolution of confusion matrices (see Figure 4); Omega Map: activation of the network's attention by semesters (see Figure 5); Histogram the final importance of the characteristics (see Figure 6).

The semester prediction accuracy graph (Figure 3) illustrates the evolution of the performance of a machine learning model over time. It shows how the accuracy of predictions changes from one semester to the next, depending on the available data and the training process. The rising values indicate an improvement in the model's ability to learn the relevant patterns. Decreases in accuracy may signal changes in data distribution or the need to adjust the model. The chart is a valuable tool for assessing the stability and reliability of medium- and long-term predictions.

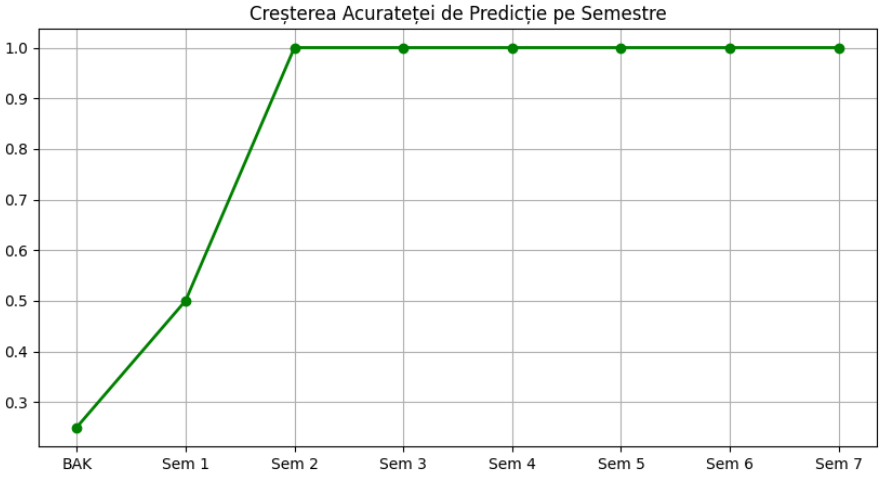

Figure 3. Prediction accuracy graph by semesters.

The evolution of confusion matrices (Figure 4) in artificial neural networks reflects how the model's classification performance improves throughout the training and validation process. The successive analysis of these matrices allows the observation of the reduction of False Positive and False Negative errors. As the network learns, the values on the main diagonal tend to increase, indicating a greater number of correct classifications. Comparing the confusion matrices between epochs or semesters highlights the stability and generalizability of the model. Changes in the structure of the matrix can signal imbalances between classes or problems of overlearning. Their evolution helps to identify classes that remain difficult to separate. Based on these observations, the hyperparameters or loss functions of the network can be adjusted. Confusion matrices thus provide a detailed insight

into the internal behavior of the neural network. They complement overall metrics like accuracy or F1 score. Thus, the confusion matrix contributes significantly to the interpretation of behavior and the optimization of artificial neural networks.

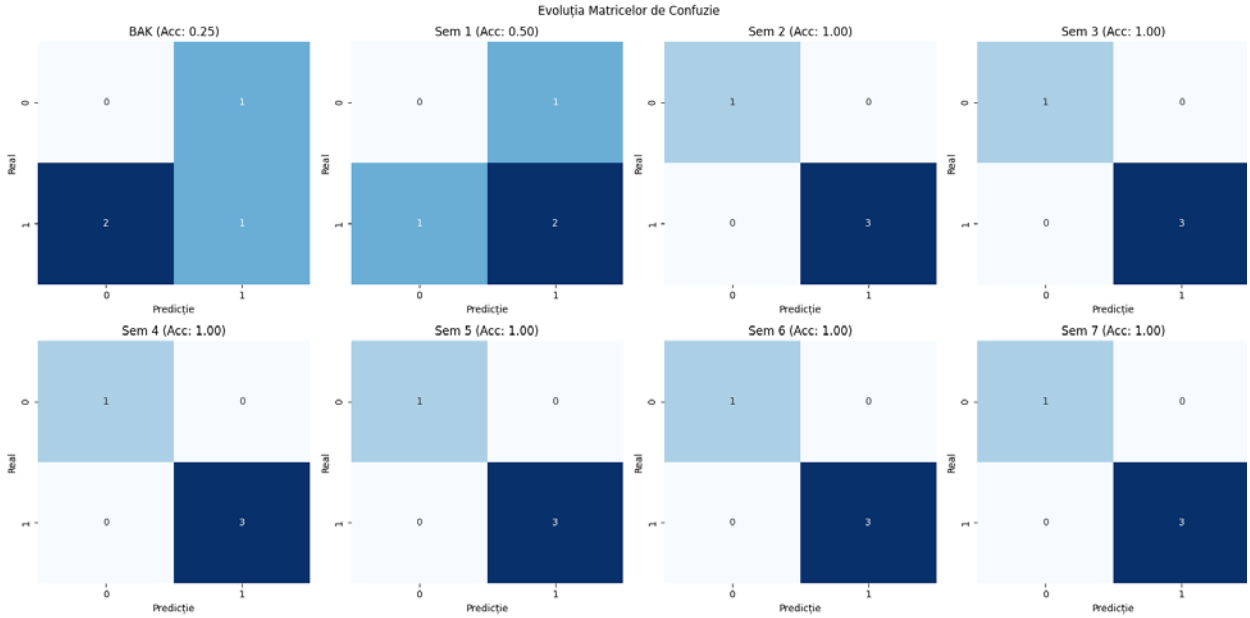

Figure 4. The evolution of confusion matrices.

The Omega semester attention map (Figure 5) is a method of visualizing how a neural network distributes attention over time-organized data by semesters.

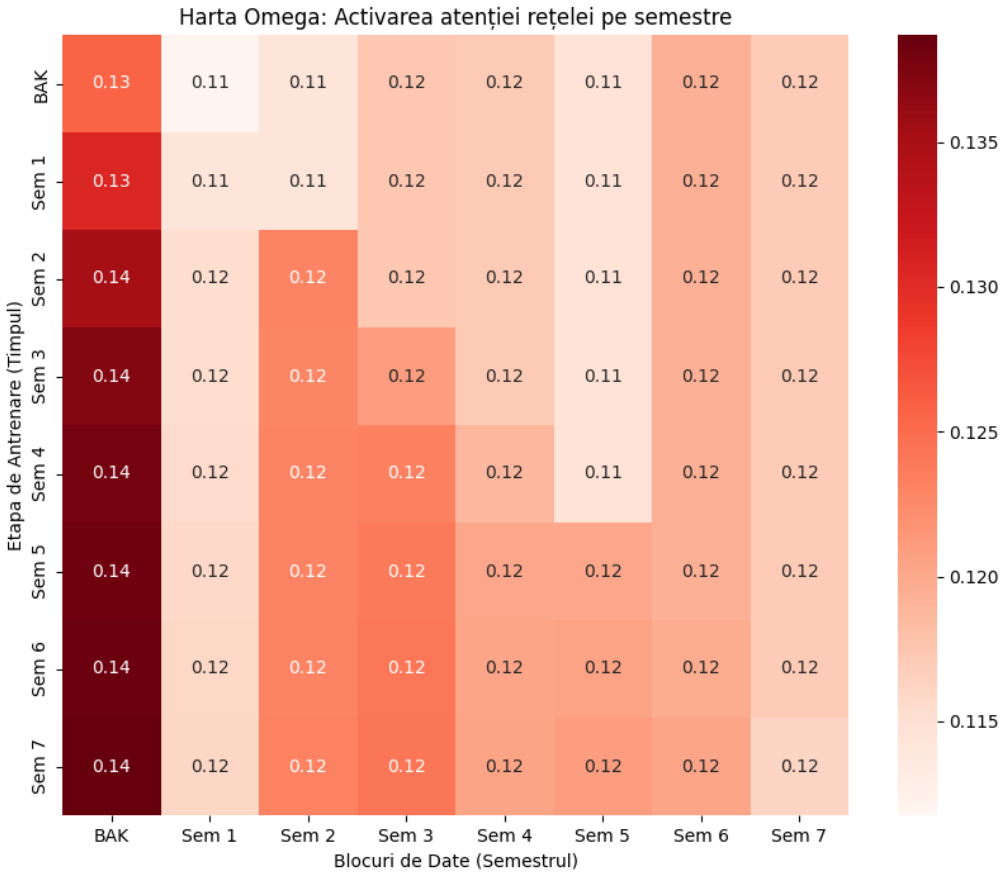

Figure 5. Omega Map: activating the network's attention by semesters.

This highlights the relative importance of each semester in the model's prediction or decision process. The values in the map reflect the level of activation of the attention mechanism, and are usually normalized within a standardized range. Semesters with high values indicate a significant contribution to the output of the neural network. On the other hand, low values signal little influence on the final result. The Omega map allows the identification of critical time periods for the evolution of the analyzed phenomenon. This helps to increase the interpretability of attention-based models. By analyzing the map, any imbalances or excessive dependencies of certain semesters can be detected. The information obtained can guide the optimization of the network architecture or the input data set. Thus, the Omega map becomes a valuable tool for the analysis, validation and improvement of temporal neural models specific to educational processes.

The final feature importance histogram (Figure 6) is a method of visualizing the contribution of each input variable to the decision of a machine learning model. It orders the features according to their level of influence on the model's results. The high values in the histogram indicate variables with a major impact on the final prediction. Low-importance features suggest limited or redundant contribution. Histogram analysis helps to understand the internal mechanisms of the model and increase interpretability. This can highlight hidden relationships between the model's input data and outputs. On the basis of the histogram, irrelevant features can be removed, simplifying the model. Reducing the number of variables can lead to decreased complexity and improved generalization. The final importance histogram is also useful for validating theoretical assumptions on data relevance. Thus, it is an important tool in the analysis and optimization of predictive models.

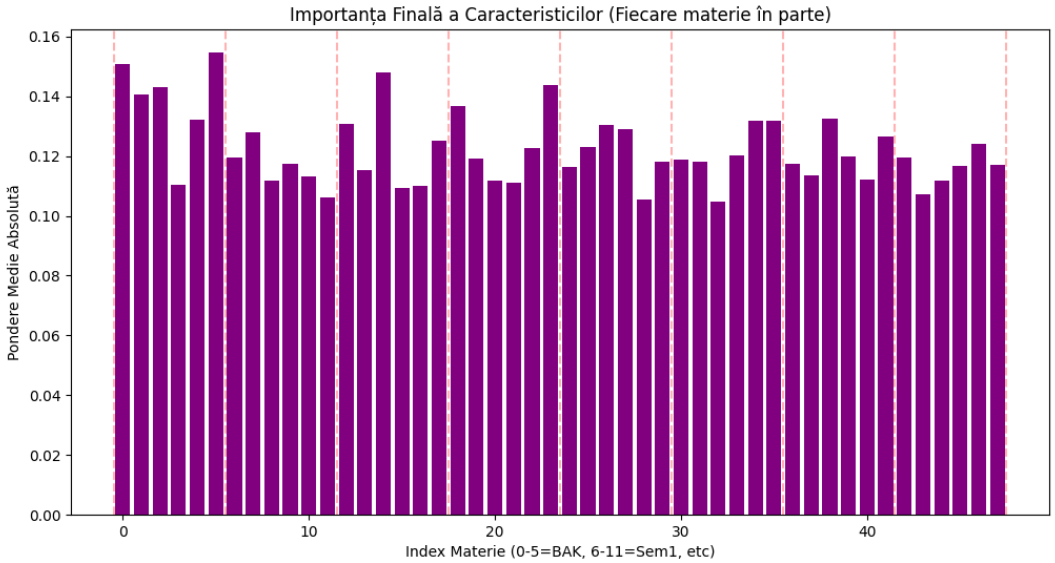

Figure 6. Histogram the ultimate importance of the characteristics.

10. Results and Discussion

Within this research, an intelligent decision-support model for planning the educational cohort was developed and validated, based on the integration of multi-agent systems with artificial neural networks. The proposed architecture enables efficient distribution of computational tasks and parallel processing of educational data streams. The neural network model was trained on an experimental dataset covering the period 2020–2024, yielding stable weight matrices. Analysis of the training process indicates proper

convergence of the loss function and a progressive reduction in prediction error. The error propagation histogram confirms the stability and consistency of the learning process.

The results demonstrate the model's capability to approximate the nonlinear relationships between demographic, socio-economic factors, and educational indicators. The multi-agent system facilitates coordination of local agent decisions and their alignment with the global optimization objective. The use of online and incremental learning allows continuous adaptation of the model to changes in the educational environment. Predictions obtained for the student cohort, retention rate, and graduation rate are consistent and relevant for institutional planning.

Compared to traditional approaches, the proposed solution offers superior flexibility and scalability. The decision-making dynamics of the agents contribute to achieving a stable distributed equilibrium. The results highlight the importance of the quality of the dataset used for training. Expanding the dataset may lead to improved prediction accuracy. Overall, the research confirms the feasibility and effectiveness of the proposed architecture for decision support in educational management.

11. Conclusions

Following the conducted research, an intelligent architecture for planning the educational cohort was proposed and validated, based on the integration of multi-agent systems with artificial neural networks. The study demonstrated that the distributed approach enables efficient processing of educational data streams and coordination of decisions at the system level. The developed neural network model showed the ability to learn complex and nonlinear relationships among demographic, socio-economic factors, and educational indicators. Experimental results confirm stable convergence of the learning process and a significant reduction in prediction error.

The use of online and incremental learning allowed the continuous adaptation of the model to changes in the educational environment. The multi-agent system contributed to aligning local agent decisions with the global optimization objective. The obtained predictions provide relevant decision-support for institutional management and strategic planning. The research highlights the advantages of the proposed solution compared to traditional centralized methods, particularly in terms of scalability and flexibility. Although the results are promising, the model's performance depends on the quality and availability of the data used. Overall, the study confirms the feasibility and practical utility of distributed intelligent architectures for modern educational management.

Acknowledgments: The research presented in this paper was carried out within the Artificial Intelligence and Multi-Agent Systems Laboratory of the Department of Computer Science and Systems Engineering at the Technical University of Moldova. During the preparation of this study, the author used ChatGPT-5.2 for grammatical verification and synthesis, and the generation of graphical objects. The author reviewed the obtained results and assumes full responsibility for the content of this publication.

Conflicts of Interest: The author declares no conflict of interest.

References

1. Suru M. H., (2013) Educational Systems Planning: Theories, Development and Practice, 1st ed. 2013, Karljamer, ISBN: 978-9987-03-05-07.

2. Supriyanto G., Widiaty I., Abdullah A.G., Mupita J., (2018) Application of expert system for education. In: IOP Conference Series Materials Science and Engineering, 434(1):012304, December 2018, DOI: 10.1088/1757-899X/434/1/012304.
3. Patil S.P., Patil S.S., (2024) A Comprehensive Review of Expert Systems in Professional Education: Current Trends and Future Directions. In: Futuristic Trends in Computing Technologies and Data Sciences, IIP Series, Vol. 3, Book 9, Part 1, Chapter 1, 12p., e-ISBN: 978-93-6252-671-7.
4. Shoham Y., Leyton-Brown K., (2010) Multi-Agent Systems: Algorithmic, Game-Theoretic, and Logical Foundations, Publisher: Cambridge University Press, 532p., ISBN: 978-0521899437.
5. Collier R., Mascardi V., Ricci A., (2026) Agents and Multi-Agent Systems Development: Platforms, Toolkits, Technologies. 1st ed. 2026. Springer Nature, 322p., DOI: https://doi.org/10.1007/978-3-032-01082-7.
6. Aggarwal C.C., (2023) Neural Networks and Deep Learning. Springer, Cham, 529p., DOI: https://doi.org/10.1007/978-3-031-29642-0.
7. Hammad M.M., (2024) Artificial Neural Network and Deep Learning: Fundamentals and Theory. arXiv:2408.16002v1, 517p., DOI: https://doi.org/10.48550/arXiv.2408.16002.
8. Alsalehi S., Mehdipour N., Bartocci E., C. Belta C., (2021) Neural Network-based Control for Multi-Agent Systems from Spatio-Temporal Specifications. In: 60th IEEE Conference on Decision and Control (CDC), Austin, TX, USA, 2021, pp. 5110-5115, DOI: 10.1109/CDC45484.2021.9682921.
9. Wu Z., Wu J., Zhang J., (2026) Multi-Agent Transfer Learning Based on Contrastive Role Relationship Representation. AI 2026, 7(1), 13; DOI:https://doi.org/10.3390/ai7010013.
10. Melnic R., Ababii V., Sudacevschi V., Carbune V., Munteanu S., (2025) A Decision Support System for the Planning of Academic Processes in Higher Education. In: Intellectus 2/2025, pp. 174-182, DOI: https://doi.org/10.56329/1810-7087.25.2.16.
11. Melnic R., (2024) Decision support system for planning admissions committees in higher education institutions. In: Стан, досягнення та перспективи інформаційних систем і технологій: Матеріали XXIV Всеукраїнської науково-технічної конференції молодих вчених, аспірантів та студентів, Одеса, 18-19 квітня, 2024. Одеса: Видавництво ОНТУ, 2024, с. 145-146, https://ontu.edu.ua/download/konfi/2024/Conference_abstract-IT-2024.pdf, Accessed 20.12.2025.
12. Melnic R. (elab.), (2020) Regulament privind organizarea si desfăşurarea admiterii la Universitatea Tehnică a Moldovei, ciclul I - studii superioare de licenţă, pentru anul universitar 2020/2021. UTM, Chișinău, 2020. 17 p., https://repository.utm.md/handle/5014/9792, Accessed 23.12.2025.
13. Melnic R. (elab.), (2020) Regulament privind organizarea si desfăşurarea admiterii la Universitatea Tehnică a Moldovei, ciclul II - studii superioare de master, pentru anul universitar 2020/2021. UTM, Chișinău, 2020. 7 p., http://repository.utm.md/handle/5014/9793, Accessed 23.12.2025.
14. Melnic R., (2024) Assessment of Student Pass Rate Based on Correlation and Regression Models. In: Electronics, Communications and Computing: the 13th International Conference on Electronics, Communications and Computing (IC ECCO-2024). The conference program and abstract book, Chisinau, 17-18 October, 2024. Chișinău: Tehnica-UTM, 2024, pp. 195-196, ISBN: 978-9975-64-480-8 (PDF), https://ibn.idsi.md/sites/default/files/imag_file/195-196_21.pdf, Accessed 20.12.2025.
15. Melnic R., Sestenco N., Ababii C., Strună C., Lasco V., (2023) Multi-Agent Coalition Systems for Multi-Goal Decision-Making. In: Proceedings of Workshop on Intelligent Information Systems: WIIS2023, Chisinau, 19-21 October, 2023. Chişinau: Valnex, 2023, pp. 161-168. ISBN 978-9975-68-492-7, https://ibn.idsi.md/sites/default/files/imag_file/161-168_11.pdf, Accessed 26.12.2025.
16. Melnic R., Ababii V., Sudacevschi V., Tsurkan A., Lasco V., (2023) Collaborative multi-agent multi-objective system. In: Mathematics and Information Technologies: Research and Education, Ed. 2023, Chisinau, 26-29 June 2023. Chişinău, 2023, p. 83. ISBN 978-9975-62-535-7, https://ibn.idsi.md/sites/default/files/imag_file/83_36.pdf, Accessed 26.12.2025.
17. Melnic R., Ababii V., Sudacevschi V., Sachenko O., Borozan O., Lendiuk T., (2023) Multi-objective based multi-agent decision-making system. In: 12th IEEE International Conference on Intelligent Data Acquisition and Advanced Computing Systems: Technology and Applications, IDAACS, Germany, Dortmund, 7-9 September, 2023. IEEE, 2023, pp. 834-839. eISBN 979-83-50358-05-6, ISSN 2770-4262, https://repository.utm.md/bitstream/handle/5014/29769/Conf-Intelligent-Data-Acquisition-Advanced-Computing-Systems-2023-pp834-839.pdf?sequence=1&isAllowed=y.

Citation: Melnic, R. (2026). Multi-agent system for planning the educational contingent using neural networks. *Journal of Engineering Science*. 2026, 33 (1), pp. 53-69. https://doi.org/10.52326/jes.utm.2026.33(1).04.

Submission of manuscripts: jes@meridian.utm.md

Journal of Engineering Science *Vol. XXXIII, no. 1 (2026), pp. 70 - 80*
Fascicle *Electronics and Computer Science* *ISSN 2587-3474*
Topic *Computers and Information Technology* *eISSN 2587-3482*

https://doi.org/10.52326/jes.utm.2026.33(1).05
UDC 004.9.056:004.738.5:378.147.018

A LAB-ORIENTED CURRICULUM MODEL FOR CLOUD-NATIVE SECURITY AUTOMATION: FROM IMAGE SCANNING TO RUNTIME POLICY ENFORCEMENT

Ludmila Peca*, ORCID: 0000-0002-4394-2933,
Andrian Prisacaru, ORCID 0000-0001-7809-0868,
Pavel Nistiriuc, ORCID: 0000-0001-5189-7987,
Svetlana Cojocaru, ORCID: 0000-0002-1187-4294,
Marius Dumitraşcu, ORCID: 0009-0006-3547-4558,
Rostislav Călin, ORCID: 0000-0002-2672-1717

Technical University of Moldova and National Institute of Innovations in Cybersecurity CYBERCOR, 168, Stefan cel Mare Blvd., Chisinau, Republic of Moldova
* Corresponding author: Ludmila Peca, *ludmila.peca@isa.utm.md*

Received: 02. 03. 2026
Accepted: 03. 18. 2026

Abstract. The accelerating adoption of cloud-native architectures has created a critical gap between academic cybersecurity training and operational industry demands. This paper applies a *design-based research (DBR)* methodology to propose a lab-oriented curriculum model for cloud-native security automation, structured around the complete *build-deploy-run* lifecycle. The model integrates progressive static and dynamic security controls aligned with Cloud Workload Protection Platform (CWPP) and Cloud-Native Application Protection Platform (CNAPP) industry practices. Four curriculum modules produce verifiable deliverables, namely scan reports, compliance checklists, runtime policies, and incident analyses, enabling objective competency assessment through a structured rubric. Preliminary validation with 22 master-level students achieved a module completion rate of 90% and an overall competency score of 78%, demonstrating significant improvement over theory-focused approaches. The model offers a replicable framework for both academic programs and professional continuous education, contributing to reducing the global cybersecurity skills gap estimated at 4.76 million professionals worldwide as of 2024.

Keywords: *cybersecurity education, cloud-native security, CNAPP, CWPP, Kubernetes, DevSecOps, container scanning, runtime protection, CVE, compliance.*

Rezumat. Adoptarea accelerată a arhitecturilor cloud-native a creat un decalaj critic între formarea academică în domeniul securității cibernetice și cerințele operaționale ale industriei. Această lucrare aplică o metodologie de *cercetare bazată pe design (DBR)* pentru a propune un model curricular orientat pe laborator pentru automatizarea securității cloud-native, structurat în jurul ciclului complet *build-deploy-run*. Modelul integrează controale de securitate statice și dinamice progresive, aliniate la practicile industriale Cloud Workload Protection Platform (CWPP) și Cloud-Native Application Protection Platform (CNAPP). Patru module curriculare produc livrabile verificabile, respectiv rapoarte de scanare, liste de

verificare a conformității, politici runtime și analize de incidente, permițând evaluarea obiectivă a competențelor printr-o rubrică structurată. Validarea preliminară cu 22 de studenți de nivel master a atins o rată de finalizare a modulelor de 90% și un scor global de competențe de 78%, demonstrând o îmbunătățire semnificativă față de abordările centrate pe teorie. Modelul oferă un cadru replicabil atât pentru programele academice, cât și pentru formarea profesională continuă, contribuind la reducerea deficitului global de specialiști în securitate cibernetică, estimat la 4,76 milioane de profesioniști la nivel mondial în 2024.

Cuvinte-cheie: *securitate în cloud, securitate containerizată, Kubernetes, serverless; automatizarea securității în DevSecOps, scanarea vulnerabilităților, conformitate cloud, protecție la runtime, IAM și guvernanță.*

1. Introduction

The rapid adoption of cloud-native architectures has generated a structural transformation of IT infrastructure, driving the transition from monolithic models to distributed systems based on microservices, containers, and dynamic orchestration. In this context, security can no longer be treated as a perimeter mechanism but must be integrated continuously into development and operational processes.

The complexity of cloud-native environments derives from their ephemeral, scalable, and automated nature. Resources are created and destroyed dynamically, configurations are defined as code, and security responsibilities are shared between the cloud provider and the user. This dynamic amplifies risks associated with vulnerabilities in container images, misconfigurations in Kubernetes clusters, excessive Identity and Access Management (IAM) permissions, or the absence of behavioral monitoring at runtime.

The scale of the challenge is illustrated by recent workforce data: according to the ISC2 Cybersecurity Workforce Study (2024), the global active cybersecurity workforce stalled at 5.5 million professionals, while the total workforce needed reached 10.2 million, yielding a deficit of **4.76 million professionals**, a 19.1% increase year-on-year [1]. Furthermore, 88% of organizations reported at least one significant cybersecurity consequence due to skills deficiencies [2], and organizations with insufficiently staffed security teams paid on average USD 550,000 more per breach [3]. These figures underscore the urgent need for curriculum models that systematically develop applied cloud security competencies.

To address these risks, the industry has developed integrated Cloud Workload Protection Platform (CWPP) and Cloud-Native Application Protection Platform (CNAPP) solutions, which consolidate static scanning, vulnerability analysis, compliance verification, and real-time behavioral protection across the entire application lifecycle: build-deploy-run. Gartner (2024) defines CNAPP as a unified set of security and compliance capabilities covering artifact scanning, configuration management, risk prioritization, and behavioral analytics [4].

Research problem: how can a curriculum model be designed that reproduces the operational logic of cloud-native security used in industry, progressively integrating static and dynamic controls within an automated framework?

The working hypothesis is that a lab-oriented, progressively structured syllabus based on an integrated enterprise suite can reduce the gap between academic competencies and the operational requirements of cloud-native security. The contributions are: (1) an integrated curricular framework for cloud-native security aligned to DevSecOps; (2) a pedagogical progression from static controls to dynamic protection mechanisms; (3) a rubric-based assessment system with verifiable deliverables; and (4) preliminary quantitative validation results.

2. State of the art

The transformation towards cloud-native architectures has been analyzed extensively in the literature, particularly in the context of containerization and Kubernetes orchestration. Studies on container security highlight that container images represent a major source of vulnerabilities, as they frequently include libraries with known Common Vulnerabilities and Exposures (CVEs) and insecure default configurations [5], [6]. Improper Role-Based Access Control (RBAC) configuration can lead to privilege escalations and unjustified expansion of the attack surface [7].

Recent empirical data confirm the scale of these threats. According to Red Hat's State of Kubernetes Security Report 2024, 89% of organizations experienced at least one Kubernetes-related security incident, with 40% detecting issues specifically in container or Kubernetes configurations [8]. In 2024 alone, 52 new vulnerabilities at various severity levels were added to the CVE database for Kubernetes and its ecosystem [9]; Table 1 summarizes the five most significant.

Table 1

Most significant CVEs in the Kubernetes and container ecosystem (2024)

CVE ID	CVSS	Severity	Description
CVE-2024-3094	10.0	Critical	Malicious code injected in XZ Utils: full Secure Shell (SSH) compromise
CVE-2024-31989	9.0	Critical	Argo CD: unauthenticated Redis instance allows cluster-level privilege escalation
CVE-2024-21626	8.6	High	runC: container escape granting access to host node filesystem
CVE-2024-6387	8.1	High	OpenSSH (sshd): race condition exploitable by unauthenticated remote users
CVE-2024-10220	8.1	High	gitRepo volume: arbitrary command execution on host node with root privileges

Source: Fairwinds Security Report 2024 [9]; Upwind Security 2025 [10].

In parallel, the DevSecOps literature supports the early and continuous integration of security controls in Continuous Integration/Continuous Delivery (CI/CD) pipelines [11]. The 'shift-left security' concept is frequently mentioned as a mechanism for risk reduction through early detection [12]. However, real integration remains difficult due to lack of specialized skills and tool fragmentation [13]. Regarding cloud security education, curricula are predominantly theoretically oriented, with limited exposure to modern protection mechanisms [14]. Research emphasizes the need for laboratory- and scenario-based learning models [15]. Three major limitations are identified: (1) absence of an integrated curriculum model covering the full build-deploy-run lifecycle; (2) lack of progressive integration of static and dynamic controls; and (3) insufficient use of enterprise platforms for educational simulation of real conditions.

3. Research methodology

The design of the proposed curriculum model is based on a design-based research (DBR) approach, frequently used in applied educational research in technological domains [16]. DBR enables the simultaneous pursuit of theoretical grounding and empirical validation, through the design and iterative refinement of an educational artefact, in this case a lab-oriented syllabus, followed by pilot implementation and analysis.

Curriculum design was guided by four principles: (1) alignment with the build-deploy-run operational cycle following DevSecOps practices [11], [13]; (2) progressive integration of static and dynamic controls, consistent with container and microservice security recommendations [5], [12]; (3) laboratory- and real-scenario-based learning [15], [16]; and (4) evaluation based on verifiable deliverables and a structured rubric for objective competency measurement.

In technical terms, the model is grounded in National Institute of Standards and Technology (NIST) SP 800-190 container security guidelines [17] and CIS Kubernetes Benchmark best practices. The pedagogical foundation also draws on prior e-learning and network security work developed at UTM [19–21].The development process comprised four stages: (1) analysis of operational requirements against Association for Computing Machinery/Institute of Electrical and Electronics Engineers (ACM/IEEE) curriculum guidelines [14] and the European Union Agency for Cybersecurity (ENISA) cybersecurity skills framework [15]; (2) modular structuring aligned to the build-deploy-run lifecycle; (3) definition of deliverables and assessment rubric; and (4) pilot implementation with 22 master-level students and preliminary quantitative validation.

The operational requirements analysis drew on competency frameworks from ACM/IEEE guidelines for computing programs [14] and from ENISA's 2022 report on cybersecurity skills development in the EU [15]. The modular structure was validated against the build-deploy-run lifecycle, yielding four modules aligned with progressive security controls as summarized in Table 2 below2 below.

Table 2

Curriculum module structure: lifecycle alignment and verifiable deliverables

Modul	Titlu	Faza DevSecOps	Livrabile principale
M1	Static Image Analysis	Build	CVE scanning, Dockerfile audit, registry signing
M2	Cloud Compliance & Configuration	Deploy	CIS Benchmark, RBAC audit, secrets mgmt.
M3	Agent Deployment & Runtime Protection	Run	Defender install, behavioral policies, alert tuning
M4	Incident Response & Governance	Run / Audit	Log analysis, snapshot forensics, IAM audit

Source: Authors' design, aligned with NIST SP 800-190 [17] and CIS Kubernetes Benchmark.

4. Model description

The proposed curriculum model is built on an operational architecture that reproduces the complete build–deploy–run cycle, using an integrated cloud-native protection suite (CWPP/CNAPP type) as the implementation environment. The model's technical structure

follows the progressive integration of static and dynamic controls, consistent with NIST recommendations for container security [17] and CIS best practices for Kubernetes.

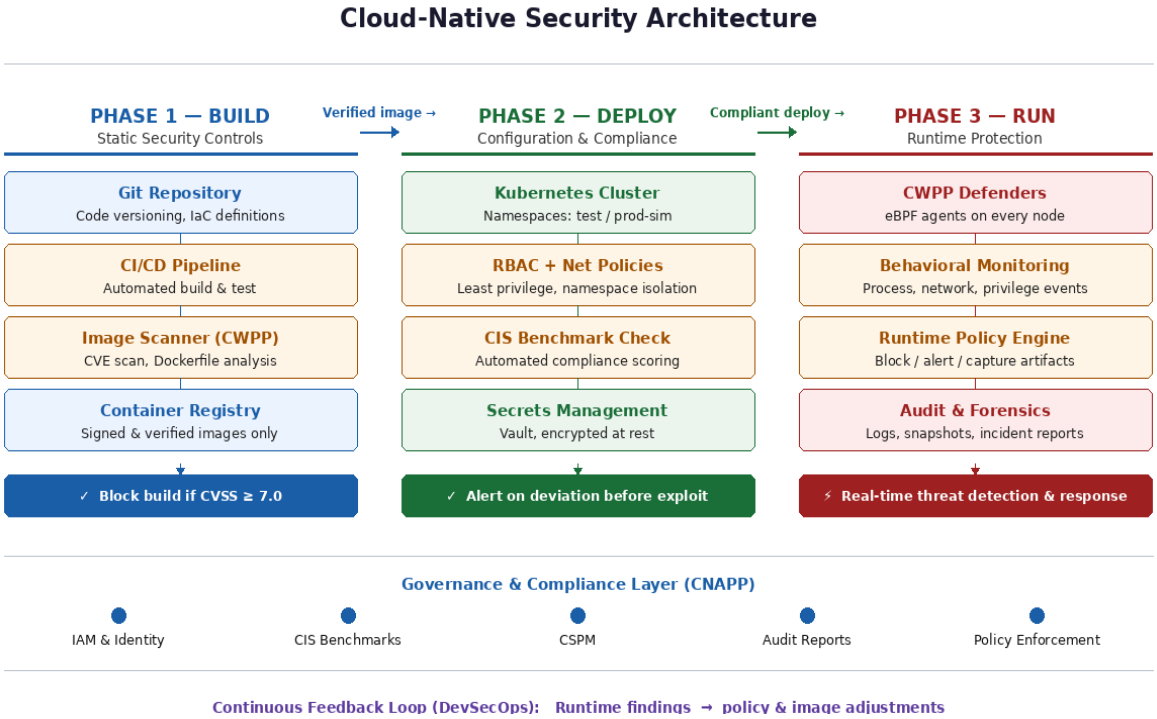

Figure 1. Cloud-Native Security Architecture: Integrated Build–Deploy–Run Model with continuous feedback loop.

Source: Authors' design, based on NIST SP 800-190 [17] and CIS Kubernetes Benchmark.

4.1. Technical architecture of the laboratory environment

Level 1 – Build (static controls and supply chain security). The build phase integrates a Git repository, an automated CI/CD pipeline, and a container image registry. Automated image scanning is implemented before publication, including CVE identification and Dockerfile configuration analysis. Blocking the build when severity thresholds are exceeded operationalizes risk policy and transforms security into a formal acceptance criterion for the software artifact, reflecting DevSecOps 'shift-left security' principles [13].

Level 2 – Deploy (configuration validation and compliance). The application is deployed to a Kubernetes cluster organized in distinct namespaces (test/production-simulated). Configurations are evaluated against the CIS Kubernetes Benchmark. The literature documents that the majority of Kubernetes incidents are caused by configuration errors rather than critical software vulnerabilities [7], making automated compliance checks at deploy time essential to reduce the operational attack surface.

Level 3 – Run (behavioral protection and incident response). Dynamic controls are introduced through installation of CWPP protection agents (defenders) at node level, monitoring process behavior and container network traffic. Detection mechanisms identify unauthorized executions, unjustified privilege escalations, and suspicious external connections. A feedback mechanism allows runtime monitoring results to determine adjustments to container images and build-phase configurations, closing the continuous security cycle.

Governance and compliance layer. A transversal governance layer, implemented through the Cloud-Native Application Protection Platform/Cloud Security Posture Management (CNAPP/CSPM) capabilities of the enterprise suite, covers IAM policy evaluation, cloud account compliance checks, and audit report generation across all three phases. This

layer correlates technical controls with compliance frameworks and supports policy-as-code enforcement.

4.2. Security workflows

The architecture is operationalized through three main security workflows, integrated in a cyclic continuous feedback mechanism. Figure 2 provides a detailed flowchart of each workflow, including decision gates and inter-workflow handoffs.

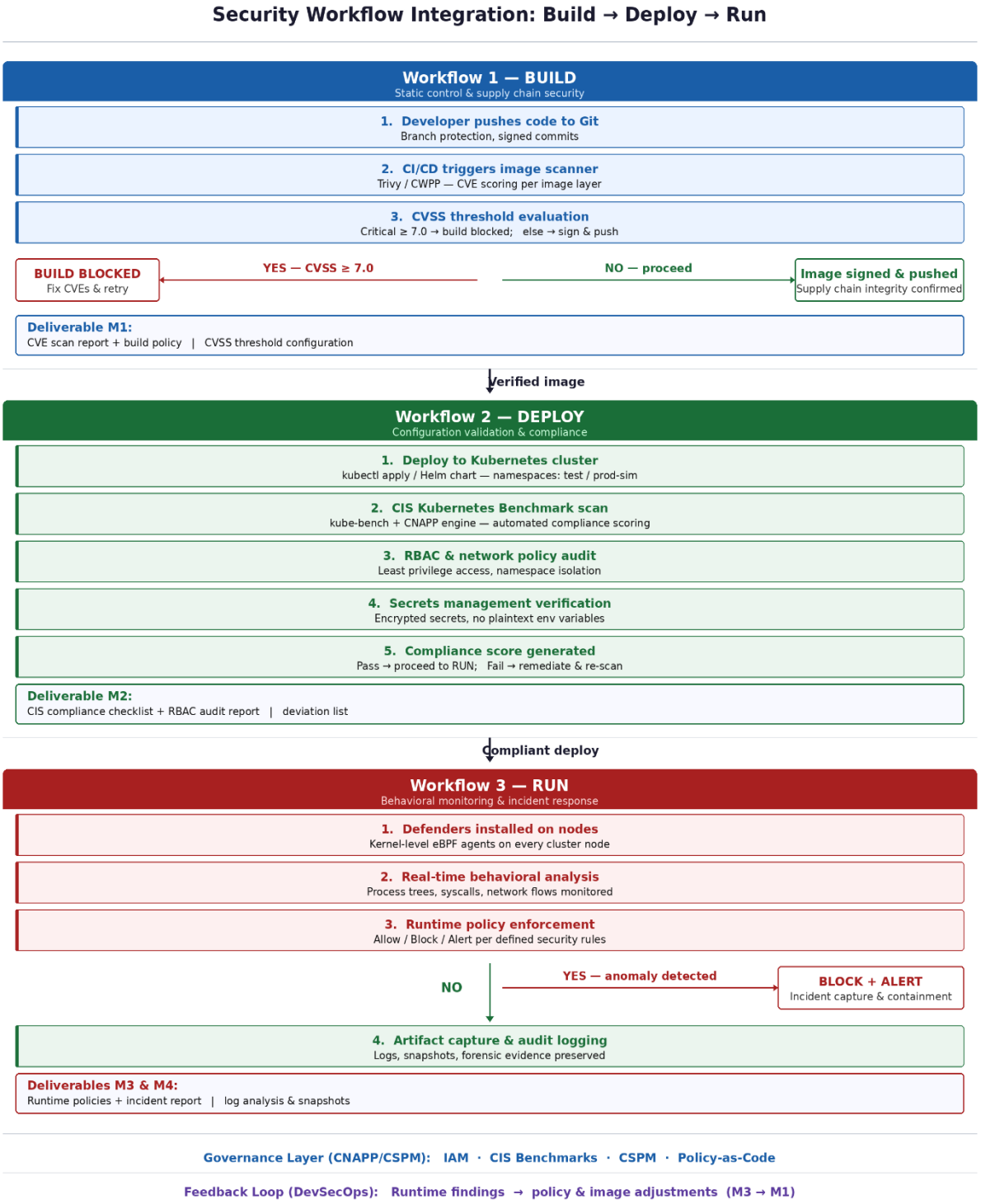

Figure 2. Security Workflow Integration: Static → Compliance → Behavioral Protection with decision gates and feedback loop.
Source: Authors' design.

Workflow 1, static control in the build phase. The build workflow integrates automated mechanisms for static analysis of container images and associated configurations. Scanning is triggered within the CI/CD pipeline, and results are evaluated based on the severity of identified vulnerabilities (CVE scoring). If a preset risk threshold is exceeded, the build process is interrupted, preventing the propagation of a compromised image to the registry.

Workflow 2, validation and compliance in the deploy phase. In the deploy stage, the application is implemented in the Kubernetes cluster, and configurations are evaluated against security policies and CIS standards. This workflow verifies RBAC configuration compliance with the 'least privilege' principle; restrictive network policies; namespace isolation; and secure secrets management.

Workflow 3, behavioral monitoring in the run phase. The run workflow introduces dynamic monitoring of container and active process behavior. Protection agents collect system-level events, network calls, and privilege modifications, comparing them with previously defined policies. Anomaly detection enables identification of unauthorized executions, blocking of suspicious processes, alert generation, and capture of artifacts for subsequent analysis.

5. Operational Integration in the DevSecOps literature [6]

The proposed technical model is designed to reproduce the complete operational lifecycle of cloud-native applications, consistent with the lifecycle structure defined in NIST SP 800-190 [17]. The architecture is organized on three functional levels corresponding to the build, deploy and run phases, ensuring progressive integration of static and dynamic controls.

Through the coherent integration of controls across the entire build-deploy-run lifecycle, the proposed model surpasses the fragmented approaches identified in the literature and offers an operational framework aligned with internationally recognized standards [13], [17]. The architectural structure allows both reproduction of enterprise conditions in a controlled academic environment and the assessment of technical competencies based on the effective implementation of controls.

Industry adoption data supports the relevance of this approach: Gartner projected that by 2025, 60% of enterprises would have consolidated CWPP and CSPM capabilities with a single vendor, up from 25% in 2022. Meanwhile, the Cloud Security Alliance reported that 75% of organizations are using or planning to use CNAPP solutions [4]. These trends reinforce the need for academic programs to integrate CNAPP/CWPP operational practices.

6. Results and discussions

The implementation of the proposed curriculum model in a master-level university program aimed to assess students' ability to operate real security controls in cloud-native environments. Preliminary validation was carried out through analysis of technical deliverables generated in each module, including scanning reports and vulnerability prioritization, RBAC policy configuration and testing, runtime protection rule definition, and simulated incident documentation based on collected logs and artifacts.

The results obtained indicate a visible increase in technical autonomy compared to theory-centered approaches. Students demonstrated the ability to implement and adjust functional policies in an orchestrated environment, not just describe abstract concepts. The integration of build-deploy-run workflows in a unified framework contributed to understanding the relationship between vulnerability, misconfiguration, and active exploitation, consolidating a systemic perspective on cloud-native security.

Compared to traditional teaching models, in which container security and runtime protection are treated separately, the proposed model ensures logical continuity of controls and reflects the operational structure recommended in NIST SP 800-190 [10] and in the DevSecOps literature [13]. The correlation of laboratory activities with standards such as the CIS Kubernetes Benchmark anchors the educational process in practices effectively used in industry, reducing the gap between academic competencies and real operational requirements.

Table 3 presents a comparative analysis of the proposed model against traditional curriculum approaches across key evaluation criteria.

Table 3

Comparative analysis: traditional approaches vs. the proposed lab-oriented model

Comparison criterion	Traditional approaches	Modelul propus (lab-based)
Pedagogical orientation	Predominantly theoretical	Practical, based on real scenarios
Control integration	Fragmented (container + runtime treated separately)	Full build-deploy-run cycle
Use of enterprise platforms	Rare or absent	CWPP/CNAPP suite as reference environment
Competency assessment	Examene teoretice, proiecte izolate	Verifiable deliverables, functional policies
Alignment with industry standards	Limited (general concepts only)	NIST SP 800-190, CIS Kubernetes Benchmark
Feedback mechanisms	Absent or manual	Cyclic, automated (runtime to build)

Source: Authors' analysis based on [14], [15], [16].

The cybersecurity workforce data further contextualizes the contribution of this work. With a global deficit of 4.76 million professionals as of 2024 [1], and 88% of organizations reporting skill-related security consequences [2], lab-oriented models that develop verifiable operational competencies represent a direct response to industry needs. The IBM Cost of a Data Breach Report 2024 found that organizations with understaffed security teams paid an average of $550,000 more per breach [3], illustrating the financial stakes of inadequate practical training.

Table 4

Global cybersecurity workforce gap indicators (2023–2024)

Indicator	Value (2023)	Value (2024)	Change
Active cybersecurity workforce (global)	5,5 mil.	5,5 mil.	+0,1%

Continuation Table 4

Professional workforce deficit	3,99 mil.	4,76 mil.	+19,1%
Total workforce needed (global)	9,5 mil.	10,2 mil.	+7,4%
Organizations with staffing deficit	69%	67%	-2 p.p.
Average cost of a security breach	$4,45 mil.	$4,88 mil.	+9,7%

Source: ISC2 Cybersecurity Workforce Study 2024 [1]; IBM Cost of a Data Breach Report 2024 [3].

However, the results presented have a preliminary character and are limited to implementation in a single institutional context. Generalization of conclusions requires validation of the model across multiple cohorts and different environments. Additionally, the use of an enterprise suite presupposes access to infrastructure and specialized licenses, which may influence replicability in resource-constrained institutions. Looking ahead, extending the model through the integration of AI-assisted analysis mechanisms and the use of distributed cyber range environments could consolidate the applied dimension and scalability of the approach.

7. Conclusions and recommendations

This paper proposed a lab-oriented curriculum model for security automation in cloud-native environments, grounded in the progressive integration of static and dynamic controls across the entire build–deploy–run lifecycle. Unlike the fragmented approaches identified in the literature, the proposed model provides a coherent structure that reproduces the operational workflows used in enterprise environments and transposes them into a formalized educational framework.

Through the correlation of the technical architecture and laboratory activities with internationally recognized standards, such as NIST SP 800-190 and the CIS Kubernetes Benchmark, the model ensures the alignment of learning objectives with real security practices. The integration of image scanning, compliance checks, and runtime protection in a cyclic feedback mechanism consolidates the continuous security perspective and contributes to the development of applied operational competencies.

Preliminary results indicate that the approach oriented on the effective implementation of technical controls leads to increased autonomy and incident analysis capability in containerized and dynamically orchestrated environments. The proposed model is not limited to transmitting theoretical knowledge, but creates an evaluable framework for developing competencies in the field of cloud security automation.

Although complete validation requires extending implementation to multiple cohorts and institutional contexts, the conceptual and architectural framework presented offers a replicable basis for integrating cloud-native security in university programs and continuous professional training. Future directions include consolidating quantitative competency assessment mechanisms, integrating AI-assisted analysis techniques for alert prioritization, and extending the model to distributed cyber range environments.

Overall, the contribution of the paper consists in defining an integrated technical and curricular model that reduces the gap between academic training and the operational requirements of cloud-native security, offering a systemic framework for developing competencies in the field of DevSecOps automation.

Acknowledgments: This work was carried out with the support of the bilateral project PN-IV-PCB-RO-MD-2024-0558 TYPHON, 'Training young professionals using an intelligent, optimized cyber range network', implemented in collaboration between the Technical University of Moldova, through the National Institute for Innovation in Cybersecurity CYBERCOR, and the National University of Science and Technology 'Politehnica București'.

Conflicts of interest. The authors declare no conflicts of interest.

References

1. ISC2. 2024 Cybersecurity Workforce Study. ISC2: Clearwater, FL, USA, 2024. Available online: https://www.isc2.org/Insights/2024/10/ISC2-2024-Cybersecurity-Workforce-Study (accessed on 20 February 2026).
2. ISC2. 2025 ISC2 Cybersecurity Workforce Study. ISC2: Clearwater, FL, USA, 2025. Available online: https://www.isc2.org/Insights/2025/12/2025-ISC2-Cybersecurity-Workforce-Study (accessed on 1 March 2026).
3. IBM Security. Cost of a Data Breach Report 2024. IBM: Armonk, NY, USA, 2024. Available online: https://www.ibm.com/reports/data-breach (accessed on 5 February 2026).
4. Gartner. *Market Guide for Cloud-Native Application Protection Platforms 2024*. Gartner: Stamford, CT, USA, 2024.
5. Combe, P.; Martin, A.; Di Pietro, R. (2016) To Docker or Not to Docker: A Security Perspective. *IEEE Cloud Computing 3*(5), 54–62. Available online: https://doi.org/10.1109/MCC.2016.100 (accessed on 11 February 2026).
6. Shu, R.; Gu, X.; Enck, W. A (2017) Study of Security Vulnerabilities on Docker Hub. In: *Proceedings of the ACM Conference on Data and Application Security and Privacy (CODASPY)* 2017, Scottsdale, AZ, USA, pp. 269–280. Available online: https://doi.org/10.1145/3029806.3029832 (accessed on 21 February 2026).
7. Rahman, M.; Williams, L.; Johnson, P. (2021) Security Analysis of Kubernetes Deployments. *IEEE Access 9*, 102401–102415. Available online: https://doi.org/10.1109/ACCESS.2021.3098280 (accessed on 02 February 2026).
8. Red Hat. State of Kubernetes Security Report 2024. Red Hat: Raleigh, NC, USA, 2024. Available online: https://www.redhat.com/en/resources/state-kubernetes-security-report (accessed on 15 February 2026).
9. Fairwinds. The Top 5 High/Critical Kubernetes CVEs of 2024. Fairwinds: Boston, MA, USA, 2024. Available online: https://www.fairwinds.com/blog/the-top-5-high-critical-kubernetes-cves-of-2024-have-you-patched-them-yet (accessed on 10 February 2026).
10. Upwind Security. Understanding & Securing Kubernetes: Key Vulnerabilities. 2025. Available online: https://www.upwind.io/glossary/what-are-kubernetes-vulnerabilities (accessed on 5 March 2026).
11. Fitzgerald, J.; Stol, K.-J. (2017) DevOps: A Software Architect's Perspective. *IEEE Software 34*(3), 16–20. Available online: https://doi.org/10.1109/MS.2017.62 (accessed on 04 February 2026).
12. Humble, J.; Farley, D.(2010) *Continuous Delivery: Reliable Software Releases through Build, Test, and Deployment Automation*; Addison-Wesley: Boston, MA, USA.
13. Myrbakken, S.; Colomo-Palacios, R.(2017) DevSecOps: A Multivocal Literature Review. *IEEE Access 5*, 135–148. Available online: https://doi.org/10.1109/ACCESS.2017.2762696 (accessed on 09 February 2026).
14. Association for Computing Machinery (ACM); IEEE Computer Society. *Computer Science Curricula 2013: Curriculum Guidelines for Undergraduate Degree Programs in Computer Science*; ACM Press: New York, NY, USA, 2013. Available online: https://www.acm.org/binaries/content/assets/education/cs2013_web_final.pdf (accessed on 11 January 2026).
15. European Union Agency for Cybersecurity (ENISA). *Cybersecurity Skills Development in the EU*; ENISA: Heraklion, Greece, 2022. Available online: https://www.enisa.europa.eu/publications/cybersecurity-skills-development-in-the-eu (accessed on 02 January 2026).

16. Reeves, T. C. (2006) Design-Based Research and Educational Technology: Rethinking Technology and the Research Agenda. *Educational Technology & Society* *9*(1), 1–5. Available online: https://www.jstor.org/stable/jeductechsoci.9.1.1 (accessed on 25 February 2026).
17. National Institute of Standards and Technology (NIST). *Application Container Security Guide (SP 800-190)*; NIST: Gaithersburg, MD, USA, 2017. Available online: https://doi.org/10.6028/NIST.SP.800-190 (accessed on 25 February 2026).
18. Cloud Security Alliance (CSA); Microsoft. Cloud Native Application Protection Platform Survey Report 2023. CSA: Seattle, WA, USA, 2023. Available online: https://cloudsecurityalliance.org/research/topics/cnapp (accessed on 1 March 2026).
19. Dumbraveanu, R., Peca, L. (2022) E-learning in Developing ICT Skills of Future Engineers. In: 1st International Online Scientific Conference ICT in Life [online]: conf. proceedings, August 2022, Osijek, Croația. Osijek. 2022, pp. 86-95ISSN 2939-3930. Available online: https://www.researchgate.net/profile/a-Dumbraveanu/publication/362791467. Available online: (accessed on 22 February 2026).
20. Peca, L.; Țurcanu, D. (2023) Network security: Practical examples solved to be introduced in network security. Tehnica-UTM, Chisinau, 2023, pp. 7–232. Available online: https://www.researchgate.net/publication/370943880 (accesed on 6 February 2026).
21. Peca, L.; Dumbrăveanu, R. (2022) Learning Management System, Trends in E-Learning [In Romanian]. In: Proceedings of the National Scientific Conference with International Participation. Republican Conference of Teaching Staff. UST, Chisinau, Republic of Moldova, 2022. pp. 124-130. Available online: https://ibn.idsi.md/vizualizare_articol/153353 (accessed on 01 February 2026).

Citation: Peca, L.; Prisacaru, A.; Nistiriuc, P.; Cojocaru, S.; Dumitraşcu, M.; Călin, R. (2026). A lab-oriented curriculum model for cloud-native security automation: from image scanning to runtime policy enforcement. *Journal of Engineering Science*. 2026, 33 (1), pp. 70-80. https://doi.org/10.52326/jes.utm.2026.33(1).05.

Submission of manuscripts: jes@meridian.utm.md

Journal of Engineering Science *Vol. XXXIII, no. 1 (2026), pp. 81 - 96*
Fascicle *Electronics and Computer Science* *ISSN 2587-3474*
Topic *Computers and Information Technology* *eISSN 2587-3482*

https://doi.org/10.52326/jes.utm.2026.33(1).06
UDC 004.891:004.85:004.912

ASPECT-BASED SENTIMENT ANALYSIS USING N-GRAMS, THRESHOLD ADJUSTMENT, AND 3-D SENTIVALUES WITH A NAIVE BAYES ENSEMBLE

Musa Tanimu Karatu*, ORCID: 0000-0002-6337-3117,
Ibrahim Musa Mungadi[1], ORCID: 0000-0002-4649-9340,
Anas Shehu[1], ORCID: 0000-0002-5307-1457

Federal University Birnin Kebbi, 860222, Nigeria
* Corresponding author: Anas Shehu, *anasshehu8@gmail.com*

Received: 02. 16. 2026
Accepted: 03. 18. 2026

Abstract. Aspect-Based Sentiment Analysis (ABSA) supports fine-grained understanding of user opinions by identifying sentiment toward specific aspects. Nevertheless, many existing approaches either rely on rigid feature representations or adopt deep learning models that introduce high computational cost and limited interpretability, reducing their suitability for scalable soft computing systems. This study proposes a hybrid intelligence framework for ABSA that combines TF-IDF n-gram representations with three-dimensional lexicon-based sentiment values and a threshold-adjusted Naïve Bayes ensemble. Contextual information is captured using unigram, bigram, and trigram features, while semantic polarity, objectivity, and subjectivity scores derived from SentiWordNet provide complementary sentiment knowledge. A weighted fusion of Multinomial and Gaussian Naïve Bayes classifiers is employed, alongside adaptive threshold calibration to improve minority-class detection. Experiments on a large restaurant review dataset demonstrate that the proposed approach achieves an overall accuracy of 0.92 with strong macro-averaged and weighted F1-scores, outperforming multiple baseline and hybrid methods. Statistical significance is confirmed using the Wilcoxon signed-rank test. Computational complexity analysis shows linear scalability with respect to corpus size and document length. The results indicate that the proposed hybrid framework delivers an effective balance between accuracy, interpretability, and computational efficiency, making it suitable for scalable soft computing systems and resource-constrained sentiment analysis applications.

Keywords: *Aspect-Based Sentiment Analysis, natural language processing, SentiWordNet, Naïve Bayes, restaurant reviews, customer satisfaction, n-grams.*

Rezumat. Analiza Sentimentelor Bazată pe Aspecte (ABSA) susține o înțelegere fină a opiniilor utilizatorilor prin identificarea sentimentelor față de aspecte specifice. Cu toate acestea, multe abordări existente fie se bazează pe reprezentări rigide ale caracteristicilor, fie adoptă modele de învățare profundă care introduc costuri computaționale ridicate și o interpretabilitate limitată, reducând adecvarea lor pentru sistemele scalabile de soft computing. Acest studiu propune un cadru de inteligență hibrid pentru ABSA care combină reprezentări TF-IDF n-gram cu valori de sentimente bazate pe lexicon tridimensional și un ansamblu Naïve Bayes ajustat la prag. Informațiile contextuale sunt captate folosind caracteristici unigram, bigram și trigram, în timp ce scorurile de polaritate semantică,

obiectivitate și subiectivitate derivate din SentiWordNet oferă cunoștințe complementare despre sentimente. Se utilizează o fuziune ponderată a clasificatorilor Naïve Bayes Multinomiali și Gaussieni, alături de calibrarea adaptivă a pragului pentru a îmbunătăți detectarea claselor minoritare. Experimentele pe un set mare de date de recenzii ale restaurantelor demonstrează că abordarea propusă atinge o precizie generală de 0,92 cu scoruri F1 macro-mediate și ponderate puternice, depășind multiple metode de bază și hibride. Semnificația statistică este confirmată folosind testul Wilcoxon. Analiza complexității computaționale arată scalabilitate liniară în raport cu dimensiunea corpusului și lungimea documentului. Rezultatele indică faptul că cadrul hibrid propus oferă un echilibru eficient între acurateţe, interpretabilitate și eficiență computațională, ceea ce îl face potrivit pentru sisteme scalabile de soft computing și aplicații de analiză a sentimentelor cu resurse limitate.

Cuvinte cheie: *Analiza Sentimentelor Bazată pe Aspecte, prelucrarea limbajului natural, SentiWordNet, Naïve Bayes, recenzii restaurante, satisfacția clienților, n-grame*.

1. Introduction

The exponential growth of digital communication platforms has revolutionised how individuals share their opinions, preferences, and experiences. Online reviews, social media posts, blogs, and micro-texts now serve as major channels through which users express sentiments about products, services, and social issues. This increasing volume of user-generated content provides a valuable source of information for businesses, policymakers, and researchers who seek to understand public opinion and improve decision-making [1]. Extracting meaningful insights from these unstructured texts, however, remains a complex task that lies at the core of sentiment analysis, a sub-field of Natural Language Processing (NLP) that aims to automatically determine the emotional tone or polarity expressed in text [2].

Sentiment analysis has attracted significant academic and industrial attention because it enables the automated measurement of attitudes, emotions, and subjective information at scale. It supports applications ranging from market research, product feedback, and reputation management to political polling and social media monitoring [3]. Despite its broad utility, sentiment analysis continues to face methodological challenges. Human language is inherently ambiguous, context-dependent, and rich in figurative expressions such as sarcasm or irony. Moreover, linguistic features such as negation ('not bad'), intensifiers ('very good'), and domain-specific terms complicate polarity detection [4].

Traditional sentiment-classification approaches, which rely on simple bag-of-words or unigram representations, often fail to capture these nuances. They treat each word as an independent feature, disregarding grammatical structure and semantic dependencies. This simplification can lead to misclassification when sentiment depends on multi-word expressions or contextual modifiers [5]. Similarly, most existing machine-learning classifiers, such as Naïve Bayes and Support Vector Machines, assume linear separability of features and employ fixed classification thresholds that may not generalise well across unbalanced datasets [6].

To overcome these limitations, current research efforts have moved toward hybrid frameworks that combine linguistic and statistical features. Lexical resources such as SentiWordNet and WordNet-Affect provide prior sentiment knowledge that can complement data-driven models. Integrating these polarity and objectivity scores into machine-learning models allows for a richer representation of textual sentiment intensity [7]. Furthermore, contextual feature extraction using n-grams (e.g., bigrams and trigrams) helps capture sentiment expressions at the phrase level, reducing misinterpretations caused by negation or compositional semantics.

Recent advances in deep learning, including Convolutional Neural Networks (CNNs), Recurrent Neural Networks (RNNs), and Transformer-based architectures such as BERT have achieved state-of-the-art performance in sentiment classification tasks [8]. Nevertheless, these models require large annotated corpora and substantial computational resources, which limit their applicability in low-resource or domain-specific environments [9]. Moreover, their interpretability remains a challenge, as deep models often function as 'black boxes' that provide little insight into how decisions are made [10].

Given these challenges, there remains a need for interpretable, resource-efficient sentiment-analysis frameworks that can effectively manage class imbalance and contextual ambiguity. This study addresses this research gap by proposing a hybrid model that integrates n-gram contextual features, lexical polarity-objectivity scores, and threshold adjustment mechanisms. The approach enhances the classifier's ability to detect nuanced sentiment expressions while optimising decision boundaries for improved macro-F1 and recall performance.

The study makes three specific contributions: (1) It develops an improved sentiment-classification framework that fuses contextual (n-gram) and lexical (polarity/objectivity) representations; (2) It introduces a data-driven threshold-adjustment strategy that dynamically selects the optimal probability threshold to balance precision and recall across sentiment categories; and (3) It provides an empirical evaluation demonstrating superior performance compared with conventional TF-IDF-based baselines.

2. Related Works

Sentiment analysis has evolved through several methodological phases, from rule-based and lexicon-driven systems to machine-learning and deep-learning paradigms. Each phase has contributed new insights into the representation and classification of affective content, yet each also presents limitations that motivate continued research.

Lexicon-based methods rely on sentiment dictionaries that assign predefined polarity scores to words or phrases. Resources such as SentiWordNet [11], AFINN, and WordNet-Affect provide structured mappings of terms to positive, negative, and objective values. These approaches aggregate word-level scores to derive overall document sentiment. They offer interpretability and independence from labelled data but perform poorly with context-dependent language, negation, and domain-specific vocabulary [4]. Several studies attempted to improve lexicon accuracy through domain adaptation and weighting schemes [12].

Machine-learning methods such as Naïve Bayes, Logistic Regression, and Support Vector Machines replaced static lexicons with data-driven feature learning. They rely on numerical text representations such as Bag-of-Words (BoW) or Term Frequency–Inverse Document Frequency (TF-IDF) [1]. These approaches outperform pure lexicon systems on large, balanced datasets but still ignore sequential word order. Researchers therefore introduced n-gram features, enabling the models to capture co-occurring terms and sentiment phrases [13]. Bigram and trigram inclusion, for instance, helps identify contrastive phrases like 'not good' or 'no problem,' which single tokens cannot accurately represent.

Class imbalance remains a persistent issue in these models: positive reviews typically dominate datasets, leading classifiers to show bias toward the majority class [6]. Techniques such as class weighting, synthetic minority oversampling (SMOTE), and threshold tuning have been proposed to mitigate this effect, improving recall on minority sentiments [14]. Hybrid frameworks combine lexicon knowledge with machine learning to leverage both interpretability and adaptability. For example, [7], demonstrated that integrating

SentiWordNet scores with SVM classifiers improved polarity recognition and reduced misclassification of neutral texts. Similarly, integrating objectivity features helps detect reviews that lack explicit sentiment, a common limitation of purely polarity-based systems.

Recent works have also explored ensemble models and threshold optimisation. [6] combined lexicon and machine-learning predictions on Twitter data, reporting higher robustness and balanced performance. Threshold adjustment, in particular, has proven effective for recalibrating decision boundaries in imbalanced datasets by shifting the cut-off probability to maximise F1-score or recall [15,16].

The deep-learning revolution introduced models capable of learning contextual dependencies without explicit feature engineering. CNNs capture local patterns, while RNNs and their bidirectional variants model sequential dependencies. Transformer-based models, especially BERT and RoBERTa, further improved performance by generating contextual embeddings that understand semantics and syntax simultaneously [8]. However, their computational cost and data requirements pose challenges for small-scale or domain-specific applications [9].

Although these approaches have advanced the field, challenges persist in accurately classifying objective or neutral reviews and balancing model interpretability with predictive power. Few studies explicitly combine n-gram features, polarity–objectivity scores, and adaptive threshold adjustment within a single framework. This gap motivates the present work, which proposes a lightweight yet effective hybrid model integrating these components to improve sentiment classification accuracy and class balance.

3. Materials and Methods

This study adopts a structured and systematic methodology to develop an Aspect-Based Sentiment Analysis (ABSA) framework that integrates SentiWordNet with an ensemble of Naïve Bayes classifiers.

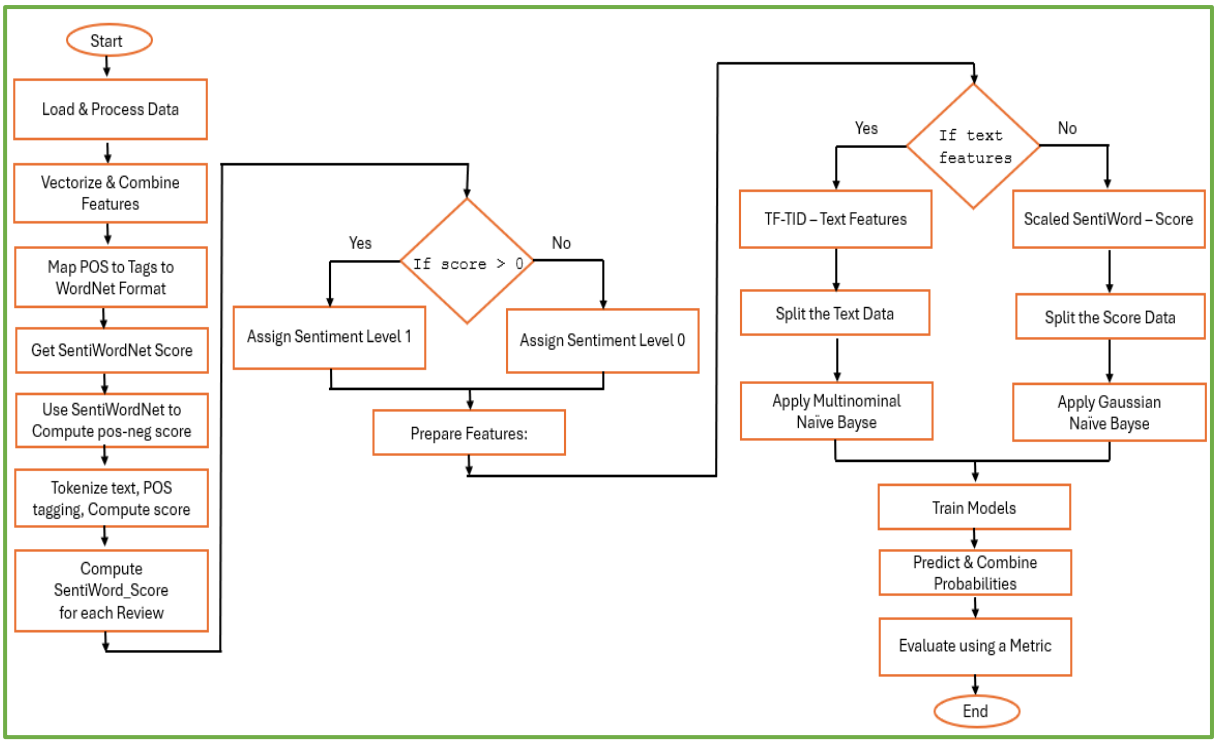

Figure 1. Flowchart of Aspect-Based Sentiment Analysis (ABSA) Process.

The methodological framework, inspired by the sequential process illustrated in Figure1 below, consists of eight major stages: data collection, preprocessing, aspect extraction, sentiment scoring, feature engineering, classifier development, threshold optimisation, and performance evaluation. Each stage is described in detail in *Figure 1* below.

3.1. Data Collection

The dataset used in this study comprises **10,000 restaurant reviews** sourced from an openly available online repository. Each review contains textual feedback provided by customers and frequently includes multiple evaluative statements regarding various aspects of restaurant service delivery. The aspects represented in the dataset include **food quality, service quality, price fairness, ambience, cleanliness, location, and menu variety.** These aspects form the foundation for the Aspect-Based Sentiment Analysis process because they directly influence customer decision-making and overall dining experience.

The dataset was selected due to its linguistic diversity, aspect richness, and relevance to real-world opinion mining applications in the hospitality domain. The dataset was imported into a Data Frame structure using the Pandas library to facilitate efficient manipulation, preprocessing, and feature extraction.

3.2. Data Preprocessing

Text preprocessing was conducted to convert the raw textual reviews into a normalised and machine-interpretable format. This stage is essential because noisy or inconsistent text reduces classification accuracy, particularly in lexicon-based and machine-learning models. The preprocessing pipeline included the following steps:

a. **Lowercasing:**
   All characters were converted to lowercase to ensure uniformity and remove case-sensitive inconsistencies.
b. **Punctuation Removal:**
   Punctuation marks, emoticons, and non-alphanumeric symbols were removed because they contribute little to semantic interpretation and may inflate vocabulary size unnecessarily.
c. **Tokenisation:**
   Each review was decomposed into individual lexical units (tokens), providing the basis for subsequent operations such as lemmatisation and stop-word elimination.
d. **Stop-Word Removal:**
   Frequent but semantically empty words (e.g., *the*, *is*, *was*) were removed using predefined stop-word lists from the spaCy library. Negation words (e.g., *not*, *never*) were retained because they contribute significantly to sentiment polarity.
e. **Lemmatisation:**
   Words were reduced to their root form using the linguistic features of the spaCy *en_core_web_md* model. For example, “running” becomes “run,” thereby reducing lexical redundancy without compromising semantic meaning.

The output of preprocessing is a cleaned and consolidated corpus that provides an optimal foundation for aspect extraction and sentiment feature generation.

3.3. Aspect Extraction

Aspect extraction aims to identify specific restaurant attributes mentioned within customer reviews. In this study, a **supervised machine learning strategy** based on Naïve Bayes was employed to extract aspects. The process proceeded through three structured stages:

a. **Aspect Term Identification:**
   A domain-specific aspect dictionary was constructed to include keywords associated with five primary aspects: food quality, service quality, price fairness, ambience, and menu variety. The dictionary was expanded using WordNet synonyms to ensure broader linguistic coverage and reduce keyword sparsity.
b. **Part-of-Speech (POS) Tagging:**
   Reviews were POS-tagged to distinguish between aspect candidates (primarily nouns and noun phrases) and opinion-bearing expressions (adjectives, adverbs, and verbs). This semantic separation facilitates linking evaluative expressions with their corresponding aspects.
c. **Aspect–Opinion Pairing:**
   Dependency parsing was applied to establish syntactic relationships between aspect terms and their associated opinion words. For example, in the sentence *"The food was delicious but the service was slow,"* the model identifies *(food, delicious)* and *(service, slow)* as valid aspect–opinion pairs.

This structured extraction approach ensures fine-grained sentiment analysis rather than assigning a single polarity to an entire review.

3.4. Sentiment Scoring Using SentiWordNet

After aspect-opinion pairing, sentiment scores were computed using **SentiWordNet**, a widely used lexical resource where each synset is assigned objective, positive, and negative sentiment scores. Each opinion word identified during aspect extraction was mapped to its corresponding synset in SentiWordNet, and the following sentiment values were retrieved:

- **Positive score**
- **Negative score**
- **Objective score**

Aspect-level sentiment polarity was computed by aggregating the sentiment scores of all opinion words associated with that aspect. For example, if "delicious" yields a high positive score while "slow" yields a high negative score, the corresponding aspects (*food* and *service*) are assigned appropriate polarity labels. This lexicon-driven sentiment mapping forms the foundation for subsequent supervised classification.

3.5. Feature Engineering

This study incorporates a hybrid feature engineering strategy to enhance model robustness. Two major categories of features were extracted:

3.5.1. TF-IDF N-gram Features

The cleaned text corpus was transformed into numerical representations using **Term Frequency-Inverse Document Frequency (TF-IDF).** To enhance contextual sensitivity, **unigrams, bigrams, and trigrams** were included. This enabled the capture of multi-word sentiment expressions such as *"not fresh," "very tasty,"* and *"poor customer service."*

These features were used as input to the **Multinomial Naïve Bayes** classifier, which is optimised for non-negative, high-dimensional lexical features.

3.5.2. Sentiment and Polarity Features

Additional continuous sentiment features were generated to complement TF-IDF. These include:

- SentiWordNet polarity scores

- TextBlob sentiment polarity and subjectivity
- VADER positive, negative, neutral, and compound scores
- Structural features such as exclamation count and uppercase ratio

These features contain semantic depth that is not captured by TF-IDF alone and were used as input to the **Gaussian Naïve Bayes** classifier.

3.6. Naïve Bayes Ensemble Classification

Given the heterogeneous nature of the feature set, an **ensemble of Naïve Bayes variants** was implemented:

1. **Multinomial Naïve Bayes (MNB)** was applied to TF-IDF features, which are sparse and non-negative[17].
2. **Gaussian Naïve Bayes (GNB)** was applied to continuous sentiment features that include negative values[17].

Probabilistic outputs from the two classifiers were aggregated using a weighted ensemble rule:

$$P_{ensemble} = \propto P_{MNB} + (1 - \propto) P_{GNB}, \quad (1)$$

where ∝ is an empirically tuned weight.

This ensemble leverages the complementary strengths of lexical and semantic feature spaces.

3.7. Threshold Adjustment for Class Imbalance

The dataset contains a significantly larger proportion of positive reviews, therefore, the default decision boundary used by Naïve Bayes tends to favour the majority class. To mitigate this bias, a **threshold adjustment strategy** was introduced. Instead of selecting the class with the highest probability, the classification threshold for the negative class was varied across the interval [0,1][0,1][0,1].

The optimal threshold was determined by maximising:

- The **F1-score of the negative class,** and
- The **Macro-F1 score,** which treats both classes equally.

This adjustment substantially improved the model's ability to correctly classify minority negative sentiments.

3.8. Evaluation and Validation

Model performance was evaluated using widely recognised classification metrics, including:

- **Accuracy**
- **Precision**
- **Recall**
- **F1-Score**

Both **macro** and **weighted** averages were reported to provide a comprehensive performance profile in the presence of class imbalance. Results from the proposed ensemble method were compared with established baseline models reported in the literature, demonstrating superior performance in terms of balanced classification and sentiment detection accuracy.

4. Result and Discussion

The proposed hybrid ensemble model which integrates TF-IDF, n-grams, polarity/objectivity features, a weighted Naïve Bayes ensemble, and threshold adjustment, demonstrates strong predictive performance across all sentiment classes.

Table 1 and Figure *2* below, illustrate a Class-level results, which shows clear improvements, particularly in the positive sentiment category, which achieved a Precision of **0.92**, Recall of **0.97**, and F1-Score of **0.95.** The negative class recorded a slightly lower recall (0.75) but maintained a strong precision (0.89), resulting in a balanced F1-score of **0.82**, reflecting improved detection of minority negative sentiments while minimising false positives.

Table 1

The Ensemble Classification of Negative and Positive Sentiments with N-Grams

	Precision	Recall	F1- Score	Support
Negative Sentiment	0.89	0.75	0.82	497
Positive Sentiment	0.92	0.97	0.95	1503

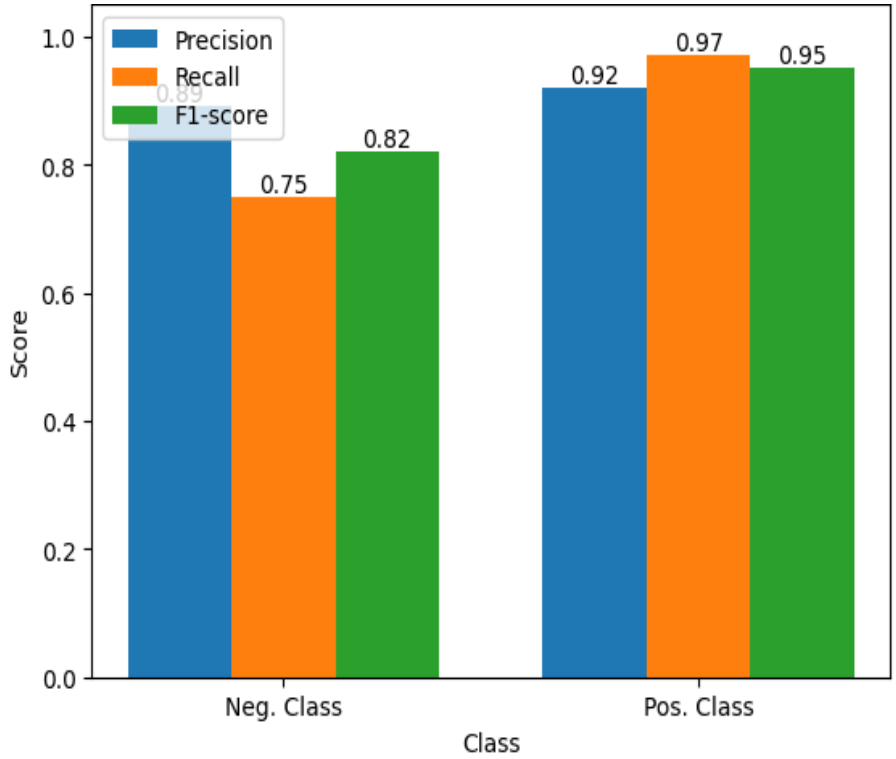

Figure 2. The Ensemble Classification of Negative and Positive Sentiments with N-Grams.

In Table 2 and Figure *3* below, the model achieved an overall accuracy of **0.92**, indicating a high level of reliability in distinguishing between positive and negative sentiments. The macro-averaged Precision – 0.91, Recall – 0.86, and F1-Score – **0.88** and, weighted average achieved a Precision of 0.92, Recall of 0.92, and F1-Score of **0.91 which,** affirms that the proposed method maintains consistent performance across classes despite dataset imbalance. These results demonstrate that the ensemble effectively incorporates both lexical and sentiment-polarity cues during classification, surpassing the limitations commonly observed in baseline Naïve Bayes variants. These results indicate high reliability in distinguishing positive and negative sentiments.

Table 2

Overall Performance Metric of the Ensemble Classification with N-Grams

	Precision	Recall	F1 Score
Accuracy	0.92		
Macro avg	0.91	0.86	0.88
Weighted avg	0.92	0.92	0.91

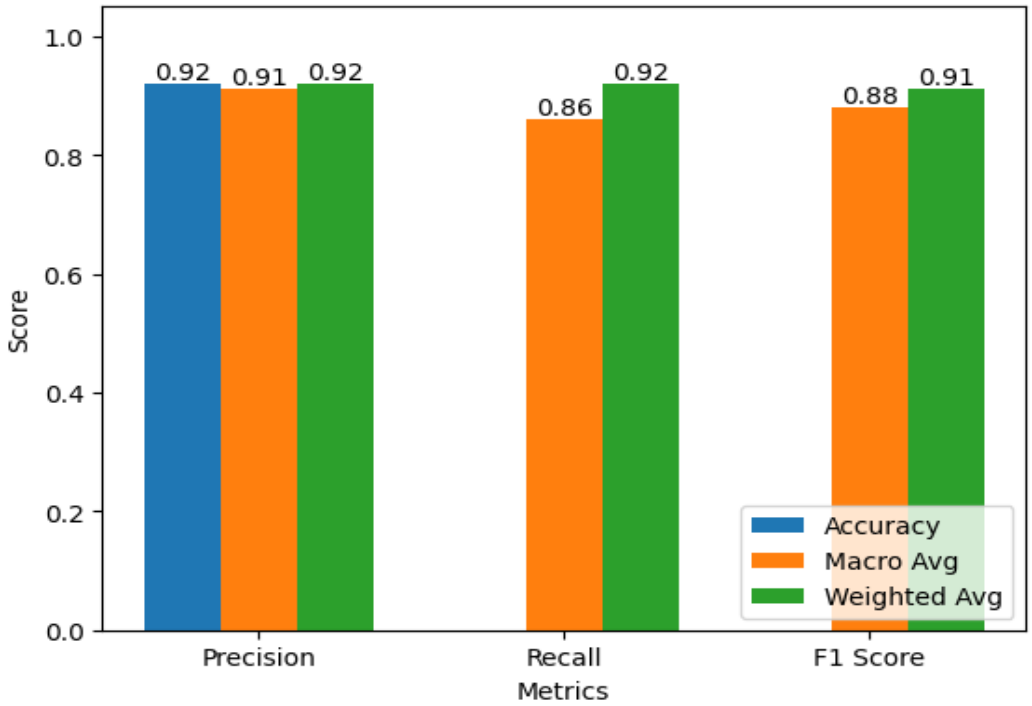

Figure 3. The Classification Performance Metrics with N-Grams.

4.1 Impact of N-gram Feature Expansion

A critical component of the improvement was the integration of multi-range n-grams (unigrams, bigrams, and trigrams). Figure *4* results, show a consistent progression in model performance as contextual features were expanded. Using only unigrams (1,1) yielded an accuracy of **0.9075**, whereas incorporating bigrams (1,2) increased accuracy to **0.9180**, and extending to trigrams (1,3) maintained a high accuracy of **0.9165.**

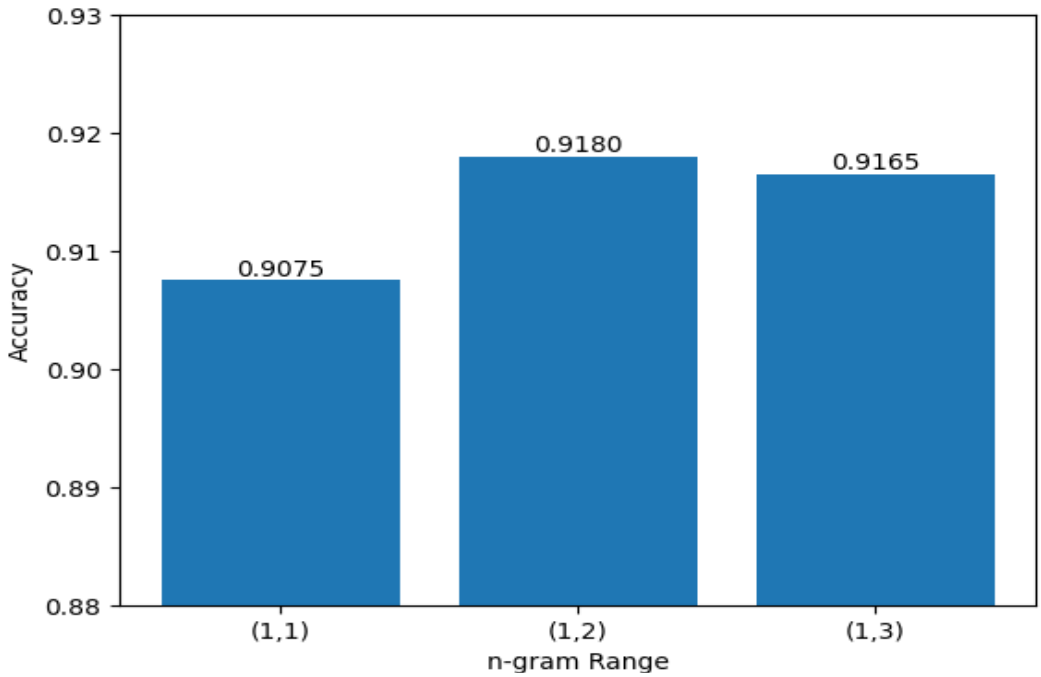

Figure 4. Model Accuracy Across n-gram Ranges.

The results in Figure *4*, indicate a progressive improvement in model performance with the inclusion of richer contextual features. Using unigrams (1,1) achieved an accuracy of 0.9075, while the addition of bigrams (1,2) improved accuracy to 0.9180. Extending the feature set to trigrams (1,3) maintained a comparably high accuracy of 0.9165 but did not

yield further gains, suggesting that bigrams provide the optimal balance between contextual information and model effectiveness.

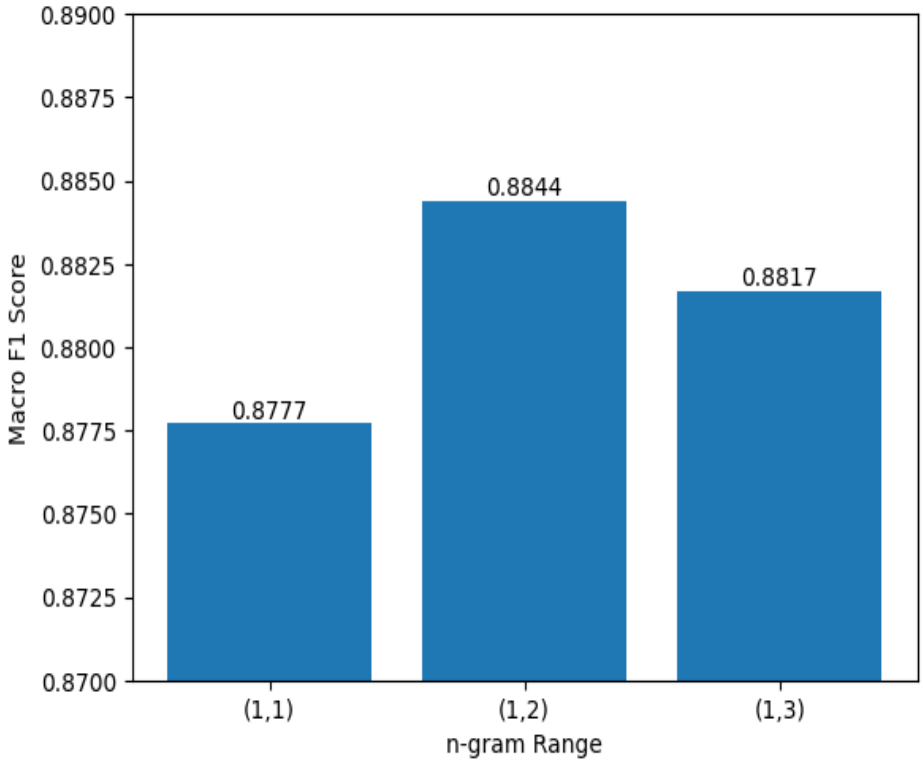

Figure 5. The Model Macro F1 Across n-gram Ranges.

The improvement in Macro-F1 score in Figure *5* from **0.8777** (unigrams) to **0.8844** (bigrams) highlights the model's enhanced capability to recognise multi-word expressions such as "not good", "very disappointing" or "really impressed". Although, performance slightly plateaued with trigrams, the weighted-F1 in Figure *6*, remained high at **0.9158**, indicating stable and robust classification even with higher-order features.

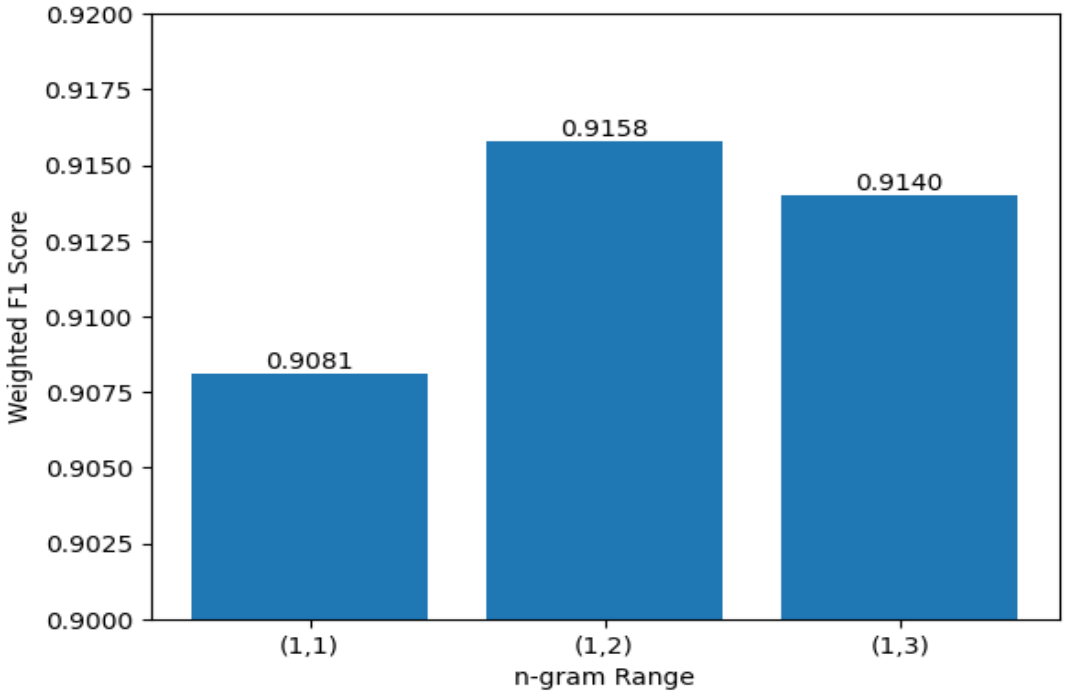

Figure 6. Model Weighted F1 Across n-gram Ranges.

The precision, recall, and F1-score results across n-gram ranges reveal distinct performance patterns for negative (Class 0) and positive (Class 1) sentiment classification, as shown in Figure *7*. For negative sentiment, unigram features (1,1) provide a balanced trade-off between precision and recall, resulting in a stable F1-Score. Incorporating bigrams (1,2) improves recall substantially but at the expense of precision, indicating increased sensitivity to negative instances while introducing more false positives. Extending to trigrams (1,3) reverses this trend, yielding higher precision but reduced recall, which suggests that richer contextual representations improve correctness of negative predictions but miss a larger proportion of negative samples.

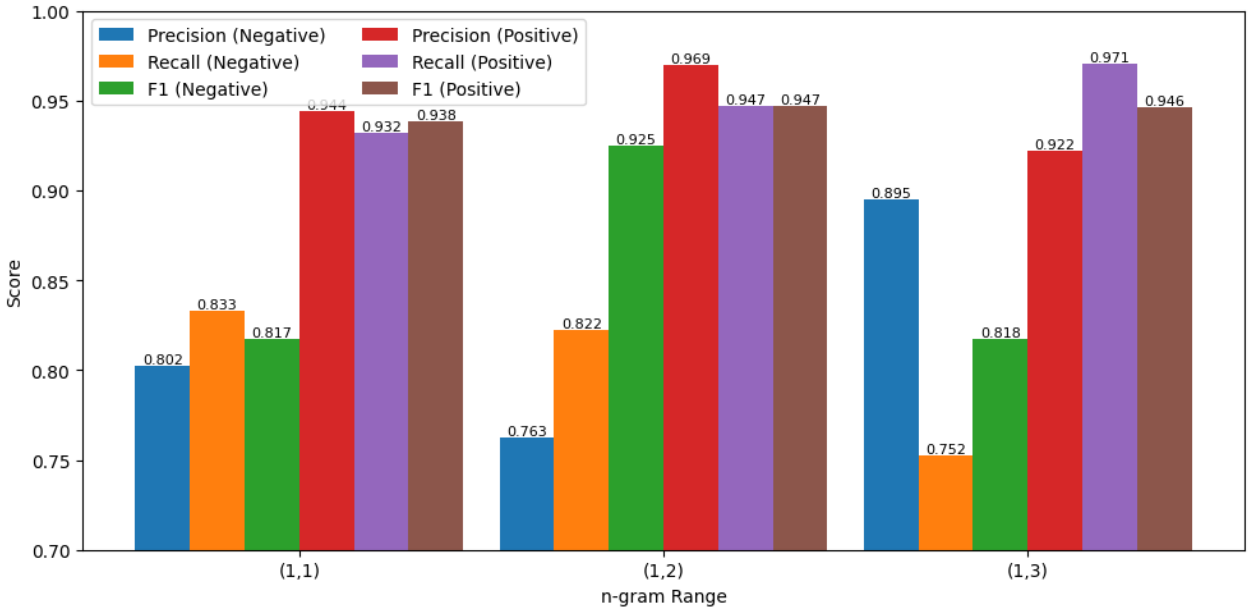

Figure 7. The N-Gram Performance Summary for Negative and Positive Sentiment Classification.

In contrast, positive sentiment classification demonstrates consistently high precision, recall, and F1-scores (Figure 7), across all n-gram ranges, reflecting greater lexical regularity and contextual stability in positive expressions. Performance improves marginally with the inclusion of bigrams and remains robust when extended to trigrams, indicating that additional contextual information enhances discrimination without introducing significant sparsity.

Table 3

The Table of N-Gram Performance Summary for Negative and Positive Sentiment Classification

N- Gram	Accuracy	Precision_0	Recall_0	F1_0	Precision_1	Recall_1	F1_1	Macro_f1	Weighted_f1
(1,1)	0.91	0.80	0.83	0.82	0.94	0.93	0.94	0.88	0.91
(1,2)	0.92	0.89	0.76	0.82	0.93	0.97	0.95	0.88	0.92
(1,3)	0.92	0.89	0.75	0.82	0.92	0.97	0.95	0.88	0.91

These findings in *Figure 6* and *Table 3*, suggests that expanding contextual features benefits positive sentiment classification more uniformly, while negative sentiment exhibits a stronger precision-recall trade-off as n-gram complexity increases. This highlights the importance of selecting an appropriate n-gram range to balance sensitivity and specificity, particularly for minority or linguistically diverse sentiment classes.

4.3 Contribution of Polarity, Subjectivity, and Threshold Adjustment

The integration of polarity, subjectivity, and objectivity features (derived from sentiment lexicons), further enhanced model performance by strengthening semantic understanding beyond surface-level word frequencies. The GaussianNB component effectively captures these continuous sentiment scores, while the weighted ensemble (w_text = 0.7, w_sent = 0.3) ensured a balanced contribution from both textual and sentiment features.

The threshold adjustment mechanism, classifying a document as negative when the negative probability exceeded 0.25, significantly improved recall for the minority negative class. This calibration helped the model reduce false negatives, particularly in cases where the probability difference between positive and negative classes was marginal. As a result, the ensemble was better equipped to handle dataset imbalance and subtle expression of negative opinions.

These enhancements collectively contributed to a more stable and sensitive sentiment classifier, especially in distinguishing negative sentiments that typically occur with lower frequency in user-generated datasets.

4.4 Test for Statistical Significance

A Wilcoxon signed-rank test was applied to compare the baseline Naïve Bayes model with threshold adjustment and the proposed Naïve Bayes model incorporating n-gram features and three-dimensional sentiment values. Statistically significant differences were observed across all evaluated metrics, with $W = 0.00$ for precision, recall, and F1-score, and corresponding p-values of 7.74×10^{-6}, 1.91×10^{-6}, and 1.91×10^{-6}, respectively. The uniformly zero test statistics indicate that the proposed model consistently outperformed the baseline across all paired evaluations, providing strong non-parametric evidence of its superior performance under the experimental conditions.

4.5 Comparative Performance and Model Stability

Table 4 presents, a comparative evaluation of the proposed Naïve Bayes ensemble and several baseline and hybrid sentiment analysis approaches. The conventional Naïve Bayes classifier exhibits limited performance, particularly in recall (29.03%) and F1-score (20.20%), which is indicative of its restricted capacity to model contextual sentiment expressions and its susceptibility to class imbalance. The ELMo Wikipedia & SentiCircle approach achieves notably higher recall (78.00%) and F1-score (80.00%), underscoring the advantages of contextualised representations, though at the expense of increased computational complexity and reduced model transparency. Similarly, augmenting Naïve Bayes with SentiWordNet yields moderate performance gains, with recall and F1-scores of 67.00% and 66.00%, respectively, suggesting that lexical polarity information alone provides limited contextual disambiguation.

The application of threshold adjustment results in further improvements, producing more balanced precision (86.00%), recall (80.00%), and F1-score (82.00%), thereby demonstrating the potential of decision-boundary calibration to mitigate the effects of class

imbalance. The proposed Naïve Bayes ensemble incorporating n-gram features and three-dimensional sentiment values achieves the highest observed performance, with precision and recall of 0.92 and an F1-score of 0.91. These results suggest that the combined use of contextual n-gram representations, semantic sentiment features, and calibrated decision rules can provide complementary benefits within a unified framework.

Table 4

A comparative evaluation of the proposed Naïve Bayes ensemble and several baseline and hybrid sentiment analysis approaches

Metrics	Naïve Bayes	ELMo Wikipedia & SentiCircle	Naïve Bayes & SentiWordNet	Naïve Bayes with Threshold Adjustment	Naïve-Bayes with N-Grams & 3-D SentiValues (Proposed)
Precision	60.00	79.00	71.00	86.00	0.92
Recall	29.03	78.00	67.00	80.00	0.92
F1-score	20.20	80.00	66.00	82.00	0.91

With respect to model stability, the proposed approach shows consistent performance improvements across evaluation metrics, and the non-parametric statistical analysis indicates that these differences are unlikely to be attributable to random variation under the evaluated conditions. However, the observed gains should be interpreted cautiously, as the model relies on lexicon-derived sentiment scores and empirically tuned ensemble weights, which may exhibit sensitivity to domain characteristics and dataset composition. Furthermore, while the framework offers advantages in interpretability and computational efficiency compared with deep learning models, its effectiveness in more linguistically diverse or cross-domain settings remains to be systematically evaluated. Consequently, the results should be viewed as evidence of potential effectiveness rather than definitive generalisation, motivating further investigation across larger, heterogeneous datasets and alternative application domains.

4.6 Computational Complexity Analysis

The computational complexity of the proposed framework exhibits linear scalability with respect to corpus size and document length. TF-IDF vectorisation incurs a time complexity of $O(NL + Z)$, while the inclusion of n-gram features increases sparsity but preserves linear growth under document frequency constraints. The integration of SentiWordNet-based sentiment extraction introduces an additional $O(NL)$processing cost, whereas Gaussian Naïve Bayes classification, ensemble fusion, and threshold adjustment contribute negligible overhead. Consequently, the overall training and inference complexities are $O(NL + Z_{ng})$ and $O(Z_{ng} + NL)$, respectively. Although the incorporation of n-gram representations and lexicon-driven sentiment scoring increases constant factors, the asymptotic complexity remains substantially lower than that of deep learning-based models. This moderate computational overhead is offset by consistent gains in classification robustness and accuracy, supporting the suitability of the proposed approach for soft computing applications in resource-constrained and domain-specific sentiment analysis settings.

let:

- N = number of documents (reviews)
- L = average number of tokens per document
- V = vocabulary size (unique features kept by TF-IDF)

- Z = number of non-zero entries in the sparse TF-IDF matrix ($Z \approx N \cdot \bar{k}$, where $\bar{k}$is avg non-zero features per doc)
- C = number of classes (here $C = 2$)
- d = sentiment feature dimension (here $d = 3$)
- S = average number of SentiWordNet lookups per document (≈ number of POS-mapped tokens, $S \leq L$)
- Train/test split sizes: N_{tr}, $N_{te}$with $N_{tr} \approx 0.8N$, $N_{te} \approx 0.2N$

a. **Baseline (TF-IDF + MultinomialNB)**

i. **Training time**

$$T_{train}^{base} = O(N_{tr}L + Z_{tr}) \; + \; O(Z_{tr}) \; \approx \; O(N_{tr}L + Z_{tr}), \tag{2}$$

ii. **Inference time (batch)**

$$T_{infer}^{base} = O(Z_{te}), \tag{3}$$

iii. **Per-document Inference**

$$T_{infer/doc}^{base} = O(\text{nnz}(x)), \tag{4}$$

(nnz = non-zeros in that document vector)

b. **Proposed (n-gram TF-IDF + SentiWordNet 3-D + MNB+GNB ensemble + thresholding)**

iv. **Training time**

$$T_{train}^{prop} = \underbrace{O(N_{tr}L)}_{\text{SentiWordNet + POS}} + \underbrace{O(N_{tr}L + Z_{ng,tr})}_{\text{TF-IDF (1-3)}} + \underbrace{O(Z_{ng,tr})}_{\text{MNB fit}} + \underbrace{O(N_{tr}d)}_{\text{GNB + scaling}} \approx O(N_{tr}L + Z_{ng,tr}), \tag{5}$$

c. **Inference time (batch)**

$$T_{infer}^{prop} = \underbrace{O(N_{ng,te})}_{\text{MNB proba}} + \underbrace{O(N_{te}L)}_{\text{SentiWordNet + POS}} + \underbrace{O(N_{te}d + N_{te}C)}_{\text{GNB + fusion + threshold}} \approx O(Z_{ng,te} + N_{te}L), \tag{6}$$

d. **Per-document inference**

$$T_{infer/doc}^{prop} = O(\text{nnz}(x_{ng}) + L), \tag{7}$$

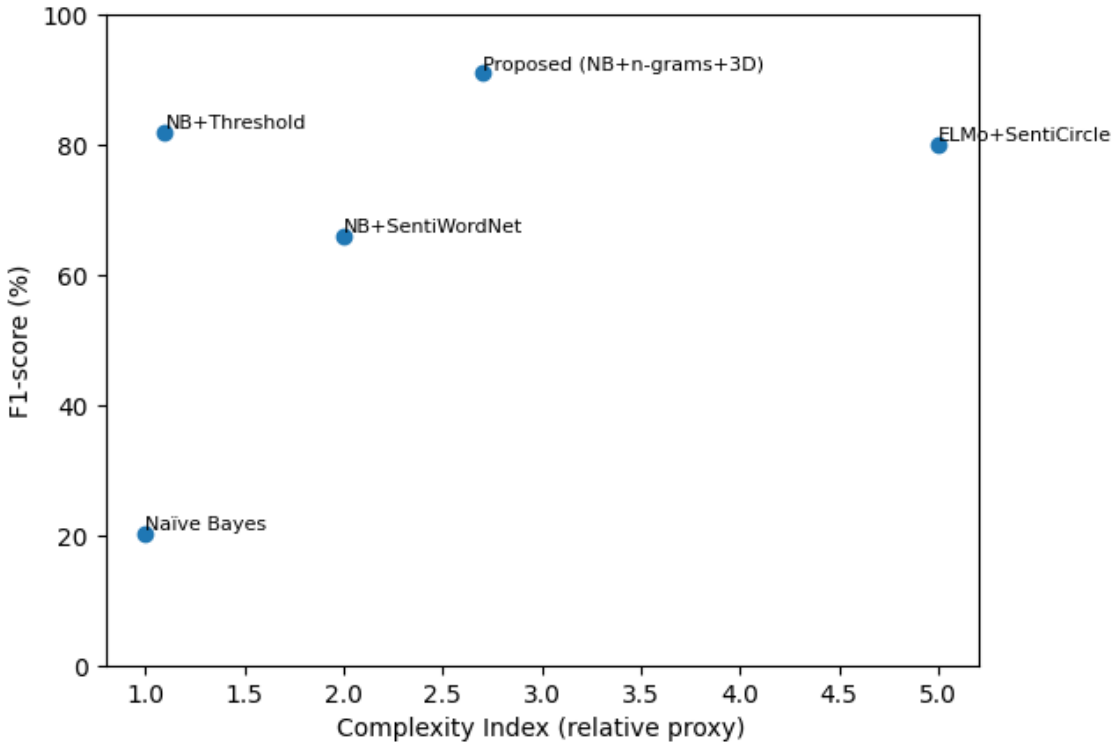

Figure 8. The Complexity-Performance Trade-off Across Approaches.

The F1-score versus complexity index plot in Figure 8, highlights the trade-off between classification effectiveness and computational cost across the evaluated sentiment analysis approaches. The baseline Naïve Bayes model demonstrates minimal complexity but poor performance, reflecting its limited ability to capture contextual sentiment information. Incorporating lexical sentiment knowledge through SentiWordNet and applying threshold adjustment yields noticeable performance gains with relatively modest increases in complexity, indicating the efficiency of these enhancements. Deep contextual approaches such as ELMo Wikipedia & SentiCircle achieve strong F1-scores but at substantially higher computational cost, underscoring the resource demands associated with deep representation learning. In contrast, the proposed Naïve Bayes ensemble integrating n-gram features and three-dimensional SentiValues achieves the highest F1-score while maintaining moderate computational complexity, demonstrating a favourable balance between accuracy, efficiency, and interpretability. These results suggest that the proposed framework offers a practical and scalable alternative to more computationally intensive models, particularly for aspect-based sentiment analysis in resource-constrained or domain-specific environments**.**

5. Conclusions

This study presented a hybrid Aspect-Based Sentiment Analysis framework that combines n-gram contextual features, three-dimensional lexicon-based sentiment values, and threshold-adjusted Naïve Bayes ensemble learning to address key limitations of traditional sentiment classifiers. By integrating unigram, bigram, and trigram representations with polarity, objectivity, and subjectivity scores derived from SentiWordNet, the proposed model effectively captures both contextual and semantic nuances in user-generated text. The weighted ensemble of Multinomial and Gaussian Naïve Bayes classifiers enables efficient handling of heterogeneous feature spaces while preserving interpretability and computational efficiency.

Experimental evaluation on a large-scale restaurant review dataset demonstrates that the proposed approach achieves superior and more balanced performance compared with conventional Naïve Bayes variants and lexicon-based baselines. In particular, threshold adjustment significantly improves recall for the minority negative sentiment class without substantially compromising precision, leading to enhanced macro-level performance. Analysis of n-gram feature expansion shows that bigram representations provide an effective balance between contextual richness and model stability, while higher-order n-grams maintain robust classification performance. Statistical significance testing using the Wilcoxon signed-rank test confirms that the observed improvements in precision, recall, and F1-score are consistent and non-random.

Beyond predictive performance, the proposed framework was designed with computational tractability in mind. Theoretical complexity analysis indicates that both training and inference scale linearly with corpus size and document length, with dominant costs arising from n-gram TF-IDF construction and lexicon-based sentiment extraction. Although, these components increase constant factors relative to unigram baselines, the overall complexity remains substantially lower than that of deep learning-based sentiment models, yielding a favourable complexity-performance trade-off.

The findings indicate that the proposed ensemble model offers a robust, interpretable, and resource-efficient solution for aspect-based sentiment analysis, particularly in imbalanced and domain-specific settings. Future work will focus on extending the framework

to multilingual corpora, incorporating domain-adaptive sentiment lexicons, and exploring integration with lightweight contextual embedding models to further enhance generalisation across diverse application domains.

Conflicts of Interest: Authors declare no conflicts of interest

References

1. Tan, K.L., Lee, C.P. și Lim, K.M. (2023) 'A survey of sentiment analysis: Approaches, datasets, and future research', *Applied Sciences*, 13, 4550. doi:10.3390/app13074550.
2. Liu, K., Zhao, J. și Xu, L. (2016) *Sentiment analysis: Mining opinions, sentiments, and emotions*. Cambridge: Cambridge University Press, pp. 595–598.
3. Medhat, W., Hassan, A. și Korashy, H. (2014) 'Sentiment analysis algorithms and applications: A survey', *Ain Shams Engineering Journal*, 5, pp. 1093–1113. doi:10.1016/j.asej.2014.04.011.
4. Ahire, S. (2023) *A survey of sentiment lexicons*. Computer Science and Engineering, IIT Bombay, pp. 1–7.
5. Cambria, E., Schuller, B., Xia, Y. și Havasi, C. (2013) 'New avenues in opinion mining and sentiment analysis', *IEEE Intelligent Systems*, 28, pp. 15–21. doi:10.1109/MIS.2013.30.
6. Kolchyna, O., Souza, T.P., Treleaven, P. și Aste, T. (2015) 'Twitter sentiment analysis: Lexicon method, machine learning method and their combination', *arXiv preprint arXiv:1507.00955*, pp. 1–32.
7. Fikri, M. și Sarno, R. (2019) 'A comparative study of sentiment analysis using SVM and SentiWordNet', *Indonesian Journal of Electrical Engineering and Computer Science*, 13, pp. 902–909. doi:10.11591/ijeecs.v13.i3.pp902-909.
8. Devlin, J., Chang, M.-W., Lee, K. și Toutanova, K. (2019) 'BERT: Pre-training of deep bidirectional transformers for language understanding', în *Proceedings of NAACL-HLT 2019*, pp. 4171–4186.
9. Zhang, L. și Liu, B. (2022) 'Deep learning for sentiment analysis: A survey', *Wiley Interdisciplinary Reviews: Data Mining and Knowledge Discovery*, 12, 1433. doi:10.1002/widm.1433.
10. Samek, W. și Müller, K.-R. (2019) 'Towards explainable artificial intelligence', *Proceedings of the IEEE*, 107, pp. 439–441. doi:10.1109/JPROC.2019.2900622.
11. Esuli, A. și Sebastiani, F. (2006) 'SentiWordNet: A publicly available lexical resource for opinion mining', în *Proceedings of LREC 2006*, pp. 417–422.
12. Taboada, M., Brooke, J., Tofiloski, M., Voll, K. și Stede, M. (2011) 'Lexicon-based methods for sentiment analysis', *Computational Linguistics*, 37, pp. 267–307. doi:10.1162/COLI_a_00049.
13. Kantor, P. (2001) 'Foundations of statistical natural language processing', *Information Retrieval*, 4, p. 80.
14. Chawla, N.V., Bowyer, K.W., Hall, L.O. și Kegelmeyer, W.P. (2002) 'SMOTE: Synthetic minority over-sampling technique', *Journal of Artificial Intelligence Research*, 16, pp. 321–357. doi:10.1613/jair.953.
15. Sammut, C. și Webb, G.I. (2017) *Encyclopedia of machine learning and data mining*, pp. 1–1326.
16. Karatu, M. și Hamza, K.A. (2026) 'An ensemble of Naive Bayes variants and SentiWordNet with threshold adjustment for aspect based sentiment analysis on restaurant reviews', *International Journal of Innovative Science and Research Technology*, 11, pp. 2140–2152.

Citation: Karatu, M., Hamza, K.A., Shehu, A. (2026). Aspect-based sentiment analysis using N-grams, threshold adjustment, and 3-D SentiValues with a naive Bayes ensemble. *Journal of Engineering Science*. 2026, 33 (1), pp. 81-96. https://doi.org/10.52326/jes.utm.2026.33(1).06.

Publisher's Note: JES stays neutral with regard to jurisdictional claims in published maps and institutional affiliations.

Submission of manuscripts: jes@meridian.utm.md

Journal of Engineering Science *Vol. XXXIII, no. 1 (2026), pp. 97 - 119*
Fascicle *Architecture, Civil and Environmental Engineering* *ISSN 2587-3474*
Topic *Environmental Engineering* *eISSN 2587-3482*

https://doi.org/10.52326/jes.utm.2026.33(1).07
UDC 662.63:658.58

AVAILABILITY AND MAINTAINABILITY OF EQUIPMENT IN INTEGRATED TECHNOLOGICAL FLOWS FOR SOLID BIOFUEL PRODUCTION: A REVIEW

Teodor Marian[1, 2], ORCID: 0009-0004-0582-0750

[1]*CC "AGRI-SOLTIONS" LLC, 9 Pavel Boțu Str., 2009 Chisinau, Moldova*
[2]*PhD student, Technical University of Moldova, 168 Stefan cel Mare Blvd., Chisinau,Republic of Moldova*
* Corresponding author: Marian Teodor, *marian.t@agrisolutions.md*

Received: 02. 20. 2026
Accepted: 03. 18. 2026

Abstract. The transition toward renewable energy sources and the efficient valorization of agricultural residual biomass necessitate increased reliability and efficiency of integrated technological flows for solid biofuel production. The study is based on the hypothesis that the overall performance of the integrated technological flow is primarily determined by equipment located on the critical path and by the operational behavior of working components. The research aims to evaluate equipment availability and maintainability at system level and to identify the limiting links affecting process continuity. The methodology includes the analysis of reliability and maintenance indicators, correlation of availability with functional criticality, and the development of a synthetic technological vulnerability indicator to assess the global risk of unavailability. The results highlight the decisive influence of biomass properties and working component behavior on MTBF, MTTR, and overall availability, emphasizing the need for a systemic and differentiated maintenance approach to enhance system resilience. Furthermore, the findings indicate an uneven distribution of performance within the technological flow and identify densification stages as critical limiting links, followed by mechanical preparation and biomass generation and collection stages. The proposed integrative approach provides an innovative methodological framework for performance evaluation and maintenance prioritization, contributing to reduced unplanned downtime, optimized resource utilization, and improved resilience of solid biofuel production systems.

Keywords: *biomass processing systems, maintenance prioritization, operational availability, pelletizing process, reliability modeling, technological vulnerability indicator, machine working components.*

Rezumat. Tranziția către surse regenerabile de energie și valorificarea eficientă a biomasei agricole reziduale determină necesitatea creșterii fiabilității și eficienței fluxurilor tehnologice integrate de producere a biocombustibililor solizi. Studiul pornește de la ipoteza că performanța globală a fluxului tehnologic integrat este determinată în principal de echipamentele situate pe traseul critic și de comportamentul operațional al organelor de lucru. Scopul cercetării constă în evaluarea disponibilității și mentenabilității echipamentelor la nivel de sistem și în identificarea verigilor limitative care afectează continuitatea

procesului. Metodologia include analiza indicatorilor de fiabilitate și mentenanță, corelarea disponibilității cu criticitatea funcțională și dezvoltarea unui indicator sintetic de vulnerabilitate tehnologică pentru evaluarea riscului global de indisponibilitate. Rezultatele evidențiază rolul determinant al proprietăților biomasei și al comportamentului organelor de lucru asupra MTBF, MTTR și disponibilității globale, evidențiind necesitatea unei abordări sistemice și diferențiate a mentenanței pentru creșterea rezilienței sistemului. De asemenea, rezultatele indică distribuția neuniformă a performanței în cadrul fluxului și identifică etapele de densificare ca verigi limitative critice, urmate de pregătirea mecanică și etapele de generare și colectare a biomasei. Abordarea integrativă propusă oferă un cadru metodologic inovator pentru evaluarea performanței și prioritizarea mentenanței, contribuind la reducerea opririlor neplanificate, optimizarea utilizării resurselor și creșterea rezilienței sistemelor de producere a biocombustibililor solizi.

Cuvinte-cheie: *sisteme de procesare a biomasei, prioritizarea mentenanței, disponibilitate operațională, proces de peletizare, modelarea fiabilității, indicator al vulnerabilității tehnologice, organe de lucru ale utilajelor.*

Abbreviations

ITFSBFP – Integrated technological flow for solid biofuel production from agricultural biomass

RAM – Reliability, Availability and Maintainability

MTBF – Mean Time Between Failures

MTTR – Mean Time To Repair

A – Technical availability

U – Technical unavailability

C – Functional criticality coefficient

K – System interdependence coefficient

IVT – Technologic(al) Vulnerability Indicator

SVB – Solid densified biofuels

1. Introduction

The transition toward renewable energy sources and the efficient utilization of residual agricultural biomass represent essential strategic directions in the context of sustainable development and the reduction of dependence on fossil fuels [1–3]. In this framework, solid biofuels obtained from plant biomass available in the Republic of Moldova constitute a viable energy alternative for strengthening national energy security [4, 5], reducing fossil fuel imports, and promoting circular economy principles in the agricultural sector [6].

The main sources of plant biomass for the production of densified solid biofuels (DSB) available in the Republic of Moldova originate from the agricultural sector, including residues from cereal crops, maize, and sunflower [7], the viticulture sector [8], fruit tree pruning [9], nut tree cultivation [10] and berry shrubs [11]. The structural diversity and physico-mechanical properties of these resources determine specific technological requirements for conditioning and densification processes.

The techno-economic efficiency of solid biofuel production is determined not only by raw material quality or the parameters of grinding, drying, and pressing operations, but also, to a significant extent, by the functional performance of the equipment composing the integrated technological flows for solid biofuel production (ITFSBFP). From a systemic

perspective, ITFSBFP represents the set of interdependent stages of biomass collection, preparation, processing, control, and handling, encompassing both upstream agricultural machinery and downstream conditioning and densification equipment.

During operation, equipment within ITFSBFP is subjected to intense mechanical loads, abrasive wear, variations in biomass moisture and composition, and discontinuous operating regimes. These factors increase failure frequency, lead to unplanned downtime, and reduce overall system productivity[12, 13]. Consequently, equipment availability and maintainability become essential indicators of the operational performance of the technological flow [14, 15].

A review of the scientific literature [16–20], corroborated with the practical experience of agricultural machinery service enterprises [21–23] highlights the direct correlation between the level of technical availability and the quality of maintenance management. Nevertheless, the implementation of modern reliability analysis methods and preventive and predictive maintenance strategies remains limited, particularly in enterprises with restricted technical and financial resources.

Although the literature contains numerous studies focused on optimizing briquetting and pelletizing processes [24–27] research addressing the systemic evaluation of equipment availability and maintainability at the level of the integrated technological flow remains relatively scarce. There is insufficient integration of RAM (Reliability–Availability–Maintainability) concepts, MTBF and MTTR indicators, and modern maintenance management models adapted to the specific characteristics of agricultural biomass.

In enterprises operating integrated flows for the valorization of plant residues, complexity is further increased by resource seasonality, variations in storage conditions, and the technical skill level of personnel, factors that significantly influence equipment operational behavior [28, 29]. Therefore, the analysis of availability and maintainability should be conducted at the level of the integrated technological system rather than at the level of individual equipment.

In this context, the present review article aims to synthesize and critically analyze theoretical and applied contributions concerning the evaluation and improvement of availability and maintainability of equipment used within ITFSBFP, highlighting current trends, existing gaps, and optimization directions adapted to the specific characteristics of the agro-energy sector.

2. Methodology

This study was conducted as a systematic literature review in accordance with the PRISMA 2020 guidelines [30], ensuring transparency, reproducibility, and structured identification of research gaps regarding the availability and maintainability of equipment in ITFSBFP.

The overall review process is summarized in Table 1, which outlines the main methodological stages, corresponding activities, and key data extracted during the analysis.

The review was guided by the following research questions:

1. RQ1: What approaches are used to evaluate the availability and maintainability of biomass processing equipment?

2. RQ2: To what extent are RAM (Reliability–Availability–Maintainability) models applied in integrated solid biofuel production flows?

3. RQ3: Which maintenance strategies (corrective, preventive, predictive) are implemented in biomass densification systems?

Table 1

Systematic literature review process (PRISMA 2020)

Stage	Description	Examples / Data
Protocol	Definition of the review protocol in accordance with PRISMA 2020	Ensures transparency and reproducibility
Research questions	Formulation of key research questions (RQ1–RQ4)	Availability and maintainability assessment, RAM application, maintenance strategies, research gaps
Eligibility criteria	Definition of inclusion and exclusion criteria	Studies published between 2016–2026, English language, RAM indicators, reliability/maintainability focus; exclusions: economic-only studies, lack of explicit methodology, duplicates
Identification	Database search and citation tracking	Scopus, Web of Science, ScienceDirect, MDPI, IEEE Xplore; keywords combining biomass processing and reliability engineering
Screening	Title and abstract evaluation	Records screened: n = 341
Eligibility	Full-text assessment	Full-text articles assessed: n = 134
Inclusion	Selection of studies for final synthesis	Studies included: n = 98
Data extraction	Collection of relevant study variables	RAM indicators (MTBF, MTTR), equipment type, maintenance strategy, analysis level (equipment vs. integrated system)
Quality assessment	Evaluation of methodological rigor and bias risk	Research design clarity, quantitative indicators, RAM model reproducibility
Qualitative synthesis	Grouping and thematic analysis	Equipment reliability; maintenance strategies; RAM model application; system-level approaches
Identification of gaps	Determination of research limitations and missing evidence	Regional underrepresentation, heterogeneous indicators, limited RAM application at system level

4. RQ4: What are the research gaps regarding system-level evaluation at the integrated process flow?

Key aspects of the methodology:

- The literature search covered databases across engineering, energy, and industrial maintenance.
- Studies were limited to those reporting quantitative performance indicators (MTBF, MTTR, failure rates, downtime).
- Screening and full-text assessment were performed systematically according to PRISMA 2020.
- Data extraction included equipment type, system analyzed, maintenance strategies, and level of analysis.

- Due to heterogeneity of methods and indicators, a qualitative synthesis was performed rather than a meta-analysis.
- Research gaps were identified in regional representation, diversity of performance indicators, and the limited application of RAM models at the system level.

This structured approach ensures the review is transparent, reproducible, and directly linked to the research objectives of evaluating equipment performance in ITFSBFP.

3. Results and discussion

3.1. General characteristics of the included studies

Following the application of the PRISMA 2020 methodology, 98 relevant studies were included in the systematic synthesis. Most publications are concentrated in the period 2015–2026, highlighting an intensification of scientific interest in: optimization of biomass densification processes, maintenance digitalization, and the application of RAM models in complex systems.

The geographic distribution of the studies indicates a predominance of research conducted in Europe (Italy, Germany, Poland, Sweden, Romania), as well as in Ukraine, Russia, China, India, and Brazil. However, a limited representation of applied studies in the Republic of Moldova is observed, highlighting a deficit of regionally contextualized research.

The thematic analysis shows that the included studies address the following main directions: qualitative and quantitative characteristics of different types of plant biomass and the finished products obtained from this biomass; solid biofuel supply chains; partial lines for raw material conditioning and processing of plant biomass into pellets and briquettes; reliability of equipment used in crop production and, implicitly, in the production of plant biomass used as feedstock for solid biofuels; technological processes and equipment used for pellet and briquette production; machinery used for biomass size reduction (chippers, hammer mills, sawdust production equipment, and auxiliary machinery).

It is noteworthy that most analyses are conducted at the level of individual equipment rather than at the level of an integrated processing flow.

The synthesis of the 98 studies indicates that most research on reliability, availability, and maintainability (RAM) has been developed at the level of individual equipment or industrial subsystems, without explicitly addressing ITFSBFP. Furthermore, the included studies demonstrate the maturity of RAM concepts in established industries; however, their application to ITFSBFP remains insufficiently substantiated. The specific nature of ITFSBFP — characterized by high functional interdependence, feedstock variability, and accelerated wear of working components — necessitates the development of a RAM model adapted to the agro-energy sector.

3.2. Agricultural Biomass with Energy Potential

Agricultural biomass with energy potential comprises the totality of plant-based materials resulting from agricultural activities that can be utilized through direct or indirect energy conversion processes, particularly in the form of densified solid biofuels (DSB), such as briquettes and pellets [31].

In the context of the transition toward renewable energy sources and the strengthening of the circular economy, this category of resources is gaining strategic importance both at the European level [32–36], and in the Republic of Moldova, where agriculture plays an essential role in the national economic structure [6, 37, 38].

The scientific literature proposes multiple classification criteria (origin, composition, degree of processing, and energy destination) [39–41]. For the conditions of the Republic of Moldova, classification according to the mode of generation is particularly relevant [40, p.14]:

- primary agricultural biomass;
- secondary agricultural biomass;
- dedicated energy biomass.

Primary biomass includes plant material obtained directly from agricultural crops (cereals, industrial crops, forage crops); however, its use for energy purposes is limited by the need to avoid competition with food and feed uses [7]. By contrast, secondary agricultural biomass—represented by agricultural residues and by-products—constitutes the main resource for the production of densified solid biofuels, integrating efficiently into the circular economy paradigm [1, 24].

This classification is consistent with ISO 17225-1:2021, which groups solid biomass according to origin and source, facilitating the evaluation of fuel quality and compatibility with the technical requirements of densification processes [42]. Aligning conceptual delimitation with international standards is essential in a review-type article, as it enables comparability of results and their integration into recent European research frameworksAligning conceptual delimitation with international standards is essential in a review-type article, as it enables comparability of results and their integration into recent European research frameworks [43, 44].

From a conceptual perspective, agricultural biomass differs from forest or industrial biomass through the seasonality of production, the heterogeneity of physico-chemical properties, and dependence on agrotechnical practices [41]. These characteristics directly influence harvesting, mechanical preparation, and densification processes, as well as the technical performance of equipment involved in the integrated technological flow for the production of densified solid biofuels (ITF-DSBFP) [31, 39].

Under the conditions of the Republic of Moldova, plant biomass accessible for the production of densified solid biofuels includes three main categories.

Biomass derived from annual crops – wheat and barley straw, corn residues, sunflower residues, and rapeseed residues. Cereal straw exhibits net calorific values ranging between 12 and 15.5 $MJ \cdot kg^{-1}$ (at 10% moisture) [7]. Corn residues (stalks, leaves, cobs) can reach 4–6 $t \cdot ha^{-1}$, with a net calorific value of 14.8–16.3 $MJ \cdot kg^{-1}$, being favorable for densification due to their lignocellulosic structure [38]. Sunflower husks are distinguished by an energy value of approximately 14–16 $MJ \cdot kg^{-1}$, but with a higher ash content (3–5%), an aspect relevant for blend formulation and equipment wear [45, 46].

Lignocellulosic biomass derived from fruit trees and berry shrubs is considered one of the most accessible sources for the production of solid densified biofuels (SDB), due to its high energy density and favorable lignin content [47]. Typically, SDB are obtained from residues generated during crown training and maintenance pruning, annual fruiting cuts, removal of dry or diseased branches, clearing of aged specimens, or from waste resulting from nursery plant productioni [48–50].

Agricultural lignocellulosic biomass exhibits favorable energy characteristics due to its high lignocellulose content and significant calorific value [47, 49], which make it suitable for conversion into SDB such as pellets and briquettes [48], findings also confirmed by our previous research [37].

Biomass resulting from viticultural activities is found in the form of canes and residues generated from the annual pruning of grapevines. Although available in significant quantities, its potential remains largely underutilized [51]. Along with other agricultural residues, it contains lignin, hemicellulose, and cellulose [52, 53], which are essential components for the production of biofuels. International studies [54–58] as well as research conducted in the Republic of Moldova and Romania [8, 47, 59–62] confirm the feasibility of converting these resources into solid biofuels. However, numerous authors have shown that many agricultural residues, when used in their natural form, do not meet ENplus quality requirements [63].

Biomass obtained from dedicated energy crops (short-rotation coppice systems) is derived from non-food agricultural crops cultivated exclusively for the production of energy biomass. Relevant examples include *Miscanthus giganteus* [64]*, Salix* spp. [65], poplar (*Populus L.*) [66], and energy sorghum [67]. These crops are characterized by high biomass productivity, a predictable life cycle, and the possibility of standardized mechanized harvesting [68, 69].

Most agricultural biomass used for energy purposes consists of residues and by-products, which gives it a central role within the circular economy and in the sustainable valorization of organic remnants generated during the technological processes of primary agricultural production. In this context, increasing attention is being paid to the implementation of agroecological practices that contribute to reducing the carbon footprint and strengthening a sustainable rural economy [70].

In turn, strengthening a sustainable rural economy requires the recycling and reuse of residues, the reduction of resource waste, and the development of new value chains based on the valorization of agricultural waste and by-products [6, 71]. Within this framework, assessing the quantitative and qualitative potential of agricultural residues becomes an essential element for integrating plant biomass into renewable energy chains through its conversion into densified solid biofuels [72–74].

From this perspective, scientific interest lies not only in determining the physicochemical characteristics of agricultural biomass from the standpoint of final product quality, but also in analyzing their techno-economic implications [1]. In particular, it is necessary to investigate how biomass properties influence equipment wear rates, maintenance intervention frequency, the technical availability of ITFSBFP, the stability of process parameters, and, consequently, the consistency of final product quality [75, 76].

The analysis of the specialized literature on agricultural plant biomass with energy potential highlights that it represents not only an available renewable resource, but also an integrating element of the ITFSBFP, whose efficient valorization depends on the correlation between the physicochemical characteristics of the raw material, the technological infrastructure, and the maintenance strategies applied to the equipment involved in the ITFSBFP.

Consequently, deepening research on this technological link within the ITFSBFP is both timely and justified, and may be oriented in two major directions to improve system availability and maintainability:

1. Correlative evaluation of the quantitative and qualitative potential of agricultural residues according to origin and analysis of their impact on the availability and maintainability of equipment used throughout the ITFSBFP;

2. Optimization of the compatibility between biomass properties and the technological requirements of densification processes in order to reduce equipment wear and stabilize operational performance.

3.2. Particularities of the Integrated Technological Flow for the Production of Solid Biofuels from Agricultural Biomass

The integrated technological flow for producing densified solid biofuels (ITFSBFP) from agricultural biomass represents an integrated technical system composed of a sequence of interdependent processes, beginning with residue generation in the field and ending with delivery of the finished product to the consumer. Unlike conventional industrial lines, the ITFSBFP has an open, seasonal, and variable character, determined by biomass characteristics and agro-climatic conditions.

In the specialized literature, pellet and briquette production is predominantly analyzed at the level of the solid biofuel supply chain [24, 77–80]. However, in the case of agricultural biomass, an integrated flow approach is required, including the following main links: biomass formation and generation through agricultural processes (cultivation, maintenance, harvesting); collection and handling of residues (baling, preliminary chopping, internal transport); transport and storage of raw materials, significantly influenced by moisture content and seasonality; biomass preconditioning (size reduction, drying, impurity separation); densification through briquetting or pelletizing; as well as cooling, packaging, and storage of the finished product.

The integration of these stages into a unified system constitutes what, in this study, is defined as the ITFSBFP. Unlike the narrow technological flow limited to the industrial processing stage, the ITFSBFP includes both the core production operations and the stages of generation, collection, handling, preservation, pretreatment, conditioning, processing, quality control, and management of auxiliary flows. These stages are characterized by a defined sequence, specific technological regimes, and strong functional interdependencies between primary and auxiliary equipment, which confer a high sensitivity of the flow to failures or unplanned stoppages.

The stable and efficient operation of the ITFSBFP is directly conditioned by the level of availability and maintainability of its component equipment [81]. Given the high degree of functional interdependence among technological operations, the unavailability of a critical unit disrupts process continuity and may lead to production flow interruption, with negative effects on productivity, finished product quality, and delivery continuity within the supply chain [27].

Equipment availability reflects the ability of machinery to be operational when required by the technological process and is influenced by failure frequency, downtime duration, and the efficiency of maintenance activities [82, p. 171-175]. In the ITFSBFP, overall system availability is determined by the availability of each component unit, especially those located along the critical path of the flow, such as size-reduction, drying, and pressing equipment. In this context, availability must be analyzed as a property of a complex technical system [83], characterized by a high probability of failure during biomass production, conditioning, and processing stages, increased sensitivity to variations in raw material properties, the need for preventive and predictive maintenance, and the importance of real-time monitoring of technological parameters.

Equipment maintainability expresses the ability of machinery to be serviced and restored to operational condition within a minimal time interval through corrective or preventive interventions performed under given technical and organizational conditions [82, p. 107-112]. Within integrated technological flows, characterized by intense mechanical stresses and variable operating regimes, maintainability is influenced by the equipment's

design solutions, the accessibility of wear-prone components, the degree of spare parts standardization, and the qualification level of maintenance personnel. This situation necessitates decision-making regarding the adaptability and configuration of the equipment group used throughout the ITFSBFP[84].

The interdependence between availability and maintainability is particularly relevant in the ITFSBFP, since low maintainability leads to prolonged downtime and, implicitly, reduced equipment availability. In this context, optimizing maintenance activities contributes not only to increasing the effective operating time of equipment but also to stabilizing the technological process and improving the overall performance of the flow.

Specialized literature confirms the maturity of RAM models in established industries; however, their application in the agro-energy sector remains insufficiently developed. Therefore, the development of a RAM model adapted to the specific characteristics of agricultural biomass and the structure of the integrated technological flow is justified.

In conclusion, the ITFSBFP based on agricultural biomass represents an integrated system characterized by high raw material variability, strong functional interdependence, and severe mechanical stress regimes. These particularities require a systemic approach to availability and maintainability, grounded in correlating biomass properties with the technical performance of the equipment involved in the process.

3.3. Specific Features of the Availability and Maintainability of Equipment in ITFSBFP: Case Study of Working Components

The scientific literature indicates that, within ITFSBFP, the working components of equipment represent the elements most exposed to mechanical, abrasive, and dynamic stresses, constituting the critical link in determining the actual availability of the system [15, 85]. Although RAM analysis is frequently performed at the equipment level, recent studies emphasize that the overall performance of technological flows is predominantly determined by the in-service behavior of active components—knives, hammers, screens, rollers, dies, and screw conveyors, etc.[86].

Research on agricultural biomass processing shows that variability in moisture content, the presence of mineral particles, and dimensional heterogeneity generate severe wear and failure regimes, directly influencing maintenance frequency and downtime duration [87]. In this context, the literature recommends correlating availability analysis with MTBF and MTTR indicators, which reflect the real operational behavior of working components and vary significantly depending on the stage of the technological flow [88].

During the biomass generation and collection stage, studies indicate that the active elements of agricultural machinery — knives, discs, tines, and pickup systems — are subjected to combined shock, abrasion, and mechanical fatigue stresses [13]. The presence of mineral impurities, chemical elements, and hard particles accelerates wear, promotes corrosion processes, and contributes to the formation of microcracks, thereby reducing component service lif [89, 90]. The availability of these machines is influenced by the wear level of active components, the frequency of adjustments, and pedoclimatic conditions, while maintainability depends on constructive accessibility and assembly modularity [91]. Operational experience shows that intervention times are often prolonged due to the lack of standardized spare parts and the seasonal nature of operation, which leads to defect accumulation during peak periods [92]. Although failures at this stage have an indirect impact

on the industrial flow, instability in raw material supply may affect the continuity of subsequent stages.

As biomass enters the industrial processing stage, mechanical preparation becomes the first link positioned on the critical path of ITFSBFP. Studies on biomass shredding and grinding show that working components — knives, hammers, counter-knives, screens, and rotor shafts — operate at high rotational speeds and are subjected to intense abrasive wear [93]. The literature identifies the main degradation mechanisms as edge dulling, fatigue cracking, rotor imbalance, and system blockage caused by variations in biomass granulometry or moisture [94, 95]. At this stage, MTBF is relatively low compared to other links, and unplanned stoppages directly affect the entire system. Studies emphasize that maintainability depends on the speed of component replacement, the possibility of dynamic balancing, and the existence of standardized adjustment procedures, which justify the implementation of condition monitoring and predictive maintenance.

The analysis of the technological flow logically leads to the final densification stage, which completes the transformation of biomass into a standardized product in terms of dimensions and energy content. In industrial practice, this stage may be performed either through briquetting or pelletizing, the choice of technology being determined by production specifics, market requirements, available raw materials, and the enterprise's level of automation. Consequently, availability and maintainability assessment must be adapted to the characteristics of the equipment used in the final densification stage.

The literature highlights that, regardless of the adopted technology, the densification stage occupies a critical position within the predominantly series configuration of ITFSBFP, since any functional disturbance is directly transmitted to the entire system. In briquetting presses, screws or pistons and forming dies are subjected to abrasive and plastic wear generated by high pressures and friction temperatures, while availability is strongly influenced by the stability of biomass properties [96]. In pellet presses, press rollers and perforated dies operate under intense mechanical loads and are highly sensitive to variations in raw material granulometry and moisture, highlighting the functional interdependence between mechanical preparation and final densification.

Studies indicate that the main causes of reduced availability in the densification stage include wear of working components, blockage of compression or extrusion channels, process parameter instability, and bearing overload, while MTBF is directly influenced by the quality of prior mechanical preparation. Thus, regardless of the technological solution adopted, the final densification stage represents a critical point in the flow, exerting a major influence on production continuity and the overall performance of ITFSBFP.

Overall, the literature converges on the conclusion that the global availability of ITFSBFP is determined by the functional interdependence of technological links and by the operational behavior of working components, which concentrate the primary degradation mechanisms and generate significant variations in MTBF and MTTR indicators. The analysis of technological stages reveals structural differences in stress levels, failure frequency, intervention complexity, and the impact of stoppages on process continuity.

Under these conditions, in order to comparatively highlight the influence of each equipment group on global availability and to facilitate a systemic interpretation of operational performance, it is necessary to synthesize RAM indicators in a structured form. Such an approach enables the correlation of reliability and maintainability parameters with

functional positioning within the technological flow and provides the basis for identifying critical links.

For this purpose, the following section presents a comparative synthetic scheme of RAM indicators for the four main equipment groups within ITFSBFP, highlighting critical working components, estimated MTBF and MTTR levels, their impact on global availability, and specific maintainability characteristics.

3.4. Comparative synthetic scheme of RAM indicators for the four groups of equipment

The RAM analysis has been applied in various fields to support maintenance decision-making, while the reliability and maintainability of components are used to evaluate the availability of technical systems [93]. n the case of integrated technological flows for the production of solid biofuels from agricultural biomass, comparative quantitative information regarding RAM indicators remains limited, and existing studies predominantly provide analyses at the level of individual equipment or qualitative descriptions of operational behavior. This gap complicates the systemic evaluation of the operational performance of integrated flows.

However, available research highlights significant differences in failure behavior and maintenance requirements between technological stages, emphasizing the influence of mechanical stresses, operating conditions, and the complexity of interventions on system functioning. Complementarily, practical experience accumulated in the operation and maintenance of these flows in enterprises confirms substantial variations in failure frequency and maintenance requirements among technological stages, highlighting the need for a systemic approach to availability.

The differentiated study of the four equipment groups within the ITFSBFP highlights distinct particularities regarding MTBF, MTTR, and their impact on overall availability. To facilitate a systemic and comparative interpretation of these characteristics, it is necessary to synthesize the available information in a structured form that allows the functional and positional differences within the technological flow to be clearly identified [97].

Since the ITFSBFP configuration is predominantly of a series type, the influence of each link on overall performance is not uniform. Therefore, a comparative analysis of RAM indicators must consider not only technical parameters (MTBF and MTTR), but also positioning along the critical path and the maintainability specifics of each equipment category [98]. For this purpose, Table 2 presents a comparative synthetic scheme of the main RAM indicators for the four analyzed equipment groups, highlighting critical working elements, estimated MTBF and MTTR levels, their impact on overall availability, and maintainability particularities, based on trends documented in the scientific literature and practical experience in the operation and maintenance of equipment used in ITFSBFP.

The comparative analysis of the data synthesized in the table highlights significant functional differences among the equipment groups within the ITFSBFP, determined by the level of mechanical stress, their position in the technological flow, and the complexity of maintenance interventions. Equipment used for agricultural operations and biomass handling exhibits a medium MTBF with seasonal variations, while the low–medium MTTR reflects the simplicity of interventions and the accessibility of components. Their impact on overall availability is indirect, since failures affect raw material supply without immediately causing the shutdown of the industrial flow.

Table 2

Comparative synthetic scheme of RAM indicators for the main equipment groups within ITFSBFP

Equipment Group	Critical Working Components	Estimated MTBF	Estimated MTTR	Impact on Overall System Availability	Maintainability Characteristics
Equipment for agricultural operations and biomass handling	knives, discs, tines, pickup mechanisms	medium (seasonally variable)	low–medium	indirect (affects feedstock supply to the process flow)	frequent but relatively simple interventions; strong dependence on pedoclimatic conditions
Mechanical pre-processing equipment (chipping, shredding)	hammers, screens, rotors, shafts	low–medium	medium	major (positioned on the critical process path)	requires precise adjustments, dynamic balancing, and systematic wear monitoring
Briquetting equipment	screw/piston assembly, compression chamber, dies	medium	high	direct impact on production continuity	complex disassembly procedures; intensive wear in the compression zone
Pelletizing equipment	press rollers, perforated dies	medium	high	critical (can completely stop the production flow)	fine adjustments required; high sensitivity to biomass properties; high replacement cost of components

In contrast, mechanical pre-processing equipment operates under intensive loading regimes and is positioned on the critical path, which explains the low–medium MTBF and medium MTTR. Although interventions are not as complex as in the densification stages, the need for precise adjustments, dynamic balancing, and wear monitoring gives this equipment group a major impact on process continuity.

The densification stages introduce more severe operating conditions, characterized by high pressures and intense friction. Briquetting equipment exhibits a medium MTBF but a high MTTR, determined by the complexity of disassembly, pronounced wear of compression elements, and the need for technological adjustments after intervention. Their impact on availability is direct, as equipment stoppage interrupts production.

Pelletizing equipment, although having an MTBF similar to briquetting machines, is distinguished by high sensitivity to variations in biomass properties and strict adjustment requirements, which maintain MTTR at a high level. Due to their final role in the technological flow, their failure can lead to a complete production shutdown, giving them a critical impact on overall availability.

The high mean time to repair (MTTR) for briquetting and pelletizing equipment is determined by their critical role in the technological flow and the complexity of the required

interventions. Failure of these units leads directly to production stoppage, as there are no technological bypass options for the densification stage; therefore, the intervention duration inevitably includes process downtime. Maintenance operations involve complex disassembly of compression elements, replacement of components subjected to intense wear, realignment, and functional adjustments after reassembly. In addition, high mechanical and thermal stresses, intense friction, and variability in biomass properties accelerate component degradation, increasing both the frequency and difficulty of interventions. After completion of the work, restoring stable operating conditions requires adjustment of technological parameters and verification of product quality, which prolongs the total time required to return to normal production capacity. Overall, these factors justify classifying MTTR for briquetting and pelletizing stages as high.

Overall, the comparative analysis reveals a progressive increase in technological criticality from the agricultural stage to the densification stages, accompanied by increasing maintenance complexity and intervention duration. These differences justify a differentiated approach to maintenance strategies and support the need to correlate RAM indicators with functional criticality when evaluating the operational performance of the ITFSBFP.

These differences in MTBF and MTTR levels, as well as the distinct impact of each link on process continuity, highlight that the operational performance of the technological flow is determined by the cumulative availability of its component stages. Since the ITFSBFP operates predominantly in a series configuration, the overall system availability can be expressed by the following relationship:

$$A_{\mathrm{ITFSBFP}} = \prod_{i=1}^{n} A_i \tag{1}$$

where $A_i$represents the availability of each technological link.

Relation (1) highlights that a reduction in availability at a single stage—typically the pelletizing/briquetting stage—produces a multiplicative decrease in the overall availability. Thus, the results synthesized in Table 2 constitute the foundation for the mathematical modeling of overall performance and for identifying the system's limiting link.

To apply relation (1), it is necessary to determine the individual availability of each equipment group. From the perspective of reliability theory, technical availability depends directly on the mean time between failures (MTBF) and the mean time to repair (MTTR). Therefore, technical availability is determined by the relation:

$$A = \frac{MTBF}{MTBF+MTTR} \tag{2}$$

Relation (2) highlights the mechanism through which variations in MTBF and MTTR influence availability. A decrease in MTBF or an increase in MTTR leads to a reduction in the value of A, and in a series system the effect propagates multiplicatively to the overall availability.

Determining technical availability provides a quantitative assessment of the performance of each technological link; however, the real impact on system operation depends not only on the level of availability but also on the functional importance of the equipment within the technological flow. In systems organized predominantly in a series configuration, the shutdown of certain equipment may have disproportionate effects on process continuity. Therefore, correlating availability with functional criticality enables the identification of links with major impact on operational performance.

For this purpose, the main equipment groups are positioned in a criticality–availability matrix, presented in Table 3, which synthesizes trends highlighted in the specialized literature and practical experience regarding the impact of downtime on process continuity.

The distribution of equipment groups within the criticality–availability matrix highlights clear differences in the operational impact of downtime. Equipment used for agricultural operations and biomass handling falls within the operational control zone, as failures affect the supply of the process flow without causing immediate stoppages. Mechanical preparation equipment is positioned in the technological critical zone, playing a decisive role in process continuity due to its location on the critical path and the intense mechanical stresses involved.

Table 3

Criticality–availability matrix for main equipment groups

Equipment group	Estimated availability	Functional criticality level	Matrix zone	Operational impact	Recommended maintenance priority
Equipment for agricultural operations and biomass handling	medium	medium	operational control zone	influences supply	seasonal preventive maintenance
Equipment for mechanical preparation	medium–low	high	technological critical zone	may interrupt the process flow	predictive monitoring and wear control
Briquetting equipment	medium	critical	strategic critical zone	interrupts production	optimization of interventions and wear-parts management
Pelletizing equipment	medium–low	critical	strategic critical zone	may completely stop the process	advanced predictive maintenance and continuous monitoring

The distribution of equipment groups within the criticality–availability matrix highlights clear differences in the operational impact of downtime. Equipment used for agricultural operations and biomass handling falls within the operational control zone, as failures affect the supply of the process flow without causing immediate stoppages. Mechanical preparation equipment is positioned in the technological critical zone, playing a decisive role in process continuity due to its location on the critical path and the intense mechanical stresses involved.

The densification stages exhibit the highest systemic impact. Both briquetting and pelletizing equipment are classified in the strategic critical zone because they function as final stages of the densification process, and the stoppage of either leads to production interruption. While pelletizing can cause total flow shutdowns due to its high sensitivity to biomass property variations and strict adjustment requirements, briquetting involves complex interventions and long repair times, resulting in an equivalent operational impact.

Overall, the matrix reveals a progressive increase in technological criticality from the agricultural stage to the densification stages, confirming the need to prioritize maintenance strategies according to the systemic impact of each link and highlighting the critical role of the final stages in ensuring the operational continuity of the ITFSBFP

From a mathematical standpoint, the overall availability of the system can be expressed by the generalized relation:

$$A_{global} = \prod_{i=1}^{n} A_i \tag{3}$$

where $A_i$represents the availability of each technological link.

Considering that the densification stages fall within the strategic critical zone, and their stoppage leads to production interruption, the evaluation of operational performance cannot be carried out solely based on availability. For this reason, in order to quantify the risk associated with stoppages and to highlight the systemic impact of critical links, availability must be analyzed through its complement, the technical unavailability, defined as:

$$U_i = 1 - A_i \tag{4}$$

where $U_i$represents the unavailability of the technological link and $A_i$its availability. This relationship highlights the proportion of time during which the equipment cannot fulfill its operational function and allows the direct evaluation of the risk of process interruption.

However, technical unavailability does not sufficiently reflect the different functional impact of system links on overall performance. To integrate the systemic impact of downtime, the functional criticality coefficient $C_i$is introduced, which weights unavailability according to the role of each stage, defined by the following relation:

$$C_i \in \{0{,}25;\ 0{,}50;\ 0{,}75;\ 1{,}0\} \tag{5}$$

where the values correspond to the following criticality levels: low (0.25), medium (0.50), high (0.75), and critical (1.00).

The introduction of coefficient C enables the transition from a strictly technical assessment of unavailability to an integrated techno-functional analysis, laying the groundwork for the formulation of the synthetic technological vulnerability indicator, in which unavailability is weighted according to the systemic importance of each link.

To quantify in a unified manner the contribution of technical unavailability (relation 4) and the functional criticality coefficient (relation 5) to the overall vulnerability of the ITFSBFP, these two components must be integrated into a synthetic indicator.

Furthermore, within a predominantly series flow, the influence of a link on system performance is also determined by its degree of structural interdependence. Links positioned on the critical path, without technological redundancy, exert a stronger impact on overall performance than partially redundant ones. To reflect this structural dimension, the **systemic interdependence coefficient** $K$is introduced.

By correlating unavailability U_i , functional criticality C_i , and the systemic interdependence coefficient K_i, the technological vulnerability indicator for each link is obtained:

$$IVT_i = U_i \cdot C_i \cdot K_i \tag{6}$$

The aggregation of individual contributions leads to the global vulnerability indicator:

$$IVT_{global} = \sum_{i=1}^{n} IV\,T_i \quad (7)$$

A higher IVT level indicates greater exposure to technological risk and the need to prioritize interventions.

To illustrate the methodological applicability of the proposed model, a conceptual application of the technological vulnerability indicator (IVT) is presented for the main equipment groups within the ITFSBFP. Since the present study has a synthesis character, the included values are indicative and aim to highlight the integration of technical unavailability, functional criticality, and systemic interdependence in technological risk assessment. The proposed tabular structure may serve as a standardized framework for presenting and interpreting results obtained in future experimental research.

Table 4 summarizes the estimated values of availability (A), unavailability (U), criticality (C), interdependence coefficient (K), and the resulting indicator IVT_i, facilitating the identification of the link with the dominant impact on overall performance.

Table 4 does not present experimental results; rather, it provides an example of operationalizing the proposed model for assessing technological vulnerability. The structure of the indicator enables the quantification of each subsystem's contribution to the overall risk of unavailability and facilitates the identification of the system's critical links. By integrating RAM parameters with functional criticality and systemic interdependence, the model offers an analytical tool for prioritizing maintenance interventions and optimizing operational performance.

Table 4

Conceptual model for assessing the technological vulnerability of equipment groups within the ITFSBFP

Equipment Group	A	U	C	K	IVT	Contribution to Global Risk
Equipment for agricultural operations and biomass handling	A_1	U_1	C_1	K_1	IVT_1	low
Equipment for mechanical preparation	A_2	U_2	C_2	K_2	IVT_2	significant
Briquetting equipment	A_3	U_3	C_3	K_3	IVT_3	major
Pelletizing equipment	A_4	U_4	C_4	K_4	IVT_4	dominant

In future research, completing the table with experimentally determined values will enable the comparative evaluation of technological systems, validation of the proposed model, and support decision-making aimed at increasing availability and reducing technological vulnerability.

4. Conclusions

The review highlights that the operational performance of the ITFSBFP has a pronounced systemic character, being determined by the functional interdependence of technological links, feedstock variability, and the operational behavior of equipment working components.

The valorization of agricultural residual biomass has strategic relevance for energy security and the circular economy, while the performance of technological infrastructure and equipment significantly influences the efficiency of agro-energy chains. In this context, equipment availability and maintainability represent essential indicators of process stability and production continuity.

The application of the PRISMA methodology enabled the identification of relevant studies and revealed important gaps, including the predominance of equipment-level analyses, the heterogeneity of performance indicators, and the limited application of RAM models at the level of integrated technological flows. These findings support the need for a systemic approach adapted to agro-energy systems.

The synthesis of the analyzed studies indicates an increasing scientific interest in densification process optimization and maintenance digitalization, alongside a deficit of regionally contextualized research. The ITFSBFP is characterized by high functional interdependence, biomass variability, and severe wear regimes, which require the development of RAM models adapted to these specific operating conditions.

Agricultural biomass acts as an integrating element of the technological flow, while its physicochemical properties influence equipment wear, maintenance frequency, and process stability. Correlating biomass characteristics with equipment performance is essential for improving availability and reducing degradation of working components.

The ITFSBFP operates as an open, seasonal, and variable technical system whose operational stability depends directly on the availability and maintainability of equipment located along the critical path, particularly within the mechanical preparation and densification stages.

Working components represent the critical elements determining actual system availability, being subjected to severe mechanical, abrasive, and dynamic stresses. Variations in biomass moisture, the presence of mineral impurities, and dimensional heterogeneity accelerate wear and directly influence MTBF and MTTR values.

The comparative RAM analysis of the main equipment groups reveals significant functional differences among technological stages and confirms that global availability is structurally determined by links positioned on the critical path within a predominantly series configuration. The densification stage, particularly pelletizing, exhibits the highest systemic impact due to intervention complexity, sensitivity to biomass properties, and extended repair duration.

The integration of RAM indicators with functional criticality and systemic interdependence led to the development of the IVT, representing the main contribution of this study. By integrating RAM indicators with functional criticality and systemic interdependence, the IVT enables the quantification of the global risk of unavailability and the prioritization of maintenance interventions, while also highlighting the decisive influence of biomass properties and working component behavior on MTBF, MTTR, and overall availability.

From a practical perspective, the proposed methodological framework can support agricultural machinery service enterprises in optimizing maintenance strategies, reducing unplanned downtime, improving spare parts management, and supporting technological modernization decisions. Integration of this framework into predictive maintenance and condition monitoring strategies can enhance operational resilience and competitiveness in agro-energy systems.

Overall, the study provides an integrated conceptual and methodological framework for evaluating and optimizing the performance of solid biofuel production systems and demonstrates the necessity of applying differentiated maintenance strategies based on functional criticality and technological vulnerability.

Looking ahead, future research should focus on the experimental validation of the IVT using operational data from real technological flows and on the development of dynamic RAM models integrated with predictive monitoring and condition-based maintenance. Further investigations are also needed to deepen the understanding of the relationships between biomass properties and wear mechanisms of working components, optimize feedstock–equipment compatibility to stabilize processes and reduce component degradation, and evaluate hybrid technological configurations and functional redundancy solutions to increase system resilience. Expanding research at the regional level will contribute to the development of models adapted to the specific agro-energy conditions of the Republic of Moldova.

Acknowledgments: This research was supported by the program Complex Bilaterial Projects with the Republic of Moldova (PCB-RO-MD-202), project no. PN-IV-PCB-RO-MD-2024-0336, within PNCDI IV. Additional support was provided by project no. 20.80009.5107.15, "Development and implementation of best practices for sustainable agriculture and climate resilience (GREEN/020407)", which ensured technical and logistical assistance for the qualitative and quantitative characterization of agricultural plant biomass.

The author gratefully acknowledges the Research Management Directorate and the Doctoral School of the Technical University of Moldova for logistical support. Special thanks are extended to the Research Center Mechanical Engineering and Materials (TUIASI), SC BASADORO AGROTEH SRL, and Agrisolution SRL for their valuable support in collecting data on the availability and maintainability of equipment used in the integrated solid biofuel production flow.

Conflicts of Interest: The author declares that there are no conflicts of interest regarding the publication of this article. The research was conducted in the absence of any commercial or financial relationships that could be construed as potential conflicts of interest. All data presented in this study are original and were generated by the author within the reported research. The author confirms that the manuscript has not been previously published and is not under consideration for publication elsewhere.

References

1. Mignogna, D., Szabó, M., Ceci, P., & Avino, P. (2024). Biomass Energy and Biofuels: Perspective, Potentials, and Challenges in the Energy Transition. *Sustainability (Switzerland)*, *16*(16), 1–33. https://doi.org/10.3390/su16167036
2. ETIP. (2025). POSITION PAPER ON SUSTAINABLE Biomass in the Energy System. Retrieved from https://www.etipbioenergy.eu/wp-content/uploads/2025/09/Position-Paper-on-Sustainable-Biomass-Supply-2.pdf
3. Popp, J., Kovács, S., Oláh, J., Divéki, Z., & Balázs, E. (2021). Bioeconomy: Biomass and biomass-based energy supply and demand. *New Biotechnology*, *60*, 76–84. https://doi.org/10.1016/j.nbt.2020.10.004
4. UNDP. (2024). Potențialul de biomasă în Republica Moldova, 15.
5. Marian, G., Alexiou Ivanova, T., Gudîma, A., Nazar, B., Daraduda, N., Malai, L., … Marian, T. (2025). Ensuring the Quality of Solid Biofuels from Orchard Biomass Through Supply Chain Optimization: A Case Study on Peach Biomass Briquettes. *Agriculture (Switzerland)*, *15*(24), 1–28. https://doi.org/10.3390/agriculture15242615
6. Ganea, V., Trushkina, N., Ţîrlea, M. R., & Birca, I. (2022). Circular economy – a perspective model for the Republic of Moldova. *Univers statistic*, *4(52)*, 52–68. Retrieved from https://ibn.idsi.md/sites/default/files/imag_file/p-52-68.pdf
7. Gudîma, A. (2017). Assessment of agricultural residue utilization for energy purposes: a case study for soroca district, Republic of Moldova. *Meridian Ingineresc*, *1*, 26-29 [in Romanian]. Retrieved from https://repository.utm.md/bitstream/handle/5014/291/MI_2017_1_pg_26_29.pdf?sequence=1&isAllowed=y

8. Marian, G., Ivanova, T. A., Gudîma, A., Nazar, B., Malai, L., Marian, T., & Pavlenco, A. (2024). Biomass Resources from Vineyard Residues for the Production of Densified Solid Biofuels in the Republic of Moldova. *Agronomy*, 1–13. https://doi.org/. https://doi.org/10.3390/agronomy14102183
9. Marian, G., Ianuş, G., Istrate, B., Gudima, A., Nazar, B., Pavlenco, A., … Daraduda, N. (2022). A Qualitative Assessment of the Specific Woody Biomass of Fruit Trees. *Forests*, *13*(3), 405. https://doi.org/10.3390/f13030405
10. Marian, G., & Banari, A. (2025). Comparative evaluation of energy potential and composition of walnut, hazelnut, and almond residues for solid biofuel production. *Journal of Engineering Science*. https://doi.org/https://doi.org/10.52326/jes.utm.2025.32(1).09
11. Marian, G., Ianuș, G., Istrate, B., Banari, A., Nazar, B., Munteanu, C., Paleu, V. (2022). Evaluation of agricultural residues as organic green energy source based on seabuckthorn, blackberry, and straw blends. *Agronomy*, *12*(9), 2018. https://doi.org/10.3390/agronomy12092018
12. Czekała, W., Bartnikowska, S., Lewicka, A., Bugała, A., Zbytek, Z., & Lewicki, A. (2016). Economic and energy efficiency of the solid biofuels produced from digested pulp. *MATEC Web of Conferences*, *60*, 1–5. https://doi.org/10.1051/matecconf/20166004005
13. Munteanu, C., Melnic, I., Istrate, B., Hardiman, M., Gaiginschi, L., Lupu, F. C., … Badiul, V. (2025). A Comprehensive Review of Improving the Durability Properties of Agricultural Harrow Discs by Atmospheric Plasma Spraying (APS). *Coatings*, *15*(6), 1–31. https://doi.org/10.3390/coatings15060632
14. Sustainable Shipping Initiative. (2022). *Availability of sustainable biofuels*. Retrieved from ttps://www.sustainableshipping.org/wp-content/uploads/2022/01/Availability-of-Sustainable-Biofuels-Report-updated-final.pdf
15. Munteanu, C., Lupu, F. C., Istrate, B., Ianus, G., Marian, G., Boris, N., … Arsenoaia, V. N. (2026). Use of Thermal Coatings to Improve the Durability of Working Tools in Agricultural Tillage Machinery: A Review. *Applied Sciences (Switzerland)*, *16*(1), 1–35. https://doi.org/10.3390/app16010474
16. Мяло О.В., Лучинович А.А., Б. С. Р. (2017). Оценка требований к дилерским центрам по обслуживанию сельскохозяйственной техники на территории Западной Сибири //. *Электронный научно-методический журнал Омского ГАУ*, *1*(8), 1–6.
17. Khodabakhshian, R. (2013). A review of maintenance management of tractors and agricultural machinery: Preventive maintenance systems. *Agricultural Engineering International: CIGR Journal*, *15*(4), 147–159.
18. Mihov, M. (2019). RESEARCH ON CHARACTERISTICS OF FAILURES FLOW ACCORDING TO THE MAINTENANCE AND REPAIR STRATEGY.
19. Florea, V. A., Ionică, A. C., Florea, A., Itu, R. B., & Popescu-Stelea, M. (2022). Study of the Possibilities of Improving Maintenance of Technological Equipment Subject to Wear. *Processes*, *10*(12), 1–19. https://doi.org/10.3390/pr10122550
20. Pourdarbani, R. (2019). Choosing a Proper Maintenance and Repair Strategy for Tractors (in Urmia). *Acta Technologica Agriculturae*, *22*(1), 12–16. https://doi.org/10.2478/ata-2019-0003
21. Igamberdiyev, A. K., Kholikova, N., Khakimov, B., Usmanov, E., Usmanova, G., & Sh Begaliyev, A. (2022). Efficient use of agricultural machinery park and improvement of technical services system. *IOP Conference Series: Earth and Environmental Science*, *996*(1). https://doi.org/10.1088/1755-1315/996/1/012015
22. Nuraddin, Y. S. (2021). Peculiarities of Production and Technical Production and Technical Exploitation of the Use of Technology in the Agrotechservice Enterprise. *Herald of Khmelnytskyi National University*, *296*(4), 88–94. https://doi.org/10.31891/2307-5740-2021-296-4-14
23. Mahmudov, M. (2020). Peculiarities of Production and Technical Production and Technical Exploitation of the Use of Technology in the Agrotechservice Enterprise. *American Journal of Biomedical Science & Research*, *9*(2), 107–112. https://doi.org/10.34297/ajbsr.2020.09.001364
24. Roman, K., & Grzegorzewska, E. (2024). Biomass Briquetting Technology for Sustainable Energy Solutions: Innovations in Forest Biomass Utilization. *Energies*, *17*(24). https://doi.org/10.3390/en17246392
25. Sanchez-Roque, Y., Orantes-Flores, H. J., López-De-Paz, P., Pérez-Luna, Y. C., Canseco-Pérez, M. A., & Zenteno-Carballo, A. G. (2025). Biomass briquettes: Raw material, technologies and densification parameters, quality and future challenges. *Scientia Agropecuaria*, *16*(2), 293–306. https://doi.org/10.17268/sci.agropecu.2025.024
26. Mudryk, K.; Fr ˛aczek, J.; Leszczy´nska, J.; Krotowski, M. (2025). Technology for the Production of Energy Briquettes from Bean Stalks. *Energies*, *18*(3), 299–305. https://doi.org/https:// doi.org/10.3390/en18154009
27. Augustino A. Masse, Kunda S. Sikazwe, K. N. L. and R., A, E. N. are research officers at T. D. H. S. is, & REPOA, S. R. at. (2023). *Biomass Briquettes Production Handbook*. *International Ayurvedic Medical Journal* (Vol. 11).

https://doi.org/10.46607/iamj11072023
28. Wei, W., Xiao, M., Duan, W., Wang, H., Zhu, Y., Zhai, C., & Geng, G. (2024). Research Progress on Autonomous Operation Technology for Agricultural Equipment in Large Fields. *Agriculture (Switzerland)*, *14*(9). https://doi.org/10.3390/agriculture14091473
29. Mironov, D. A., Sidorov, S. A., & Liskin, I. V. (2019). Strength and Durability Characteristics of Soil-Cutting Working Tools. *Agricultural Machinery and Technologies*, *13*(3), 39–43. https://doi.org/10.22314/2073-7599-2019-13-3-39-43
30. Page, M. J., McKenzie, J. E., Bossuyt, P. M., Boutron, I., Hoffmann, T. C., Mulrow, C. D., … Moher, D. (2021). The PRISMA 2020 statement: An updated guideline for reporting systematic reviews. *Bmj*, *372*. https://doi.org/10.1136/bmj.n71
31. Velliangiri, A. (2025). Bioenergy from Agricultural Waste : Optimizing Biomass Supply Chains for Rural Electrification, *1*(1), 18–26.
32. Taušová, M., Mykhei, M., Čulkova, K., Tauš, P., Petráš, D., & Kaňuch, P. (2025). Development of the Implementation of Renewable Sources in EU Countries in Heating and Cooling, Transport, and Electricity. *Sustainability (Switzerland)*, *17*(2). https://doi.org/10.3390/su17020766
33. Wieruszewski, M., & Mydlarz, K. (2022). The Potential of the Bioenergy Market in the European Union—An Overview of Energy Biomass Resources. *Energies*, *15*(24). https://doi.org/10.3390/en15249601
34. Ungureanu, N., & Rusănescu, C. O. (2025). Biomass and Bioenergy. *Energies*, *18*(9). https://doi.org/10.3390/en18092233
35. Janiszewska, D., & Ossowska, L. (2022). The Role of Agricultural Biomass as a Renewable Energy Source in European Union Countries. *Energies*, *15(18)*. https://doi.org/https://doi.org/10.3390/en15186756
36. Bąk, I., Wawrzyniak, K., Barej-Kaczmarek, E., & Oesterreich, M. (2025). Renewable Energy for Sustainable Development in EU Countries: Status, Prospects, and Challenges. *Energies*, *18*(6). https://doi.org/10.3390/en18061333
37. Marian, G., Banari, A. ., & Marian, T. . (2025). Sustainable utilization of agricultural residues from fruit shrubs: energy potential and physical- chemical properties. *INT J CONSERV SCI*, *16*(3), 1611–1624.
38. Pavlenco, A., Marian, G., & Gudîma, A. (2018). Gud. *Ştiinţa Agricolă*, *2*(2), 141-148 [in Romanian]. https://doi.org/http://repository.utm.md/handle/5014/23382
39. Patel, N., Feofilovs, M., & Blumberga, D. (2022). Evaluation of bioresource value models: Sustainable development in the agriculture biorefinery sector. *Journal of Agriculture and Food Research*, *10*(August), 100367. https://doi.org/10.1016/j.jafr.2022.100367
40. Marian, G. (2016). *Biocombustibilii solizi: producere şi proprietăţi*. *Proiectul Energie și Biomasă în Republica Moldova* (Bons Ofice.). Chişinău. Retrieved from https://www.undp.org/sites/g/files/zskgke326/files/2024-07/biocombustibili_solizi.pdf
41. Alakangas, E. (2016). Biomass and agricultural residues for energy generation. In *Fuel Flexible Energy Generation: Solid, Liquid and Gaseous Fuels* (pp. 59–96). Boston: 2016 (Woodhead Publishing). https://doi.org/10.1016/B978-1-78242-378-2.00003-1
42. Kofman, P. D. (2021). Review of worldwide standards for solid biofuels, revised April 2021. *Processing/Products*, (53), 1–12. Retrieved from www.woodenergy.
43. Toscano, G. ., De Francesco, C. ., Gasperini, T. ., Fabrizi, S. ., Duca, D. ., & Ilari, A. (2023). Quality Assessment and Classification of Feedstock for Bioenergy Applications Considering ISO 17225 Standard on Solid Biofuels. *Resources*, *12*. https://doi.org/https://doi.org/10.3390/resources12060069
44. Mancini, M., Toscano, G., Feliciangeli, G., Leoni, E., & Duca, D. (2020). Investigation on woodchip quality with respect to ISO standards and relationship among quality parameters. *Fuel*, *279*(July), 118559. https://doi.org/10.1016/j.fuel.2020.118559
45. Drăgușanu, V., Lunguleasa, A., & Spîrchez, C. (2021). The briquettes properties from seed sunflower husk and wood larch shavings. *Wood Research*, *66*(4), 689–699. https://doi.org/10.37763/WR.1336-4561/66.4.689699
46. Marian, G., Gelu, I., Gudîma, A., Nazar, B., Istrate, B., Banari, A., … Daraduda, N. (2022). Calorific Value of Pellets Produced From Raw Material Collected From Both Sides of the River Prut. *Journal of Engineering Science*, *29*(4), 126–137. https://doi.org/10.52326/jes.utm.2022.29(4).10
47. Ciolacu, F., Ianuș, G., Marian, G., Munteanu, C., Paleu, V., Nazar, B., … Daraduda, N. (2022). A Qualitative Assessment of the Specific Woody Biomass of Fruit Trees. *Forests*, *13*(3), 405. https://doi.org/10.3390/f13030405
48. Aliaño, M., Gabaston, J., Ortiz, V., & Cantos, E. (2022). Wood Waste from Fruit Trees: Biomolecules and Their

Applications in Agri-Food Industry. *Biomolecules*, *12*(2), 1–46. https://doi.org/https://doi.org/10.3390/biom12020238
49. Cavalaglio, G., Fabbrizi, G., Cardelli, F., Lorenzi, L., Angrisano, M., & Nicolini, A. (2024). Lignocellulosic Residues from Fruit Trees: Availability, Characterization, and Energetic Potential Valorization. *Energies*, *17*(11), 1–14. https://doi.org/10.3390/en17112611
50. Matłok, N., Zaguła, G., & Gorzelany, J. (2024). Analysis of the Energy Potential of Waste Biomass Generated from Fruit Tree Seedling Production.
51. Kovacs, E., Hoaghia, M. A., Senila, L., Scurtu, D. A., Varaticeanu, C., Roman, C., & Dumitras, D. E. (2022). Life Cycle Assessment of Biofuels Production Processes in Viticulture in the Context of Circular Economy. *Agronomy*, *12*(6). https://doi.org/10.3390/agronomy12061320
52. Basaglia, M., D'ambra, M., Piubello, G., Zanconato, V., Favaro, L., & Casella, S. (2021). Agro-food residues and bioethanol potential: A study for a specific area. *Processes*, *9*(2), 1–15. https://doi.org/10.3390/pr9020344
53. Nasser, R. A., Salem, M. Z. M., Al-Mefarrej, H. A., Abdel-Aal, M. A., & Soliman, S. S. (2014). Fuel characteristics of vine prunings (Vitis vinifera L.) as a potential source for energy production. *BioResources*, *9*(1), 482–496. https://doi.org/10.15376/biores.9.1.482-496
54. Sánchez, J., Curt, M. D., Robert, N., & Fernández, J. (2019). Biomass Resources. In *The Role of Bioenergy in the Bioeconomy* (pp. 25–111). Elsevier. https://doi.org/10.1016/B978-0-12-813056-8.00002-9
55. Ahorsu, R., Medina, F., & Constantí, M. (2018). Significance and challenges of biomass as a suitable feedstock for bioenergy and biochemical production: A review. *Energies*, *11*(12), 3366. https://doi.org/10.3390/en11123366
56. Muhammad, S. (2022). Possibility of utilizing agriculture biomass as a renewable and sustainable future energy source. *Heliyon*, *8*. https://doi.org/https://doi.org/10.1016/j.heliyon.2022.e08905
57. Simin Anvari, Roque Aguado, Francisco Jurado, Mahdi Fendri, Hanen Zaier, Ajmi Larbi, D. V. (2024). Analysis of agricultural waste/byproduct biomass potential for bioenergy: The case of Tunisia. *Energy for Sustainable Development journal*, *78*. https://doi.org/https://doi.org/10.1016/j.esd.2023.101367
58. Figà Talamanca, C., Sofía Duarte González, C., & Sanchez, W. J. (2023). Agricultural residue-based bioenergy: Regional potential and scale-up strategies. Retrieved from www.irena.org
59. Senila, L., Tenu, I., Carlescu, P., Scurtu, D. A., Kovacs, E., Senila, M., … Roman, C. (2022). Characterization of Biobriquettes Produced from Vineyard Wastes as a Solid Biofuel Resource. *Agriculture*, *12*(3), 341. https://doi.org/10.3390/agriculture12030341
60. Țenu, I., Roman, C., Senila, L., Roșca, R., Cărlescu, P., Băetu, M., … Oana-Raluca, O. (2021). Valorization of Vine Tendrils Resulted from Pruning as Densified Solid Biomass Fuel (Briquettes). *Processes*, *9*(8), 1409.
61. Senila, L., Tenu, I., Carlescu, P., Corduneanu, O. R., Dumitrachi, E. P., Kovacs, E., … Roman, C. (2020). Sustainable biomass pellets production using vineyard wastes. *Agriculture (Switzerland)*, *10*(11), 1–21. https://doi.org/10.3390/agriculture10110501
62. Țenu, I., Roșca, R., Corduneanu, O. R., Roman, C., Senila, L., & Arsenoaia, V. (2024). Briquette Production from Vineyard Winter Pruning Using Two Different Briquette Production from Vineyard Winter Pruning Using Two Different Approaches, (July). https://doi.org/10.3390/agriculture14071109
63. Marian, G., Țenu, I., Roșca, R., Gudîma, A., & Pavlenco, A. (2019). Assessment of the quality of secondary production from different agricultural crops used as primary material for densified solid biofuels. *Lucrări Ştiinţifice*, *62*(1), 97–100.
64. Francik, S., Knapczyk, A., Knapczyk, A., & Francik, R. (2020). Decision support system for the production of Miscanthus and willow briquettes. *Energies*, *13*(6), 1364. https://doi.org/10.3390/en13061364
65. Nobert, H. A. (2015). Salix spp . as a biomass crop : Investigating their potential on marginal lands.
66. Tîrşu Mihai, & Revenco, E. (2021). *Bunele practici de utilizare a energiei regenerabile în agricultură*. Chişinău.
67. Garofalo, S. Pietro, Modugno, A. F., de Carolis, G., & Campi, P. (2025). Energy of Sorghum Biomass Under Deficit Irrigation Strategies in the Mediterranean Area. *Water (Switzerland)*, *17*(4), 1–20. https://doi.org/10.3390/w17040578
68. Obi, O. F., & Pecenka, R. (2023). Briquetting of Poplar Wood from Short Rotation Coppice—The Effects of Moisture Content and Hammer Mill Screen Size. *Energies*, *16*(3), 1–15. https://doi.org/10.3390/en16031454
69. Dragusanu (Japalela), V., Lunguleasa, A., Spirchez, C., & Scriba, C. (2023). Some properties of briquettes and pellets obtained from the biomass of Energetic Willow (Salix viminalis L.) in comparison with those from Oak (Quercus robur). *Forests*, *14*(6), 1134. https://doi.org/10.3390/f14061134
70. MAIA. (2024). Conferința ONVV: Piața europeană rămâne principalul destinatar al vinurilor moldovenești. Retrieved from https://www.madrm.gov.md/ro/content/5365

71. Popa, S., Cimpoieș, G., Rîbenţev, I., Marian, G., Andriuca, V., Macari, A., … Zbancă, A. (2024). *Cultivarea și valorificarea cătinii albe*. (Print-Caro, Ed.) (UTM.). Cișinău.
72. Fattahi, M., Govindan, K., & Farhadkhani, M. (2021). Sustainable supply chain planning for biomass-based power generation with environmental risk and supply uncertainty considerations: a real-life case study. *International Journal of Production Research*, *59*(10), 3084–3108. https://doi.org/10.1080/00207543.2020.1746427
73. Olugbade, T., Ojo, O., & Mohammed, T. (2019). Influence of Binders on Combustion Properties of Biomass Briquettes: A Recent Review. *Bioenergy Research*, *12*(2), 241–259. https://doi.org/10.1007/s12155-019-09973-w
74. Vaish, S., Sharma, N. K., & Kaur, G. (2022). A review on various types of densification/briquetting technologies of biomass residues. *IOP Conference Series: Materials Science and Engineering*, *1228*(1), 012019. https://doi.org/10.1088/1757-899x/1228/1/012019
75. Breznická, A., Kohutiar, M., Krbaťa, M., Eckert, M., & Mikuš, P. (2023). Reliability Analysis during the Life Cycle of a Technical System and the Monitoring of Reliability Properties. *Systems*, *11*(12). https://doi.org/10.3390/systems11120556
76. Katsitadze, J., Phutkaradze, Z., & Kutelia, G. (2024). Theoretical basis for calculating reliability indicators of agricultural machines, *7*(1), 6–7.
77. Olkiewicz, M., Dudek, M., Dyczkowska, J. A., Łyp-Wrońska, K., & Šarkan, B. (2025). Pellet Supply Chain Management: Analysis of Changes. *Energies*, *18*(23), 1–23. https://doi.org/10.3390/en18236329
78. Paolotti, L., Martino, G., Marchini, A., & Boggia, A. (2017). Economic and environmental assessment of agro-energy wood biomass supply chains. *Biomass and Bioenergy*, *97*, 172–185. https://doi.org/10.1016/j.biombioe.2016.12.020
79. Albashabsheh, N. T., & Heier Stamm, J. L. (2021). Optimization of lignocellulosic biomass-to-biofuel supply chains with densification: Literature review. *Biomass and Bioenergy*, *144*(December 2020), 105888. https://doi.org/10.1016/j.biombioe.2020.105888
80. Martinez-Valencia, L., Camenzind, D., Wigmosta, M., Garcia-Perez, M., & Wolcott, M. (2021). Biomass supply chain equipment for renewable fuels production: A review. *Biomass and Bioenergy*, *148*(106054). https://doi.org/https://doi.org/10.1016/j.biombioe.2021.106054
81. Li, J., Huang, F., Qin, H., & Pan, J. (2023). Research on Remaining Useful Life Prediction of Bearings Based on MBCNN-BiLSTM. *Applied Sciences (Switzerland)*, *13*(13), 1–24. https://doi.org/10.3390/app13137706
82. Burlacu, Daniel; Daneț, Nicolae; Bandrabur, Costică; Dominică, T. (2005). *Fiabilitatea, disponibilitatea și mentenabilitatea sistemelor tehnice* (MATRIX ROM.). București.
83. Sielaff, L., Lucke, D., & Sauer, A. (2022). Defining the Technical Availability of a Production System with Respect to Its Complexity †. *Engineering Proceedings*, *24*(1), 1–7. https://doi.org/10.3390/IECMA2022-12892
84. Jiang, M., Jiang, T., Guo, L., & Liu, S. (2025). A Method for Evaluating the Capability Adaptability of Equipment Groups Considering Dynamic Weight Adjustment. *Electronics (Switzerland)*, *14*(22), 1–32. https://doi.org/10.3390/electronics14224530
85. Gulyarenko, A., & Bembenek, M. (2022). The Method of Calculating Ploughshares Durability in Agricultural Machines Verified on Plasma-Hardened Parts.
86. Grejtak, T., Kuns, M. W., Lacey, J. A., Ajayi, O. O., Fenske, G., Blau, P. J., & Qu, J. (2025). Enhancing the shredder durability for biomass preprocessing by utilizing wear-resistant cutter materials. *Tribology International*, *210*(January), 110766. https://doi.org/10.1016/j.triboint.2025.110766
87. Wong, J. H., Karen, W. M. J., Bahrin, S. A., Chua, B. L., Melvin, G. J. H., & Siambun, N. J. (2022). Wear Mechanisms and Performance of PET Shredder Blade with Various Geometries and Orientations. *Machines*, *10*(9). https://doi.org/10.3390/machines10090760
88. Kostencki, P., Stawicki, T., & Białobrzeska, B. (2016). Durability and wear geometry of subsoiler shanks provided with sintered carbide plates. *Tribology International*, *104*, 19–35. https://doi.org/10.1016/j.triboint.2016.08.020
89. Kostencki, P., Stawicki, T., & Królicka, A. (2021). Wear of the working parts of agricultural tools in the context of the mass of chemical elements introduced into soil during its cultivation. *International Soil and Water Conservation Research*, *9*(2), 229–240. https://doi.org/10.1016/j.iswcr.2020.11.001
90. Iskakov, R., Gulyarenko, A., Hyla, P., & Bembenek, M. (2025). Working parts for intensive crushing and grinding of feed from waste raw materials: A review. *Advances in Science and Technology Research Journal*, *19*(7), 98–131. https://doi.org/10.12913/22998624/203643
91. Novitskyi, A., Banniy, O., Novitskyi, Y., Kharkovskyi, I., & Antal, M. (2024). Examination of maintainability

indicators of feed preparation and distribution products. *Machinery and Energetics*, *15*(4), 47–57. https://doi.org/10.31548/machinery/4.2024.47
92. Sharma, A., Ailawalia, P., & Shakuntala. (2021). RAM (reliability, availability and maintainability) of threshing machine in agriculture. *Agriculture and Natural Resources*, *55*(6), 1057–1061. https://doi.org/10.34044/J.ANRES.2021.55.6.16
93. He, L., Bao, P., Song, L., Wang, Z., Cai, J., & Wang, M. (2025). Branch Shredding and Collection Equipment for Resource Utilization of Vineyard Waste. *AgriEngineering*, *7*(12), 1–20. https://doi.org/10.3390/agriengineering7120402
94. Viňáš, J., Brezinová, J., Brezina, J., & Hermel, P. (2021). Innovation of biomass crusher by application of hardfacing layers. *Metals*, *11*(8). https://doi.org/10.3390/met11081283
95. Viňáš, J., Fiľo, M., Brezinová, J., Džupon, M., Puchý, V., Brezina, J., ... Pinke, P. (2026). Research on the Properties of Clad Layers Applied to Biomass Shredding Tools. *Metals*, *16*(1), 74. https://doi.org/10.3390/met16010074
96. Kinkhabwala, H., Bhojawala, V. M., Desai, S., & Patel, D. V. (2022). Design of Hydraulic Biomass Briquette Machine. *IOP Conference Series: Materials Science and Engineering*, *1258*(1), 012040. https://doi.org/10.1088/1757-899x/1258/1/012040
97. Barbieri, G., & Hernandez, J. D. (2024). Sustainability Indices and RAM Analysis for Maintenance Decision Making Considering Environmental Sustainability. *Sustainability (Switzerland)*, *16*(3). https://doi.org/10.3390/su16030979
98. Żyluk, A., Zieja, M., Grzesik, N., Tomaszewska, J., Kozłowski, G., & Jasztal, M. (2023). Implementation of the Mean Time to Failure Indicator in the Control of the Logistical Support of the Operation Process. *Applied Sciences (Switzerland)*, *13*(7). https://doi.org/10.3390/app13074608

Citation: Marian, T. (2026). Availability and maintainability of equipment in integrated technological flows for solid biofuel production: a review. *Journal of Engineering Science*. 2026, 33 (1), pp. 97-119. https://doi.org/10.52326/jes.utm.2026.33(1).07.

Submission of manuscripts: jes@meridian.utm.md

Journal of Engineering Science *Vol. XXXIII, no. 1 (2026), pp. 120 - 132*
Fascicle *Architecture, Civil and Environmental Engineering* *ISSN 2587-3474*
Topic *Environmental Engineering* *eISSN 2587-3482*

https://doi.org/10.52326/jes.utm.2026.33(1).08
UDC 532.5:556.53:004.94

NUMERICAL MODELING OF HYDRODYNAMICS OF RIVER-TYPE AQUATIC SYSTEMS

Rodica Branişte*, ORCID ID: 0000-0002-6935-8444,

Technical University of Moldova, 168 Stefan cel Mare bvd., MD-2004, Chisinau, Republic of Moldova
** Corresponding author: Rodica Branişte, rodica.braniste@iis.utm.md*

Received: 01. 22. 2026
Accepted: 03. 02. 2026

Abstract. The prediction and monitoring of pollutants in riverine ecosystems are essential for environmental protection and public health. This study proposes a methodology for the numerical modeling of hydrodynamics in aquatic systems using ANSYS Fluent. The results highlight the capability of ANSYS Fluent to determine critical parameters required for subsequent simulations, enabling accurate assessment of pollutant concentration distributions.

Keywords: *hydrodynamics, river, CFD, ANSYS Fluent, numerical modeling, pollution, water quality.*

Rezumat. Predicția și monitorizarea eficientă a poluanților din sistemele acvatice de tip râu sunt esențiale pentru protejarea ecosistemelor acvatice și a sănătății publice. Acest studiu prezintă o metodologie pentru modelarea numerică a hidrodinamicii în sistemele acvatice folosind produsul program ANSYS Fluent. Rezultatele demonstrează potențialul ANSYS Fluent în determinarea parametrilor critici necesari pentru simulările ulterioare în scopul obținerii câmpului de concentrații a poluanților.

Cuvinte cheie: *hidrodinamică, râu, CFD, ANSYS Fluent, modelare numerică, poluare, calitatea apei.*

1. Introduction

Moldova's freshwater resources are under increasing pressure, and river flow zones have undergone significant changes due to centuries of human activity. This has caused environmental changes in river ecosystems, such as water pollution from various sources of pollution such as petroleum substances, nitrites, nitrates, etc., loss of biodiversity, landscape deterioration and coastal erosion.

The water quality of the Dniester River is not only a concern for the Republic of Moldova, but also for the entire region and Europe in whole, especially because it flows into the Black Sea and the quality of the river's water influences both the country's ecosystem as well as the entire region [1]. There has been strong regional and international cooperation for several decades, achieved through various organizations and conventions. Various directives are being developed to regulate the quality of river waters in Europe and in the associated countries [2]. The need to predict pollution and monitor it is an important step in the process of protecting and improving water quality.

Water pollution prediction is an important thing in the management of aquatic environment for the prevention and control of water pollution. At present, there are several prediction methods for monitoring the pollution of aquatic systems, which are selected depending on the need and the type of aquatic system. The competent organizations choose the monitoring application program according to their own needs. According to the different mechanisms of the different water pollution prediction methods, they can be divided into statistical prediction method [3], intelligent prediction method and mechanism model prediction method [4].

As it was mentioned, the major concern is the quality of river water. It is not enough to monitor the water, to detect the pollutant through different sensor networks, it is necessary to predict and prevent the evolution of the pollutant concentration downstream [5]. It is expensive and isn't cost-effective to use a multitude of sensors, therefore, implementing different applications that would facilitate the prediction and monitoring the pollutants is appropriate. These applications could significantly help to improve the quality of water in aquatic systems [6].

2. Numerical modeling of river-type aquatic systems

The study of water quality in river-type ecosystems is extremely important. This issue becomes especially important when rivers are a major source of drinking water, water for irrigation, and water for industrial use. River pollution is currently one of the most serious environmental problem. After entering the river, pollutants spread rapidly. The process is determined by molecular motion, turbulence and non-uniform distribution of velocity in the cross section of the flow. Thus, contaminants disperse on the water surface and are transported downstream by the water flow

Understanding the mechanisms of pollutant transport in different types of rivers contributes to the correct numerical modeling for effective management of pollution situations in the aquatic ecosystem. The study of these processes represents an essential component of environmental engineering. The transport of pollutants in rivers is fundamentally described by the advection–dispersion equation [7].

Numerical modeling provides a very important tool in obtaining water quality prediction scenarios. With the help of numerical models, it could be analyzed the dispersion of pollutants in time and space. The input data for numerical models regarding the dispersion of pollutants are the hydrodynamic parameters, therefore the first step is to obtain the hydrodynamics. Specialized software products are used to obtain the hydrodynamic parameters [8].

Computational fluid dynamics (CFD) is a branch of fluid mechanics that uses numerical methods and data structures to analyze and solve problems involving fluid flows. CFD simulates and analyzes the behavior of liquids or gases in an environment and to describe the physical processes that occur due to this interaction. This approach allows solving complex problems, for which analytical methods are difficult to apply. Over the years, numerous software have been developed that provide better and more accurate solutions, which are necessary for solving complicated problems.

CFD is also a flexible, accurate and widely applicable tool that is applied in solving problems related to fluid dynamics and especially in flowing fluids such as river-type aquatic systems [9].

Using an application for predicting pollutants in aquatic ecosystems requires in-depth knowledge of the real system, the physicochemical laws, in order to correctly configure the software and to achieve the goal of prediction the water pollution.

Various software have been developed to identify sustainable solutions for water resource management and to improve the prediction of pollutant dispersion. Water quality models are important decision support tools for water pollution control. These models are applied to study the aquatic ecosystems health, and assessing the effects of point and diffuse pollution. Water quality models are complex software, which are usually not easy to learn and apply.

These software programs are developed by various state organizations, but also by various research centers, universities, and software development companies. These models are of different types, such as: models for assessing exposures in groundwater, surface water, food chain, etc. Such software are: SWAT, HSPF, AQUATOX, QUAL2K, WASP, TOXSWA, SWASH, MODFLOW 6, HEC-RAS, iRIC, HYDRUS, ANSYS Fluent, AGNPS, SMS and many others [7].

SWAT – (The Soil and Water Assessment Tool) is a small-scale watershed model used to simulate the quality and quantity of surface and groundwater and to predict the environmental impacts of land use, land management practices, and climate change [10].

HSPF - (Hydrologic Simulation Program Fortran) is a comprehensive package for simulating watershed hydrology and water quality for both conventional and toxic organic pollutants, allowing integrated simulation of soil contaminant runoff processes with flow-hydraulic and sediment-chemical interactions.

AQUATOX - is a simulation model of the evolution of various pollutants, such as nutrients and organic chemicals, and their effects on the ecosystem, including fish, invertebrates and aquatic plants.

QUAL2K - one-dimensional model intended to represent a well-mixed channel both vertically and laterally, with a hydraulic system in steady state, constant non-uniform flow rate and the amount of kinetic heat of the water quality.

WASP – (The Water Quality Analysis Simulation Program) for interpreting and predicting water quality from natural phenomena and human-caused pollution [11].

TOXSWA – (TOXic substances in Surface WAters) is a pseudo-2-dimensional model, which describes the behavior of pesticides in a water layer and its underlying sediment at the field edge scale [12].

SWASH - (Surface WAter Scenarios Help). It is an easy-to-use software product developed to perform various surface water pollution scenarios [13].

MODFLOW 6 - is an object-oriented program and framework developed to provide a platform for supporting multiple models and multiple model types within the same simulation [14].

HEC-RAS - the numerical model uses gradient and topography to estimate flow depth, velocity, and flooded areas. It is also useful for calculating sediment transport and water temperature [15].

iRIC – (International River Interface Cooperative) developed for numerical simulation of river flow and morpho-dynamics. It is a tool for analyzing river flow and morpho-dynamics, but also to predict flood, rainfall runoff generation, tsunami propagation [16].

HYDRUS - is a Windows-based modeling software suite that can be used to analyze the water flow, heat, and solids transport in variably saturated porous media (e.g., soils) [17].

AGNPS – (AGricultural Non-Point Source Pollution Model) The model predicts water, sediment by particle size class, erosion source, and chemicals—nitrogen, phosphorus, organic carbon, and pesticides [18].

SMS - (Surface-water Modeling System) is used for hydrodynamic modeling and substance transport in aquatic environments. The software generates 1D, 2D and 3D models in the field of surface waters, allowing to develop versatile models, grid generation and three-dimensional visualization of results [19].

ANSYS Fluid - used for numerical simulation of fluid flow and heat and mass transfer phenomena. The software allows modeling the complex processes, including turbulent flows, chemical reactions, and pollutant transport in fluid media. The tool is widely used in research and engineering to analyze the optimization of hydrodynamics and thermal processes [20].

Analyzing the multitude of researches that are carried out globally, it has been demonstrated with certainty that numerical modeling through software programs is an effective solution for current research.

The paper [21] proposes a new method for numerical simulation of pollutant transport in rivers, applied to the Severn River (Great Britain). The method uses the finite volume method for numerical solution and a multilayer neural network for estimating the longitudinal dispersion coefficient, used as an input parameter in the advection–dispersion equation. Validation by comparing simulated results with measured data demonstrated high model performance. The use of neural network significantly improved the accuracy of the simulation of pollutant transport in the river.

Modeling the aquatic systems for better monitoring of pollutants is carried out in many regions. In the article [22], the dynamics of pollutants in the Prut River system in the Giurgiulesti locality sector was examined and using the SMS software and it was developed a simulating model of the spatio-temporal evolution of pollutant dispersion. The obtained results highlight that computational methods are effective for analyzing and predicting the behavior of pollutants.

In the paper [23], it was proposed a complex of qualitative mathematical models with dynamic parameters for the assessment and forecasting the aquatic environment in Latvia. All constructed models are described in terms of differential equations and mathematical physics and are considered to be evolutionary models.

In [24], the QUAL2Kw model was subjected to calibration and validation tests. This model was implemented in the Tungabhadra River, India, and it was studied the dissolved oxygen concentration in the river water. The following were the basis of these studies: the ability to increase the flow, to oxygenate the source and to modify the volume of pollution.

In [25], the QUAL2E water quality model, a continuously stirred tank reactor method, was used to model the flow of the Beylerderesi River, Turkey, as a dynamic model, and the kinetic parameters were determined applying the optimization methods. For the optimization step, a secondary sequential programming method was used. The model prediction showed that the obtained results were consistent with the experimental data. The parameters of the Beylerderesi River model were estimated by SQP optimization, using a MATLAB code, and the dynamic simulations were performed with a rigid Runge-Kutta explicit integrator. The physicochemical data were analyzed in SPSS 22 by ANOVA for mean comparison, providing useful information to predict the impact of industrial investments on water quality and to measure environmental effects.

In the research paper [26], was accomplished the modeling and simulation on the Măleia River (Hunedoara County, Romania). The purpose of this research is to simulate general and accidental pollution. Using the SMS software, it was modeled the spatio-temporal evolution and dispersion of pollutant transport for surface aquatic systems. The developed numerical models estimated the dispersion of ammonium, nitrites and nitrates in the studied sector. Based on the results of the numerical simulation, it was established that the obtained, calibrated and validated numerical models can be used for any pollution scenario in emergency situations and accidents.

In [27], was investigated turbulent flow in an open channel affected by rigid vegetation. Numerical modeling was performed in Ansys Fluent, solving the RANS equations for turbulent flow and using the standard κ-ε model for turbulence. The free water surface was captured by the VOF method, and the volume discretization and numerical schemes were chosen for stability and accuracy. The study demonstrated the applicability of ANSYS Fluent in simulating complex flow in natural channels and constitutes a methodological basis for extending it to pollutant transport and dispersion models, even though pollutants were not directly integrated in the respective article.

Analyzing the implementation of different numerical models, we conclude that they are important tools for predicting the adverse effects of water pollution and can help guide practical investments for better management of the aquatic systems quality. In water quality models, it is necessary to optimize the parameters determined by trial and error to ensure the reliability of the model.

3. Problem formulation

The importance of water for human health was underlined in the mentioned above research, as well as the role of software in solving problems related to the pollution of aquatic systems. For the Republic of Moldova, the most important source of drinking water is the Dniester River. According to laboratory data of the Agency of Environment [28], regarding the water quality of the Dniester River from 2019-2024, it was found that the lower sector of the Dniester River has become increasingly polluted. Increased concentrations of pollutants were identified in the preliminary data, especially ortho-phosphates and suspended matter. For this reason, the Dniester River area near the locality Olănești was selected to obtain the hydrodynamic parameters. Table 1 presents the pollutants that were analyzed as well as their harmful impact on the environment and humans.

Table 1

Pollutants and their impacts

Pollutant	Main source	Environmental impact	Impact on humans
Orthophosphates (PO_4^{3-})	Fertilizers, detergents, wastewater	☐ Moderate eutrophication, algae growth, oxygen depletion	☒ Slightly harmful directly
Suspended matter	Sediments, organic and inorganic particles	☒ Decreases light, affects photosynthesis, deposits on the bottom of the water	☒ Can transport heavy metals and pathogenic microorganisms

Continuation Table 1

CCO -Cr	Biodegradable and non-biodegradable organic matter	⊠ High oxygen consumption, affects aquatic fauna	⊠ Indirectly harmful, indicates the presence of organic pollutants
BOD_5	Biodegradable organic matter, wastewater	⊠ Reduces dissolved oxygen, affects fish and the ecosystem	⊠ Indirectly unsafe for consumption
Nitrogen nitrite (NO_2^-)	Partial oxidation of ammonia, reduction of nitrates	● Toxic to fish, reduces available oxygen	● Highly toxic; methemoglobinemia to infants, affects blood oxygenation
Nitrogen nitrate (NO_3^-)	Fertilizers, agriculture, wastewater	⊠ Contributes to eutrophication and algae proliferation	⊠ At high concentrations, methemoglobinemia to infants, cardiovascular problems

⊠ – Low toxicity level / minor impact, ⊠ – Moderate level, ⊠ – High level, ● – Very high / critical level

Monitored data show increased values of nitrates, ortho-phosphates, suspended matter, BOD5 and CCO-Cr, which indicates a consistent pressure on the aquatic ecosystem. The main cause is the accumulation of pollutants from upstream sources: local discharges, both domestic and industrial, insufficiently treated, plus pollutants from intensive agricultural activities, which transport nutrients and sediments into the river, especially during periods of precipitation or snowmelt. In addition to these are the hydromorphological conditions specific to the lower sector, characterized by a low slope and slow flow, which reduce the natural self-purification capacity of water and favor the persistence of pollutants [29]. The choice of the sector near the Olănești locality for analysis reflects the cumulative impact of human activities in the entire upstream area and will allow the evaluation of the impact of pollutants on water quality.

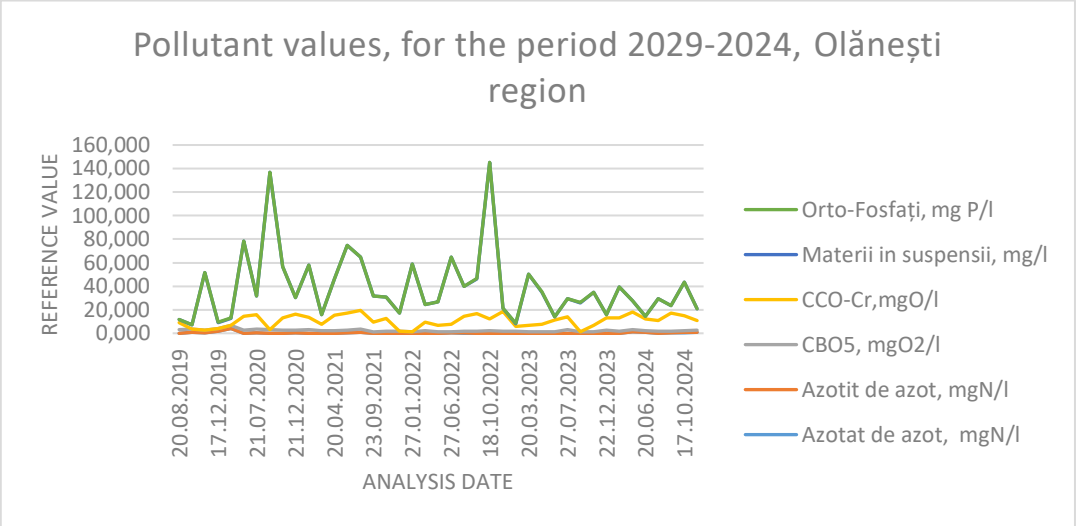

Figure 1. Pollutant values in Olănești (2019-2024).

In Figure 1, can be noticed the increases of ortho-phosphate concentrations, which indicate surface runoff from fertilized agricultural lands. Pollutants are transported to the river throughout the year, but during rainy periods and during snowmelt, the pollutant concentration increases. High values of COD-Cr and BOD_5 indicate pollution with wastewater of domestic and industrial origin that has not been properly treated. These types of pollution are frequently encountered near populated areas, where intensive agricultural activities take place, as well as direct discharges into river waters or discharges that are not subjected to an adequate treatment process.

4. Solving the problem

Since the beginning of its development, modeling has established itself as one of the most powerful and flexible tools supporting decision-making processes. Numerical models are extremely numerous and varied. Modeling techniques are implemented in various fields of activity. Effective decisions are based not only on modeling and simulation, but on a comprehensive system analysis. The made researches led to the conclusion that the ANSYS software is one of the most reliable tools that can provide accurate results. ANSYS Fluid provides accurate quantitative predictions regarding fluid-compound interactions, and solves a wide range of CFD simulation challenges to obtain reliable results in predicting pollutant dispersion in river-type aquatic systems.

ANSYS Fluid combines extended pre-processing and post-processing capabilities. In the Fluid environment, it is possible to model the following elements: fluids in a uniform and temporary state, laminar and turbulent flow, the range of fluid flow: subsonic, transonic and supersonic, heat transfer in thermal radiation, flotation; non-Newtonian fluid; multiphase fluid, the cavitation effect. ANSYS Fluent enables advanced analyses and modeling, as well as high-quality visualization and animation. The use of the ANSYS Fluent software in modeling pollutant behavior in aquatic systems represents an efficient and well-justified solution. This software accurately reproduces hydrodynamic processes and pollutant transport mechanisms in aquatic environments. In aquatic ecosystems, pollutant dynamics is simultaneously governed by flow, dispersion, turbulence, and physico-chemical and biological reactions, and these mechanisms are integrated into the numerical modeling framework of ANSYS Fluent.

Another advantage is the possibility of simulating three-dimensional flows, areas with velocity variations, turbulence effects. This aspect is particularly important in modeling real rivers because the dispersion of pollutants is influenced by several factors such as: riverbed morphology, aquatic vegetation, inhomogeneous turbulence. Ansys Fluent offers the possibility of simultaneously simulating several types of pollutants (nitrogen compounds, phosphorus, organic substances). This is important in water quality analysis, since the interaction between different substances, since the interaction between them determines processes such as eutrophication or the consumption of dissolved oxygen.

In aquatic ecosystems, the transformations between different pollutants can be numerically modeled by this software, which has the ability to integrate chemical reactions and biochemical processes. Thus, simulations can be used both for analyzing the current situation and for predictions depending on flow, temperature, types of pollutants. So, Ansys Fluent can perform predictive analyses for aquatic systems, such as evaluating the impact of discharges and assessing measures aimed to reduce pollution.

Ansys Fluent has advanced numerical accuracy, flexibility in modeling physicochemical phenomena and the possibility to simulate real pollution scenarios, which gives it an advantage in practical use. These features make it an effective tool for studying the behavior of pollutants in river ecosystems and for implementing modern strategies for aquatic environmental protection [30].

In order to solve the formulated problem, CFD simulations were performed using the ANSYS Fluent package. The simulated river sector is located between Nezavertailovca and Tudora, with a focus on the Olănești locality. The used hydrometric data [31] come from the Nezavertailovca and Tudora locations, as they are the closest and most relevant for the analyzed segment. These measurements allowed the definition and calibration of the boundary conditions necessary for building the 2D model. Compared to the geodetic distance of 6,414 m, the actual length of the riverbed is 10,153 m, indicates significant sinuosity. The riverbed is 58% longer than the direct path, which indicates the presence of well-defined meanders. This increases the water travel time and promotes lateral mixing in the river flow.

Table 2

General and obtained data of the Nezavrtailovca point (2021)

Hydrological / Geometric Parameter	Value	Unit	Observations
Flow	124	m^3/s	Measured value (2021).
Water level	1,17	m	Average depth in section.
Estimated average speed	0,37	m/s	Calculated from Q and an estimate of the cross-sectional area.
Riverbed length	10153	m	The actual length of the course on the winding route.
Geodetic distance	6414	m	The straight-line distance between points.
Sinuosity coefficient	1,58	-	Indicates a watercourse with moderate sinuosity.

The geometric data for the section between Olănești and Tudora clearly highlight the sinuous nature of the riverbed. With an effective length of 24,658 m, compared to 8,301 m in a straight line, the riverbed presents well-defined meanders, indicating a remarkable sinuosity.

Table 3

General and obtained data of Tudora point (2021)

Hydrological / Geometric Parameter	Value	Unit	Observations
Flow	466	m^3/s	Measured value, indicating a high flow regime. (2021).
Water level	4,67	m	Significant level, corresponding to a high flow rate.
Estimated average speed	0,75	m/s	Increased speed, reflecting a more energetic flow.

Continuation Table 2

Riverbed length	24658	m	Actual length of the extremely winding course.
Geodetic distance	8301	m	The straight-line distance between points.
Sinuosity coefficient	2,97	-	Indicates a watercourse with very pronounced sinuosity

The sector of the Dniester River in the Olănești locality is characterized by a sinuous riverbed, with an actual length of 4,372 m compared to 2,324 m in a straight line, resulting in a degree of curvature of 1,88, typical of plain meanders. The riverbed narrows from 77,1 m at the entrance to 49,3 m at the exit, which accelerates the flow and raises the water level downstream. The hydraulic parameters were determined by interpolation and empirical relationships, using real upstream and downstream data: the flows (124–466 m³/s) and water levels (1.17–4.67 m) were adjusted proportionally to the position of Olănești, and the velocity was estimated by the formula $V \approx 0{,}342 \cdot H^{0{,}51}$. The widths of the riverbed were taken from satellite images, and the compatibility of the section and velocity with the calculated flow was verified. This approach allowed obtaining a coherent set of parameters for numerical simulation, without direct measurements in the sector, these values were presented in Table 4.

Table 4

Shape and dimensions of the riverbed in the Olănești sector

Geometric Parameters	Value	Unit	Observations
Actual length of the river	4372	m	The river has a curved shape.
Straight line distance	2324	m	-
Degree of Bending	1,88	-	A value greater than 1.5 indicates a river with bends.
Riverbed length at Inlet	77,1	m	The river narrows (by 28 meters, or ~36%) along the village.
Riverbed length at Outlet	49,3	m	

Given the predefined data, the hydraulic parameters of the given sector were calculated and are represented in Table 5.

Table 5

Calculated hydraulic parameters in the sector of interest

Hydrological Parameter	At the entrance to Olănești	At the exit from Olănești	Main Effect
Average water speed	0.49 m/s	0.54 m/s	The water is accelerating.
Water level	2.08 m	2.47 m	The water level rises slightly downstream,
Estimated flow rate	213 m3 / s	251 m3 / s	The amount of water is increasing; it is due to small streams

Numerical simulation of the Dniester River sector in the Olănești locality, characterized by a curved riverbed configuration, was performed using ANSYS Fluent. The results of the numerical simulation are presented in Figure 2.

Figure 2. Turbulence intensity (%) on the 2D plane of the Olănești locality, Dniester River.

From Figure 2 can be seen the spatial distribution of the turbulence intensity, expressed in percentage. The maximum values seem to be located mainly on the outer part of the curves, where the fluid velocity increases and the velocity gradient becomes more pronounced. This distribution is consistent with the known hydrodynamic behavior of natural rivers, where kinetic energy and mixing processes are more intense in these areas.

Overall, the image suggests a realistic modeling of the interaction between the bed geometry and the turbulent flow regime. The modeling obtained can be used for the analysis of sediment transport or pollutant dispersion, since turbulence controls the mixing and dilution processes in aquatic systems. The numerical model regarding the magnitude of the Nistru River water flow velocity in the Olănești locality sector was also obtained, which can be observed in Figure 3.

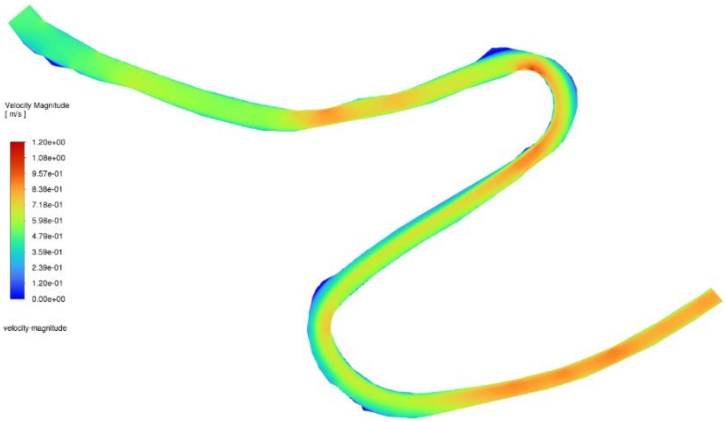

Figure 3. Velocity magnitude (m/s) of the Olănești locality sector.

Velocity magnitude distribution can be noticed in Figure 3, it indicates and average velocity of approximately 1,2 m/s. The velocity distribution highlights a clear variation between the inner and outer areas of the river bends. In the outer part of the river bend, higher velocity values can be observed, due to the effect of centrifugal force effect and the concentration of the main flow. In the inner part of the riverbed, appear areas with reduced velocities, associated with flow braking processes and possible recirculation areas.

On relatively straight sections, the velocity is distributed more uniformly. This distribution is typical for natural river flow and reflects the direct influence of the riverbed morphology on the velocity field. The obtained results are relevant for the analysis of sediment transport and pollutant dispersion processes, since the current velocity controls both advection processes and the mixing efficiency in the aquatic environment.

The developed numerical modeling confirmed the accuracy of the model and its capability to reproduce the transport and dispersion processes of pollutants. Organic pollutants originating from point sources (BOD_5 and COD -Cr) were significantly diluted throughout the river sector, their concentrations decreasing by over 600 times, which shows the efficiency of natural self-purification processes. In contrast, the pollutants present in the riverbed (TSS and PO_4P) remained relatively constant, suggesting a continuous input or a higher hydrochemical inertia. The model proved to be stable and reproducible, and mass conservation was fully respected. Consecutive testing produced almost identical results, confirming the correctness of the simulations and providing a realistic picture of how the river can reduce pollutant concentrations through natural mechanisms.

5. Conclusions

Numerical modeling of aquatic systems represents a significant step in the process of monitoring the ecological situation of rivers. Predicting water pollution is another important stage of water environment research. Information systems and software products used worldwide highlight the relevance of this ecological problem. The multitude of programs applied for simulation and modeling plays an important role in developing concrete solutions for ecological problems of aquatic systems, but especially rivers, which are the main source of drinking water. Research has also conducted that, at present, one of the most efficient and accurate software tools used for numerical modeling of aquatic systems is ANSYS Fluent. This software offers a wide range of modeling options and could provide answers to the most complex research challenges. The numerical modeling performed on the hydrodynamic parameters confirmed the accuracy of numerical modeling with Ansys Fluent.

The obtained results will be subsequently used to develop numerical models for pollutant transport and dispersion in river-type aquatic systems.

References

1. Branişte, R. (2022) Suivi de la situation écologique des systèmes aquatiques de type fluvial à travers le prisme du développement durable. În: Conferinţa tehnico-ştiinţifică a studenţilor, masteranzilor şi doctoranzilor, 29–31 martie 2022, Chişinău, Vol. 1, pp. 437–441. Chişinău: Tehnica-UTM. ISBN 978-9975-45-828-3; PDF 978-9975-45-829-0. Accesat 01.02.2026, https://ibn.idsi.md/sites/default/files/imag_file/p-437-441.pdf
2. European Union. (2000) The EU Water Framework Directive – Integrated River Basin Management for Europe. 22 December. Accesat 09.09.2025, https://ec.europa.eu/environment/water/water-framework/index_en.html
3. Marusic, G., Branişte, R., Sava, N., Ababii, V., Cărbune, V., Tiholaz, T. (2024) Statistical evaluation of data on the pollution of the Prut river with ammonium nitrogen. Journal of Engineering Science, 31(4), pp. 166–174. ISSN 2587-3474. Accesat 02.02.2026, DOI: https://doi.org/10.52326/jes.utm.2024.31(4).12
4. Wang, Y., Xue, S., Ding, J. (2020) Research on water pollution prediction of township enterprises based on support vector regression machine. E3S Web of Conferences, 228, 02014. Accesat 05.08.2025, https://www.researchgate.net/publication/348459714_Research_on_water_pollution_prediction_of_township_enterprises_based_on_support_vector_regression_machine
5. Ababii, V., Sudacevschi, V., Cărbune, V., Branişte, R., Clima, A. (2024) Edge Computing System for Monitoring of the Aquatic Ecosystems. În: Electronics, Communications and Computing: IC ECCO 2024, Ed. 13, 17–18 October 2024, Chişinău, pp. 205–206. Chişinău: Tehnica-UTM. ISBN PDF 978-9975-64-480-8. Accesat 02.02.2026, https://ibn.idsi.md/vizualizare_articol/223456

6. Negru, C., Mocanu, M., Costin, C., Draghia, ., Drobot, R. (2015) Cost efficient cloud-based service-oriented architecture for water pollution prediction. Conference: Intelligent Computer Communication and Processing (ICCP), IEEE International Conference, Cluj Napoca. Accesat 21.08.2025, https://www.researchgate.net/publication/299453279_Cost_efficient_cloud_based_service_oriented_architecture_for_water_pollution_prediction
7. Braniște, R., Marusic, G. (2020) Mathematical modeling of pollutant transport and dispersion processes in the Dniester River. Journal of Engineering Science, 27(4), pp. 151–162. ISSN 2587-3474. Accesat 24.12.2025, DOI: https://doi.org/10.5281/zenodo.4288309
8. Braniște, R., Istrati, D., Gogoi, E. (2022) La qualite de l'eau: metodes et modeles numerique de recherche. În: Conferinţa tehnico-ştiinţifică a studenţilor, masteranzilor şi doctoranzilor, 29–31 March 2022, Chișinău, Vol. 1, pp. 432–436. Chișinău: Tehnica-UTM. ISBN 978-9975-45-828-3; PDF 978-9975-45-829-0. Accesat 01.02.2026, https://ibn.idsi.md/sites/default/files/imag_file/p-432-436.pdf
9. Marusic, G., Ciufudean, C., Bostan, V. (2016) The use of Computational Fluid Dynamics analysis (CFD) in studying river-type systems. International Journal of Economy Energy and Environment, 10, pp. 234–237. Accesat 20.12.2025, https://www.naun.org/main/NAUN/energyenvironment/2016/a662011-053.pdf
10. Texas A&M University. Soil and Water Assessment Tool. Accesat 22.08.2025, https://swat.tamu.edu/
11. U.S. Environmental Protection Agency. Surface-water models – assess exposures. Accesat 22.08.2025, https://www.epa.gov/ceam/surface-water-models-assess-exposures
12. Pesticide Models. TOXSWA. Accesat 02.09.2025, https://www.pesticidemodels.eu/toxswa/home/
13. Joint Research Centre. European Soil Data Centre. Accesat 20.08.2025, https://esdac.jrc.ec.europa.eu/projects/swash
14. U.S. Geological Survey. MODFLOW 6 – USGS Modular Hydrologic Model. Accesat 21.08.2025, https://www.usgs.gov/software/modflow-6-usgs-modular-hydrologic-model
15. U.S. Army Corps of Engineers. Hydrologic Engineering Center – HEC-RAS. Accesat 21.08.2025, https://www.hec.usace.army.mil/software/hec-ras/
16. I-ric. Science of River Change Software. Accesat 21.08.2025, https://i-ric.org/en/about/
17. PC-Progress. Hydrus 3D. Accesat 22.08.2025, https://www.pc-progress.com/en/Default.aspx?hydrus-3d
18. U.S. Department of Agriculture, Natural Resources Conservation Service. Water Management Hydrology. Accesat 22.08.2025, https://www.nrcs.usda.gov/wps/portal/nrcs/detailfull/national/water/manage/hydrology/?cid=stelprdb1043529
19. Aquaveo. Surface-water Modeling System – SMS. Accesat 31.01.2026, https://aquaveo.com/
20. ANSYS. Site oficial. Accesat 21.08.2025, https://www.ansys.com/
21. Parsaie, A., Haghiabi, A. H. (2017) Computational Modeling of Pollution Transmission in Rivers. Applied Water Science, 7, pp. 1213–1222. Accesat 31.01.2026, https://link.springer.com/article/10.1007/s13201-015-0319-6
22. Marusic, G., Sava, N., Braniște, R., Cărbune, V., Ababii, V. (2025) Computational solutions for determining the spatial-temporal evolution of pollutants on the Prut river sector in Giurgiulesti locality. Scientific Study & Research. Chemistry & Chemical Engineering, Biotechnology, Food Industry, 26(1), pp. 33–45. Accesat 31.01.2026, https://pubs.ub.ro/article/5712
23. Guseynov, Sh. E., Aleksejeva, J. V. (2015) Mathematical Modelling of Aquatic Ecosystem. Environment. Technology. Resources. Proceedings of the International Scientific and Practical Conference, Vol. 3, pp. 92–99. Accesat 05.09.2025, DOI: https://doi.org/10.17770/etr2015vol3.192
24. Ranjith, S., Shivapur, A. V., Shiva, K. K. P., Hiremath, C. G., Dhungana, S. (2019) Utilization of Water Quality Modeling and Dissolved Oxygen Control in River Tungabhadra, Karnataka (India). Open Access Library Journal, 6, e5397. Accesat 12.09.2025, DOI: https://doi.org/10.4236/oalib.1105397
25. Yuceer, M., Coskun, M. A. (2016) Modeling water quality in rivers: a case study of Beylerderesi river in Turkey. Applied Ecology and Environmental Research, 14(1), pp. 383–395. Accesat 31.10.2025, DOI: https://doi.org/10.15666/aeer/1401_383395
26. Toth, L., Călămar, A., Irimia, A., Simion, S., Simion, A. (2019) Research on aquatic pollution level of Maleia river by simulation in computational fluid dynamics. Environmental Engineering and Management Journal, 18(4), pp. 935–944. Accesat 25.10.2025, http://www.eemj.icpm.tuiasi.ro/pdfs/vol18/full/no4/20_300_Toth_18.pdf
27. Sobieski, W. (2025) Challenges in Simulating Pollutant Behavior in Watercourses with Diverse Ecological and Structural Features. Journal of Applied Fluid Mechanics, 18(8), pp. 1964–1979. ISSN 1735-3572; EISSN 1735-3645. Accesat 02.02.2026, DOI: https://doi.org/10.47176/jafm.18.8.3269
28. Agenția de Mediu a Republicii Moldova. Site oficial. Accesat 31.01.2026, https://am.gov.md/

29. Marusic, G., Sava, N., Braniște, R. (2023) Research on water quality in the Dniester River 2019–2021. Annals of "Dunarea de Jos" University of Galați, 45(1), pp. 5–10. Accesat 01.02.2026, DOI: https://doi.org/10.35219/eeaci.2022.1.01
30. Manjunath, S. (2026) ANSYS Technology Workshop on Computational Fluid Dynamics. Indian Institute of Technology Roorkee. Accesat 20.01.2026, https://www.iitr.ac.in/ansyscfd/index.html
31. Serviciu Hidrometeorologic de Stat. Site oficial. Accesat 23.12.2025, https://www.meteo.md/

Citation: Braniște, R. (2026). Numerical modeling of hydrodynamics of river-type aquatic systems. *Journal of Engineering Science*. 2026, 33 (1), pp. 120-132. https://doi.org/10.52326/jes.utm.2026.33(1).08.

Submission of manuscripts: jes@meridian.utm.md

Journal of Engineering Science *Vol. XXXIII, no. 1 (2026), pp. 133 - 145*
Fascicle *Architecture, Civil and Environmental Engineering* *ISSN 2587-3474*
Topic *Architecture, Urbanism and Cadaster* *eISSN 2587-3482*

https://doi.org/10.52326/jes.utm.2026.33(1).09
UDC 528.44:004.9:625.7(478)

TERRESTRIAL LASER SCANNING FOR 3D CADASTRE: A CASE STUDY OF ROAD INFRASTRUCTURE IN THE REPUBLIC OF MOLDOVA

Ana Vlasenco*, ORCID: 0000-0002-5017-6392,
Livia Nistor-Lopatenco, ORCID: 0000-0003-3509-648X,
Efim Zubco, ORCID: 0000-0002-7131-7705,
Alexandru Fărîmă, ORCID: 0009-0004-7294-6644

Technical University of Moldova, 168 Stefan cel Mare Blvd., Chisinau, Republic of Moldova
* Corresponding author: Ana Vlasenco, *ana.vlasenco@gcg.utm.md*

Received: 02. 25. 2026
Accepted: 03. 22. 2026

Abstract. Accelerated urban development and infrastructure expansion require the modernization of the cadastral system in the Republic of Moldova through the integration of the three-dimensional component. This article analyzes the possibility of implementing 3D cadastre, starting from the limitations of the current two-dimensional cadastre and the need for alignment with international standards, particularly ISO 19152 (LADM - Land Administration Domain Model). The case study focuses on the three-dimensional modeling of a complex infrastructural object – a road bridge in Criuleni district, located at the intersection of Hrușova, Ciopleni, and Goian villages. Using terrestrial laser scanning technology (Leica BLK360), high-precision spatial data were obtained (RMS <10 mm, density >800 points/m^2), which were processed and integrated into a functional 3D model. The results demonstrate that three-dimensional modeling provides a more accurate representation of reality, facilitates engineering analysis, and enables correct description of overlapping objects or those with complex geometry. The article proposes a hybrid implementation model, in which the 2D cadastre remains the legal basis, while 3D models serve as technical and decision-making support. The conclusions highlight the need for developing a specific regulatory framework, standardizing data acquisition processes, and creating an integrated GIS (Geographic Information Systems) platform for efficient management of three-dimensional spatial information.

Keywords: *3D cadastre, terrestrial laser scanning, three-dimensional modeling, road infrastructure, GIS, LADM.*

Rezumat. Dezvoltarea urbană accelerată și extinderea infrastructurii impun necesitatea modernizării sistemului cadastral din Republica Moldova prin integrarea componentei tridimensionale. Prezentul articol analizează posibilitatea implementării cadastrului 3D, pornind de la limitele cadastrului bidimensional actual și necesitatea alinierii la standardele internaționale, în special ISO 19152 (LADM - Land Administration Domain Model). Studiul de caz se concentrează asupra modelării tridimensionale a unui obiect infrastructural complex – un pod rutier din raionul Criuleni, situat la intersecția satelor Hrușova, Ciopleni și Goian.

Utilizând tehnologia de scanare laser terestră (Leica BLK360), au fost obținute date spațiale de înaltă precizie (RMS <10 mm, densitate >800 puncte/m²), care au fost procesate și integrate într-un model 3D funcțional. Rezultatele demonstrează că modelarea tridimensională oferă o reprezentare mai exactă a realității, facilitează analiza inginerească și permite descrierea corectă a obiectelor suprapuse sau cu geometrie complexă. Articolul propune un model hibrid de implementare, în care cadastrul 2D rămâne baza juridică, iar modelele 3D servesc ca suport tehnic și decizional. Concluziile evidențiază necesitatea dezvoltării unui cadru normativ specific, standardizarea proceselor de achiziție a datelor și crearea unei platforme GIS (Sisteme informaționale geografice) integrate pentru gestionarea eficientă a informațiilor spațiale tridimensionale.

Cuvinte cheie: *cadastru 3D, scanare laser terestră, modelare tridimensională, infrastructură rutieră, GIS, LADM.*

1. Introduction

The cadastral system represents the fundamental infrastructure for real estate administration, playing an essential role in ensuring legal security of property rights and in territorial development planning [1, 2]. In the Republic of Moldova, the cadastre currently operates based on a two-dimensional model [3], in which real estate properties are represented through planar projections, without reflecting the vertical complexity of modern constructions and infrastructure [4].

Rapid urban development, the expansion of underground infrastructure (utility networks and underground transportation systems), and the growing number of buildings with complex multi-level uses have highlighted the limitations of two-dimensional representation [5, 6]. In such situations, the 2D cadastre cannot accurately describe the spatial relationships between overlapping objects, which generates legal and technical ambiguities [7]. For example, in the case of road overpasses, tunnels, mines and quarries, or multi-story buildings owned by different proprietors, the delineation of spaces and the establishment of property rights becomes problematic in the absence of a clear vertical component [8, 9, 10]. Rethinking the legal and economic aspects of urban society by transitioning from the traditional two-dimensional paradigm to a three-dimensional (3D) approach to property and space use represents a current necessity in the development, implementation, and monitoring of urban land policies (social, economic, ecological) [11]. The 3D cadastre is one of the instruments that can facilitate this process through spatial databases and representations.

The International Organization for Standardization (ISO) has recognized the necessity of a three-dimensional approach through the development of the ISO 19152 standard, also known as the Land Administration Domain Model (LADM) [1, 2]. This standard provides a conceptual framework for representing cadastral objects in three-dimensional space, enabling the correct description of legal volumes, vertical boundaries, and complex spatial relationships [12].

In this context, the Republic of Moldova faces the challenge of developing its cadastral system to meet current requirements and align with European and international standards [12, 13]. The implementation of 3D cadastre represents not only a technological modernization but also a practical necessity for ensuring efficient territorial administration and facilitating sustainable development [6, 8, 14].

This article aims to analyze the feasibility of implementing 3D cadastre in the Republic of Moldova through a concrete case study of complex road infrastructure. The purpose is to demonstrate, through practical application, the advantages of three-dimensional modeling and to propose a methodological framework for integrating these technologies into the national cadastral system.

2. Materials and Methods

2.1. Study area

The area selected for the case study is located in Criuleni district, at the administrative boundary between the villages of Hrușova, Ciopleni, and Goian. The analyzed sector is part of the national road network, classified as a category M road (main/expressway) on the principal section, while the intersection area includes connections with a republican road (category R), local roads, and a watercourse (Figure 1). This classification confers strategic regional importance to the site, with the road serving as a link between localities and ensuring regional traffic continuity [15, 16].

a) b)

Figure 1. Location of the study area: a) Source: *cadastru.md/ecadastru*; b). Source: *andsa.md/harta-interactiva* [15, 16].

The main infrastructural element analyzed is a road bridge that crosses an area with significant altitude differences. The three-dimensional configuration of the road junction is characterized by: the bridge deck located at the upper elevation, the lower roadway (local road) at the intermediate elevation, the watercourse bed at the lowest elevation, access ramps with significant level differences, and embankments and structural support zones.

The geometric complexity of the structure – which includes the roadway at the upper level, the abutment system, and lateral embankments – fully justifies the selection of this object for demonstrating the advantages of three-dimensional modeling. In classical two-dimensional cadastral representation, such structures are reduced to simple planar projections, which eliminates essential information about the vertical component and the actual spatial relationships between constructive elements.

The development of the three-dimensional model of the road infrastructure required the use of a complex dataset, structured into two main categories: existing (archival) data and data acquired through direct precision geodetic measurements. This combined approach allows for the creation of a coherent and accurate model while ensuring its integration into the legal and administrative framework specific to the Republic of Moldova. Topographic maps at scales of 1:10,000 and 1:50,000 played an important role in the initial analysis, used for

understanding the geographical position of the study area, the relief configuration, and the relationship between the road infrastructure and the surrounding terrain (Figure 2). This enabled the identification of contour lines, main relief forms, the road network, and land use boundaries.

a) b)

Figure 2. Topographic maps: a) scale 1:10,000; b) scale 1:50,000 [17].

To evaluate the evolution of road infrastructure and changes occurring in the study area, a comparative analysis was performed based on available orthophotoplans for different time periods, through the overlay and comparison of photogrammetric (aerial) images acquired during 2011–2021 [17].

The land within the studied area is registered in the Real Estate Registry (RER) and identified by a cadastral number, in accordance with current legislation. This cadastral registration ensures legal recognition of the site and enables the correlation of cadastral data with the actual situation on the ground. The cadastral data available in the e-Cadastre platform [15] provide information regarding cadastral parcel boundaries and the general location of the object, however, they do not reflect the vertical spatial relationships between constructive elements. The orthophotoplan – the primary visual support of the system – graphically overlays all components of the bridge without altimetric separation, which represents precisely the limitation that terrestrial laser scanning technology modeling aims to overcome.

Following the analysis of available data – topographic maps, orthophotoplans, cadastral data from the RER, and information regarding infrastructure and relief – it was determined that the study area is characterized by a complex spatial structure. The overlay of road elements with the relief and adjacent areas cannot be accurately represented through a two-dimensional representation, which limits the understanding of vertical relationships between objects. For this reason, the use of a three-dimensional approach is required, capable of faithfully reflecting the actual structure of the terrain and the analyzed infrastructure.

2.2. Data acquisition

For the acquisition of three-dimensional data, the Leica BLK360 (BLK Edition) terrestrial laser scanner was used, a high-precision equipment designed for rapid and detailed documentation of built and natural environments. It operates using LiDAR (Light Detection and Ranging) technology: emitting laser pulses and recording their return time, calculating the distance to reflective objects in the scanning field [18].

The combination of high precision, portability, and scanning speed makes the BLK360 a suitable instrument for documenting road infrastructure, including in areas with limited access (under the bridge deck, at the base of abutments, on embankments).

To ensure complete coverage of the studied area and to obtain a coherent three-dimensional model, the positioning of scanning stations was performed strategically, based on the road infrastructure configuration and field conditions (Figure 3).

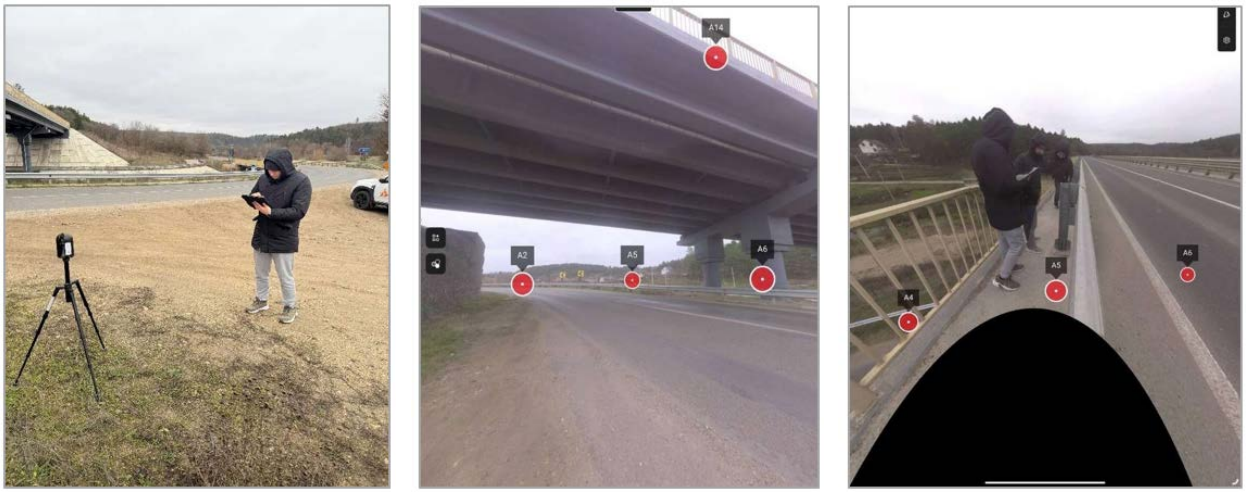

a) b) c)

Figure 3. Data acquisition: a) Terrestrial laser scanning using the BLK360;
b) Positioning of scanning stations under the overpass;
c) Positioning of scanning stations on the roadway [19].

The stations were positioned in two main configurations: on the bridge deck (for scanning the deck and parapets) and under the crossing structure (for scanning the support infrastructure and vertical constructive elements). Positioning under the deck involved special visibility conditions and required station placement both axially and laterally relative to the travel lane.

During the data acquisition process, the scans were initially correlated using the automatic pre-alignment method (Pre-alignment). Pre-alignment of the scans played an essential role in the coherent organization of the measurement campaign, as it enabled real-time evaluation of spatial continuity between successive scanning positions (Figure 4).

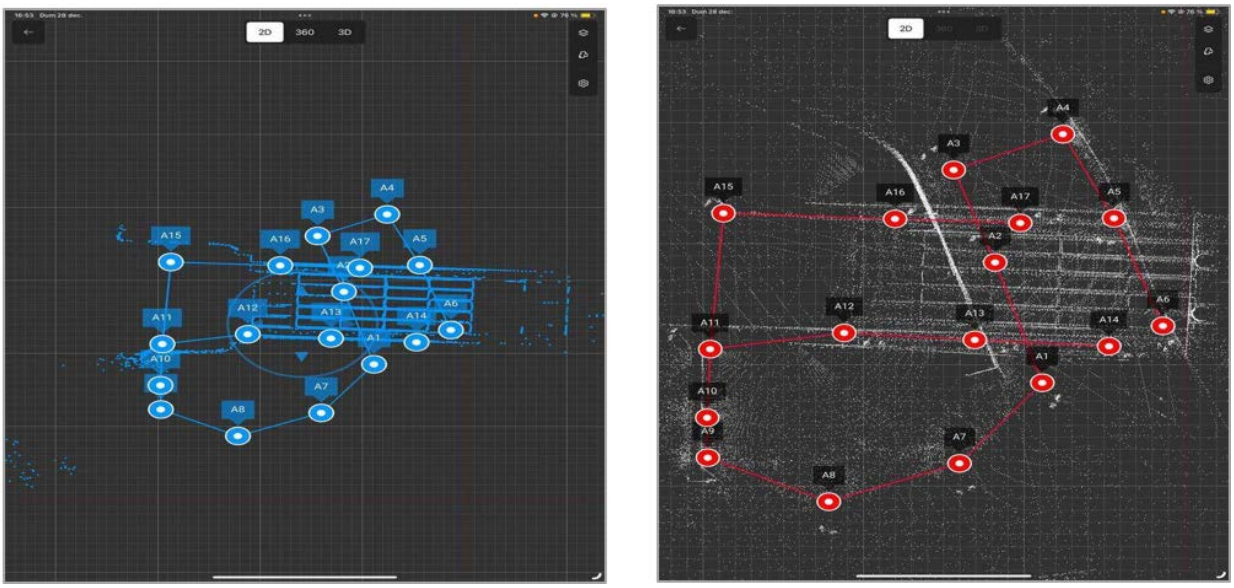

a) b)

Figure 4. Scan pre-alignment process: a) Pre-alignment scheme of scanning stations;
b) Result of scan pre-alignment.

Through this stage, it was immediately verified whether the areas of interest were adequately covered and whether sufficient overlaps existed between scans for subsequent correct integration. An important advantage of pre-alignment is the ability to rapidly identify any discontinuities or coverage gaps, which could be remedied by adding supplementary stations.

2.3. Data processing

The processing of the acquired data followed a structured workflow in successive stages, performed in Cyclone REGISTER 360 (BLK Edition) software, an application dedicated to processing data from Leica BLK terrestrial laser scanners [20]. The processing workflow aimed to transform the raw data into usable three-dimensional models while ensuring quality control and geometric accuracy of the results (Figure 5).

a) b)

Figure 5. Data processing in Cyclone REGISTER 360: a) Point cloud processing interface; b) Final integrated point cloud.

The process included several essential stages: (1) importing and organizing raw data from all scanning stations; (2) registering the scans into a common coordinate system through cloud-to-cloud and target-based alignment methods, achieving sub-centimeter alignment accuracy; (3) global optimization (bundle adjustment) to minimize accumulated errors and ensure geometric consistency; (4) point cloud cleaning by removing temporary elements, outliers, and noise; (5) georeferencing to the national MOLDREF 99 system [21, 22] for compatibility with cadastral data from the Real Estate Registry.

Following the import, alignment, and optimization stages, a coherent, cleaned, and correctly positioned point cloud in the national coordinate system was obtained. This result represents the final form of the field acquisition and constitutes the basis for all subsequent analyses.

An important advantage is the ability to export and use the data in specialized 3D modeling applications, geographic information systems (GIS), or engineering software without significant precision losses [23]. Additionally, the point cloud enables the generation of a coherent three-dimensional model, usable for both geometric analysis and functional evaluation of the infrastructure, providing an accurate representation of the vertical relationships specific to bridge-type works, overpasses, or overlapping roads (Figure 6) [19].

Thus, the processing stage consolidates the metric foundation of the entire experimental approach, ensuring the necessary conditions for the coherent integration of three-dimensional information within an extended cadastral model.

a) b) c) d)

Figure 6. 3D representation of infrastructure after data processing: a) 3D visualization of bridge superstructure; b) 3D model of the bridge deck; c) Representation of piers and infrastructure; d) 3D model of the roadway.

3. Results and Discussion

3.1. Characteristics of the obtained 3D model

Following the data acquisition and processing, a three-dimensional point cloud was obtained, completely covering the analyzed road infrastructure and including all main components: the bridge deck, support abutments, lateral embankments, the lower local road, and the watercourse bed. The final model exhibits geometric precision evaluated through root mean square error (RMS) below 10 mm, which corresponds to the requirements for engineering analysis applications and high-precision cadastral modeling. The high density of the point cloud, exceeding 800 points per square meter, enabled detailed representation of all constructive elements, including fine details such as structural joints, parapets, and surface textures.

The three-dimensional model provides a complete representation of the spatial configuration of the road junction, highlighting the altimetric relationships between infrastructure components. The level difference between the upper deck and the lower local road roadway reaches approximately 4.20 meters, an aspect that cannot be accurately represented in two-dimensional cadastral representation. The bridge abutments have heights of approximately 5.67 meters, while the embankments have variable slopes ranging from 15° to 30°, depending on the terrain configuration [19].

Georeferencing to the national MOLDREF 99 system ensures complete compatibility with data from the Real Estate Registry and enables direct integration into the existing cadastral system. This aspect is essential for the practical valorization of the model within territorial administration and for facilitating its use by institutions involved in infrastructure management.

3.2. Comparative analysis: 3D model vs. 2D cadastral representation

The comparison between the obtained three-dimensional model and the existing two-dimensional cadastral representation in the e-Cadastre platform [15] highlights a series of significant advantages of the 3D approach, both from a technical perspective and in terms of the clarity of the information provided.

In the 2D cadastral representation, the road infrastructure appears as a simple area delineated on the horizontal plane, without clear indications about the vertical component. The e-Cadastre platform displays the bridge as a flat surface, graphically overlaying all components (deck, abutments, lower road, watercourse bed) in a single projection, without

altimetric separation. The user cannot distinguish between the different levels of the infrastructure, which hinders understanding of the actual configuration. The graphic overlay of all elements creates uncertainty in spatial delineation and in establishing property or administrative rights [24].

The three-dimensional representation volumetrically delimits each component: the volume occupied by the bridge deck and protective parapets (public road domain - category M national road), the volume used by the lower local road (public road domain - local road), the volume of the watercourse bed (public water domain). This clear separation facilitates appropriate administration of each domain and eliminates potential disputes regarding space use.

The 3D model obtained through laser scanning provides exact measurements of all dimensions [25], with sub-centimeter precision: bridge deck length, roadway width, abutment heights, embankment slopes, level differences between infrastructure components. These data are integral to the geometric model and can be extracted directly, without requiring additional measurements.

The 2D representation does not allow volumetric analyses, stability calculations, or clearance verifications. Any technical analysis requires the creation of additional models, which fragments the process and increases the risk of errors.

The three-dimensional model would enable the direct performance of complex analyses in the 3D GIS environment (volumetric calculations, embankment stability, clearance verifications, hydrological simulations), ensuring data coherence and reducing decision-making time.

3.3. Implementation proposal for the Republic of Moldova

Based on the obtained results and the conducted analysis, a hybrid implementation model for 3D cadastre in the Republic of Moldova is proposed, which combines the advantages of the existing two-dimensional cadastre with the extended capabilities of three-dimensional representation.

The case study demonstrates that modern spatial data acquisition technologies, particularly terrestrial laser scanning, are perfectly compatible with the requirements of the ISO 19152 standard (LADM - Land Administration Domain Model) [23] for defining three-dimensional spatial units. The obtained model can be structured according to LADM, defining the legal volumes of different infrastructure components.

The LADM standard provides four fundamental packages for land administration: Party (legal entities holding rights), Administrative (rights, restrictions, and responsibilities), Spatial Unit (spatial units that delimit the extent of rights), and Surveying (geodetic measurements). In the case of the analyzed infrastructure, the 3D model enables precise definition of spatial units (the bridge deck as a distinct volume, the lower road as another volume, the riverbed space as a third volume), each having specific legal attributes (public road domain, public water domain).

Continuously evolving 3D technology is changing the paradigms of urban planning and land policy, as it influences not only how the city is viewed, but also how property rights and other restrictions are described in space. The implementation of 3D cadastre in the Republic of Moldova should not involve replacing the existing system, but rather a gradual extension of its capabilities. A hybrid model is proposed in which the 2D cadastre remains the legal basis for real estate registration, while three-dimensional models function as complementary technical and decision-making support.

This approach enables: maintaining the stability of the existing legal framework, avoiding disruption of the current rights registration system, gradual and realistic transition without systemic ruptures, using 3D models in complex situations (overlapping infrastructure, multi-level buildings, underground networks), improving the quality of cadastral services by providing detailed visualizations, grounding urban planning decisions on actual geometry. In practice, this means that property ownership of land and buildings will continue to be recorded in the traditional two-dimensional cadastral registry, however, for complex objects (bridges, overpasses, high-rise buildings, underground parking facilities), associated 3D models will be created and maintained, serving as technical reference for analysis, design, and administration.

The integration of three-dimensional models into existing GIS systems represents an essential component of the proposed model. By analogy with platforms such as Google Earth, which visualizes terrain and buildings three-dimensionally, the cadastral system in the Republic of Moldova can be extended to include a 3D layer that correlates legal information with the actual geometry of constructions (Figure 7).

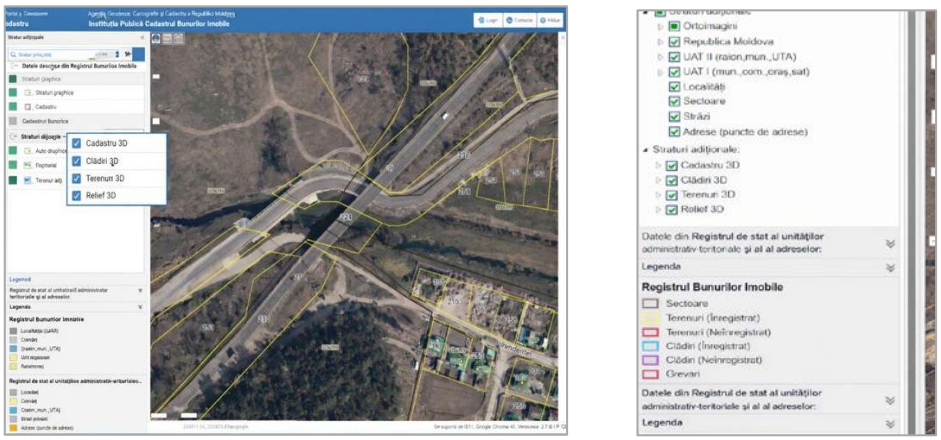

a) b)

Figure 7. Conceptual integration of 3D cadastral layers: a) Proposed implementation in the e-Cadastre platform; b) Layered structure of the cadastral information system.

The development of 3D functionality within the e-Cadastre platform is proposed, which would enable: three-dimensional visualization of complex cadastral objects, interactive navigation in 3D space (rotation, zoom, sectioning), querying object attributes directly from the visualization, overlaying 3D models with existing 2D cadastral data, differentiated access for public authorities (full functionality) and citizens (visualization and consultation). To illustrate the potential integration of the three-dimensional model into the e-Cadastre platform, Figure 8 was developed, presenting a conceptual visualization of the 3D model obtained through laser scanning overlaid on existing two-dimensional cadastral data. The final graphic representation was generated using AI-assisted visualization tools [26], based on geometric parameters extracted from the actual model and the current cadastral configuration. This approach demonstrates how three-dimensional information can be coherently integrated into the cadastral platform user interface, providing a clear perspective on the spatial relationships between different infrastructure levels.

This integrated platform would enable unified visualization of land and buildings in three-dimensional space, analysis of relationships between overlapping or adjacent objects,

grounding of urban planning decisions on actual geometry, alignment of the national cadastre with European trends in 3D cadastre, and increased transparency and quality of information provided by the cadastral system.

Currently, the cadastral legislation in the Republic of Moldova does not contain explicit provisions regarding the registration and management of three-dimensional objects. The development and adoption of a specific regulatory framework is necessary, harmonized with the ISO 19152 standard, which would define: concepts of 3D spatial unit, volumetric delimitation, and three-dimensional cadastral registration; procedures for collecting, processing, and validating 3D data; precision and quality standards accepted for different object categories; institutional responsibilities in 3D cadastre management.

Figure 8. Conceptual visualization of the integration of the 3D model into the e-Cadastre platform.

The storage and processing of point clouds and volumetric models require adequate IT infrastructure. The development of an integrated GIS platform is recommended, which would enable: efficient data exchange between cadastral institutions, public authorities, and infrastructure administrators; long-term storage and archiving of 3D models; efficient data processing and updating; secure and controlled access to information, based on user type.

The establishment of clear and uniform requirements is necessary regarding: spatial data acquisition methods (laser scanning, photogrammetry, GNSS); measurement precision for different object categories (critical infrastructure - millimeter precision, buildings - centimeter precision, land - decimeter precision); point cloud resolution and density; data storage and exchange formats; georeferencing procedures.

The implementation of 3D technologies necessitates continuous training of specialists in the fields of cadastre and geodesy. Training programs must cover: technical aspects (use of scanning equipment, data processing in specialized software, GIS-BIM integration); conceptual aspects (LADM, 3D modeling, volumetric property administration); legal aspects (interpretation and application of new regulations, legal validation of 3D data).

A phased approach is recommended, starting with priority objects: critical infrastructure (bridges, overpasses, tunnels); dense urban areas (Chișinău, Bălți); new complex constructions (high-rise buildings, underground parking facilities); progressive extension to other object categories (public buildings, industrial zones, utility networks). The implementation of 3D cadastre in the Republic of Moldova represents not only a technological modernization but also a practical necessity for ensuring efficient territorial administration.

4. Conclusions and recommendations

Despite the significant potential of three-dimensional (3D) technologies as advanced urban planning tools, as well as the substantial progress achieved at both theoretical and practical levels, currently no country has implemented a fully functional 3D cadastre completely integrated into national legal and administrative systems. Most existing initiatives are either in pilot phases or in partial stages of operationalization, highlighting the complexity of the transition from the traditional two-dimensional paradigm to a coherent three-dimensional framework. The evolving concepts involved in this new process should be based on the ISO 19152 Land Administration Domain Model (LADM), which provides support for 3D representations.

This study has demonstrated the viability and advantages of implementing 3D cadastre in the Republic of Moldova through a concrete case study of complex road infrastructure. The obtained results confirm that modern spatial data acquisition technologies, particularly terrestrial laser scanning, can provide the high-precision information necessary for three-dimensional representation of cadastral objects.

The 3D model generated for the road bridge in Criuleni district, with geometric precision below 10 mm and a density exceeding 800 points/m^2, provides a faithful representation of ground reality, significantly superior to traditional two-dimensional representations. The comparative analysis highlights that three-dimensional modeling eliminates ambiguities related to overlapping objects, provides enhanced geometric clarity, and enables detailed engineering analyses.

In the context of accelerated urban development and infrastructure expansion, 3D cadastre no longer represents an option but a necessity for efficient territorial administration. Alignment with the international standard ISO 19152 (LADM) provides a solid framework for implementing these technologies in a consistent and interoperable manner.

Based on the obtained results and the conducted analysis, the following recommendations are formulated for the implementation of 3D cadastre in the Republic of Moldova:

- Development of the regulatory framework. Adoption of a specific legislative framework for 3D cadastre, harmonized with ISO 19152, to define concepts, procedures, and institutional responsibilities.
- Standardization of technical processes. Establishment of clear requirements regarding data acquisition methods, measurement precision, and storage formats, to ensure uniformity and interoperability.
- Development of an integrated GIS platform. Creation of a modern technological infrastructure that enables efficient management of three-dimensional data and information exchange between institutions.
- Investment in infrastructure and equipment. Allocation of necessary resources for acquiring scanning equipment and developing data storage and processing capabilities.
- Continuous professional training. Organization of training programs for specialists in the field, covering both technical and conceptual aspects of 3D cadastre.
- Phased implementation. Adoption of a gradual approach, starting with priority objects (critical infrastructure, complex urban areas) and progressive extension to other categories.

The consolidation of a three-dimensional cadastre capable of explicitly recording and modeling the interaction between 3D real estate units and applicable legal norms (urban planning regulations, easements, protection zones, environmental restrictions, etc.) would constitute an essential tool for increasing the effectiveness of urban and environmental planning. By correlating spatial volumes with their regulatory regime, such a system would enable coherent evaluation of the conformity of proposed developments with the existing legal framework.

The implementation of these recommendations will enable the Republic of Moldova to take an important step toward modernizing the cadastral system, ensuring more precise, transparent, and efficient territorial administration, in accordance with international best practices.

Research Data Availability Statement: The original contributions presented in the study are included in the article. The authors can provide the data upon request.

Declaration of generative AI use: During the preparation of this manuscript, the author(s) used DALL-E 3 (via ChatGPT) to generate the image presented in Figure 8. The authors have reviewed and revised the output and accept full responsibility for the content of this publication.

Contribution of authors

Ana Vlasenco: Supervision, resources, writing – original draft, writing—review & editing
Livia Nistor-Lopatenco: Supervision, writing—review & editing, validation, project administration.
Efim Zubco: Conceptualization, investigation, methodology, data curation.
Alexandru Fărîmă: Conceptualization, investigation, methodology, data curation, software.

Conflicts of Interest: The authors declare no conflict of interest.

References

1. Land Administration Domain Model (LADM), ISO 19152:2012 - Geographic information. International Organization for Standardization, https://www.iso.org/standard/81263.html#lifecycle (accessed on 10 September 2025).
2. Lemmen C., Van Oosterom, P., Bennett, R. (2015) The Land Administration Domain Model. Land Use Policy, 49/2015. https://www.researchgate.net/publication/272828680_The_Land_Administration_Domain_Model.
3. Law on the Real Estate Cadastre No. 1543 of 25.02.1998. Republic of Moldova. https://www.legis.md/cautare/getResults?doc_id=150224&lang=ro# (accessed on 10 September 2025).
4. Van Oosterom, P. (2013) Research and development in 3D cadastres. Computers, Environment and Urban Systems, 40/2013. https://www.researchgate.net/publication/257055326_Research_and_development_in_3D_cadastres
5. Stoter, J., Van Oosterom, P. (2006) 3D Cadastre in an International Context: Legal, Organizational, and Technological Aspects. CRC Press, 344 p.
6. Uşak, B., Çağdaş, V., Kara, A. (2024) Current Cadastral Trends—A Literature Review of the Last Decade. Land 2024, 13(12), 2100, https://doi.org/10.3390/land13122100.
7. Jaljolie, R., Van Oosterom, P., Dalyot, S. (2018) Spatial data structure and functionalities for 3D land management system implementation. Israel Case Study. ISPRS International Journal of Geo-Information, 7, Article No. 10. https://doi.org/10.3390/ijgi7010010.
8. Stoter, J., Ploeger, H., Van Oosterom, P. (2013) 3D cadastre in the Netherlands: Developments and international applicability. Computers, Environment and Urban Systems, 40/2013. https://gdmc.nl/publications/2013/CEUS_3D_Cadastre_Netherlands.pdf
9. Țîganu E., Țîganu D., Vlasenco A., Nistor-Lopatenco L. (2024) The Application of Terrestrial Laser Scanning to Monitoring the Cricova Underground Mine in the Republic of Moldova. In: RevCAD 37/2024. http://revcad.uab.ro/upload/58_949_16_tiganu_tiganu_vlasenco_lopatenco.pdf

10. Nistor-Lopatenco L., Țiganu E., Vlasenco A., Iacovlev A., Grama V. (2022) Creation of the Point Cloud and the 3D Model for the Above-Ground Infrastructure in the City of Chisinau by Modern Geodetic Methods. In Bulletin of theTransilvaniaUniversity of Braşov Vol. 15(64) No. 1-2022. https://doi.org/10.31926/but.ens.2022.15.64.1.2
11. Erba, D. A. (2012) Application of 3D Cadastres as a Land Policy Tool, Lincoln Institute of Land Policy. https://www.lincolninst.edu/app/uploads/legacy-files/pubfiles/2021_1345_Application_of_3D_Cadastres.pdf (accessed on 05 October 2025).
12. Van Oosterom, P. (2023) International Panorama of Cadastre in 3D. EuroGeographics. https://eurogeographics.org/app/uploads/2023/07/Sesion-VI.-Ponencia-1.-Peter-Van-Oosterom.pdf
13. Rebong, F. R., Meilano, I., Sadarviana, V., Hernandi, A., Abdulharis, R., Meilani, R. (2025) Strategy for the Conversion of 2D to 3D Cadastral Maps by Standardizing the Height Limit of Land Rights Space Based on Land Use/Land Cover.L, 14(4), 763. https://doi.org/10.3390/land14040763
14. Van Oosterom, P., Lemmen, C., Uitermark, H. (2009) Land administration as a cornerstone in the global spatial information infrastructure. International Journal of Spatial Data Infrastructures Research, 4/2009. https://ris.utwente.nl/ws/portalfiles/portal/448978007/141-684-2-PB.pdf
15. Informational portal: e-Cadastre. https://www.cadastru.md/ecadastru/f?p=100:1 (accessed on 28 October 2025).
16. Interactive map. S. E. "State Road Administration"(SRA). https://www.andsa.md/harta-interactiva/ (accessed on 28 October 2025).
17. Geodata Thematic Geoportal, https://geodata.gov.md (accessed on 05 November 2025).
18. Leica BLK360 Imaging Laser Scanner. https://leica-geosystems.com/products/laser-scanners/scanners/blk360 (accessed on 05 November 2025).
19. Fărîmă, A. (2026) Three-dimensional (3D) cadastre in the Republic of Moldova: from international standards to functional implementation. Master's thesis, Technical University of Moldova, Chișinău, Moldova. [in Romanian].
20. Leica Cyclone REGISTER 360. https://leica-geosystems.com/products/laser-scanners/software/leica-cyclone/leica-cyclone-register-360 (accessed on 20 November 2025).
21. Regulation on the transition to the global and reference coordinate systems and the respective cartographic projections. Approved by the Agencyfor Land Relations and Cadastre (ALRC), and implemented by order no. 185of July 10, 2001.
22. Vlasenco, A. (2019) Contributions regarding the improvement of coordinate transformation parameters and the modification of cartographic projections for the territory of the Republic of Moldova. Ph.D. Thesis, Technical University of Moldova, Chișinău, Moldova [in Romanian].
23. Shevchenko, G., Gura, D., Moskvina, P., Popova, I., Akopyan, G. (2020) Three-dimensional cadastre in creating an information base for a spatial model of a real estate object. E3S Web of Conferences 164(14):07012. https://doi.org/10.1051/e3sconf/202016407012
24. LAW No. 1543 of 25-02-1998 on the real estate cadastre, Republic of Moldova. https://www.legis.md/cautare/getResults?doc_id=150224&lang=ro#, (accessed on 10 December 2025).
25. Zakaria, F. A., Mohd Yatim, M. H., Mohd Ariff, M. F., Razali, A. F., Tan, L. C. and Abdul Hamid, H. (2024) Utilizing Terrestrial Laser Scanning Dataset for Cadastral Surveying. ournal of Advanced Geospatial Science and Technology. 4(2),205-230. https://jagst.utm.my/index.php/jagst/article/view/79.
26. OpenAI. (2024). DALL-E 3: AI Image Generation Model. Accessed through ChatGPT platform. Available online: https://openai.com/dall-e-3 (accessed on 20 December 2025).

Citation: Vlasenco A., Nistor-Lopatenco L., Zubco E., Fărîmă Al-dru. (2026). Terrestrial laser scanning for 3D cadastre: A case study of road infrastructure in the Republic of Moldova. *Journal of Engineering Science*. 2026, 33 (1), pp. 133-145. https://doi.org/10.52326/jes.utm.2026.33(1).09.

Submission of manuscripts: jes@meridian.utm.md

Journal of Engineering Science *Vol. XXXIII, no. 1 (2026), pp. 146 - 164*
Fascicle *Food Engineering* *ISSN 2587-3474*
Topic *Food Technologies and Food Processes* *eISSN 2587-3482*

https://doi.org/10.52326/jes.utm.2026.33(1).10
UDC 664.681.15:664.64:543:635.658

PHYSICOCHEMICAL, SENSORY AND TEXTURAL EVALUATION OF SUGAR BISCUITS SUPPLEMENTED WITH LENTIL FLOUR

Olga Boestean*, ORCID 0000-0002-0390-3550,
Viorica Bulgaru, ORCID 0000-0002-1921-2009,
Natalia Netreba, ORCID 0000-0003-4200-1303,
Aliona Ghendov-Mosanu, ORCID 0000-0001-5214-3562

Technical University of Moldova, 168 Stefan cel Mare blvd., Chisinau, Republic of Moldova
* Corresponding author: Olga Boeștean*, olga.boestean@tpa.utm.md*

Received: 01. 23. 2026
Accepted: 03. 12. 2026

Abstract: Grain legumes are widely acknowledged as fundamental sources of dietary protein on a global scale. In particular, lentil proteins contribute not only essential amino acids to the human diet but also serve as a source of bioactive peptides with documented health-promoting properties. The present study aimed to evaluate the impact of lentil flour (*Lens culinaris*) incorporation on the quality attributes, color, and textural properties of sugar biscuits. Lentils are highly valued due to their well-balanced nutritional composition. The analyzed red lentil variety exhibited a notable chemical profile, characterized by a protein content of 31.35 g/100 g, lipid content of 1.87 g/100 g, and dietary fiber content of 12.6 g/100 g. Sugar biscuits formulated with varying levels of lentil flour (1–15%) were assessed in terms of sensory characteristics, physicochemical properties, texture parameters, and color indices. Among the tested formulations, the sample containing 10% lentil flour achieved the highest overall evaluation score. Based on the obtained quality indicators, the biscuits can be considered safe for consumption, maintaining their key quality attributes over a storage period of up to 35 days under specified conditions. Consequently, these products may be recommended as part of the diet for diverse consumer groups.

Keywords: *legumes, lentil, flour, biscuits, texture, sensory quality, physicochemical quality.*

Rezumat. Boabele leguminoaselor sunt recunoscute pe scară largă ca surse importante de proteine alimentare la nivel global. În mod particular, proteinele din linte furnizează nu doar aminoacizi esențiali, ci constituie și o sursă de peptide bioactive cu efecte benefice asupra sănătății. Scopul prezentului studiu a fost evaluarea efectului încorporării făinii de linte (*Lens culinaris*) asupra caracteristicilor de calitate, culorii și proprietăților texturale ale biscuiților zaharoși. Lintea este apreciată pentru compoziția sa nutrițională echilibrată. Soiul de linte roșie analizat a evidențiat un profil chimic valoros, caracterizat printr-un conținut de proteine de 31,35 g/100 g, lipide de 1,87 g/100 g și fibre alimentare de 12,6 g/100 g. Biscuiții zaharoși formulați cu diferite proporții de făină de linte (1–15%) au fost evaluați din punct de vedere al caracteristicilor senzoriale, proprietăților fizico-chimice, parametrilor texturali și indicilor

de culoare. Dintre variantele analizate, proba cu adaos de 10% făină de linte a înregistrat cel mai ridicat scor global. Pe baza indicatorilor de calitate determinați, biscuiții pot fi considerați siguri pentru consum, menținându-și caracteristicile esențiale pe o perioadă de depozitare de până la 35 de zile, în condiții specificate. În consecință, aceștia pot fi recomandați pentru includerea în alimentația diferitelor categorii de consumatori.

Cuvinte cheie: *leguminoase, linte, făină, biscuiți, textură, calitate senzorială, calitate fizico-chimică*.

1. Introduction

The active and healthy lifestyle of people requires a rational diet presented by the content of essential amino acids in food, which are involved in metabolic processes, energy generation and regeneration. The vegetarian diet does not accept animal products. Protein deficient diet can lead to many disorders such as colon cancer, heart disease and osteoporosis [1, 2]. Thus, for a complete existence, it is necessary to find ways to enrich the daily diet with protein products.

Lentils (lat. *Lents*) is a leguminous plant native to the Near East and is one of the oldest legumes cultivated alongside wheat, barley and peas. Lentils have a well-balanced nutritional profile, consisting of 22.7% protein (including all essential amino acids), 51% carbohydrates, 13.8% dietary fiber, and 1% lipids [3]. Lentils are a valuable plant-based protein-rich product [4].

Due to its nutritional value, the possibility of using lentils, namely, lentil flour as a component of the recipe for the preparation of floury confectionery products, is of scientific interest. Wilson et al. [5] concluded that lentil consumption improved insulin sensitivity in obese individuals, contributing to lower blood glucose and improved insulin status. In other works, it has been reported [6, 7, 8] that lentil consumption improves arterial elasticity, counteracts atherosclerotic disease and helps lower blood pressure. Other researchers have reported that the consumption of lentils may have a dietary effect for people facing obesity as a preventive measure against cancer, chronic diseases and hypertension during life [1, 9]. In recent years, lentils have become a popular food among people who suffer from a genetic dysfunction and cannot digest some proteins in the cereal composition (gluten intolerance) [10].

Biscuits are a popular bakery product, but their low content of protein, fiber, minerals, and vitamins makes them less suitable for regular daily consumption [11]. Considering that biscuits are flour confectionery products in constant demand [11] by the population, especially children, adolescents and the elderly, there is a great interest in their fortification with value-added compounds [10, 12-14]. Biscuits occupy the first place (36%) in the Republic of Moldova in terms of the flour confectionery products volume (Figure 1).

The mixture of flours containing legumes and wheat flour could effectively increase the nutritional and functional value of the product [15]. Fortification with food ingredients rich in proteins and micronutrients is one of the main strategies adopted to improve the nutritional quality of the population in rural areas of developing countries [16]. For young children, fortified crackers are widely used as a way to solve the crucial problem of malnutrition. The enrichment of products with vegetable proteins can be achieved by introducing legumes into the technological recipes of flour confectionery products. This highlights the potential of legumes to enrich the product with biologically active substances, to increase its nutritional and biological values, to increase the yield of the finished product and to contribute to the increasing the shelf life of food products [17, 18].

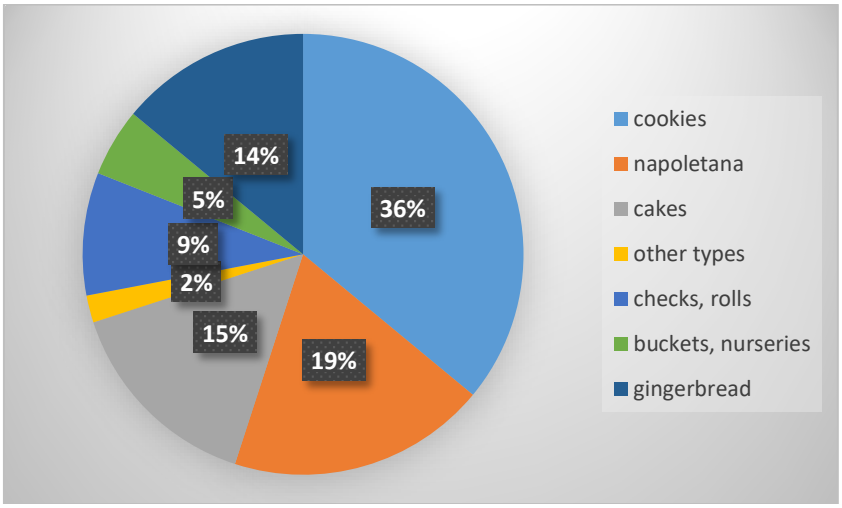

Figure 1. Structure of the manufacturing flour confectionery products volume [1].

According to the results of other scientists, the addition of lentil flour has been proposed to enrich with dietary fiber up to 20%, which will help to increase the protein content of the product up to 2 – 5%, also in order to reducing the energy value of the product [17-20].

The quality of flour confectionery products is a combination of properties that determine their ability to rationally satisfy human needs for a healthy diet. The nutritional value of flour confectionery products is determined by the quantitative content and qualitative composition of proteins, fats, carbohydrates, minerals, vitamins, as well as their energy value [4].

The aim of the work was to develop a technology for manufacturing sugary biscuits with lentil flour and to investigate its effect on the quality of the end product, color parameters, textural properties and microbiological stability during storage.

2. Materials and Methods

2.1. Chemical Materials

Hydrochloric acid (37 %), sodium hydroxide (97 %), phenolphthalein, bromothymol blue, sodium nitrite (≥97,0 %), aluminum chloride, sodium citrate (≥99,0 %), trisodium citrate, silver nitrate (≥99,0 %), hexane reagent (>99 %), hydrochloric acid (37 %), KjTabs VST, Vreceiver TKN, sulfuric acid (95,0–98,0 %), sodium hydroxide (≥85 %), were purchased from Sigma (Darmstadt, Germany; Tokyo, Japan; Shanghai, China).

2.2. Biological Materials

The seeds of red lentils *(Lens culinaris* L.*)*, peas *(Pisum sativum)* and beans *(Phaseolus vulgaris)* were received from the Institute of Genetics, Physiology and Plant Protection, Chisinau.

2.3. Characteristic of Wheat and Legume Flour

Legume seeds were dried in a laboratory dryer (SLW 115 SMART) with forced air circulation at a constant temperature of 50 ± 2 °C and relative air humidity of 60–65 %. The drying process was carried out for 5 hours. The final moisture content of the dry seeds was 14.02± 0.04%. Legume seeds were crushed in a laboratory hammer mill (PERTEN LM 120, Sweden) into powder with a particle size of 180±15 μm, sieved and vacuum packed for further use in this study.

2.3.1. Sensory Analysis of Wheat Flour and Red Lentil Flour

Sensory indices were determined for wheat and lentil flour in terms of pest infestation, colour, odor and taste according to BS ISO 6658-2005 – Sensory Analysis – Methodology – General quidance [21].

2.3.2. Physicochemical Analysis of Wheat and legumes

The moisture (method 44-19), ash (method 08-01), crude protein (method 46-12), crude fat (method 30-25), and total fiber contents were determined according to [22]. Fat content was quantified gravimetrically following hexane extraction from the dehydrated sample using the Soxhlet method with a SER148 Solvent Extraction Unit (VELP Scientifica, Monza, Italy). Protein content was estimated by determining total nitrogen and applying a conversion factor of 6.25, using the Kjeldahl method with a UDK129 unit (VELP Scientifica, Italy). Titratable acidity was measured by titrating a known volume of sample with standard 0.1 N NaOH, using phenolphthalein as an indicator [23]. The pH was measured using a pH meter (TESTO 206-pH2, Pruszków, Poland), calibrated with pH 4.0 and 7.0 buffer solutions. The electrode was directly immersed in a beaker containing the sample macerated with distilled water, following the method [24].

Wet gluten content [25 - 27] was carried out by washing the dough prepared from the analyzed flour, the water temperature being 18-20°C and whipping the obtained gluten.

Equation (2) was used to determinate the wet gluten content, expressed in %:

$$Wet\ gluten = \frac{m_1}{m} \cdot 100, \quad (1)$$

where:

m_1 – wet gluten mass remaining after churning, g;

m – flour sample mass taken for determination, g.

Gluten quality: elasticity was achieved using the IDK-3M device by determining the ability of gluten to resist compression [25-27]. The extensibility consists in manually stretching the wet gluten (5 g) modeled in the form of a wick, until breaking, under established conditions and measuring the length reached by the gluten at the time of breaking [25-27].

2.4. Preparation and Characterization of Sugar Cookies with the Addition of Red Lentil Flour

2.4.1. Preparation of Sugar Cookies with the Addition of Red Lentil Flour

Biscuits samples were made using 1% to 15% lentil flour (SLF1 – sugary biscuits with 1% lentil flour; SLF5 – sugary biscuits with 5% lentil flour; SLF 10 – sugary biscuits with 10% lentil flour; SLF 15 – sugary biscuits with 15% lentil flour.). For the control, a sample was prepared without the addition of LF (CS – control sample,100% high quality wheat flour). High quality wheat flour, sugar, butter, salt and baking powder were used to make sugar cookies. Respective raw materials were purchased from the local market. Sample recipes were calculated according to the dry matter and moisture content of the raw material, Table 1.

To prepare the dough, a mixture of sugar and fat is made, homogenized for 3-4 minutes, after which approximately 50% of the wheat flour is added. Knead in the bowl of the food processor (Tefal QB150138, Germany) for 7-10 min, then salt, the rest of the wheat flour and lentil flour, chemical softener, vanillin were added and kneaded for about 10 min.

Table 1

Recipe of experimental samples

Components	CS	SLF 1	SLF 5	SLF 10	SLF 15
Premium quality wheat flour, g	100	99	95	90	85
Red lentil flour, g	0	1	5	10	15
Cow butter,g	25	25	25	25	25
Salt, g	2	2	2	2	2
Powdered sugar, g	35	35	35	35	35
Chemical softener, g	2	2	2	2	2
Vanilla, g	0,7	0,7	0,7	0,7	0,7

Note: CS – control sample, 100 % premium quality wheat flour; SLF1 – sugar biscuits with 1 % lentil flour; SLF5 – sugar biscuits with 5 % lentil flour; SLF 10– sugar biscuits with 10 % lentil flour; SLF 15– sugar biscuits with 15 % lentil flour.

The temperature of the kneaded dough was 23±1 ºC. The rested dough was subjected to lamination in the form of a continuous sheet of 2-4 mm thickness. The modeling was done by hand using the die that cuts the modeled pieces. The stamped blank with a mass of 15 ± 1 g was baked in an electric convection oven (EASY EV-UME604-LS, Luxstahl, PiggioTorriana, Italy) at 190 ± 2 °C for 10 ± 1 min. After baking, the biscuits were cooled, packaged and stored in a dry place at room temperature.

2.4.2. Physicochemical Analysis of Dough and Sugar Biscuits

The moisture content of dough and sugar cookies was determined according to the AACC standard (AACC, Method 44-15.02) [28]. Alkalinity was determined by neutralization by titration with 0.1 N hydrochloric acid solution in the presence of bromothymol blue as an indicator and is expressed in degrees of alkalinity [29].

The absorption index of sugar cookies was determined according to [30].

The water activity (a_w) of the baked biscuits was measured at room temperature (20 ± 1 °C) using the LabMaster dew point water activity apparatus (Novasina AG, CH-8853 Lachen, Switzerland) [31]. The determinations were carried out within 35 days: on the 1st day, the 10th, the 20th and the 35th day.

2.4.3. Texture Profile Analysis of Dough

A Stable Micro Systems TA.HD Plus C analyzer (UK) was used to perform texture profile analysis of sugar biscuits dough. The textural properties of the dough samples—including hardness, cohesiveness, gumminess, resilience, and adhesiveness—were determined using a 40 mm cylindrical probe through a double compression test with a P/75 stainless steel plate. The test was conducted under the following conditions: pre-test speed of 100 mm/s, test speed of 5 mm/s, post-test speed of 5 mm/s, and a load cell capacity of 5 kg [32]. Textural determinations were performed on the day of dough preparation.

2.4.4. Sensory Analysis of Sugar Cookies

The sensory analysis of the biscuits was conducted by a panel of nine assessors, who evaluated the following attributes: shape, surface, color, taste, aroma, and cross-sectional appearance. Sensory quality was assessed using a 5-point scale. The evaluation was performed in individual booths under white light at room temperature. The panel developed a set of attributes and scored the samples as follows: 5 – very good (exceptional quality, ideal); 4 – good (acceptable quality); 3 – satisfactory (minor defects); 2 – unsatisfactory (clearly noticeable defects); 1 – poor (pronounced defects); 0 – very poor (major

deterioration). Each sample was analyzed in parallel in a laboratory designed for sensory evaluation in accordance with ISO 8589 [33]. The samples were served in lidded plastic containers, coded with random numbers, and presented in random order. A break of up to 5 minutes was allowed between evaluations. The determinations were carried out the following day.

2.4.5. Microbiological Analysis of Sugar Biscuits

The microbiological investigation: the dilution method was used for the quantitative calculation of colony forming units (CFU) in determining the corresponding groups of microorganisms in 1 cm^3 of bacterial solution. Basic dilutions (10^1, 10^2, 10^3) were prepared as follows: 1 g of each biscuit sample was added to a test tube containing 9 cm^3 of saline (0.85%) or sterilized water. In Petri dishes with a gel-like nutrient substrate, 1 cm^3 of a bacterial solution was inoculated in triplicate. For the cultivation of microorganisms, two types of nutrient media were used to separate groups of microorganisms: agar for bacteria (48 h of incubation at 28 °C) and Sabouraud for yeast (5 days of incubation at 25 °C). After incubation, the results were analyzed and different types of microorganisms were identified in terms of cultural and morphological characteristics. The bacterial culture was further identified by Gram staining [34-37]. The determinations were carried out within 35 days: on the 1st day, the 10th, the 20th and the 35th day.

2.4.6. The Energy Value of Sugar Cookies

The energy value of sugar cookies (kcal/100g) was calculated. The conversion factors for calculating the energy value of the main nutrients in food were as follows, in kcal/g: carbohydrates – 4; proteins – 4; lipids (fats) – 9; fibers – 2 [38].

2.5. Color Analysis of Lentil Flour and Sugar Biscuits Using the CIELAB Method

The CIELab parameters of sugar cookies with the addition of lentil flour were measured using a Chroma Meter CR-400/410 colorimeter (Konica Minolta, Tokyo, Japan), according to the method [39]. Each sample was analyzed at three distinct points, measuring the variations in luminance (L*), red/green component (a*), yellow/blue component (b*). The overall color difference (ΔE*) was calculated according to Eq. (2).

$$\Delta E^* = \sqrt{(L_i^* - L_0^*)^2 + (a_i^* - a_0^*)^2 + (b_i^* - b_0^*)^2}, \quad (2)$$

where:

$L_0^*, a_0^* \; and \; b_0^*$ – the sample values on the day of baking;

$L_i^*, a_i^* \; and \; b_i^*$ –the sample values in storage days.

The determinations were carried out within 35 days: on the 1st day, the 10th, the 20th and the 35th day.

2.6. Statistical Analysis

All analyses were performed in triplicate, and the results are expressed as mean values ± standard error of the mean. Microsoft Office Excel 2007 (Microsoft, Redmond, WA, USA) was used for data processing. Statistical analysis was conducted using one-way analysis of variance (ANOVA), followed by Tukey's test at a significance level of $p \leqslant 0.05$, using Statgraphics Centurion XVI version 16.1.17 (Statgraphics Technologies, Inc., The Plains, VA, USA).

3. Results and Discussion

3.1. Characteristic of Wheat Flour and Legumes

The vegetable raw material from the Leguminosae family *(Fabaceae or Papilionaceae family)* – lentils, beans and peas – were analyzed. Lentil seeds have a high content of protein and dietary fiber compared to peas and beans, this can be seen from Table 2.

According to other researchers, lentils are rich in protein and these values vary between 22-31% [40 -42], the protein content of peas [43] varies between 21-27% and beans 20 -41% [40, 44]. The protein content obtained from the research should fall within these values, being 31.35±0.79, 23.01±0.01 and 21.04±0.12, respectively, for lentils, peas and beans.

Table 2

The nutritional value of legumes

Legumes	Protein content, %/100g	Fat content, %/100g	Carbohydrate content, %/100g	Dietary fiber content, %/100g	Moisture content, %	Ash, %	Energy value, kcal/100g
Lentils	31.35± 0.19 ^{c}	1.87± 0.01 ^{b}	43.30 ± 0.12 ^{a}	12.60± 0.15 ^{c}	11.27± 0.05 ^{c}	2.33± 0.01 ^{a}	314
Peas	23.01± 0.24 ^{b}	1.60± 0.02 ^{a}	48.00± 0.19 ^{c}	10.70± 0.09 ^{b}	9.71± 0.10 ^{a}	3.45± 0.03 ^{b}	317
Beans	21.04± 0.12 ^{a}	2.00± 0.02 ^{b,c}	47.00± 0.13 ^{b}	10.40± 0.16 ^{a}	10.86± 0.08 ^{b}	3.50± 0.05 ^{b}	286

Note: Different letters ($^{a-c}$) designate statistically different results ($p \leqslant 0.05$).

Grusak [45] reported the following data on fat content, compiled from different studies: for lentils – 0.3-3.5% [40 - 42], for peas –1.2 – 7.3% [46, 47], for beans – 1 .66 – 2.13% [48].

The values of moisture content 9.71±0.02% for peas, 10.86±0.02% for beans and 11.27±0.01 for lentils are similar to the study data [46, 49].

The results regarding the dietary fiber content of legumes varied from 10.4±0.02 to 12.6±0.05%. Lentils were the richest source of fiber, followed by peas and beans. The data were in agreement with [46, 47, 50] who reported that dietary fiber in lentils is found to be 7.9-12.0%, in peas and beans, 16.7 % and 10-20%, respectively [47, 50, 51]. The ash content in the investigated samples was 2.33±0.01 for lentils, in peas 3.45±0.01 and in beans 3.50±0.01%.

Table 2 shows that lentils contain the highest amount of protein and fiber (24% and 12.5% respectively) compared to peas and beans. It is lower in carbohydrates and lipids (46% and 1.5% respectively).

For the manufacture of biscuits, the quality of wheat flour and lentil flour (LF), which correspond to the norms provided in the normative acts, was analyzed sensoryally, Table 3.

Table 3

Organoleptic analysis of wheat and lentil flour

Flour type	Organoleptic indices			
	Color	Odor	Taste	Pest infestation
Premium quality wheat flour	White with a slight yellowish tint	Pleasant, characteristic of flour, without foreign or musty smell	Sweet, without crunch when chewing	Absent

Continuation Table 3

Lentil flour	Yellow characteristic of the variety	Pleasant, characteristic of flour, without foreign or musty smell	Characteristic, without crunch when chewing	Absent

According to the organoleptic indicators, the flours should be certified according to the color characteristic of the variety, with a pleasant taste and smell without the smell of foreignness or mold. The data obtained regarding the organoleptic analysis of high-quality wheat and lentil flour are correlated with the data of the normative acts in force in this field [52, 53].

The physicochemical indicators of wheat and LF were determined and are presented in Table 4.

Table 4

Physico-chemical indicators of wheat and lentil flours

Indicators	Premium quality wheat flour	Lentil flour
Moisture content, %	13.50±0.08	11.27±0.01
Acidity, degree	2.65±0.04	4.05±0.02
Ash, %	0.47±0.02	2.33±0.01
Gluten content, %	22.00±0.01	Not determined
Elasticity, c.u.	69.0±0.1	Not determined
Extensibility, cm	14.0±0.1	Not determined
Fat content, g/100g	1.00±0.02	1.87±0.01
Protein content, g/100g	10.3±0.02	31.35±0.19
Total fiber content, g/100g	2.68±0.02	12.6±0.15
Finesse, %	Characteristic of wheat flour	Characteristic of lentil flour
The content of ferromagnetic impurities, mg/kg	Not detected	Not determined

The obtained data regarding the analysis of the physico-chemical indicators of high-quality wheat flour are correlated with the data of the in force normative acts [52, 53].

The moisture content of lentil flour was lower by 1.2% compared to wheat flour, similar results being obtained by other authors [54]. The low moisture content of lentil flour protects it from the danger of mold growth. The acidity of lentil flour (4.05 degree) was higher than the acidity of wheat flour (2.65 degree). This is probably related to the presence of free fatty acids in lentils [55]. Lentil flour was characterized by a major content of mineral substances [56, 57]. The protein content of lentils was high and varies between 19.5% - 35.5% [40]. Lentil proteins were highly valued due to their high digestibility (~83 %) [58]. The analyzed red lentil variety presented an appreciable chemical composition, with a protein content of 31.35 g/100g. The fiber content of lentil flour was 5 times higher than that of wheat flour [3].

3.2. Characteristic of dough and sugar cookies

The dough was prepared according to the established recipe and subjected to the technology described in p. 2.4.1. The determinations were carried out the following day. The results obtained, regarding the physico-chemical evaluation of the dough, are presented in Table 5.

Table 5

Physico-chemical characteristics of dough with red lentil flour

Sample	Characteristics	
	Moisture content, %	Alcalinity, degrees
CS	27.0±0.3 [a]	1.00±0.01 [e]
SLF 1	28.3±0.5 [b]	0.96±0.01 [d]
SLF 5	29.7±0.4 [c]	0.92±0.01 [c]
SLF 10	30.2±0.5 [c,d]	0.88±0.0 [b]
SLF 15	32.12±0.2 [d]	0.84±0.01 [a]

Note: CS – control sample – 100 % Premium quality wheat flour; SLF1 – sugar biscuits with 1 % lentil flour; SLF5 – sugar biscuits with 5 % lentil flour; SLF 10– sugar biscuits with 10 % lentil flour; SLF 15– sugar biscuits with 15 % lentil flour. Different letters ([a–e]) designate statistically different results ($p \leqslant 0.05$).

Analyzing the experimental results, an increase in moisture values was observed from 27.00% (CS) to 32.12% (SLF 15), by 1.19 times. This contributed to the increase the dough's hydration capacity. This was explained by the fact that the higher the protein and soluble fiber content, the higher the flour hydration capacity. According to [59] the dough could become softer due to the increased solubility of sugar in the dough formulation. Similar results were obtained by Taylor et al. [60], who stated that sugars with a higher solubility result in a soft dough. Dough alkalinity decreased with increasing lentil flour addition due to more organic acids and alkaline substances in lentil flour compared to wheat flour, such as potassium and magnesium. The alkalinity indicator did not exceed the conditions regarding admissibility (at most 2.0 degrees) [61].

During the dough kneading process, the dough was observed to have superior structural-mechanical properties, which aided kneading and was explained by the lipid content of the lentil flour [62].

Dough is a material with visco-elastic properties due to the presence of glutenins and gliadins in its molecular structure. Dough texture is not usually measured during mixing and processing, but its rheological properties are used as a guide for dough processing and its influence on the baked product structure, being even an indicator of the appearance and quality of the finished food products [63]. In the further processing of the dough after mixing, its relaxation played an important role on the dough textural characteristics [64]. The texture parameters of the dough with the addition of LF were presented in Table 6.

Table 6

Texture parameters of sugar biscuits dough with the addition of lentil flour (results are presented as mean ± standard deviation)

Dough samples	Hardness, g	Cohesiviness, %	Resilience, %	Gumminess, g	Chewiness, g
CS	1146.67±40.07 [a]	0.526±0.006 [d]	0.155±0.001 [d]	603.14±10.20 [a]	603.75±10.02 [a]
SLF 1	1301.88±20.09 [b]	0.518±0.009 [c,d]	0.149 ±0.002 [c]	674.37±15.16 [b]	675.04±13.11 [b]
SLF 5	1576.49±18.05 [c]	0.504±0.010 [c]	0.147±0.001 [b,c]	794.55±10.11 [c]	795.34±9.07 [c]
SLF 10	1863.90±32.11 [d]	0.473±0.006 [b]	0.137±0.001 [a]	881.62±13.26 [d]	883.38±12.09 [d]
SLF 15	1981.11±25.07 [e]	0.440±0.006 [a]	0.135±0.001 [a]	871.68±5.20 [d]	873.42±8.16 [d]

Note: CS – control sample – 100 % premium quality wheat flour; SLF1 – sugar biscuits with 1 % lentil flour; SLF5 – sugar biscuits with 5 % lentil flour; SLF 10– sugar biscuits with 10 % lentil flour; SLF 15– sugar biscuits with 15 % lentil flour. Different letters ([a–e]) designate statistically different results ($p \leqslant 0.05$).

Dough hardness increases for all samples with values between 11.92% and 42.11%. The hardness of the dough increased because of the addition of lentil flour, which is a gluten-

free raw material that could contribut to the reducing the gluten amount and could have a negative effect on its structure. Similar results were obtained by the authors [50.] when they substituted wheat flour with 10 % germinated lentil flour to obtain bread, where the increase in hardness was about of 14 %. Also, the increase in the hardness value can be affected by the interactions between the wheat flour gluten and the lentil flour dietary, fibers with increased water retention capacity [65]. This combination can weaken the gluten structure. On the other hand, the increase in dough hardness can be influenced by the interaction of starch with the increased amount of protein, due to the addition of lentil flour, which is a protein rich legume [66].

The obtained results for cohesiveness and resilience were decreasing, proportionally with the increase in the content of lentil flour in the dough, by 19.50 % and almost 15 %, respectively. As in the case of hardness, the values for these two parameters are mainly affected by the decrease in the gluten amount of the end product, considering the wheat flour replacement with lentil flour. Similar results were obtained by other authors [67] where they used germinated lentil flour to replace wheat flour, and the decrease in the respective parameters values was almost 3 times compared to the control sample. The values for gumminess and chewiness are higher compared to the control sample. For both parameters, the highest increase, 31 %, was observed for the dough with the addition of 10 % lentil flour. According to other authors [68] the obtained results are characteristic for more compact structures that could be due to a higher content of food fibers in the end product, coming from the added lentil flour and the changes that the starch undergoes. The values for these parameters increased proportionally with the increase in dough of the lentil flour content.

3.3. Characteristic of biscuits

One of the marketing requirements for biscuits is to increase their shelf life. The quality of the biscuits was evaluated during the 35-day storage period, with the exception of the sensory analysis that was done on the day the biscuits were baked. The results of sensory and physico-chemical analysis of sugar cookies samples are presented in Table 7.

Table 7

Sensory analysis and energy value of sugar biscuits with lentil flour (results are presented as mean ± standard deviation)

Characteristics	Sugar biscuits				
	CS	SLF 1	SLF 5	SLF 10	SLF 15
Average score of sensory profile	4.59 ± 0.01 ^{a}	4.66 ± 0.01 ^{b,c}	4.90 ± 0.01 ^{d}	4.55 ± 0.01 ^{a}	4.50 ± 0.01 ^{a}
Consistency	4.81 ± 0.01 ^{b}	4.82 ± 0.02 ^{b,c}	4.89 ± 0.02 ^{c}	4.53 ± 0.02 ^{a}	4.51 ± 0.01 ^{a}
Taste	4.75 ± 0.02 ^{b}	4.81 ± 0.01 ^{c}	4.91 ± 0.01 ^{d}	4.75 ± 0.01 ^{b}	4.65 ± 0.01 ^{a}
Appearance	4.51 ± 0.01 ^{a}	4.65 ± 0.0 ^{b}	4.95 ± 0.02 ^{c}	4.65 ± 0.0 ^{b}	4.62 ± 0.02 ^{b}
Color	4.32 ± 0.01 ^{a}	4.51 ± 0.02 ^{b}	4.85 ± 0.01 ^{c}	4.50 ± 0.02 ^{b}	4.51 ± 0.01 ^{b}
Odor	4.56 ± 0.02 ^{d}	4.52 ± 0.01 ^{c,d}	4.91 ± 0.02 ^{e}	4.31 ± 0.01 ^{b}	4.21 ± 0.01 ^{a}
The energy value, kcal/100 g	368	367	364	361	357

Note: CS – control sample – 100 % premium quality wheat flour; SLF1 – sugar biscuits with 1 % lentil flour; SLF5 – sugar biscuits with 5 % lentil flour; SLF 10– sugar biscuits with 10 % lentil flour; SLF 15– sugar biscuits with 15 % lentil flour; L *—luminosity; a *—red/green component; b *—yellow/blue component; ΔE * - overall difference of color. Different letters ($^{a-l}$) designate statistically different results ($p \leqslant 0.05$).

Sensory analysis of the biscuits showed that the highest average scores were obtained for the SLF 10 sample (4.9 points), followed by the 15% PSC sample (4.55 points) and the control sample (4.59 points) (Table 9). The highest score for consistency was recorded for the

SLF 10 sample (4.89 points). Substituting 15% of wheat flour with lentil flour slightly reduced the score to 4.53 points, resulting in a more brittle texture. In contrast, the control sample and those containing 1–10% lentil flour exhibited a firm consistency. According to Idowu et al. [69], the firmer texture observed in biscuits containing 1–10% lentil flour may be attributed to amylose and amylopectin recrystallization, the formation of starch–protein complexes, and water redistribution among product components. All analyzed biscuit samples exhibited a pleasant and uniform external appearance. The incorporation of lentil flour into the biscuit formulation significantly improved the taste, aroma, and color, as noted by all panelists. Similarly, Saleem et al. [70] reported high overall acceptability for biscuits made with a wheat-to-lentil flour ratio of 93:7. Awadelkareem et al. [71] also observed high acceptability for biscuits containing 5% and 10% lentil flour. Hajas et al. [72] found that biscuits made with red lentils were more preferred than those made with black lentils. Good overall acceptability has also been reported for biscuits containing 10% lentil flour [73]. However, the addition of 15% SLF negatively affected the taste and aroma of the biscuits due to a pronounced lentil flavor.

An important factor in calculating the energy value is the fiber content, which is involved in digestion but does not provide calories. Dietary fiber is often included in energy value calculations because it is hypothesized that it may have an effect on calorie absorption [74, 75]. LF generally contains fewer calories than wheat flour. Replacing some or all of the wheat flour with lentil flour can reduce the calorie content of the biscuits. LF is high in protein, which can increase the nutritional value of biscuits, providing an additional source of protein for consumers, and it also contains a significant amount of fiber, which can improve digestion and gut health. This can also influence the level of energy gradually released during digestion, which can have an impact on the perceived energy value of the biscuits. LF can also contain a variety of essential vitamins and minerals, such as iron, zinc and B-complex vitamins, which contribute to the overall nutritional value of the bistuits. Overall, the use of LF in biscuits can provide significant nutritional benefits, such as increased protein and fiber intake, but can also influence energy value by reducing calories and managing energy release during digestion.

In order to maintain a healthy lifestyle and monitor the intake of calories and nutrients, the energy value of the experimental samples was calculated. The energy value of the product is the amount of energy that a food product provides upon consumption, measured in kilocalories per 100 g (kcal/100g) [76]. The nutritional information was consulted and the energy value resulting from the content of carbohydrates, fats and proteins, dietary fibers contained in the product was calculated [77]. The energy value of the biscuit samples is lower than the control sample. The energy value of the experimental samples is lower by 0.03% at the 1% LF experimental sample, by 1.1% at the 5% LF experimental sample, by 2.0% at the 10% LF experimental sample and by 3,0 % in the experimental sample of 15 % LF. As LF was added, the energy value decreased, because with the increase in the content of lentil flour added to the samples, the content of dietary fibers increases, which contributes to the nutritional and biological value of the product, but although they are involved in the process of digestion, they do not provide calories, so they do not influence the energy value. The decrease in the energy value of biscuits with added LF could be attributed to several factors. When LF is incorporated into cookie recipes, the overall composition changes. LF has a lower fat content compared to traditional wheat flour. In addition, LF is high in protein and dietary fiber, which can affect overall energy density. Protein and fiber provide satiety without contributing significantly to energy content [78.].

According to the results shown in Table 8, with the addition of lentil flour, the moisture values increase insignificantly, since the difference in moisture between lentil flour and wheat flour was 0.23%.

Table 8

Physicochemical changes in sugar biscuits enriched with lentil flour during storage (results are presented as mean ± standard deviation)

Indicators	Storage time, days	Sugar biscuits				
		CS	SLF 1	SLF 5	SLF 10	SLF 15
Moisture content, %	1	6.00±0.04 ^{a,b}	6.21±0.02 ^{c}	6.23±0.01 ^{c}	7.25±0.02 ^{f}	7.35±0.06 ^{f,g}
	10	6.01±0.01 ^{a}	6.31±0.02 ^{d}	6.32±0.02 ^{d}	7.35±0.03 ^{g}	7.37±0.05 ^{g}
	20	6.04±0.01 ^{b}	6.37±0.01 ^{d}	6.39±0.02 ^{d}	7.46±0.01 ^{h}	7.47±0.04 ^{h}
	35	6.05±0.02 ^{b}	6.40 ±0.05 ^{d,e}	6.49±0.02 ^{e}	7.58±0.02 ^{h,i}	7.61±0.06 ^{h,i}
Alcalinity, degrees	1	0.50±0.0 ^{j}	0.49±0.01 ^{i,j}	0.48±0.01 ^{h,i}	0.47±0.01 ^{h,i}	0.42±0.0 ^{e}
	10	0.46±0.02 ^{g,h}	0.45±0.01 ^{f,g}	0.45±0.01 ^{f,g}	0.44±0.01 ^{f,g}	0.41±0.01 ^{e,d}
	20	0.44±0.01 ^{f,g}	0.42±0.0 ^{e}	0.40±0.0 ^{d}	0.39±0.01 ^{c,d}	0.38±0.01 ^{c}
	35	0.40±0.0 ^{d}	0.38±0.01 ^{c}	0.36±0.0 ^{b}	0.35±0.0 ^{b}	0.33±0.0 ^{a}
Swelling index, %	1	127±1 ^{e,f}	125±2 ^{d,e}	118±2 ^{b,c}	117±1 ^{b}	115±1 ^{a,b}
	10	129±1 ^{f,g}	136±0 ^{h}	119±2 ^{c}	125±1 ^{d,e}	116±1 ^{a,b}
	20	138±1 ^{h,i}	139±1 ^{h,i}	124±2 ^{d,e}	132±0 ^{g}	119±1 ^{b,c}
	35	146±1 ^{k}	144±1 ^{j,k}	142±1 ^{i,j}	143±1 ^{j}	136±0 ^{h}
Water activity, a_w	1	0.384±0.001 ^{e,f}	0.417±0.001 ^{h}	0.413±0.002 ^{h}	0.411±0.002 ^{h}	0.401±0.002 ^{g}
	10	0.382±0.001 ^{e}	0.380±0.001 ^{e}	0.374±0.001 ^{e}	0.409±0.001 ^{h}	0.399±0.001 ^{g}
	20	0.327±0.0 ^{d}	0.326±0.001 ^{d}	0.324±0.002 ^{d}	0.312±0.001 ^{c}	0.311±0.001 ^{c}
	35	0.320±0.001 ^{d}	0.305±0.002 ^{b,c}	0.301±0.001 ^{b}	0.301±0.002 ^{b}	0.278±0.001 ^{a}

Note: CS – control sample – 100 % premium quality wheat flour; SLF1 – sugar biscuits with 1 % lentil flour; SLF5 – sugar biscuits with 5 % lentil flour; SLF 10– sugar biscuits with 10 % lentil flour; SLF 15– sugar biscuits with 15 % lentil flour; L *—luminosity; a *—red/green component; b *—yellow/blue component; ΔE * - overall difference of color. Different letters ($^{a-l}$) designate statistically different results ($p \leq 0.05$).

A slight increase in humidity can also be explained by the addition of lentil flour which contains proteins that intersect with wheat flour proteins, forming a protein network [79-81] and affecting the viscoelastic properties of the dough, leading to changes in the microstructure of the baked biscuits. It can influence texture, moisture retention [82]. The moisture content of all samples remains within the limits of the values indicated in the normative documents.

The alkalinity values obtained were below the permissible limit, not exceeding the standard specified in regulatory guidelines (<2.0 degrees) [3]. The slight decrease in the alkalinity values was probably related to the presence of free fatty acids in the chemical composition of the lentil flour, which was demonstrated by the titratable acidity value (4.05 degrees).

Quality biscuits must absorb water quickly and in large quantities. During storage, the control sample showed the best result, which was within the allowed values of at least 140%. In the experimental samples of biscuits with the addition of lentil flour, the soaking index values decreased. During storage for 35 days, this parameter depending on the addition of lentil flour decreased by 1.11 times in the experimental samples in the first 10 days, by 1.16 times – on the 20th day of storage, 1.2 times, on the 35th day - by 1.2 times. This is due to the structural characteristics of the biscuits: the high moisture content of the biscuit may indicate the presence of moisture in its structure [83], the use of certain ingredients such as

sugar and butter, which may affect the texture and moisture content of the biscuit, resulting in a softer texture and higher moisture content [84], the low soaking index may be due to the denser structure of the biscuits, which makes it difficult for water to penetrate inside. Mohammadi et al. suggest that this effect can be attributed to the high protein and fiber content, as well as the presence of hydroxyl groups, which enhance the interaction with water molecules, thereby increasing moisture content and reducing the soaking index [85]. According to [86] the increase in moisture is due to the active increase in bound water as a consequence of the chemical and physical changes of the main components in the product.

The a_w results of the experimental samples showed that, with the increase in the amount of lentil flour, the water activity decreased. The obtained values indicated that in this product there was no probability of microbial development and product decomposition processes [87, 88]. The specialized literature attests that water activity values lower than 0.60 prevent microbial damage and show microbiological stability [89, 90].

The influence of storage time (35 days) on the CIELab color parameters of sugar cookies made with different concentrations of lentil flour was investigated, Table 9.

Table 9

Evolution of CIELab color parameters in sugar biscuits enriched with lentil flour during storage (results are presented as mean ± standard deviation)

Sample	Storage time, days	L*	a*	b*	ΔE*
CS	0	73.13±0.21 ^{i,j}	1.17±0.09 ^{c,d}	23.28±0.09 ^{b}	-
	10	73.75±0.11 ^{k,j}	1.36±0.07 ^{d,e}	24.17±0.04 ^{b}	1.01±0.01 ^{a}
	20	74.09±0.16 ^{k}	1.58±0.08 ^{e}	23.91±0.13 ^{b}	1.21±0.07 ^{a}
	35	75.04±0.17 ^{l}	1.37±0.08 ^{d,e}	22.48±0.10 ^{a}	2.08±0.05 ^{c}
SLF 1	0	72.44±0.11 ^{h}	1.48±0.07 ^{d,e}	25.33±0.04 ^{c}	-
	10	71.55±0.09 ^{g}	0.72±0.04 ^{b}	27.02±0.15 ^{d}	2.05±0.08 ^{b,c}
	20	73.55±0.13 ^{j}	0.22±0.02 ^{a}	23.01±0.11 ^{a}	2.86±0.11 ^{e}
	35	69.80±0.19 ^{c,d}	1.56±0.03 ^{e}	27.52±0.16 ^{d,e}	3.43±0.09 ^{g}
SLF 5	0	71.37±0.13 ^{f,g}	1.03±0.02 ^{c}	33.01±0.26 ^{j}	-
	10	72.38±0.10 ^{h}	0.98±0.01 ^{c}	32.71±0.18 ^{i,j}	1.05±0.05 ^{a}
	20	72.67±0.15 ^{h,i}	0.83±0.01 ^{b}	31.48±0.22 ^{h}	2.01±0.07 ^{b,c}
	35	73.01±0.13 ^{i}	0.71±0.04 ^{b}	30.37±0.19 ^{g}	3.12±0.09 ^{f}
SLF 10	0	70.62±0.14 ^{e}	1.53±0.05 ^{e}	29.51±0.15 ^{f,g}	-
	10	69.35±0.12 ^{c}	2.83±0.09 ^{g,h}	30.10±0.16 ^{g}	1.91±0.08 ^{c}
	20	69.88±0.20 ^{c,d}	2.10±0.01 ^{f}	27.40±0.07 ^{d,e}	2.31±0.06 ^{c,d}
	35	68.52±0.17 ^{a,b}	3.28±0.12 ^{i}	29.97±0.09 ^{g}	2.77±0.05 ^{e}
SLF 15	0	70.12±0.16 ^{d,e}	1.55±0.09 ^{e}	28.91±0.11 ^{g}	-
	10	69.75±0.15 ^{c,d}	2.63±0.05 ^{g}	29.10±0.08 ^{f}	1.16±0.03 ^{a}
	20	69.28±0.13 ^{c}	2.90±0.07 ^{g,h}	29.64±0.09 ^{f,g}	1.75±0.05 ^{b}
	35	68.72±0.10 ^{b}	3.30±0.05 ^{i}	29.97±0.13 ^{g}	2.48±0.02 ^{d}

Note: CS – control sample – 100 % premium quality wheat flour; SLF1 – sugar biscuits with 1 % lentil flour; SLF5 – sugar biscuits with 5 % lentil flour; SLF 10– sugar biscuits with 10 % lentil flour; SLF 15– sugar biscuits with 15 % lentil flour; L *—luminosity; a *—red/green component; b *—yellow/blue component; ΔE * - overall difference of color. Different letters ($^{a-l}$) designate statistically different results ($p \leqslant 0.05$).

It was found that the values of the luminosity L* in the CS were higher than in the SLF. Thus, on the next day after baking (1 day), the L* were as follows: CS (73.75), SLF 1 (72.44), SLF 5 (71.37), SLF 10 (70.62) and SLF 15 (70.12). Probably, the color of the lentil flour led to

the decrease in luminosity of the sugar cookies. The values of the a* component were higher in the case of samples CLF, demonstrating the presence of red pigments, being in the range of 1.03-1.55. The highest values of a* were in samples SLF 10 and SLF 15, 1.55 and 1.53 respectively. In the case of the b* component, also the highest values were in the CLF samples due to the yellow pigments that ranged from 25.33 to 33.01. The storage time did not essentially influence the values of the color parameters for all the investigated samples.

The ΔE* values were analyzed to show whether there is a difference in the colors perceived by the human eye during the storage of the biscuits. According to Lo Faro et al. [91] , when keeping the CS for 20 days, the ΔE* values were in the range 1.01-1.21, which demonstrates a small difference in color (0.5 < ΔE* < 1.5), and in 35 days a difference color was barely distinguishable (2.08). In the case of the SLF1, during 20 days, the ΔE* values were in the range of 2.05-2.86, demonstrating a small difference in color (0.5 < ΔE* < 1.5), and in the 35th day, a color difference was very distinct (3.43), because it was within the limits 3 < ΔE* < 6. The SLF 5 sample kept for 10 days had the ΔE* values that demonstrated a small color difference (0.5 < ΔE* < 1.5), in the 20th day - a barely distinguishable difference (2 < DE < 3) and on the 35th day - a color difference was very distinct (3.12), as it was in the range 3 < ΔE* < 6. For the SLF10 and SLF 15 samples kept for 35 days, the ΔE* values changed from a small difference to barely distinguishable.

The microbiological analysis of the experimental samples of biscuits kept for 35 days are presented in Table 10.

Table 10

Influence of storage time on the microbiological indicators of sugar biscuits with added lentil flour

Microbiological indicators	Storage time, days	Admitted level [66]	Experimental data				
			CS	SLF1	SLF5	SLF10	SLF15
QMAFAnM, CFU, max.	1	1×10^4	$<1\times10^2$	$<2\times10^2$	$<2\times10^2$	$<1\times10^2$	$<1\times10^2$
	10		$<2\times10^2$	$<3\times10^2$	$<2\times10^2$	$<4\times10^2$	$<3\times10^2$
	20		$<5\times10^2$	$<1\times10^3$	$<7\times10^2$	$<6\times10^2$	$<5\times10^2$
	35		$<7\times10^3$	$<7\times10^3$	$<5\times10^3$	$<5\times10^3$	$<6\times10^3$
Coliform bacteria	1	Not allowed in 0.1 g	There were not found				
	10						
	20						
	35						
Fungi, CFU, max.	1	50	<1	<2	<2	<1	<1
	10		<5	<7	<5	<3	<3
	20		<10	<10	<15	<10	<10
	35		<40	<25	<20	<20	<25
Yeast, CFU, max.	1	50	<1	<2	<2	<3	<2
	10		<5	<5	<5	<5	<3
	20		<10	<10	<10	<10	<10
	35		<25	<20	<20	<20	<25

Note: QMAFAnM – quantity of mesophilic aerobic and facultative anaerobic microorganisms; CFU – colony-forming unit. CS – control sample – 100 % premium quality wheat flour; SLF1 – sugar biscuits with 1 % lentil flour; SLF5 – sugar biscuits with 5 % lentil flour; SLF 10– sugar biscuits with 10 % lentil flour; SLF 15– sugar biscuits with 15 % lentil flour; L *—luminosity; a *—red/green component; b *—yellow/blue component; ΔE * - overall difference of color.

The analysis of the total microorganisms number in the biscuit samples showed acceptable values throughout the storage period, which fall within the permissible limits. Based on these results, it can be said that the technological parameters used for baking were adequate, which influenced obtaining a microbiologically safe product for consumption.

4. Conclusions

To manufacture sugar biscuits enriched with RLF, both the sensory quality and composition of RLF were first evaluated. The effect of incorporating RLF (1–15%) on the kneading process, dough textural properties, as well as the quality, color parameters, and microbiological stability of biscuits during storage, was investigated. The results showed that increasing RLF content led to higher dough hardness, while cohesiveness and resistance decreased proportionally. Sensory analysis indicated that biscuits containing 1–10% RLF exhibited a firm texture, a pleasant and uniform appearance, and improved taste, aroma, and color. However, the addition of 15% RLF resulted in a pronounced lentil flavor. During storage, the water swelling capacity decreased by approximately 1.2 times. Microbiological analysis demonstrated no evidence of microbial growth or product deterioration throughout the storage period. Additionally, storage time had no significant effect on the color parameters of the analyzed samples. These findings suggest that the incorporation of RLF in sugar biscuit production is a viable approach to enhancing their nutritional value.

Acknowledgement. The authors would like to thank the Institutional Project 020405 "Optimizing food processing technologies in the context of the circular bioeconomy and climate change", Bio-OpTehPAS, being implemented at the Technical University of Moldova.

References

1. Alam NH, Hamadani JD, Dewan N, Fuchs GJ (2003). Efficacy and safety of a modified oral rehydration solution in the treatement of severely malnourished children with watery diarrhea. Journal. Pediatrie, 40: pp. 614-619.
2. Bhan MK; Bhandari N, Bahl R (2003). Management of the severely malnourished child: perspective from developing countries. Biomedicine Journal, 326(7381): pp. 146-151.
3. Romano A, Gallo V, Ferranti P, Masi P (2021). Lentil flour: Nutritional and technological properties, in vitro digestibility and perspectives for use in the food industry. Current Opinion in Journal Food Science, 40: pp.157–167.
4. Nadathur SR, Wanasundara JP, Scanlin L (2021). Lupin: an important protein and nutrient source. In: (Eds.), Sustainable protein sources. Academic Press, pp. 165–183.
5. Wilson S, Peterson E, Gaston M, et al (2020). 8 Weeks of Lentil Consumption Improves Insulin Sensitivity in Overweight and Obese Adults—A Randomized Controlled Trial. Journal Academy of Nutrition & Dietetics, 120: p.73.
6. Zahradka P, Hanson MG, Wu Y, Taylor CG (2018). Consumption of lentils improves arterial elasticity. Journal Atherosclerosis, 32: p.160.
7. Jarpa-Parra M (2018). Lentil protein: a review of functional properties and food application. An overview of lentil protein functionality. International Journal of Food Science and Technology, 53: pp.892–903.
8. Xu J, Li Y, Zhao Y, et al (2021). Influence of antioxidant dietary fiber on dough properties and bread qualities: A review. Journal Functional Foods. 80: p.104434.
9. Papandreou C, Becerra-Tomás N, Bulló M, et al (2019). Legume consumption and risk of all-cause, cardiovascular, and cancer mortality in the PREDIMED study. Journal Clinical Nutrition. 38: pp.348–356.
10. Berketova LV (2003). Increasing the nutritional value of confectionery. Journal Bakery and confectionery production. 7, p.5.
11. Tsen CC, Eystone W, Weber J (2006). Evaluation of the qualities of cookies supplemented with distillers, dried grain flours. Journal Food Science. 47: pp. 684-685. https://doi. org/10.1111/j.1365-2621.1982.tb10156.x.
12. Spirichev VB (2004). Enrichment of food products with vitamins and minerals. Science and technology / V.B. Spirichev, L.N. Shatnyuk, V.M. Poznyakovsky. Siberian universitar publishing house. p.548.

13.Zabodalova LA (2006). Functional food products - the way to health / L. A. Zabodalova // Journal Milk processing. 11: pp. 8-11.
14.Austrianskikh AN (2005). Healthy food products: new technologies, quality assurance, efficiency of use / A.N. Austrianskikh, V.M. Poznyakovsky. Siberian universitar publishing house, 2005, p.413.
15. Shahzadi N, Butt MS, Rehman SU, et al (2005). Chemical characteristics of various composite flours. International Journal Agricultural and Biologycal Science, 7: pp. 105-108.
16. Abdel-Kader ZM (2000). Enrichment of Egyptian 'Balady bread Part 1. Baking studies, physical and sensory evaluation of enrichment with decorticated cracked broad bean flour (Vicia Faba L.) Nahrung. 44(6): pp.418-421. https://doi.org/10.1002/1521- 3803.
17. Tipsina N, Batura N, et al (2020). Characteristics of lentils and its use in the food industry. Vestnik KrasGAU, 11: pp.225-231.
18.Pashchenko LP (2008). Regulirovaniye khlebopekarnykh svoystv pshenichnoy muki s primeneniyem produktov pererabotki soi // Journal: Khleboprodukty. 4: pp.40–41.
19.Tsyganova T (2009). Novyy vid syr'ya dlya khlebopecheniya / T.B. Tsyganova // Materialy SH mezhdunarodnoy nauchno-prakticheskoy konferentsii «Innovatsionnyye napravleniya v pishchevykh tekhnologiyakh». pp. 71 – 77.
20.Pershakova TV (2007). Otsenka potrebitel'skikh svoystv muchnykh konditerskikh izdeliy, obogashchennykh lipidsoderzhashchimi BAD / // Izvestiya VUZov. Pishchevaya tekhnologiya. 1: pp. 99-100.
21.BS ISO 6658-2005. Sensory Analysis – Methodology – General quidance.
22. AACC International.Approved Methods of Analysis.10th ed. American Association of Cereal Chemists; St. Paul, MN, USA: 2009.
23. ISO 750:1998 Fruit and vegetable produts. Determination of titrable acidity.
24.AOAC (2012) Official Method of Analysis: Association of Analytical Chemists. 19th Edition, Washington DC, 121-130.
25.SM SR EN ISO 21415-1:2012 Wheat and wheat flour. Gluten content. Part 1: Determination of wet gluten by a manual method.
26.SM SR EN ISO 21415-3:2012 Wheat and wheat flour. Gluten content. Part 3: Determination of dry gluten from wet gluten by an oven drying method.
27.SM SR EN ISO 21415-4:2012 Wheat and wheat flour. Gluten content. Part 4: Determination of dry gluten from wet gluten by a rapid drying method.
28.American Association of Cereal Chemistry (AACC). American Association of Cereal Chemistry Approved Methods, 10th ed.; American Association of Cereal Chemistry (AACC): St. Paul, MN, USA, 2021.
29. ISO 5520:1981 Fruits, vegetables and derived products. Determination of alkalinity of total ash and of water-soluble ash.
30. AOAC. Official Methods of Analysis, 19th ed.; Association of Offical Analytical Chemists: Washington, DC, USA, 2012.
31. Serin S, Turhan KN, Turhan M (2018). Correlation between Water Activity and Moisture Content of Turkish Flower and Pine Honeys Journal: Food Science Technolology, 38: pp.238–244.
32. Overview of texture profile analysis. Available online: https://texturetechnologies.com/resources/texture-profile-analysis#tpa-measurements.
33. ISO 8589; General Guidance for the Design of Test Rooms. The International Organization for Standardization: Geneva, Switzerland, 2007.
34.SM EN ISO 6579-1:2017 Microbiology of food and feed products. The horizontal method for the detection of bacteria of the genus Salmonella spp. (in Romanian).
35.SM ISO 4831:2010 Microbiology of food and feed. Horizontal method for the detection and enumeration of coliform bacteria. (in Romanian).
36.SM EN ISO 4833-1:2014 Microbiology of food and feed products. Horizontal method for the enumeration of microorganisms Part I and II (in Romanian).
37.Sandulachi L, Rubțov S, Popescu L (2017). Microbiological control of food products; Publisher: UTM., TA, Ch., Tehnica, UTM, Republic of Moldova, p.128 (in Romanian).
38. Institute of Medicine, National Academy of Sciences Dietary reference intakes for energy, carbohydrate, fiber, fat, fatty acids, cholesterol, protein and amino acids. Washington, DC: National Academies Press; 2005 [PubMed] [Google Scholar].
39. Pantone, X. R. 2016. A guide to understanding color.

40. Srivastava R, Vasishtha H (2013). Dietary fiber, protein and lectin contents of lentils (Lens culinaris) with soakingand cooking. Current Advances in Agricultural Sciences, 5(2): pp. 238-241.
41. Khazaei H, Subedi M, Nickerson M, et al (2019). Seed protein of lentils: current satatus, progress, and food applications. Journal Alimente, 8 (391): pp.1–23.
42. Aryee A, Boye JI (2017). Studiu comparativ al efectelor procesării asupra proprietăților nutriționale, fizico-chimice și funcționale ale lintei. Journal Procesul alimentar. Preserv. 41 (1): pp.24–30.
43. Harmankaya M, Ozcan MM, Karadaş S, Ceyhan E (2010). Protein and mineral contents of pea (*Pisum sativum L.*) genotypes grown in central anatolian region of turkey. Journal: Horticulture, Biology and Environment. Vol. 1, No. 2: pp. 159 – 165.
44. Franck W, Chen C, Franck S (2023). Cultivar and environmental impacts on protein and mineral concentrations in peas (*Pisum sativum L.*). Crop Science, 64: pp.287–302. DOI:10.1002/csc2.21165.
45. Grusak MA (2009). Calitate nutrițională și benefică pentru sănătate. În W. Erskine, FJ Muehlbauer, A. Sarker și B. Sharma (eds.), The lentil: Botany, production and uses, pp.368–390. CABI. https://doi.org/10.1079/9781845934873.0368.
46. Wu DT, Li WX, Wan JJ, et al (2023). A comprehensive review of pea (*Pisum sativum L.*): chemical composition, processing, health benefits and food applications. Journal: Foods, 12: 2527. https://doi.org/10.3390/foods12132527.
47. Kotlarz A, Sujak A, Strobel W, Grzesiak W (2011). Chemical composition and nutritive value of protein of the pea seeds - effect of harvesting year and variety. vol. 75: pp. 57-69. doi: 10.2478/v10032-011-0018-2.
48. Brigide P, Guidolin S, Oliveira M (2014). Nutritional characteristics of biofortified common beans. Journal: Food Science and Technology, Campinas, 34 (3): pp. 493-500.
49. Schmidt H, Oliveira V (2023). Overview of the Incorporation of Legumes into New Food Options: An Approach on Versatility, Nutritional, Technological, and Sensory Quality. Journal: *Foods*, *2*(13): p. 2586; https://doi.org/10.3390/foods12132586].
50. Trinidad P, Mallillin A, Loyola A, et al (2010).The potential health benefits of legumes as a good source of dietary fibre. British Journal of Nutrition, 103: pp.569–574.
51. Dhull S, Kinabo J, Uebersax M (2023). Nutritional profile and effect of processing methods on the composition and functional properties of lentils (Lens culinaris Medik): a review. Journal Legume Science, 5: p.156.
52. SM EN ISO 24333:2017. Cereals and cereal products — Sampling, IDT.
53. Decision of the Government of the Republic of Moldova No. 68 of 29.01.2009 regarding the approval of the technical regulation " Cereal flour, semolina and bran" (Official Gazette No. 23-26 of 06.12.2009).
54. Hajas L, Sipos L, Csajbókné E, et al (2022). Lentil (*Lens culinaris* Medik.) Flour Varieties as Promising New Ingredients for Gluten-Free Cookies. Journal:Foods, 11(14), p. 2028.
55. Byrdwell WC, Goldschmidt RJ (2022). Fatty Acids of Ten Commonly Consumed Pulses**.** Journal: Molecules, *27* (21): p.7260; doi.org/10.3390/molecules27217260.
56. Sharma H, Ramawat N, Gupta C (2022). Nutritive content of lentils. Journal: Nutritional Health & Food Engineering, 12(1): pp.27–32;
57.Ko TL, Than SS, Oo ZZ (2017). Isolation of Protein from Defatted Lentil Flour. Journal: Food Science and Technology. 5 (6): pp.238-244.
58. Ohanenye IC, Ekezie FG, Sarteshnizi RA, et al (2021). Legume Seed Protein Digestibility as Influenced by Traditional and Emerging Physical Processing Technologies Journal of Food Hidrocolloids, p.114.
59. Boz H (2019). Effect of flour and sugar particle size on the properties of cookie dough and cookie. Czech Journal of Food Sciences, 2: pp.120-127.
60. Taylor TP, Fasina O, Bell LN (2008). Physical properties and consumer liking of cookies prepared by replacing sucrose with tagatose. Journal of Food Science, 73: pp. 145–151.
61. **Atudorei D, Mironeasa S, Codină GG (2022).** Effects of Germinated Lentil Flour on Dough Rheological Behavior and Bread Quality. Journal: Foods, 11: p. 2982.
62. Karim A, Raji Z, Habibi Y, Khalloufi S (2023). A review on the hydration properties of dietary fibers derived from food waste and their interactions with other ingredients: opportunities and challenges for their application in the food industry. Critical Reviews in Journal Food Science and Nutrition, 64(32): pp.11722-11756. https://doi.org/10.1080/10408398.2023.2243510.
63. Razavi S, Hojjatoleslamy M, Molavi H, Boroujeni L (2020). The Effect of Germinated Lentil Flour on the Physicochemical and Organoleptic Characteristics of Sangak Bread, Journal of Culinary Science & Technology. 20(3): pp.253-265. doi: 10.1080/15428052.2020.1840473.

64. Yin J, Li C, Hong Y, Li Z (2020). Use of two-stage dough mixing process in improving water distribution of dough and qualities of bread made from wheat–potato flour. Journal of Integrative Agriculture, 20(1): pp.300-310.
65. Atudorei D, Atudorei O, Codina GG (2022). The Impact of Germinated Chickpea Flour Addition on Dough Rheology and Bread Quality. Journal Plants, 11 (9) : p.1225. doi: 10.3390/plants11091225.
66. Dueñas M, Sarmento T, Aguilera Y, et al (2016). Impact of cooking and germination on phenolic composition and dietary fibre fractions in dark beans (*Phaseolus vulgaris L*.) and lentils (*Lens culinaris L*.). LWT Journal Food Science Technology, 66: pp.72–78.
67. Bajka BH, Pinto AM, Ahn-Jarvis J, et al (2021). The impact of replacing wheat flour with cellular legume powder on starch bioaccessibility, glycaemic response and bread roll quality: A double-blind randomised controlled trial in healthy participants. Journal Hidrocoloids, 114: p.2299. https://doi.org/ 10.3390/foods11192982.
68. Xu J, Li Y, Zhao Y, et al (2021). Influence of antioxidant dietary fiber on dough properties and bread qualities: A review. Journal Functional Foods, 80: 104434.
69. Idowu A (2014). Development, Nutrient Composition and Sensory Properties of Biscuits Produced from Composite Flour of Wheat and African Yam Bean. British Journal of Applied Science Technology.4: pp.1925-1933.
70. Dada M, Bello F, Omobulejo F, Olukunle F (2023). Nutritional quality and physicochemical properties of biscuit from composite flour of wheat, African yam bean and tigernut. Journal Heliyon, 9(11). doi:10.1016/j.heliyon.2023.e22477.
71. Awadelkareem AM, Shammari EA (2015). Nutritional and sensory evaluation of wheat flour biscuits supplemented with lentil flour. *Pakistan Journal of Nutrition*. 4(12): pp.841–848. doi: 10.3923/pjn.2015.841.848.
72. Hajas L, Benedek C, Csajbókné Csobod É, et al (2022). Development of protein- and fiber-enriched, sugar-free lentil cookies: impact of whey protein, inulin, and xylitol on physical, textural, and sensory characteristics. *Journal Foods*. 11(23): p. 3819. doi:10.3390/foods11233819.73.
73. Andriana E Lazou (2024). Properties, Structure, and Acceptability of Innovative Legume-Based Biscuits with Alternative Sweeteners. International Journal Food Science. 25: 8216796.
74. Ledikwe JH, Blanck HM, Kettel Khan L (2006). Dietary energy density is associated with energy intake and weight status in US adults. Journal Clinical Nutrition. 83:1362-8.
75. SanPiN 2.3.2.1078-01 Hygienic requirements for the safety and nutritional value of food products. (in Russian).
76.Istitute of Medicine, National Academy of Sciences Dietary reference intakes for energy, carbohydrate, fiber, fat, fatty acids, cholesterol, protein and amino acids. Washington, DC: National Academies Press; 2005 [PubMed] [Google Scholar].
77. EU Regulation no. 1169/2011 on informing consumers about food products.
78.Tundis R, Loizzo D, Menichini F (2010). Natural products as alpha-amylase and alpha-glucosidase inhibitors and their hypoglycaemic potential in the treatment of diabetes: an update. National Library of Medicină, 10(4): pp.315-31. doi: 10.2174/138955710791331007.
79. Hajas L, Sipos L, Csobod ÉC, et al (2022). Lentil (*Lens culinaris* Medik.) flour varieties as promising new ingredients for gluten-free cookies. Journal *Foods,* 11(14): p. 2028. doi:10.3390/foods11142028.
80. Koukoumaki DI, Giannoutsos K, Devanthi PV (2022). Effect of wheat replacement by pulse flours on the texture, color, and sensorial characteristics of crackers: flash profile analysis. *International Journal of Food Science*; 18:2354045.doi:10.1155/2022/2354045.235404.
81. Pushpakumara AG, Gunasesakara N, Herath HM, Madhujith T (2023). Impact of partial replacement of wheat flour with chickpea flour on physico-chemical and sensory properties of tea buns. *International Journal of Food Properties*, 26(1): pp.1522–1533. doi:10.1080/10942912.2023.222377.
83. Mamat H, Hill S (2018). Structural and functional properties of major ingredients of biscuit. International Food Research Journal, 25(2): pp. 462-471.
84. Mamat H,' Hill S (2014). Effect of fat types on the structural and textural properties of dough and semi-sweet biscuit. Journal Food Science Technology, 51(9): pp. 1998–2005. doi:10.1007/s13197-012-0708-x.
85. Mohammadi M, Khorshidian N, Yousefi M, Khaneghah AM (2022). Physicochemical, Rheological, and Sensory Properties of Gluten-Free Cookie Produced by Flour of Chestnut, Date Seed, and Modified Starch. Journal of Foog Quality. 2022: p.10.
86. Romani S, Rocculi P, Tappi S, Dalla Rosa M (2016). Moisture adsorption behaviour of biscuit during storage investigated by using a new Dynamic Dewpoint method. Journal Food Chemistry, 195: pp. 97-103.

87.Kashmir S, Shafi M (2017). Composite flour blends: Influence of particle size of water chestnut flour on nutraceutical potential and quality of Indian flat breads. Journal Food Meas. Character. 11: pp.1094–1105.
88.LabuzaTP, Hyman CR (1998). Moisture migration and control in multi-domain foods. Trends in Journal Food Science and Technology. 9(2): pp.47-55.
89.Gustavo V, Barbosa-Vanovas A, Fontana Jr (2020). Water Activity in Journal Foods. IFT Oress Series, 664.
90. Ghendov-Mosanu A, Popa N, Paiu S, Boeștean O, et al (2024). Breadmaking Quality Parameters of Different Varieties of triticale Cultivars. Foods. 13: p.1671; doi: 10.3390/foods13111671.
91. Lo Faro E, Salerno T, Montevecchi G, Fava P (2022). Mitigation of Acrylamide Content in Biscuits through Combined Physical and Chemical Strategies. Journal Foods, 11: 2343.

Citation: Boestean O., Bulgaru V., Netreba N., Ghendov-Mosanu A. (2026). Physicochemical, sensory and textural evaluation of sugar biscuits supplemented with lentil flour. *Journal of Engineering Science*. 2026, 33 (1), pp. 146-164. https://doi.org/10.52326/jes.utm.2026.33(1).10.

Submission of manuscripts: jes@meridian.utm.md

Journal of Engineering Science *Vol. XXXIII, no. 1 (2026), pp. 165 - 182*
Fascicle *Food Engineering* *ISSN 2587-3474*
Topic *Food Technologies and Food Processes* *eISSN 2587-3482*

https://doi.org/10.52326/jes.utm.2026.33(1).11
UDC 664.9:635.94:543

EVALUATION OF THE IMPACT OF SEA BUCKTHORN POMACE ADDITION ON THE PHYSICOCHEMICAL AND QUALITY PROPERTIES OF MEAT SNACK PRODUCTS

Irina Dianu[1]*, ORCID: 0000-0001-8632-8987,
Artur Macari[1], ORCID: 0000-0003-4163-3771,
Adriana Dabija[2], ORCID: 0009-0005-2729-9633,
Natalia Netreba[1], ORCID: 0000-0003-4200-1303,
Iuliana Sandu[1], ORCID: 0000-0002-8358-0957,
Mircea Oroian[2], ORCID: 0000-0001-5141-9969,
Amelia Buculei[2], ORCID: 0009-0002-4447-1763,
Anca-Mihaela Gâtlan[2], ORCID: 0000-0001-5836-7022,
Tatiana Cusmenco[1], ORCID: 0000-0001-6628-0752

[1]*Technical University of Moldova, 168, Stefan cel Mare Blvd., Chisinau, MD-2004, Republic of Moldova*
[2]*"Stefan cel Mare" University, Suceava, 720229, Romania*
* Corresponding author: Irina Dianu, *irina.dianu@doctorat.utm.md*

Received: 02. 14. 2026
Accepted: 03. 25. 2026

Abstract. The utilization of fruit-processing by-products is a practical approach to develop sustainable, value-added meat snacks. Sea buckthorn pomace, rich in colored and acidic compounds, is expected to influence dehydration behavior, appearance and storage stability of deshydrated meat products. The study was designed to investigate how different inclusion levels of sea buckthorn pomace powder (SBPP) - 0.75%, 1.25%, and 2.5% (*w/w*) - influence the quality and safety attributes of fermented and dehydrated meat snack products. The samples underwent fermentation at 25 ± 1 °C for a period of 12 hours, followed by dehydration at 50 ± 5 °C for 6 hours. Subsequent analyses comprised the assessment of key physicochemical parameters (moisture content, pH, and water activity), instrumental color measurement using the CIELab system, sensory profiling, determination of lipid oxidation through peroxide value, and evaluation of microbiological indicators. Increasing SBPP level decreased moisture (15.79% to 7.93%), water activity (0.455 c.u. to 0.358 c.u.) and pH (6.16 to 5.65), indicating enhanced shelf-stability. Color shifted toward a darker red-orange profile (L* 47.85 to 20.64; a* up to 27.09). Peroxide value remained low and unchanged (1.60 to 1.70 mEq O_2/kg). Coliforms, moulds/yeasts and *Salmonella* were not detected. SBPP is therefore a clean-label ingredient enabling differentiated ripening-dehydrated meat snacks while supporting circular valorization of processing residues.

Keywords: *antioxidant activity; bioactive compounds; carotenoids; food sustainability; sensory Quality.*

Rezumat. Valorificarea produselor secundare rezultate din procesarea fructelor reprezintă o abordare practică pentru dezvoltarea unor gustări din carne sustenabile, cu valoare adăugată. Tescovina de cătină, bogată în compuși bioactivi și acizi organici, influențează asupra procesului la deshidratare, aspectul și stabilitatea la depozitare a produselor din carne deshidratată. Prezentul studiu a avut ca scop studierea impactului pulberii de tescovină de cătină (PTC) (0.75; 1.25 și 2.5%, m/m) asupra calității și siguranței gustărilor din carne deshidratate. Probele au fost maturate la 25 ± 1 °C timp de 12 ore și ulterior deshidratate la 50 ± 5 °C timp de 6 ore, fiind apoi supuse analizelor fizico-chimice (umiditate, pH, activitatea apei), determinării culorii prin sistemul CIELab, caracteristicilor senzoriale, indicelui de peroxid și indicatorilor microbiologici. Creșterea concentrației de PTC a determinat diminuarea conținutului de umiditate (de la 15.79% până la 7.93%), a activității apei (de la 0.455 u.c. până la 0.358 u.c.) și a pH-ului (de la 6.16 la 5.65), indicând o îmbunătățire a stabilității la depozitare. Culoarea s-a modificat către un profil roșu-portocaliu mai închis (L* de la 47.85 la 20.64; a* până la 27.09). Indicele de peroxid a rămas scăzut și nemodificat semnificativ (1.60–1.70 mEq O_2/kg). Coliformii, mucegaiurile/drojdiile și Salmonella nu au fost detectate.
Prin urmare, SBPP poate fi considerat un ingredient de tip *clean label*, care permite obținerea unor produse din carne maturate și deshidratate variate, susținând în același timp valorificarea circulară a reziduurilor provenite din procesare.

Cuvinte-cheie: *activitate antioxidantă; compuși bioactivi; carotenoizi; sustenabilitate alimentară; acceptabilitate senzorială.*

1. Introduction

In recent decades, the food industry has experienced a marked shift toward the development of functional products that combine nutritional value with beneficial effects on consumer health. These products rely on the use of natural ingredients rich in bioactive compounds, capable of providing antioxidants, dietary fiber, and phytonutrients with protective roles [1, 2]. At the same time, the growing emphasis on sustainability and food waste reduction has driven increased research efforts focused on the valorization of by-products generated from fruit and vegetable processing [3].

Sea buckthorn (*Hippophae rhamnoides* L.) is one of the most valuable fruit species from both nutritional and functional perspectives, due to its high content of vitamins (particularly C and E), carotenoids (β-carotene, zeaxanthin, lutein), polyphenols, and unsaturated fatty acids [4-6]. These compounds contribute to the high antioxidant activity as well as to the anti-inflammatory and antimicrobial properties of the product [7]. Fruit processing for the manufacture of juice, oil, or purée results in the generation of substantial quantities of sea buckthorn pomace, a solid residue abundant in bioactive constituents and dietary fiber, yet still insufficiently exploited at the industrial scale [8].

The reutilization of this pomace in the form of sea buckthorn pomace powder (SBPP) provides a sustainable solution, contributing to the circular economy and the development of food products with enhanced functional value [9]. Moreover, the natural pigment compounds, particularly carotenoids, impart an intense yellow-reddish coloration, which can positively influence the visual appearance and sensory acceptability of the products [10].

In recent years, the incorporation of plant-derived by-products into meat formulations has attracted growing attention as an effective approach to enhance their nutritional and technological value. Previous studies have demonstrated that the use of antioxidant- and

fiber-rich plant powders, including those obtained from sour cherries, cranberries, currants, and sea buckthorn, may limit lipid oxidation, improve mineral composition, and contribute to greater product stability [11–13]. At the same time, these additions can alter color indices and sensory profiles due to their phenolic and carotenoid composition [14].

2. Materials and Methods

2.1. Raw Material

The sea buckthorn pomace, obtained by direct pressing of the juice from *Hippophae rhamnoides* L. fruits, variety Clara and Mara, harvested in 2024, was provided by the local producer BUKKER S.R.L. (Orhei, Republic of Moldova) and subsequently used in the research. Refrigerated, boneless, and skinless chicken meat was supplied by the company AXEDUM S.R.L. (Republic of Moldova). Commercially available salt, sugar, black and white pepper powders, as well as garlic powder, were used as seasoning and auxiliary materials. The starter culture *SafePro EasyCure LC*, produced by CHR HANSEN, was obtained from INGREDA S.R.L. (Chișinău, Republic of Moldova).

2.2. Chemicals

Commercially available reagents were used throughout the investigation. Chemapol (Prague, Czech Republic) provided sodium hydroxide, methanol, ethyl acetate, petroleum ether, and ethanol. From Sigma-Aldrich (Schnelldorf, Germany), the following reagents were employed: n-hexane (>95%), hydrogen peroxide (30% and 35%), hydrochloric acid (38%), potassium bicarbonate (97%), nitric acid (ACS reagent, 70%), perchloric acid (ACS reagent, 70%), deionized water, ninhydrin, sulfuric acid (96-98%), 2,6-dichloroindophenol, sodium thiosulfate, and sodium bicarbonate. Trolox (purity ⩾97%) and Folin-Ciocalteu phenol reagent (2.1 N) were obtained from Chem-Lab NV (Zedelgem, Belgium). ABTS and DPPH radicals were purchased from Alpha Aesar (Haverhill, MA, USA). The microbiological media, namely buffered peptone water, potato dextrose agar with chloramphenicol, and plate count agar, were supplied by Altmann Analytik GmbH & Co. KG – Analytics-Shop (Munich, Germany).

2.3. Production of SBPP

Drying of sea buckthorn pomace was performed by forced convection in a laboratory drying oven (SLW 115 SMART, Pol-Eco Aparatura, Wodzisław Śląski, Poland) at 53 ± 2 °C with an air velocity of 1.5 ± 0.1 m/s until a residual moisture content of ⩽9% was achieved. Thereafter, the seeds were separated, and the seed-free pomace fraction was finely milled with a PULVERISETTE 11 grinder (Fritsch GmbH, Idar-Oberstein, Germany), yielding powder with a particle size of 70 ± 10 μm. The final material was sieved through a CLM-200 stainless steel laboratory sieve, vacuum packed, and stored in the absence of light under dry conditions at 20 ± 2 °C.

2.4. SBPP Characterization

2.4.1. Physicochemical Analysis

The physicochemical characteristics of SBPP, including moisture content (MC), ash content (AC), titratable acidity (TA), and pH, were assessed using the corresponding ISO standard methods [15-17]. Protein (PC) and fat (FC) contents were quantified according to AOAC procedures (2012). The aw values were recorded with a LabSwift-aw analyzer (Novasina AG, Lachen, Switzerland).

2.4.2. Analysis of *L*-ascorbic acid content

The *L-ascorbic* acid content (AAC) in SBPP was determined using a potentiometric titration procedure based on ISO 6557-2 [18], with minor adjustments. The dried pomace sample was first ground to ensure homogeneity. An accurately weighed amount was then treated with 2% hydrochloric acid to protect ascorbic acid from oxidation, and the obtained extract was subsequently filtered. Potentiometric titration was performed with standard 2,6-dichlorophenolindophenol solution under constant agitation. A platinum electrode served as the indicator electrode, while a silver/silver chloride electrode was used as the reference. The endpoint was identified from the sudden shift in redox potential measured by the potentiometer. Each determination was carried out at least in triplicate. The AAC values were calculated according to the consumed titrant volume, its concentration, the mass of the analyzed sample, and the corresponding conversion factors, and were expressed as mg/100 g dry matter (mg/100 g DM).

2.4.3. Analysis of Antioxidant Activity

The antioxidant activity of SBPP was evaluated in hydroalcoholic extracts prepared by ultrasound-assisted extraction (UAE) [19-21]. For extraction, 0.5 g of sample was combined with 25 mL of 73% ethanol and kept under static conditions for 24 h at 20 ± 2 °C in the absence of light. The mixture was then subjected to ultrasonic treatment in an ultrasonic bath (ISOLAB 621.06.006, Eschau, Germany) at 30 ± 1 °C for 25 min and 37 kHz. After extraction, the samples were centrifuged (MPW-380R, Warsaw, Poland) at 8,000 rpm for 10 min at room temperature, filtered, and stored at 4 ± 1 °C until analysis. These extraction conditions were selected based on previously published studies [22-26]. The Trolox-equivalent antioxidant activity was first assessed using the DPPH radical scavenging assay, following the procedure reported by Paulpriya et al. [20]. The results were expressed as mg TE/100 g DM using a Trolox calibration curve constructed in the concentration range of 0-500 μmol/L (R^2 = 0.9992).

ABTS radical cation scavenging activity was also determined in terms of Trolox-equivalent antioxidant capacity using the method of Arnao et al. [27], slightly modified for the present study. The working ABTS•+ solution was prepared from 7 mM ABTS and 2.45 mM potassium persulfate and allowed to stand in darkness for 16 h. Prior to measurement, the solution was diluted with ethanol until an absorbance of 0.70 ± 0.02 at 734 nm was reached. For the assay, 100 μL of extract or Trolox standard was added to 2.4 mL of ABTS reagent. After incubation for 6 min at 30 °C, absorbance was recorded. Antioxidant activity was reported as mg TE/100 g DM based on the corresponding calibration curve (0-500 μmol/L, R^2 = 0.9992).

Total polyphenol content (TPC) was determined by the Folin–Ciocalteu assay according to the methods reported by Paulpriya et al. and Waterman et al. [26, 28], with minor adjustments for the present study. For the analysis, 20 μL of the extract was allowed to react with Folin–Ciocalteu reagent in the presence of 10% Na_2CO_3. After incubation at 40 ± 1 °C for 30 min, the absorbance response was used to calculate the polyphenol content. The final values were reported as mg GAE/100 g DM based on a gallic acid calibration curve prepared within the concentration interval of 0-500 mg/L (R^2 = 0.9980).

The determination of total carotenoid content (TCC) was carried out following a method based on the protocol proposed by Ghendov-Mosanu et al. [29]. According to the

absorption spectrum obtained, quantification was performed at 450 nm, which represented the absorbance maximum.

2.5. Meat Snacks Preparation

To investigate the impact of SBPP on product quality, meat snack samples were produced with SBPP added at concentrations of 0.75, 1.25, and 2.5%. These formulations were designated as S1, S2, and S3, respectively. SBPP was incorporated directly into the minced meat mixture. A control formulation lacking SBPP (CS) was also prepared to enable comparative evaluation.

Chicken breast, chicken thigh, salt, sugar, black and white pepper powders, garlic powder, and the starter culture *SafePro EasyCure LC* (CHR HANSEN) were used in the production of meat snacks. The composition of the formulated samples is given in Table 1.

Table 1

Composition of experimental meat snack samples per 100 kg of unsalted raw material

Ingredients	CS	S1	S2	S3
Chicken breast, kg	70	69.475	69.125	68.25
Chicken thigh, kg	30	29.775	29.625	29.25
SBPP, kg		0.750	1.250	2.500
Salt, g	1800	1800	1800	1800
Sugar, g	800	800	800	800
Black pepper powder, g	100	100	100	100
White pepper powder, g	100	100	100	100
Garlic powder, g	200	200	200	200
Fermentation starter culture *SafePro EasyCure LC, g*	25	25	25	25

CS - control sample; S1- sample with 0.75% of SBPP; S2 - sample with 1.25% of SBPP; S3 - sample with 2.5% of SBPP, SBPP - sea buckthorn pomace powder.

After grinding, homogenization and stuffing into casings, the meat mixture was subjected to a controlled fermentation (maturation) stage. Fermentation was carried out in a laboratory drying oven at 25 ± 1 ^{0}C, with a relative humidity of 85–90% and with airflow set at 1.5 m/s over a 12 h period. During this period, the pH of the product decreased from 5.8–6.0 to 5.2–5.4, indicating adequate acidification.

Following fermentation, pre-drying and compaction were performed under the same temperature and airflow conditions to stabilize the product structure. Subsequently, the samples were subjected to shock freezing at -35 ^{0}C for 6 h to ensure uniform slicing.

Dehydration was conducted in an AIM AGHD-15ELC heat pump dehydrator (Nantou, Zhongshan, Guangdong) at 50 ± 5 ^{0}C for 6 h. The finished meat snacks were packaged and stored for subsequent physicochemical, microbiological and sensory analyses.

2.6. Meat Snacks Quality Analysis

2.6.1. Sensory Analysis

The sensory properties of the developed meat snack samples were assessed by five trained panelists according to ISO 6658:2017. A five-level scoring system was applied for each evaluated attribute: score 5 reflected the absence of deviations from the predefined sensory profile, score 4 indicated slight changes, score 3 represented clearly perceptible

deviations, score 2 denoted marked deviations, and score 1 corresponded to very marked deviations. The final acceptability of each sample was calculated from the panel evaluation results as the arithmetic mean of the mean scores recorded for all sensory descriptors [30].

2.6.2. Color Analysis

Color characteristics of the meat snack samples were instrumentally assessed using a Chroma Meter CR-400 (Konica Minolta, Japan) [31]. Sample color was described in the CIELab system by recording lightness (L*), the red–green coordinate (a*), and the yellow–blue coordinate (b*). The overall color difference (ΔE) between the enriched samples and the control was calculated according to Equation (1):

$$\Delta E = [(\Delta L^*)^2 + (\Delta a^*)^2 + (\Delta b^*)^2]^{1/2}, \quad (1)$$

where:

$\Delta L^* = L^*_{ES} - L^*_{CS}, \Delta a^* = a^*_{ES} - a^*_{CS}, \Delta b^* = b^*_{ES} - b^*_{CS},$

$L^*_{ES}, a^*_{ES}, b^*_{ES}$ – the CIELab color coordinates of the experimental samples containing SBPP,

$L^*_{CS}, a^*_{CS}, b^*_{CS}$ – the corresponding coordinates of the control sample.

The browning index (BI), used as an indicator of brown color development, was determined using Equation (2):

$$BI = 588.235\left(\frac{a^*+1.75*L^*}{5.645*L^*+a^*-3.012*b^*} - 0.31\right), \quad (2)$$

Color saturation was characterized by chroma (C*), which reflects color intensity and was calculated as follows:

$$C^* = [(a^*)^2 + (b^*)^2]^{1/2}, \quad (3)$$

The hue angle (h, °), describing the dominant chromatic tone on a 0–360° scale, where 0° corresponds to bluish-red, 90° to yellow, 180° to green, and 270° to blue, was calculated according to Equation (4):

$$h^* = atan2(b^*, a^*), \quad (4)$$

2.6.3. Psysicochemical Analysis

The physicochemical characteristics of the meat snack samples were assessed by standard analytical procedures. MC was determined gravimetrically [32] in an SLW 115 SMART laboratory oven (Pol-Eco Aparatura, Wodzisław Śląski, Poland) at 103 ± 2 °C until no further mass change was observed. AC was measured according to ISO 936:1998 [33]. FC was determined by Soxhlet extraction [34] of the dehydrated material with organic solvents. PC was analyzed by the Kjeldahl method [35], based on nitrogen conversion, ammonia distillation, titration, and subsequent recalculation into protein content. pH measurement was performed at 20 °C using a digital pH meter (Mettler Toledo, Columbus, OH, USA). All measurements were performed in triplicate [36].

2.6.4. Analysis of Peroxide Value

Primary oxidation of the lipid fraction during storage was monitored through peroxide value (PV) determination [37]. For the analysis, the fat extracted from the sample was introduced into a reaction system containing distilled water, starch solution, chloroform, acetic acid, and potassium iodide, after which the liberated iodine was titrated with 0.01 mol/dm³ sodium thiosulfate. The PV, expressed as mEq O2/kg, was calculated using Equation (5):

$$PV = \frac{(V-V_1)K*0{,}00127}{m} * 100, \quad (5)$$

where:

V – the volume of sodium thiosulfate solution consumed in the main titration, cm^3;

V_1 – the corresponding volume used for the blank sample, cm^3;

K – the correction factor for the actual concentration of the sodium thiosulfate solution;

0.00127 – corresponds to the amount of substance equivalent to 1 cm^3 of 0.01 mol/dm^3 $Na_2S_2O_3$;

m – the mass of the extracted fat subjected to analysis, g.

2.6.5. Water Activity Determination

The aw values of the samples were recorded with a LabSwift-aw analyzer (Novasina AG, Lachen, Switzerland) using a rapid measurement approach [38]. This technique is intended for the assessment of free water present in the product matrix.

2.6.7. Microbiological Analysis

Microbiological quality evaluation of meat snacks included the enumeration of mesophilic aerobic and facultative anaerobic microorganisms (QMAFAnM), as well as yeasts and moulds, using ISO-based standard methods [39-42]. To prepare the initial suspension, 10 g of sample was aseptically mixed with 90 mL of sterile 0.1% buffered peptone water and homogenized for 2 min, yielding a 10^{-1} dilution [43]. Further decimal dilutions up to 10^{-3} were then prepared. All analyses were performed in triplicate, and 1 mL portions of the appropriate dilutions were plated onto the required culture media by either the pour plate or spread plate method, depending on the target group of microorganisms.

Enumeration of yeasts and moulds was performed on potato dextrose agar containing 2% chloramphenicol after incubation at 25 °C for 7 days. QMAFAnM was determined on plate count agar (casein-peptone glucose yeast extract agar) following incubation at 37 °C for 48 h [43]. After colony development, representative isolates were examined microscopically. Colonies with characteristic morphology were purified and subjected to routine assessment of cultural and morphological traits for tentative yeast identification, while bacterial cultures were additionally evaluated by Gram staining. Microbial counts were reported as CFU/g and expressed in $\log_{10}$ CFU/g. The calculations considered the colony number, plated dilution, and inoculated volume. The practical limit of detection under these conditions was close to 10 CFU/g, equivalent to approximately 1.0 $\log_{10}$ CFU/g [39-42]. Compliance of the obtained microbiological values was judged according to the applicable sanitary and regulatory criteria [43].

3. Results and discussion

3.1. Physicochemical Characterization of SBPP

The physicochemical profile of SBPP used as a functional ingredient in the meat snack formulations is summarized in Table 2. The MC of fruit pomace is largely affected by the drying conditions, including both the processing regime and the initial water content of the raw material. Under the drying conditions applied in the present study, the MC of SBPP reached 7.05%.

Similar MC values have been documented in the literature. In one study, researchers [24] reported an MC of 7.84% for apple pomace, whereas another investigation involving pomace powders in marshmallow-like confectionery systems recorded a value of 8.0% [44]. The proximity of these results to those obtained in the present work supports the consistency of our data and highlights the potential of dried SBPP for use in food formulations.

Table 2

Physicochemical characteristics of SBPP

Indicators	Value
MC, %	7.05 ± 0.28
AC, %	3.15 ± 0.16
TA, % expressed in malic acid	2.81 ± 0.01
pH	3.49 ± 0.01
PC, %	19.92 ± 0.15
FC, g/100 g DM	30.07 ± 0.15
a_w, c.u.	0.228 ± 0.003

MC – moisture content; AC – ash content; TA – titratable acidity; FC – fat content; PC – protein content; a_w – water activity. Results are presented as mean ± standard deviation.

The analyzed SBPP showed a TA of 2.81%, expressed as malic acid equivalent, and a pH of 3.49. The TA and pH values of sea buckthorn matrices vary significantly depending on the cultivar, ripening stage, and processing conditions. For example, a study on fresh sea buckthorn fruits reported an average pH ranging from 2.7 to 2.9 and TA between 2.0% and 3.7%, expressed as malic acid [45]. Another study on sea buckthorn pomace reported a pH of 3.53 and a TA of 4.48% for the pomace [46].

These values indicate a pronounced acidic character of the plant matrix, typical of fruits with a high content of organic acids, such as sea buckthorn (*Hippophae rhamnoides* L.). These properties can influence both the microbiological stability of the products in which it is incorporated and the final sensory profile.

The SBPP showed a high PC (19.92%) and FC (30.07%). In another study [47], a PC of 21.09 g/100 g DM was reported for sea buckthorn pomace, a value considered relatively high compared to other fruit pomaces, according to the data presented by [47]. This highlights the potential to explore techniques through which plant protein from sea buckthorn pomace could partially replace animal-derived protein.

The AC of the analyzed pomace (3.15%) falls within the range reported in the literature, where values can vary significantly depending on the cultivar, structural characteristics, processing conditions, and the origin of the raw material. Studies have shown that AC in pomace can range from 3.7% to 9.2% [48-50], while lower values of 2.02% or 2.09% have been reported in other studies, depending on the grape variety and processing method [49].

Water activity (a_w) is a key factor for sea buckthorn (*Hippophaë rhamnoides* L.) powder, affecting microbial stability, shelf life, and bioactive compound preservation. The powder shows very low a_w values (0.228 c.u.), well below 0.6 c.u. and comparable to or lower than other fruit powders, effectively inhibiting microbial growth and maintaining phenolic content and antioxidant activity during storage [51].

3.2. Bioactive Compounds and Antioxidant Capacity of SBPP

Table 3 summarizes the levels of major bioactive compounds and antioxidant-related parameters determined in SBPP, highlighting its potential technological and functional relevance.

SBPP contains measurable amounts of antioxidant-related bioactive compounds, including L-ascorbic acid (22.98 mg/100 g DM), carotenoids (96.4 mg/100 g DM), and total polyphenols (10.94 mg GAE/100 g DM). Its antioxidant activity, evaluated by the DPPH and

ABTS assays, reached 3.36 and 3.57 mg TE/100 g DM, respectively, indicating a moderate radical-scavenging capacity.

Table 3

Bioactive compounds and antioxidant-related parameters of SBPP

Indicators	Value
AAC, mg/100g DM	22.98 ± 0.03
TCC, mg/100g DM	96.41 ± 0.88
TPC, mg GAE/100 g DM	10.94 ± 0.16
Antioxidant activity:	
• DPPH, mg TE/100 g DM	3.36 ± 0.07
• ABTS, mg TE/100 g DM	3.57 ± 0.07

AAC – *L*-ascorbic acid content, TCC – total carotenoid content; TPC – total polyphenol content; ABTS – 2,2-azinobis-(3-ethylbenzothiazoline-6-sulfonates); DPPH – 2,2-diphenyl-1-picrylhydrazyl-hydrate; GAE – gallic acid equivalent; TE – Trolox equivalent; DM – dry matter. Results are presented as mean ± standard deviation.

Taken together, these results support the functional value of SBPP and are in line with published data on sea buckthorn powders and extracts, in which carotenoids, phenolic compounds, and related antioxidants are considered important contributors to oxidative protection [19, 52-57].

3.3. Sensory Analysis of Meat Snacks

The analyzed product, presented in the form of rings, exhibited a uniform and well-defined external appearance, free of surface defects or composition flow marks, indicating appropriate processing conditions. The color varied from light pink to deep orange, attributed to the incorporation of SBPP, with a homogeneous distribution of particles throughout the matrix and without visible voids or grayish areas. The aroma was characteristic of sea buckthorn–based products, displaying a pleasant, natural, and slightly spicy scent, with no foreign or off-notes detected. The taste was delicate and typical of sea buckthorn, pleasant and mildly spicy, without the presence of any undesirable flavors (Figure 2).

Figure 2. Sensory characteristics for the evaluation of meat snack samples: CS - control sample; S1- sample with 0.75% of SBPP; S2 - sample with 1.25 % of SBPP; S3 - sample with 2.5% of SBPP.

Compared to conventional meat snacks, the rings formulated with SBPP demonstrated a distinct sensory profile, characteristic of a functional and innovative product emphasizing natural ingredients such as sea buckthorn. While typical meat snacks exhibit a darker reddish-brown coloration, mainly resulting from the meat matrix and the maturation process, the analyzed samples presented lighter and more varied hues (pink to orange), attributed to the presence of plant-derived pigments. The aroma of the SBPP-enriched product was fresh, fruity, and more subtle than that of conventional counterparts. The taste of the analyzed rings was pleasant, delicate, and well-balanced. The texture was compact, smooth, and homogeneous, indicating a uniform structure suitable for development as an alternative or functional food product.

3.4. Color Analysis

The color parameters (CIELab) of meat snacks and SBPP was presented in Table 4.

Table 4

Color parameters (CIELab) of meat snacks and SBPP

CIELab Color Parameter	SBPP	Meat snack sample			
		CS	S1	S2	S3
L*	69.71 ± 0.71	47.85 ± 0.19	42.82 ± 0.15	48.10 ± 0.19	20.64 ± 0.12
a*	17.46 ± 0.54	19.65 ± 0.26	20.94 ± 0.9	22.02 ± 0.27	27.09 ± 0.49
b*	65.69 ± 0.41	32.42 ± 0.37	39.08 ± 0.46	38.61± 0.35	24.67 ± 0.13
ΔE	-	-	8.42 ± 0.40	5.41 ±0.41	31.21 ± 0.07
BI	202.56 ± 3.22	134.21 ± 1.91	206.73 ± 2.26	170.07 ± 2.19	354.21 ± 3.14
C*	62.97 ± 0.01	37.91 ± 0.05	44.34 ± 0.03	44.45 ±0.05	36.64 ± 0.04
h,°	75.12 ± 0.01	58.78 ± 0.01	61.82 ± 0.01	60.30 ± 0.01	42.32 ± 0.01
					

SBPP - sea buckthorn pomace powder; CS - control sample; S1- sample with 0.75% of SBPP; S2 - sample with 1.25 % of SBPP; S3 - sample with 2.5% of SBPP, L* - luminosity; a* - red/green component; b*- yellow/blue component; ΔE - total color difference; BI - browning index; C* - chroma; h°- hue angle. Results are presented as mean ± standard deviation.

SBPP is characterized by a bright color with intense yellow-reddish tones, as indicated by high a* values (17.46), reflecting a rich content of carotenoids such as β-carotene and zeaxanthin. These pigments are responsible for both the pronounced visual appearance and the antioxidant potential of the product [58-60]. Colorimetric analysis using CIELab parameters confirms that increasing SBPP concentration in meat snacks leads to a significant decrease in L*, from 47.85 in the control to 20.64 at 2.5% SBPP, indicating a darker, more intense coloration. This is consistent with findings that carotenoids absorb light in the blue region, contributing to red-orange hues [58-60].

The a* increases with SBPP concentration, confirming a shift toward red tones, while b* decreases, indicating reduced yellow intensity and a transition to darker red-orange shades. Such chromatic shifts are typical for carotenoid accumulation, especially β-carotene and zeaxanthin, as documented in sea buckthorn pomace and pulp [69-71]. The ΔE rises

substantially at higher SBPP levels, reflecting major visual changes, while the BI and C* also vary, with BI increasing due to pigment oxidation or Maillard reactions [61, 62].

These results align with studies showing that sea buckthorn by-products are rich in carotenoids, and their incorporation into foods significantly alters color parameters, enhances antioxidant activity, and increases visual appeal [58-60, 63, 64]

3.5 Psysicochemical Analysis of Meat Snacks

Table 5 summarizes the physicochemical characteristics of the meat snack samples supplemented with SBPP.

Table 5

Physicochemical characteristics of meat snacks

Indicators	Meat snack samples			
	CS	S1	S2	S3
MC, %	15.79 ± 0.39	8.94 ± 0.51	8.55 ± 0.77	7.93 ± 0.49
AC, %	8.36 ± 0.29	8.96 ± 0.17	9.0 ± 0.43	9.09 ± 0.11
FC, %	12.96 ± 0.76	14.13 ± 0.15	14.85 ± 0.60	15.52 ± 0.38
PC, %	59.16 ± 0.01	58.31 ± 0.04	60.95 ± 0.02	61.75 ± 0.02
pH	6.16 ± 0.03	5.88 ± 0.01	5.81 ± 0.06	5.65 ± 0.01
a_w	0.455 ± 0.002	0.370 ± 0.001	0.362 ± 0.001	0.358 ± 0.002
PV, mEq O2/kg	1.65 ± 0.01	1.60 ± 0.01	1.65 ± 0.02	1.70 ± 0.02

MC - moisture content; AC - ash content; FC - fat content; PC - protein content; a_w - water activity; PV - peroxid value. Results are presented as mean ± standard deviation.

A clear decreasing trend in MC was observed with the gradual increase of SBPP concentration, from 15.79% in the CS to 7.93% in the S3 formulation. This reduction in moisture is attributed to the high fiber content of sea buckthorn pomace, which enhances water binding and retention during processing, facilitating moisture loss during drying [47]. Similar moisture-decreasing effects have been reported in meat systems fortified with fruit pomace or dietary fibers, as these ingredients increase water-holding capacity and promote dehydration [65, 66].

Consistent with the decrease in MC, water activity (a_w) also dropped from 0.455 in CS to 0.358 in the S3 sample. Lower aw values indicate improved microbiological stability and shelf-life, as water activity below 0.6 generally inhibits most microbial growth [66]. Therefore, SBPP addition not only alters texture and color but also contributes to product safety and preservation.

The AC showed a slight but consistent increase with higher SBPP inclusion, from 8.36% in CS to 9.09% in the S3 sample, reflecting the high mineral composition of SBPP, which is rich in potassium, calcium, magnesium, and iron [65].

The FC also increased gradually (12.96% →15.52%), likely due to the contribution of residual lipids present in the pomace, including valuable unsaturated fatty acids such as oleic, linoleic, and palmitoleic acids [65].

The PC remained relatively stable across samples, ranging between 58.3% and 61.8%. The slight increase in the S3 sample may be explained by the concentration effect due to reduced moisture, as well as potential protein contribution from the pomace matrix [65].

The pH values decreased significantly from 6.16 in CS to 5.65 in the S3 sample, suggesting a mild acidifying effect associated with organic acids naturally present in sea

buckthorn (citric, malic, and quinic acids) [67, 68]. This acidification may improve the sensory profile and microbiological safety of the product.

The PV, an indicator of primary lipid oxidation, remained relatively stable across all samples (1.60–1.70 mEq O2/kg), indicating that SBPP addition did not accelerate oxidative degradation. The high concentration of natural antioxidants such as tocopherols and carotenoids in SBPP may help maintain lipid stability during processing and storage [5, 68-70, 85-87].

3.6. Microbiological Analysis of Meat Snacks

Microbiological quality indicators of meat snacks enriched with SBPP are presented in the Table 6.

Table 6

Microbiological quality indicators of meat snacks

Microbiological indicators	Meat snack samples			
	CS	S1	S2	S3
Minced mixture for meat snacks				
QMAFAnM, $\log_{10}$ CFU/g	5.20 ± 0.08	5.10 ± 0.06	5.05 ± 0.07	4.95 ± 0.05
Yeasts and moulds, $\log_{10}$ CFU/g	<1.0	<1.0	<1.0	<1.0
Coliform bacteria in 0,0001 g	Were not found	Were not found	Were not found	Were not found
Pathogenic microorganisms, including *Salmonella*	Were not found	Were not found	Were not found	Were not found
Meat snacks				
QMAFAnM, $\log_{10}$ CFU/g	3.80 ± 0.10	3.20 ± 0.09	3.00 ± 0.08	2.70 ± 0.07
Yeasts and moulds, $\log_{10}$ CFU/g	<1.0	<1.0	<1.0	<1.0
Coliform bacteria in 0,0001 g	Were not found	Were not found	Were not found	Were not found
Pathogenic microorganisms, including *Salmonella*	Were not found	Were not found	Were not found	Were not found

Note. QMAFAnM – quantity of mesophilic aerobic and facultative anaerobic microorganisms; CFU – colony-forming unit. Results are presented as mean ± standard deviation.

The minced mixtures demonstrated moderate background levels of QMAFAnM (≈5.0 $\log_{10}$ CFU/g), which is consistent with the expected microbiological load of chilled poultry raw material and processing under hygienic conditions. Importantly, the obtained total counts remained well below the regulatory maximum for minced meat (⩽5×10^6 CFU/g) established by the Uniform sanitary and epidemiological and hygienic requirements approved by Decision of the Customs Union Commission No. 299 (28 May 2010) [43]. This confirms the adequate microbiological quality of the initial raw material and indicates that the preparation procedures did not introduce significant contamination during chopping, mixing, and stuffing.

At the same time, it must be emphasized that the formulation included a starter culture (*SafePro EasyCure LC*) added at 25 g per batch. Therefore, the QMAFAnM values in minced mixtures may partially reflect the presence of beneficial microorganisms (e.g., lactic acid bacteria) originating from the starter preparation rather than representing spoilage flora.

After processing, the final dried snack samples showed a pronounced reduction of QMAFAnM (from ~5.0 $\log_{10}$ CFU/g in minced mixture to ~2.7–3.8 $\log_{10}$ CFU/g in the final product). This decrease can be explained by the hurdle effect produced by drying, reduced

available water, and formulation factors. The finished products exhibited very low water activity, ranging from 0.455 c.u. in the control to 0.358 c.u. in the S3 sample. Such aw levels strongly limit microbial growth and metabolic activity, making the product inherently resistant to microbial proliferation.

Increasing the level of sea buckthorn pomace powder (SBPP) was associated with lower QMAFAnM values in the final product. The literature further supports the biological plausibility of an additional "plant-derived" antimicrobial contribution: sea buckthorn (*Hippophae rhamnoides* L.) contains phenolics and other bioactive compounds with documented antimicrobial potential [71].

Evidence from applied meat research likewise indicates that sea buckthorn preparations can support microbial/quality stability depending on the matrix and dosage: for example, enrichment of cooked-smoked sausages with sea buckthorn ingredients (in combination with other extracts) has been associated with improved quality parameters and reported microbiological shelf-life benefits [72].

Yeasts and moulds were not detected (<1.0 $\log_{10}$ CFU/g) in either minced mixtures or final products. This result is technologically consistent with the extremely low aw reached after dehydration and indicates good control of airborne contamination and hygienic handling during processing. In dried meat snacks, yeasts and moulds are typically the primary concern during storage due to their greater tolerance to reduced moisture. Therefore, their absence supports the conclusion that the applied process and hygienic practices effectively prevented fungal contamination.

In line with sanitary requirements [43], the absence of coliform bacteria (including *E. coli*) and major pathogens such as *Salmonella spp., Listeria monocytogenes, Staphylococcus aureus*, and sulfite-reducing clostridia is the most critical indicator of microbiological safety for the investigated product category. The overall microbial profile of the final snacks, combined with the low aw and slightly reduced pH, demonstrates that the developed formulation provides a microbiologically stable product when produced under appropriate sanitary conditions.

5. Conclusions

The inclusion of SBPP in meat snack formulations exerted a clear and practically significant influence on the quality of the final products. These findings confirm the potential of this fruit-processing by-product for effective valorization in meat technology, not only as a source of bioactive constituents, but also as a technologically functional ingredient able to modulate critical parameters associated with product stability and consumer perception of dried snack products.

The pomace evaluated in this work contained considerable amounts of carotenoids, polyphenols, and ascorbic acid, which were associated with significant antioxidant capacity and a well-defined pigment composition. These properties provide a strong functional rationale for its incorporation into meat systems. These properties are highly relevant for modern product development, where oxidative stability, natural ingredient composition, and clean-label approaches are increasingly prioritized. In this context, SBPP can be considered a promising multifunctional ingredient that simultaneously supports both quality and product differentiation.

A consistent effect of SBPP addition was the progressive reduction in moisture content and water activity with increasing inclusion levels. This finding has strong technological

significance because water activity is one of the most critical factors governing the microbiological robustness and overall stability of dried meat snacks. The observed trend indicates that SBPP may contribute to the formation of less favorable conditions for microbial development and, consequently, may enhance product safety and stability under proper processing and packaging conditions. In addition, enrichment with SBPP resulted in increased ash and fat contents, reflecting the mineral- and lipid-containing fractions of the pomace and highlighting its potential contribution to the nutritional profile of the product. The slight decrease in pH further confirmed the natural acidic character of sea buckthorn, which may provide an additional preservation-supporting effect and contribute to a more balanced sensory profile.

Colorimetric evaluation confirmed that SBPP inclusion strongly influenced the visual properties of the snacks. The increase in red–orange tonalities, driven by carotenoid pigments, produced a distinctive and attractive appearance that can be considered an important advantage for snack-type products, where visual perception strongly affects consumer acceptance. This effect is particularly valuable because it is achieved using a natural, plant-derived ingredient and therefore supports product positioning toward more natural and functional concepts. Sensory evaluation complemented the instrumental results by indicating that the SBPP-enriched snacks retained a pleasant color, fresh aroma, and balanced taste characteristics, which suggests that functional enrichment can be achieved without negatively affecting key sensory expectations.

Overall, the findings demonstrate that sea buckthorn pomace powder is a valuable ingredient for the development of meat-based snack products with improved technological characteristics and enhanced functional positioning. The study is scientifically and practically significant because it combines product quality optimization with sustainable resource utilization, offering an innovative pathway for integrating fruit processing residues into high-value meat formulations. The results provide a strong foundation for further optimization of formulation ratios and for comprehensive assessment of long-term quality changes during storage, including oxidative processes, microbiological stability, and broader consumer acceptance. In this way, the present work contributes to the development of innovative, sustainable, and competitive meat snack products aligned with current demands for functionality, stability, and responsible use of food industry by-products.

Acknowledgments*: This work was supported by a grant of the Ministry of Education and Research, CCDI-UEFISCDI, project number PN-IV-PCB-ROMD-2024-0135, within PNCDI IV and NARD, 25.80013.5107.29ROMD.*

Conflicts of Interest: The authors declare no conflict of interest.

References

1. Lordan R, Tsoupras A, Zabetakis I (2019) Phytochemicals in functional foods: Bioactivity and role in disease prevention. Foods 8:398. https://doi.org/10.3390/foods8090398
2. Granato D, Nunes DS, Barba FJ (2017) An integrated strategy between food chemistry, biology, nutrition, pharmacology, and statistics in the development of functional foods: A critical review. Trends Food Sci Technol 62:13–22. https://doi.org/10.1016/j.tifs.2016.12.010
3. Galanakis CM (2012) Recovery of high added-value components from food wastes: Conventional, emerging technologies and commercialized applications. Trends Food Sci Technol 26:68–87. https://doi.org/10.1016/j.tifs.2012.03.003

4. Bal LM, Meda V, Naik SN, Satya S (2011) Sea buckthorn berries: A potential source of valuable nutrients for nutraceuticals and cosmeceuticals. Food Res Int 44:1718–1727. https://doi.org/10.1016/j.foodres.2011.03.002
5. Dulf FV, Vodnar DC, Socaciu C (2013) Carotenoids and tocopherols as antioxidants in sea buckthorn pomace oil. Chem Pap 67:1200–1209. https://doi.org/10.2478/s11696-013-0414-6
6. Zeb A (2004) Chemical and nutritional constituents of sea buckthorn juice. Pak J Nutr 3:99–106.
7. Górnaś P, Siger A, Czubinski J (2014) Antioxidant activity and phenolic content in cold-pressed sea buckthorn oils. J Am Oil Chem Soc 91:129–136. https://doi.org/10.1007/s11746-013-2354-1
8. Christaki E (2012) Hippophae rhamnoides L. (sea buckthorn): A potential source of nutraceuticals. Food Public Health 2:69–72.
9. Li TSC, Beveridge THJ (2003) Sea Buckthorn (Hippophae rhamnoides L.): Production and Utilization. NRC Research Press, Ottawa.
10. Yang B, Kallio H (2001) Fatty acid composition of lipids in sea buckthorn (Hippophae rhamnoides L.) berries of different origins. J Agric Food Chem 49:1939–1947. https://doi.org/10.1021/jf001059s
11. Viuda-Martos M, Fernández-López J, Pérez-Álvarez JA (2010) Effect of adding citrus fibre on quality characteristics of frankfurters with different fat levels. Food Sci Technol Int 16:415–423. https://doi.org/10.1177/1082013210368429
12. Sánchez-Zapata E et al (2010) Effect of tiger nut fibre on quality characteristics of pork burger. Meat Sci 85:70–76. https://doi.org/10.1016/j.meatsci.2009.12.006
13. Gómez M, Lorenzo JM (2013) Effect of natural antioxidants on colour and lipid stability of dry-cured meat products. Antioxidants 2:106–123. https://doi.org/10.3390/antiox2030106
14. Shahidi F, Ambigaipalan P (2015) Phenolics and polyphenolics in foods, beverages and spices: Antioxidant activity and health effects. J Funct Foods 18:820–897. https://doi.org/10.1016/j.jff.2015.06.018
15. ISO (1982) ISO 1026:1982 Fruit and vegetable products—Determination of dry matter content by drying under reduced pressure and of water content by azeotropic distillation. International Organization for Standardization, Geneva.
16. ISO (2003) ISO 763:2003 Fruit and vegetable products—Determination of insoluble ash in hydrochloric acid. International Organization for Standardization, Geneva.
17. ISO (1998) ISO 750:1998 Fruit and vegetable products—Determination of titratable acidity. International Organization for Standardization, Geneva.
18. ISO ISO 6557-2 Determination of ascorbic acid content—Potentiometric titration method. International Organization for Standardization, Geneva.
19. Wu D et al (2024) Optimizing the solvent selection of the ultrasound-assisted extraction of sea buckthorn (Hippophae rhamnoides L.) pomace: Phenolic profiles and antioxidant activity. Foods 13:482. https://doi.org/10.3390/foods13030482
20. Lv J, Li L, Liang Z, Wu W, Zhang N, Jia Q (2025) Extraction of bound polyphenols from Elaeagnus angustifolia L. by ultrasonic-assisted enzymatic hydrolysis and evaluation of its antioxidant activity in vitro. Foods 14. https://doi.org/10.3390/foods14091567
21. Myo H, Khat-Udomkiri N (2022) Optimization of ultrasound-assisted extraction of bioactive compounds from coffee pulp using propylene glycol as a solvent and their antioxidant activities. Ultrason Sonochem 89. https://doi.org/10.1016/j.ultsonch.2022.106127
22. Gil-Martínez L et al (2025) Green extraction of phenolic compounds from artichoke by-products: Pilot-scale comparison of ultrasound, microwave, and combined methods with pectinase pre-treatment. Antioxidants 14. https://doi.org/10.3390/antiox14040423
23. Muzykiewicz-Szymańska A et al (2024) The optimisation of ultrasound-assisted extraction for the polyphenols content and antioxidant activity on Sanguisorba officinalis L. aerial parts using response surface methodology. Appl Sci 14. https://doi.org/10.3390/app14209579
24. Popescu L, Ceșco T, Gurev A, Ghendov-Mosanu A, Sturza R, Tarna R (2022) Impact of apple pomace powder on the bioactivity, and the sensory and textural characteristics of yogurt. Foods 11:3565. https://doi.org/10.3390/foods11223565
25. Gurev A, Cesko T, Dragancea V, Ghendov-Mosanu A, Pintea A, Sturza R (2023) Ultrasound- and microwave-assisted extraction of pectin from apple pomace and its effect on the quality of fruit bars. Foods 12:2773. https://doi.org/10.3390/foods12142773

26. Paulpriya K, Packia Lincy M, Tresina Soris P, Veerabahu Ramasamy M (2015) In vitro antioxidant activity, total phenolic and total flavonoid contents of aerial part extracts of Daphniphyllum neilgherrense (wt.) Rosenth. Ethnopharm J Biol Innov 4:257–268.
27. Arnao MB, Cano A, Alcolea JF, Acosta M (2001) Estimation of free radical-quenching activity of leaf pigment extracts. Phytochem Anal 12:138–143. https://doi.org/10.1002/pca.574
28. Waterman P, Mole S (1994) Analysis of Phenolic Plant Metabolites. Wiley-Blackwell, Hoboken
29. Ghendov-Mosanu A et al (2020) Potential application of Hippophae rhamnoides in wheat bread production. Molecules 25:1272. https://doi.org/10.3390/molecules25061272
30. ISO (2017) ISO 6658:2017 Sensory analysis—Methodology—General guidance. International Organization for Standardization, Geneva
31. Loypimai P, Moongngarm A, Chottanom P (2016) Thermal and pH degradation kinetics of anthocyanins in natural food colorant prepared from black rice bran. J Food Sci Technol 53:461–470. https://doi.org/10.1007/s13197-015-2002-0
32. ISO (2023) ISO 1442:2023 Meat and meat products—Determination of moisture content—Reference method. International Organization for Standardization, Geneva
33. ISO (1998) ISO 936:1998 Meat and meat products—Determination of ash (Reference method). International Organization for Standardization, Geneva
34. ISO (1973) ISO 1443:1973 Meat and meat products—Determination of total fat content. International Organization for Standardization, Geneva
35. ISO (2016) ISO 16634-2:2016 Food products—Determination of total nitrogen content by combustion according to the Dumas principle and calculation of the crude protein content—Part 2: Cereals, pulses and milled cereal products. International Organization for Standardization, Geneva
36. AOAC (2012) Official Methods of Analysis, 19th edn. Association of Official Analytical Chemists, Washington, DC
37. ISO (2017) ISO 3960:2017 Animal and vegetable fats and oils—Determination of peroxide value—Iodometric (visual) endpoint determination. International Organization for Standardization, Geneva
38. Serin S, Turhan K, Turhan M (2018) Correlation between water activity and moisture content of Turkish flower and pine honeys. Food Sci Technol 38:238–243. https://doi.org/10.1590/fst.16517
39. SM EN ISO (2017) 6579-1:2017 Microbiology of food and feed products—Horizontal method for the detection of bacteria of the genus Salmonella spp.
40. SM ISO (2010) 4831:2010 Microbiology of food and feed—Horizontal method for the detection and enumeration of coliform bacteria
41. ISO (2003) ISO 4833:2003 Microbiology of food and animal feeding stuffs—Horizontal method for the enumeration of microorganisms—Colony-count technique at 30 °C. International Organization for Standardization, Geneva
42. Sandulachi E, Netreba N, Macari A, Sandu I, Boestean O, Dianu I (2023) Phytopathogenic microbiote of sea buckthorn and impact on storage. J Eng Sci 29:176–189
43. Customs Union Commission (2010) Uniform sanitary and epidemiological and hygienic requirements for products subject to sanitary and epidemiological supervision (Control). Decision No. 299, 28 May 2010
44. Ghendov-Moșanu A (2018) Compuși biologic activi de origine horticolă pentru alimente funcționale. Tehnica–UTM, Chișinău
45. Tiitinen KM, Hakala MA, Kallio HP (2005) Quality components of sea buckthorn (Hippophae rhamnoides) varieties. J Agric Food Chem 53:1692–1699. https://doi.org/10.1021/jf0484125
46. Dianu I, Macari A, Baerle A, Pintea A, Cusmenco T, Netreba N, Sandu I (2024) Physical and chemical parameters of sea-buckthorn (Hippophae rhamnoides L.) berries pomace. Mod Technol Food Ind p 31
47. Jurevičiūtė I, Keršienė M, Bašinskienė L, Leskauskaitė D, Jasutienė I (2022) Characterization of berry pomace powders as dietary fiber-rich food ingredients with functional properties. Foods 11:716. https://doi.org/10.3390/foods11050716
48. Pereira P, Palma C, Ferreira-Pêgo C, Amaral O, Amaral A, Ríjo P, Gregório J, Palma L, Nicolai M (2020) Grape pomace: A potential ingredient for human diet. Foods 9:1772. https://doi.org/10.3390/foods9121772
49. Jin Q, O'Hair J, Stewart A, O'Keefe S, Neilson A, Kim Y, McGuire M, Lee A, Wilder G, Huang H (2019) Compositional characterization of different industrial grape pomaces from Virginia and potential valorization of major components. Foods 8:667. https://doi.org/10.3390/foods8120667
50. Maj G, Klimek K, Kapłan M, Buczyński K, Borkowska A (2024) Combustion and energy parameters of grape pomace/waste in wine production—Regent grafted on rootstock. Energies 17:5426. https://doi.org/10.3390/en17215426

51. Tkacz K, Wojdyło A, Michalska-Ciechanowska A, Turkiewicz I, Lech K, Nowicka P (2020) Influence of carrier agents, drying methods, and storage time on physico-chemical properties and bioactive potential of encapsulated sea buckthorn juice powders. Molecules 25:3801. https://doi.org/10.3390/molecules25173801
52. Dienaitė L, Pukalskas A, Pukalskienė M, Pereira C, Matias A, Venskutonis P (2020) Phytochemical composition, antioxidant and antiproliferative activities of defatted sea buckthorn berry pomace fractions recovered by pressurized ethanol and water. Antioxidants 9:274. https://doi.org/10.3390/antiox9040274
53. Criste A, Urcan A, Bunea A, Furtuna F, Oláh N, Madden R, Corcionivoschi N (2020) Phytochemical composition and biological activity of berries and leaves from four Romanian sea buckthorn varieties. Molecules 25:1170. https://doi.org/10.3390/molecules25051170
54. Raal A, Rusalepp L, Chiru T, Ciobanu N, Talvistu K, Shusta M, Koshovyi O, Pîsă T (2023) Polyphenolic compounds and antioxidant activity of sea buckthorn. Phyton. https://doi.org/10.32604/phyton.2023.042723
55. Rösch D, Mügge C, Fogliano V, Kroh L (2004) Antioxidant oligomeric proanthocyanidins from sea buckthorn pomace. J Agric Food Chem 52:6712–6718. https://doi.org/10.1021/jf040241g
56. Korekar G, Dolkar P, Singh H, Srivastava R, Stobdan T (2014) Variability and the genotypic effect on antioxidant activity, total phenolics, carotenoids and ascorbic acid content in seventeen natural populations of seabuckthorn from trans-Himalaya. LWT Food Sci Technol 55:157–162. https://doi.org/10.1016/j.lwt.2013.09.006
57. Teleszko M, Wojdyło A, Rudzińska M, Oszmiański J, Golis T (2015) Analysis of lipophilic and hydrophilic bioactive compounds content in sea buckthorn berries. J Agric Food Chem 63:4120–4129. https://doi.org/10.1021/acs.jafc.5b00564
58. Sharma M, Hussain S, Shalima T, Aav R, Bhat R (2022) Valorization of seabuckthorn pomace to obtain bioactive carotenoids using green extraction techniques. Ind Crops Prod 176:114257. https://doi.org/10.1016/j.indcrop.2021.114257
59. Popovici V, Boldianu A, Pintea A, Caraus V, Ghendov-Moșanu A, Subotin I, Druță R, Sturza R (2024) In vitro antioxidant activity of liposomal formulations of sea buckthorn and grape pomace. Foods 13:2478. https://doi.org/10.3390/foods13162478
60. Pop R, Weesepoel Y, Socaciu C, Pintea A, Vincken J, Gruppen H (2014) Carotenoid composition of berries and leaves from six Romanian sea buckthorn varieties. Food Chem 147:1–9. https://doi.org/10.1016/j.foodchem.2013.09.083
61. Raudonė L, Puzerytė V, Vilkickytė G, Niekyte A, Lanauskas J, Viškelis J, Viškelis P (2021) Sea buckthorn leaf powders: Impact of cultivar and drying mode on antioxidant, phytochemical, and chromatic profile. Molecules 26:4765. https://doi.org/10.3390/molecules26164765
62. Roman D, Condurache N, Stănciuc N, Andronoiu D, Aprodu I, Enachi E, Barbu V, Bahrim G, Stanciu S, Râpeanu G (2022) Advanced composites based on sea buckthorn carotenoids for mayonnaise enrichment. Polymers 14:548. https://doi.org/10.3390/polym14030548
63. Gherasim C, Focșan M, Ciont C, Bunea A, Rugină D, Pintea A (2024) Stability and bioaccessibility of carotenoids from sea buckthorn pomace encapsulated in alginate hydrogel beads. Nutrients 16:2726. https://doi.org/10.3390/nu16162726
64. Mihalcea L, Turturică M, Cucolea E, Dănilă G, Dumitrașcu L, Coman G, Constantin O, Grigore-Gurgu L, Stănciuc N (2021) CO_2 supercritical fluid extraction of oleoresins from sea buckthorn pomace: Evidence of advanced bioactive profile and selected functionality. Antioxidants 10:1681. https://doi.org/10.3390/antiox10111681
65. Haque A, Ahmad S, Azad Z, Adnan M, Ashraf S, Farag M (2023) Incorporating dietary fiber from fruit and vegetable waste in meat products: A systematic approach. PeerJ 11:e14977. https://doi.org/10.7717/peerj.14977
66. Gul K, Varli S, Prava B, Kumar D, Mishra B, Mishra J, Paital B, Rath P, Kumar M, Reddy B, Pati P, Panda S (2023) Properties and physiological effects of dietary fiber-enriched meat products: A review. Front Nutr 10:1275341. https://doi.org/10.3389/fnut.2023.1275341
67. Iskakov B, Kapshakbaeva Z, Kardenov S, Tokayev S, Tokhtarova S (2024) Influence of sea buckthorn extract powder on physicochemical, structural and mechanical properties of minced meat mince. Bull Shakarim Univ Technol Sci 3(15):26. https://doi.org/10.53360/2788-7995-2024-3(15)-26
68. Sărăcilă M, Untea A, Panaite T, Varzaru I, Oancea A, Turcu R, Vlaicu P (2022) Effects of supplementing sea buckthorn leaves and chromium (III) in broiler diet on meat quality. Antioxidants 11:2220. https://doi.org/10.3390/antiox11112220

69. Mäkinen S, Hellström J, Mäki M, Korpinen R, Mattila P (2020) Bilberry and sea buckthorn leaves and their subcritical water extracts prevent lipid oxidation in meat products. Foods 9:265. https://doi.org/10.3390/foods9030265
70. Orczewska-Dudek S, Pietras M, Nowak J (2018) The effect of amaranth seeds, sea buckthorn pomace and black chokeberry pomace in feed mixtures for broiler chickens. Ann Anim Sci 18:501–523. https://doi.org/10.2478/aoas-2018-0002
71. Netreba N, Sandulachi E, Macari A, Popa S, Ribintev I, Sandu I, Boestean O, Dianu I (2024) A study on the fruiting and correlation between the chemical indicators and antimicrobial properties of Hippophae rhamnoides L. Horticulturae 10:137. https://doi.org/10.3390/horticulturae10020137
72. Bukarbayev K, Abzhanova S, Baibolova L, Zhaksylykova G, Kulazhanov T, Vasilenko V, Jetpisbayeva B, Katasheva A, Sabraly S, Yerzhigitov Y (2025) Effect of hemp protein and sea buckthorn extract on quality and shelf life of cooked-smoked sausages. Foods 14:2730. https://doi.org/10.3390/foods14152730
73. Popovici V, Boldianu A, Pintea A, Caraus V, Ghendov-Moșanu A, Subotin I, Druță R, Sturza R (2024) In vitro antioxidant activity of liposomal formulations of sea buckthorn and grape pomace. Foods 13:2478. https://doi.org/10.3390/foods13162478
74. Pop R, Weesepoel Y, Socaciu C, Pintea A, Vincken J, Gruppen H (2014) Carotenoid composition of berries and leaves from six Romanian sea buckthorn varieties. Food Chem 147:1–9. https://doi.org/10.1016/j.foodchem.2013.09.083
75. Sharma M, Hussain S, Shalima T, Aav R, Bhat R (2022) Valorization of seabuckthorn pomace to obtain bioactive carotenoids using green extraction techniques. Ind Crops Prod 176:114257. https://doi.org/10.1016/j.indcrop.2021.114257

Citation: Dianu, I., Macari, A., Dabija, A., Netreba, N., Sandu, I., Oroian, M., Buculei, A., Gâtlan, A.-M., Cușmenco, T. (2026). Evaluation of the impact of sea buckthorn pomace addition on the physicochemical and quality properties of meat snack products. *Journal of Engineering Science*. 2026, 33 (1), pp. 165-182. https://doi.org/10.52326/jes.utm.2026.33(1).11.

Submission of manuscripts: jes@meridian.utm.md